

**Progress towards a more sensitive measurement of
the electron electric dipole moment with YbF**

Jack Alexander Devlin

A thesis presented for the degree of
Doctor of Philosophy

Department of Physics
Imperial College London
United Kingdom

27 July 2015

ABSTRACT

The electron is predicted to have a small electric dipole moment (eEDM), although so far no one has been able to measure this experimentally. The size of the eEDM is strongly connected to how badly time-reversal (T) symmetry is broken by nature. The Standard Model of particle physics, which has a small amount of T violation, predicts an unmeasurably tiny eEDM: $|d_e| \simeq 10^{-38} e\text{cm}$. However, it is suggested that there should be additional T-violating processes to account for the matter-antimatter asymmetry in the universe. These could lead to a detectable eEDM near to the current limit $|d_e| < 8.7 \times 10^{-29} e\text{ cm}$ (90% confidence).

Ramsey spectroscopy on paramagnetic, polar molecules has proved a very effective method for measuring eEDMs. In this thesis I explain the progress that has been made towards using ytterbium fluoride (YbF) for a new, improved measurement of the eEDM. I discuss the current operation of the experiment, and the systematic effects connected with the experiment. The statistical uncertainty of the experiment is analysed, and shown to be dominated by photon counting statistics. Then, a list of improvements to the machine are described, and simulated using rate equations and the optical Bloch equations. Taken together, these improvements enhance the sensitivity of the experiment by a factor of eleven, thus, it can be used in the near future to make a world-leading measurement of the electron EDM.

DECLARATION

I declare that contents of this thesis are my own work, and that contributions from other sources are appropriately acknowledged and referenced.

The copyright of this thesis rests with the author and is made available under a Creative Commons Attribution Non-Commercial No Derivatives licence. Researchers are free to copy, distribute or transmit the thesis on the condition that they attribute it, that they do not use it for commercial purposes and that they do not alter, transform or build upon it. For any reuse or redistribution, researchers must make clear to others the licence terms of this work

ACKNOWLEDGEMENTS

First and foremost, I would like to acknowledge all the other people who have worked with me on the experiment: to Dhiren and Joe, thank you for sharing all of your experience and teaching me how to run the machine. Thanks also to Izzie for many great discussions about the various ways to improve the experiment and for all your work during the last couple of years getting those improvements working. Almost none of the equipment discussed in this thesis was made without help from Ben, thank you for always taking the time to listen and advise me. Mike—your discussions in our group meetings and assistance in the molecular angular momentum calculations were invaluable. Thank you also to Jon, Steve and Val for making such excellent equipment for our machine, and to Sanja for making everything run so smoothly. I would like to particularly acknowledge my two supervisors: To Ed—I feel lucky to have had the chance to do such exciting research with you and I am very grateful for your detailed comments on my thesis. To Jony—thank you for answering so many of my questions, and for always putting things in perspective (normally with a game of Frisbee). To all members of CCM and Bay 3 in particular—you’ve made the last four years really fun, thank you.

Finally, to my family and especially to Sherena—I would never have finished this thesis without your limitless patience, interest and encouragement.

CONTENTS

1. <i>Introduction</i>	16
1.1 Why particles could have permanent electric dipole moments	16
1.2 Why particles should have permanent electric dipole moments	18
1.3 Measuring the size of the electron EDM	20
1.3.1 The eEDM interaction in atoms and molecules	21
1.3.2 Choice of molecule	23
1.3.3 Recent results	25
1.3.4 Current experiments to measure the eEDM	26
1.4 Thesis overview	30
2. <i>Overview of the experiment</i>	32
2.1 The fundamental principle behind the experiment	32
2.2 The structure of YbF	34
2.2.1 Electronic structure	35
2.2.2 Vibrational, rotational and other structure of $X^2\Sigma^+$	36
2.2.3 A $^2\Pi_{1/2}$ wavefunction	39
2.2.4 Transitions	41
2.2.5 Simplified energy level structure	43
2.3 The experimental apparatus	44
2.3.1 YbF beam machine	46
2.3.2 Laser beam generation	48
2.3.3 High voltage generation	49

2.3.4	Radio frequency generation	50
2.3.5	Magnetic field generation	51
2.4	The experimental sequence	51
2.4.1	A shot	52
2.4.2	Simplified eEDM experiment	58
2.4.3	A more comprehensive eEDM experiment: A block	60
2.4.4	Clusters	63
2.5	Data acquisition and analysis	64
2.5.1	Detectors	64
2.5.2	Extracting channels from a block	67
2.5.3	Blind	70
2.5.4	Statistical analysis of channel values	71
3.	<i>New systematic errors</i>	76
3.1	Introduction	76
3.2	Previous systematic errors	78
3.3	RF discharge systematic error	81
3.3.1	Suppressing the discharges and assigning a systematic error . .	84
3.4	RF rotation systematic	86
3.4.1	Diagnosing the problem	86
3.4.2	Amplifying the systematic	91
3.4.3	Final systematic error	94
3.5	High voltage supplies systematic	96
3.5.1	Discovery	96
3.5.2	dc charging currents	99
3.5.3	ac charging currents	101
3.5.4	Other explanations	103
3.6	Conclusion and next steps	104

4. <i>Sensitivity analysis</i>	106
4.1 Introduction	106
4.2 Shot noise limit	106
4.3 Magnetic field noise	111
4.4 Conclusion	115
5. <i>Overview of improvements to the experiment</i>	116
5.1 Increasing sensitivity by increasing signal	116
5.2 New experimental apparatus	118
5.3 The new experimental sequence	121
5.3.1 A shot	121
5.3.2 Extracting a signal proportional to the eEDM phase in the new scheme	125
5.4 Rough calculations of the increase in signal	126
5.4.1 New pumping scheme	126
5.4.2 New detection scheme	135
5.4.3 Rate equation calculations	136
5.4.4 Microwave π -pulse efficiency	137
5.5 Conclusion and overview of the next half of the thesis	139
6. <i>Derivation of the optical Bloch equations for the evolution of YbF in optical, microwave and rf fields</i>	141
6.1 Overview	141
6.2 Equation of motion	141
6.3 Coherent interaction terms	142
6.4 Relaxation terms	144
6.4.1 Relaxation terms in a two level system	146
6.4.2 Relaxation terms in a $J' = 1 \rightarrow J = 1$ system	146
6.4.3 Relaxation terms in the YbF System	149

7. <i>Solutions of the optical Bloch equations for the improved pumping and de-</i>	
<i>tection schemes</i>	152
7.1 Overview	152
7.2 Dark States	154
7.2.1 Angular momentum dark states and their destabilisation . . .	154
7.2.2 CPT dark states	164
7.3 Simulations of the new detection scheme	174
7.3.1 Dark states of the new detection scheme	175
7.3.2 Optimising the parameters for the new detection scheme . . .	180
7.3.3 Transverse Doppler broadening	185
7.3.4 Conclusion on the new detection scheme	187
7.4 Simulations of the new pumping scheme	188
7.4.1 Preliminary considerations	188
7.4.2 Initial simulation	189
7.4.3 Fraction pumped for various rf and laser powers	191
7.4.4 Comparison of results with simple models in section 5.4.1 . . .	192
7.4.5 Doppler broadening	194
7.4.6 Conclusion to the discussion of the new pumping scheme . . .	195
7.5 Conclusions on OBE simulations	196
8. <i>Conclusion and outlook</i>	199
8.1 Systematic Errors	199
8.2 Sensitivity	200
8.3 Outlook	201
Appendix	205
A. <i>Quantum mechanical rotation matrices</i>	206

<i>B. Matrix elements for YbF</i>	207
B.1 Form of the wavefunctions	208
B.1.1 $A^2\Pi_{1/2}$	208
B.1.2 $X^2\Sigma^+$	209
B.2 Calculating the projection factors	210
B.2.1 Projection factors for the rf transitions	210
B.2.2 Microwave projection factors	212
B.2.3 Optical projection factors	214
B.3 g factors	219
<i>C. Permissions</i>	221

LIST OF FIGURES

1.1	An electron undergoing the parity and time reversal transformations .	17
1.2	The energy level structure of $X^2\Sigma^+(v=0, N=0)$ at 12.5 kVcm^{-1} and ηE_{eff} as a function of the applied field.	24
1.3	Allowed regions for d_e and C_S from the Tl, YbF and ThO results . .	26
1.4	Diagram of the YbF fountain	29
2.1	Classical and quantum spin precession	33
2.2	Vibrational and rotational structure of the $X^2\Sigma^+$ term	37
2.3	Ω -doubling and hyperfine splitting in the $A^2\Pi_{1/2}(J'=1/2)$ term . .	40
2.4	A few relevant transitions between YbF energy levels	41
2.5	A simplified energy level structure for YbF	44
2.6	The YbF beam machine	45
2.7	Two pictures of the main eEDM vacuum chamber	47
2.8	The apparatus used to generate the high voltage, laser, rf and mag- netic fields used in the experiment.	48
2.9	Clearing out $X^2\Sigma^+(v=0, N=0, F=1)$ with the pump laser	53
2.10	Stark shifting of $X^2\Sigma^+(v=0, N=0)$ and effect of an rf π -pulse . . .	54
2.11	Splitting of YbF energy levels due to Zeeman and eEDM interactions	55
2.12	Measurement of spin precession angle with a second RF pulse	56
2.13	Detecting the population in $ 0,0\rangle$	57
2.14	Integrated signal in the top detector as a function of applied magnetic field.	58
2.15	Interference fringes for two electric field directions	59

2.16	Histogram and Q-Q plot of $\langle[\text{EDM}]\rangle$ from July 2013 data run	72
2.17	A histogram of $\langle[\text{EDM}]\rangle$ replicate trimmed means	73
3.1	Location of rf ammeter and rf induced discharge	81
3.2	Multipactor discharges and direction of rf leakage currents	83
3.3	Variation of $\langle[\text{EDM}]\rangle$ with manual state for March and July data runs	86
3.4	Approximate polarisation of side injected rf magnetic field.	88
3.5	Polarisation and amplitude of rf field from high voltage feedthroughs	90
3.6	The rf ferrite box	93
3.7	Control voltages and charging currents for high voltage supplies . . .	98
3.8	dc and ac charging current paths in the eEDM machine	100
4.1	Comparison of measured sensitivity to shot noise limit for March and July data runs	111
4.2	$\langle\{B\}_{\text{MAG}}\rangle$ and $\langle\{E\}_{\text{MAG}}\rangle$ for July 2013 data run	112
4.3	$\langle\{E\}_{\text{MAG}}\rangle$ versus $\langle\{\text{EDM}\}\rangle$ for quiet blocks in the July 2013 data run.	115
5.1	The improved pumping and detection regions	119
5.2	Views of the rf coils and microwave transmission lines	120
5.3	Transitions driven in the new pumping region	121
5.4	Transitions driven in the new probing regions	124
5.5	Fractional increase in $ 0,0\rangle$ if new pumping scheme is applied to a beam of rotational temperature T.	128
5.6	Levels and transitions in the simple rate model	129
5.7	Population left in the pumped levels for several laser intensities . . .	134
5.8	Number of photons scattered during the improved detection scheme predicted by the simple rate equation model.	137
5.9	MEEP Simulations of the microwave transmission line	138
5.10	Fraction of a π -pulse experienced by molecules travelling through the microwave transmission line	139

6.1	An excited state superposition decaying to a ground state superposition	148
7.1	New pumping and detection schemes	153
7.2	Angular momentum dark state if a $F = 2 \rightarrow F' = 1$ transition is driven with π -polarised light	155
7.3	Quasi-steady-state behaviour of a $F = 2 \rightarrow F' = 1$ system driven polarisation modulated light	158
7.4	Excited state population as a function of the modulation rate, strength and modulating function	159
7.5	Optimum values of the modulation rate and strength	161
7.6	Optimum modulation rate if the driving laser is detuned	162
7.7	Excited state population as a function of $\bar{\Omega}$	163
7.8	A Lambda system	165
7.9	n stable ground states coupled to a single excited state $ e\rangle$	166
7.10	Excited state population in a Lambda system as function of Δ and Ω_1	169
7.11	The fraction of the total intensity I_1/I_{tot} and the decay rate $\Delta_1/\bar{\Omega}_{\text{Av}}$ that maximise the excited state population as a function of $\bar{\Omega}_{\text{Av}}$ and γ_1	171
7.12	The detunings that maximise the excited state population in a lambda system with unequal partial decay rates	172
7.13	Maximum steady excited population from the OBEs, compared to the rate equation model for $N_g = 2$ and $N_g = 3$	174
7.14	Molecules evolving into a dark state during the new detection scheme	175
7.15	Matrix plot of the steady state solution of the density matrix for the simulation shown in Fig. 7.14	176
7.16	Evolution of the populations of the new detection scheme shown in Fig. 7.1, where each beam is detuned from resonance	178
7.17	Matrix plot of the steady state solution of the density matrix for the simulation shown in Fig. 7.16	179

7.18	Evolution of the populations of the new detection scheme shown in Fig. 7.1, with detunings and polarisation modulation	180
7.19	Average number of photons scattered in the new detection scheme as a function of the laser detunings and division of total intensity.	182
7.20	Average number of photons scattered per molecule as a function of the polarisation modulation frequency.	184
7.21	Comparison of simple rate model to optimised quantum mechanical simulation for new detection scheme	185
7.22	Number of scattered photons as a function of laser Doppler shift and velocity parallel to the probe laser beam propagation direction.	186
7.23	Evolution of the ground state populations of the new pumping scheme shown in Fig. 7.1	191
7.24	Evolution of the excited state populations of the new pumping scheme shown in Fig. 7.1	192
7.25	Increase in $ 0, 0\rangle$ population as a function of microwave and rf Rabi rate	193
7.26	Population pumped to $v > 0$ as predicted by the OBEs compared to the rate model	194
7.27	Population pumped to $ 0, 0\rangle$ as a function of laser Doppler shift	195

LIST OF TABLES

2.1	Parameters held constant during a block	61
2.2	Parameters switched during a block	62
2.3	Single point detectors that record a single value each shot.	65
2.4	Time dependent detectors that record several values over a shot. . . .	66
2.5	A few interesting channels.	69
2.6	Summary of datasets.	74
3.1	Summary of known systematic errors	77
3.2	$\langle \{E\}_{\text{R1}} \rangle$ with old and new high voltage cables	87
3.3	E-switch dependant rf polarisation angle with old and new high volt- age cables	92
3.4	Some measurements of $\langle [\text{EDM}] \rangle$ made with the <i>Applied Kilovolt</i> and <i>Bertan</i> supplies with and without the overshoot	99
3.5	ac charging current with and without overshoot for <i>Bertan</i> and <i>Applied</i> <i>Kilovolt</i> supplies.	103
4.1	Parameters relating to the eEDM statistical sensitivity for the July and March datasets	110
5.1	Evaluation of the total pumping rate for a selection of relevant cases .	132
7.1	The detunings that optimise the excited state population in a system of n lower levels coupled to a single upper level.	170

7.2	Average number of photons scattered per molecule in the new detection scheme with and without the effect of transverse Doppler shifts. .	187
7.3	Gains in sensitivity from improved experiment	198
8.1	Comparison between ACME and Imperial eEDM experiments	202
8.2	Current and projected systematic errors	203
B.1	Projection factors $\frac{1}{\mu_{A-X}} \langle \psi_{ES} \hat{\mathbf{d}} \cdot \boldsymbol{\epsilon}_p \psi_{GS} \rangle$ between the hyperfine levels of $A^2\Pi_{1/2}(\mathcal{P} = -1)$ and the hyperfine levels of $X^2\Sigma^+$	217
B.2	Projection factors $\frac{1}{\mu_{A-X}} \langle \psi_{ES} \hat{\mathbf{d}} \cdot \boldsymbol{\epsilon}_p \psi_{GS} \rangle$ between the hyperfine levels of $A^2\Pi_{1/2}(\mathcal{P} = 1)$ and the hyperfine levels of $X^2\Sigma^+$	218
B.3	g_F factors of a few of the $X^2\Sigma^+(v = 0)$ states	219

1. INTRODUCTION

This thesis discusses an experiment to measure the size of the electron's electric dipole moment (eEDM) using ytterbium fluoride (YbF) molecules. This chapter starts by discussing why an electron could have an electric dipole moment, and why it might be large enough to be detected experimentally. We then explore how eEDMs can be measured with atoms and molecules, the current limits on the eEDM and the experiments that are actively seeking to make a new measurement. Finally, we lay out the structure of the remainder of the thesis.

1.1 Why particles could have permanent electric dipole moments

Purcell and Ramsey were the first to point out that elementary particles or nucleons could have electric dipole moments (EDMs) [1] and, with their student J H Smith, the first to perform a dedicated measurement of the neutron EDM [2]. Initially, not even they were particularly surprised that the EDM they measured was consistent with zero. This is because the existence of an EDM would contravene two symmetries which seemed at the time to be well conserved, namely parity (P), which reflects spatial co-ordinates \mathbf{r} of a system through the origin ($\mathbf{r} \rightarrow -\mathbf{r}$), and time-reversal (T) which reverses the time coordinate, $t \rightarrow -t$. To see why an EDM would not respect these symmetries, consider the effect of T and P on an electron shown on the top of Fig. 1.1. This electron has spin $\hat{\mathbf{S}}$ and dipole moment $\hat{\mathbf{d}}_e$, which according to the Wigner-Eckart theorem [3, p. 184] must lie along the same axis. Thus, $\hat{\mathbf{d}}_e = d_e \hat{\boldsymbol{\sigma}}$, where $\hat{\boldsymbol{\sigma}}$ is a unit vector in the direction of $\hat{\mathbf{S}}$. Now the T transformation, shown in the bottom left of Fig. 1.1, leaves the dipole moment unchanged, but reverses the

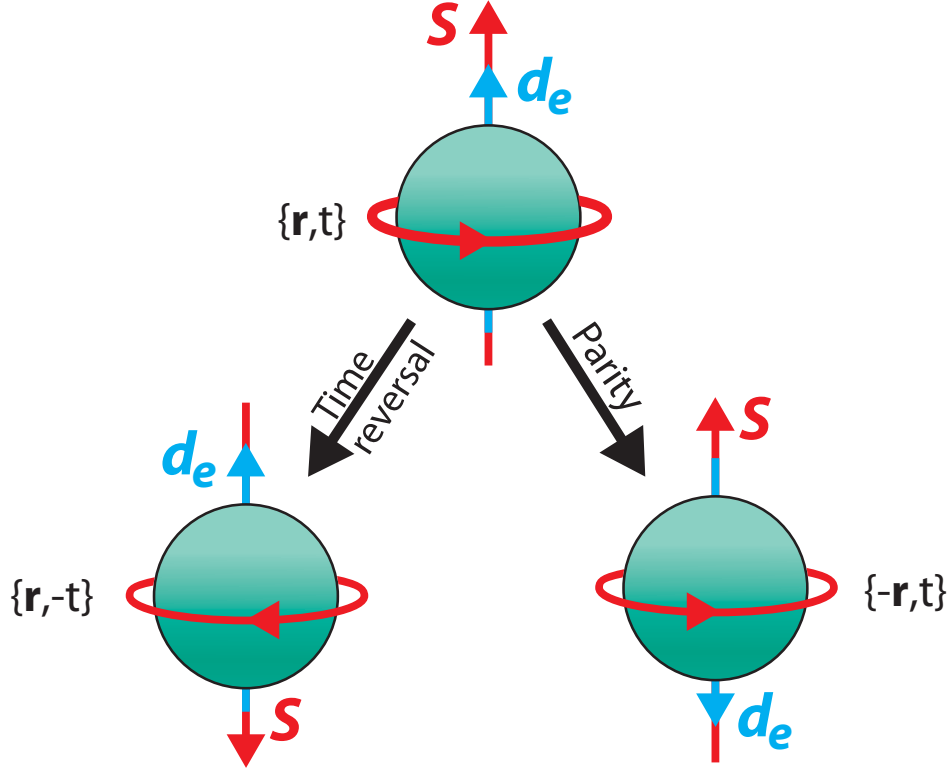


Fig. 1.1: An electron with spin \mathbf{S} and dipole moment \mathbf{d}_e undergoing the parity (P) and time reversal (T) symmetry transformations. Note that the value of d_e changes sign and hence P and T are not symmetries of an electron with an EDM.

direction of the angular momentum vector. Hence the time-reversed version of the electron is not the same as the original. Similarly, applying the P transformation, as shown in the bottom right of Fig. 1.1, reverses the direction of the polar dipole moment vector, while leaving the axial angular momentum vector unchanged.

The search for particle EDMs really began in earnest after the suggestion [4] and then discovery [5] in 1957 that parity was violated by the weak force. This proved that Purcell and Ramsey's point was correct: there really was no reason why fundamental physical laws should respect parity. For a while, it was considered that while P was violated, the combined symmetry CP, i.e. both space inversion (P) and charge-conjugation (C), would be obeyed. However, measurements of the neutral K meson [6], B meson [7] [8] and D meson [9] decays show that CP is not a good

symmetry of the weak force either.

The violation of CP symmetry led many to assume that T must also be violated. This idea stems from the CPT theorem, which states that any local, Lorentz invariant field theory must obey the combined symmetries of C, P and T [10]. Direct evidence for T-violation was first reported by the CPLEAR experiment [11] where the reaction $K^0 \leftrightarrow \bar{K}^0$ was studied. Recently, there has also been direct evidence for T violating processes in the decays of B mesons [12]. These discoveries suggest that particles could—indeed should—have electric dipole moments. Although all EDMs measured have so far been consistent with zero, nevertheless, there are good reasons for believing that the electron does have EDM and that it might be measurable in the laboratory. We explore these reasons in the following section.

1.2 Why particles should have permanent electric dipole moments

Since the weak interaction violates CP, the Standard Model (SM) of particle physics (which obeys the CPT theorem) predicts that all particles should have T-violating dipole moments. However, these are expected to be very small. Focussing on the eEDM from now on, the SM prediction [13, p.16] is¹

$$|d_e^{\text{SM}}| \simeq 10^{-38} e \text{ cm}. \quad (1.1)$$

In comparison, the current upper limit on the eEDM, set by a measurement on ThO molecules [14] is

$$|d_e^{\text{ThO}}| < 8.7 \times 10^{-29} e \text{ cm} \quad (90\% \text{ confidence}). \quad (1.2)$$

Clearly, we are very far away from being able to test the SM prediction for the value of the eEDM. Instead, probing the size of the eEDM is a test for new T-violating physics, beyond the Standard Model. There are two particular indications that new

¹ For historical reasons, EDMs are quoted in units of electron charge \times length in centimetres.

fundamental physics should exist. First, the Standard Model gives no indication of what dark matter or dark energy are. Together these make up 95% of the energy density of the universe [15]. New physics, which may be T-violating, is required to explain what these are. Second, it cannot account for the present abundance of baryonic matter over antimatter in the universe [16].

There are many proposals to go beyond the Standard Model (BSM) with theories which can solve these (and other) difficulties. A generic feature of these BSM theories is that they contain additional particles and additional sources of CP violation. The latter is important because it is a necessary (but not sufficient) condition to account for the baryon asymmetry we see today [17] [18]. These BSM theories are constrained by measurements of the eEDM because they need to have enough CP violation to produce the baryon asymmetry, but must not produce an eEDM that is too big.

It may be helpful to consider how eEDM searches constrain one popular extension to the Standard Model, supersymmetry. This theory predicts additional superpartners to the standard model fermions, with masses between 200 GeV and 1 TeV. The interactions between electrons and the superpartners have no reason to respect CP symmetry. The size of eEDM arising from a CP violating interaction with new particles of masses around Λ/c^2 depends on the specifics of the theory, but an estimate of the contribution from the simplest possible interaction [13, p. 29] is

$$d_e^{\text{NP}} \sim C \frac{m_e c^2}{\Lambda^2} \frac{e \hbar c}{2} \sin \phi^{\text{CP}}. \quad (1.3)$$

Here C is the coupling constant that characterises how strongly the new particle interacts with the electron and ϕ^{NP} is a phase which characterises how much that interaction violates CP symmetries. No one really knows what C , Λ or ϕ^{CP} should be. Typically, it is assumed that $C = \alpha/2\pi$ where α is the fine structure constant²

² Strictly speaking, this should be α evaluated at the energy scale Λ , because the value of α is lower at higher energy.

[19, Eq. 193], so that the supersymmetric eEDM arises in a similar way to the Schwinger correction to the magnetic dipole moment in QED. Evaluating Eq. (1.3) with the present experimental limit, Eq. (1.2), constrains $\Lambda \gtrsim 8.2 \text{ TeV} \times \sqrt{\sin \phi^{\text{NP}}}$. Alternative analyses lead to a slightly weaker limit $\Lambda \gtrsim 3 \text{ TeV} \times \sqrt{\sin \phi^{\text{NP}}}$ [14]. Assuming for the moment that CP-violating phase is of order 1, then current eEDM searches are already putting strong lower bounds on the mass of any supersymmetric particles, bounds which are more stringent than those placed by current generation of high energy particle physics experiments at the Large Hadron Collider (LHC) [20]. Future eEDM experiments [21] will probe energies more than 100 times higher than the LHC, and offer an opportunity to continue searching for possible signs of higher mass supersymmetry if the present series of experiments at the LHC do not discover new particles.

Of course, there is no reason why $\phi^{\text{CP}} \sim \mathcal{O}(1)$ [13, p. 30], but if $\phi^{\text{CP}} \ll 1$, this reduces the amount of CP violation available to explain the matter-antimatter imbalance, one of the key motivations of supersymmetry. Even before the failure of ATLAS and CMS to directly discover supersymmetric particles at CERN in 2013, eEDM searches were effectively ruling out [16] [22] the simplest versions of that theory (the so called minimal supersymmetric standard model, MSSM) by placing upper limits on the value of ϕ^{CP} . Ever more precise upper limits on the value of the eEDM simultaneously increase the mass scale and decrease the amount of CP violation in any new physics, thus even null results constrain the form of fundamental physics.

1.3 Measuring the size of the electron EDM

In this section we discuss the variety of ways currently used to measure the eEDM. Measuring the interaction energy $-\mathbf{d}_e \cdot \mathbf{E}$ of a free electron in an electric field is not practical, because the electron is quickly accelerated by the electric field out of the experiment. Instead the electrons used are always bound into atoms, molecules,

molecular ions or solid-state samples. We start by examining how the EDM of an electron bound in an atom or molecule can interact with an applied electric field. We then discuss two molecules used to make recent eEDM measurements, and the results of those measurements. Finally, we briefly survey the current experiments which aim to measure the eEDM.

1.3.1 The eEDM interaction in atoms and molecules

We might expect an atom with an unpaired electron, placed in an electric field \mathbf{E} , to experience interaction energy $-\hat{\mathbf{d}}_e \cdot \mathbf{E}$. This would then lead to a linear Stark shift of its energy levels, much like the Zeeman interaction $-\hat{\boldsymbol{\mu}} \cdot \mathbf{B}$ between a magnetic field and the magnetic dipole moment $\hat{\boldsymbol{\mu}}$. However, if the electrons and nucleus are treated as point particles interacting only through the Coulomb force, then there is no linear Stark shift, a result known as Schiff's theorem [23]. This can be qualitatively argued [13] as follows: an electrically neutral atom, placed in a homogeneous electric field, is not accelerated. Therefore, each of its constituent parts feels an average acceleration of zero. Since only Coulomb forces act, this means that the average electric field experienced by each charged electron and the nucleus must be zero. In other words, the applied field is on average exactly cancelled at each charged particle by rearrangement of the other charges. Hence, even if an electron did have an electric dipole moment, applying a field to an atom does not seem to allow it to be detected.

Schiff himself pointed out that his theorem does not strictly apply to a real atom, because the nucleus is not a point particle, and because there are relativistic forces as well as Coulomb forces. Taking those into account, there can be a linear Stark shift after all. The finite size of the nucleus can produce such a shift because the charge and dipole moment may be distributed differently within the nucleus. This then leads to the possibility of imperfect screening of the external electric field by the nucleus [24]. The relativistic motion of the electron causes Schiff's theorem to fail in a different way. When the electron is moving relativistically, its dipole experiences

length contraction close to the nucleus, when it is moving fastest. This means that while the average electric field acting on the electron still vanishes, a non-vanishing interaction energy between the electric field and the eEDM is possible [25]. Sandars [26] realised that in heavy elements, the relativistic effect could be so strong that the dipole moment of the entire atom could be more than two orders of magnitude larger than the dipole moment of the unpaired electron. Between 1989 and 2011 experiments on heavy atoms set all the best limits on the size of the eEDM, first with caesium [27] and then with atomic beams of thallium [28] [29] [30].

In an atomic eEDM experiment, both the finite size and relativistic effects are dependent on the polarisation of the atom in the electric field. Eventually, it was realised that if the atom has a polar bond to a second atom, then the polarising effect of the electronegative atom was much larger than any polarisation that could be applied using laboratory fields. As a result, the molecule becomes much more sensitive to P&T violating phenomena. A modest electric field is still required to align the internuclear axis (whose direction is specified by the unit vector \mathbf{n} , pointing by convention from the negative ion to the positive ion³) so that it has a non-zero projection along the total angular momentum. In a diatomic molecule like this, the interaction terms that violate P&T can be written [16] as

$$-(d_e E_{\text{eff}} + W_S C_S) \boldsymbol{\sigma} \cdot \mathbf{n}(\mathbf{E}). \quad (1.4)$$

The first term is the interaction between the electron's electric dipole moment and the effective electric field E_{eff} , which is determined by the relativistic structure of the molecule. The second term is due to a possible P&T violating weak interaction of strength $C_S G_F$ between the electron and the nucleus, where G_F is the Fermi coupling constant [31]. Here it is W_S that is determined by the molecular structure. Both effective interactions are proportional to $\boldsymbol{\sigma} \cdot \mathbf{n}(\mathbf{E})$, where $\boldsymbol{\sigma}$ is the direction of the

³ Chemists often use a different convention where \mathbf{n} points from the heavier to the lighter element in a bond.

electron spin and $\mathbf{n}(\mathbf{E})$ is that of the internuclear axis in the presence of the external field \mathbf{E} . If we choose the electric field to be along the z axis, then we can define the polarisation factor $\eta = \mathbf{n} \cdot \mathbf{z}$ which quantifies the projection of the internuclear axis onto the electric field direction.

1.3.2 Choice of molecule

There are a few molecules which could be used to measure the electron EDM. Here we focus on just two, ytterbium-174 fluoride (YbF) and thorium-232 oxide (ThO). We will discuss other molecules in passing when we review the current status of experiments to measure the eEDM.

Our group at Imperial College uses YbF to measure the eEDM. This has a number of attractive properties. First, it is a non-radioactive isotope whose spectroscopic properties are well studied and whose laser transitions can be addressed with convenient lasers. Second, it can be made relatively easily and reliably by supersonic ablation, using a source which requires remarkably little down-time or maintenance. Third, it has a simple energy level structure: its ground electronic, vibrational and rotational state, $X^2\Sigma^+$ (shown in Fig. 1.2 (a)) is split into $F = 1$ and $F = 0$ by the hyperfine interaction between the one unpaired electron spin and the fluorine nuclear spin. The $F = 1$ level is sensitive to the eEDM, with a large enhancement factor, $E_{\text{eff}} = -26 \text{ GVcm}^{-1}$ [32] and $W_S = -53 \text{ kHz}$ [33]. It can also be fairly well polarised in laboratory fields of several tens of kilovolts per centimetre, as shown in Fig. 1.2 (b). For example, an applied field of 12.5 kVcm^{-1} produces a field of $\eta E_{\text{eff}} = -15.9 \text{ GVcm}^{-1}$.

YbF also has some good properties which allow it to be used in future eEDM experiments. First, the eEDM measurement state $X^2\Sigma^+(F = 1)$ is stable. This means that there is no fundamental limit on the duration of any measurement of the eEDM splittings in YbF. Second, YbF can be buffer gas cooled, so slower, more intense beams can be produced for future experiments. Finally, YbF can also be

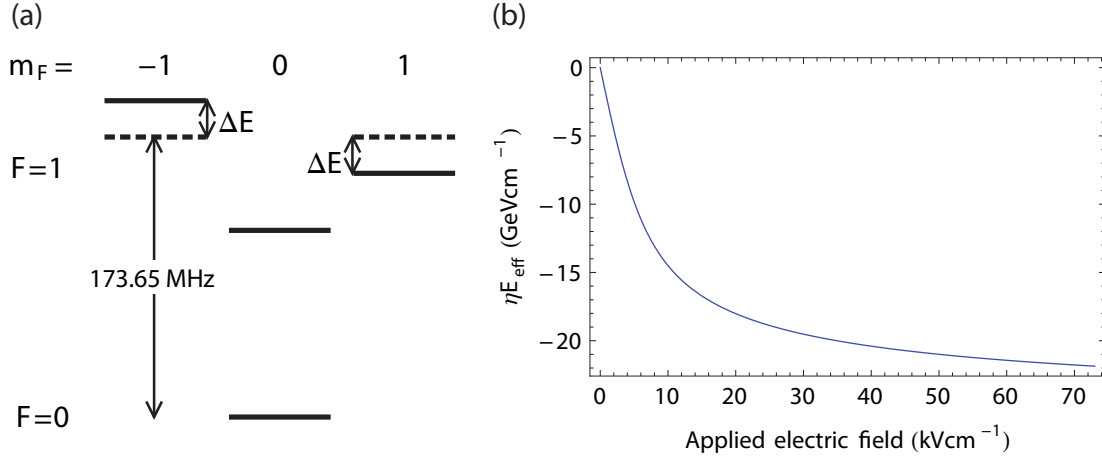


Fig. 1.2: (a) The energy level structure of the $X^2\Sigma^+$ ground rotational and vibrational level in a 12.5 kVcm^{-1} electric field applied along the quantisation axis. The Stark interaction leads to a splitting between $F=1$, $m_F=0$ and $m_F = \pm 1$. The eEDM splitting of the $m_F = \pm 1$ levels is $\pm \Delta E = \mp d_e \eta E_{\text{eff}}$. If $d_e = 1 \times 10^{-28} e \text{ cm}$, then at this field $\Delta E/h = 0.4 \text{ mHz}$. (b) ηE_{eff} as a function of the applied field in the $\text{YbF } X^2\Sigma^+ (F=1)$ level.

laser slowed and cooled. This allows many of the techniques pioneered in the field of atomic clocks to be applied to YbF molecules, in particular it suggests that we could create a fountain of YbF . This is an idea that we will return to in the following section.

ThO is the molecule chosen by the Advanced Cold Molecule eEDM (ACME) collaboration between Harvard and Yale universities. In this molecule, it is not the ground state but the metastable $H^3\Delta_1$ state which is used to measure the eEDM. This state has an even larger effective electric field $E_{\text{eff}} = -81.5 \pm 5.7 \text{ GVcm}^{-1}$ [34], and it can be completely polarised ($|\eta| = 1$) by very small applied electric fields of around 36 Vcm^{-1} . W_S is also larger at -260 kHz [33]. When a fixed static electric field is applied to the $H^3\Delta_1$ state, both polarisations of the molecule, $\eta = 1$ and $\eta = -1$ are available to be used in the experiment. The flexibility to swap between $\eta = \pm 1$, without reversing the electric field direction, allows additional rejection of some systematic effects - in particular, magnetic fields correlated with the applied electric field. Also, $^3\Delta$ states generally have small magnetic moments due to the

arrangement of the orbital and spin angular momentum. The ThO H $^3\Delta_1$ state is no exception, with a tiny magnetic moment, $|\mu| = 0.0044 \times \mu_B$ [35], so this molecule is very insensitive to magnetic field noise. While magnetic field noise is not a problem for the current generation of molecular eEDM experiments (including YbF), it may become an issue in future measurements.

The disadvantage of ThO H $^3\Delta_1$ for future experiments is that it is a metastable state, with a lifetime of around 2 ms. This puts a fundamental limit on the integration time that can be achieved with this molecule.

1.3.3 Recent results

In 2011, the group at Imperial was the first to set a new limit on the electron EDM with a polar molecule. This measurement was undertaken on a supersonic beam of YbF, and the technique and apparatus used were very similar to those described in this thesis. It is customary in reporting eEDM results to set $C_S = 0$, which we do for the time being. Doing so gives a value of $d_e = (2.4 \pm 5.7_{\text{stat}} \pm 1.5_{\text{syst}}) \times 10^{-28} e \text{ cm}$, implying an upper limit on the eEDM of $|d_e| < 10.5 \times 10^{-28} e \text{ cm}$ with 90% confidence [36]. Recently, the ACME collaboration set a new upper limit with ThO, measuring $d_e = (2.1 \pm 3.7_{\text{stat}} \pm 2.5_{\text{syst}}) \times 10^{-29} e \text{ cm}$, implying an upper limit on the eEDM of $|d_e| < 8.7 \times 10^{-29} e \text{ cm}$ with 90% confidence.

If the experiments are taken to be simultaneous measurements of d_e and C_S , then the best separate limits on these quantities come from combining the YbF, ThO and Tl eEDM, and an atomic EDM measurement with ^{199}Hg [37], as illustrated in Fig. 1.3. This gives $|d_e| < 5.4 \times 10^{-27} e \text{ cm}$ and $|C_S| < 4.5 \times 10^7$ with 95% confidence [33]. This more conservative limit on d_e is worse because the ratio of E_{eff} to W_S is almost the same in YbF, ThO and Tl, and hence the boundaries of the parameter space excluded by these experiments are almost parallel, as can be seen by Fig. 1.3.

For the remainder of the thesis, when we discuss the electron electric dipole moment, it should be taken as read that we are setting $C_S = 0$.

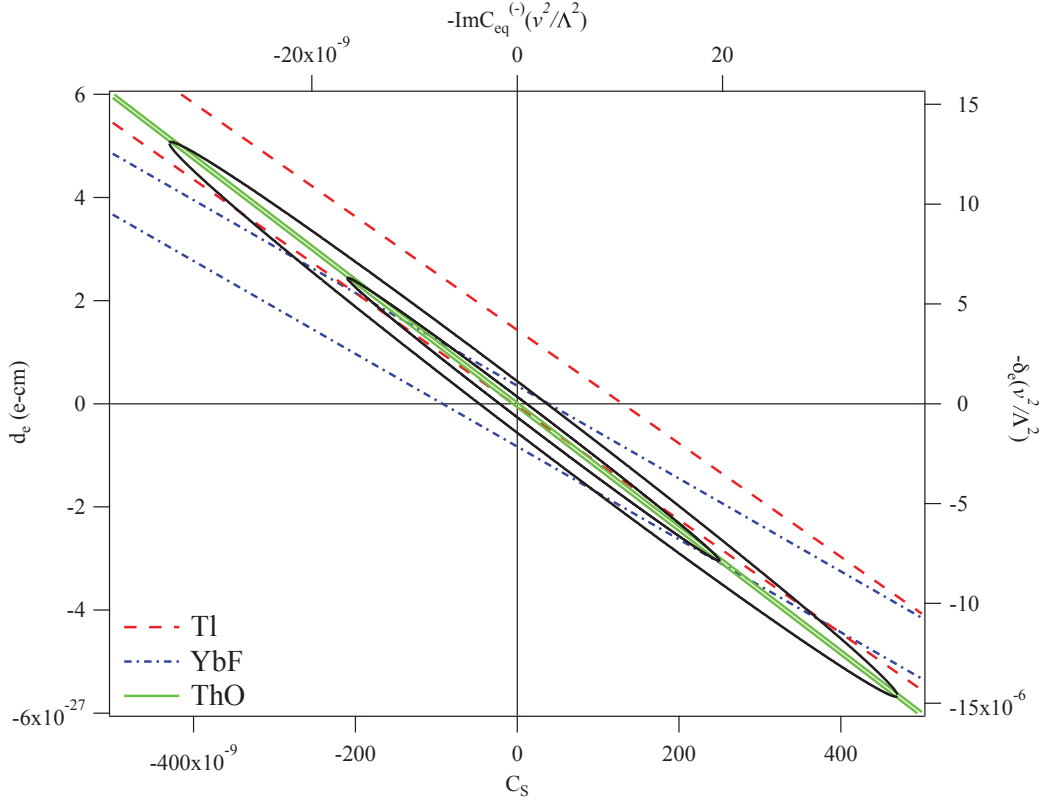


Fig. 1.3: Allowed regions for d_e and C_S from the Tl, YbF and ThO results, reproduced with permission from Ref. [33] (© APS). Also shown are 68% and 95% error ellipses representing the best fit for the paramagnetic systems and including ^{199}Hg , as discussed in the text. The meaning of the symbols in the top and right axes of the graph is discussed in Ref. [33].

1.3.4 Current experiments to measure the $e\text{EDM}$

There are a number of active experiments that seek to make new measurements of the electron EDM. The status of the Imperial experiment and the progress towards making a new measurement with YbF are discussed in detail later in this thesis, so here we focus on the other experiments.

As mentioned above, the current limit is set by the ACME collaboration using a buffer gas cooled beam of ThO molecules. This experiment builds on the techniques developed both in our YbF beam experiment, and also in a previous ex-

periment to measure the eEDM in a metastable level of lead oxide [38]. The ThO molecules are created by firing a YAG laser pulse into a solid ThO₂ target, which is located inside a cryogenically cooled cell, filled with neon buffer gas to a pressure of 10⁻³–10⁻² Torr [39]. The hot ThO molecules cooled to 20 K by collisions are swept out of a hole in the cell into a higher vacuum region, forming a 2–3 ms long pulse travelling at around 200 m s⁻¹. The molecular pulse flies between a pair of indium-tin oxide (ITO) coated, transparent, conductive glass plates charged to around ±50 V. Once inside the plates, the molecules traverse a laser beam which optically pumps molecules from the ground electronic state into the H³Δ₁ state. Soon after this, the molecules encounter a second, state preparation, laser. This performs optical pumping on the H³Δ₁ state to spin polarise the molecules into a plane perpendicular to the electric field. As will be discussed in greater detail at the beginning of the following chapter, the eEDM interaction causes the spin direction of the polarised molecules to rotate slightly. After around 1.1 ms of flight time, the rotation of the spin polarisation direction is measured using a second laser beam. The size of the rotation angle is directly proportional to the eEDM. The ACME collaboration hope to improve this experiment further [14] by using an thermochemical buffer gas source to produce more molecules. They have also changed the state preparation scheme from optical pumping to stimulated Raman adiabatic passage. As a result of these changes, they expect to be able to reduce the statistical uncertainty on their next measurement by around a factor of ten. At the conclusion to this thesis, we will return to discuss how the Imperial experiment compares with the current and future ACME experiment.

In a very different type of eEDM experiment, measurements have been made on cryogenic (4.2K) ferroelectric gadolinium gallium garnet (GGG) [40] and Eu_{0.5}Ba_{0.5}TiO₃ [41] solid state samples. In these experiments, a large voltage is applied across a paramagnetic insulator to align the electric dipole moments of the unpaired electrons parallel to the applied electric fields. A sensitive SQUID mag-

netometer then measures the resulting magnetisation in the sample. A non-zero magnetisation indicates the presence of an eEDM. This method benefits from the very large density of electron spins in the solid but at the moment, the precision is around a factor of 100 worse than the best molecular experiments. This is because the magnetic fields induced in the sample are on the order of a few atto-tesla, which are tricky to measure, even with a SQUID. To maximise the sensitivity of the magnetometer, the electric fields are reversed relatively quickly (every second or so). This can lead to systematic errors where charging currents continue to flow during the measurement of the sample's magnetisation, or errors arising from the magnetic hysteresis of the sample. Also, leakage currents can flow through the sample between the high voltage plates leading to a magnetic field which mimics a magnetisation caused by an eEDM.

We now turn to experiments that are in preparation. Tungsten carbide has been proposed as a suitable molecule to conduct an eEDM experiment, because it has a $^3\Delta_1$ ground state sensitive to the eEDM, with $E_{\text{eff}} = 36 \text{ GVcm}^{-1}$ [42]. Thus, it combines the attractive $^3\Delta$ nature of the ThO molecule with the very long lifetime of the YbF molecule. Some preliminary measurements have been carried out at the University of Michigan. At present the number of tungsten carbide molecules is quite low, with typical count rates of a few per second.

Several groups are also preparing experiments to measure the eEDM with optically trapped paramagnetic atoms, including caesium [43] and francium [44]. Although these experiments would benefit from the very long interaction times available in a trap, they are quite challenging because the effective field is much smaller for atoms than for molecules. This means that they have a very stringent requirement on the magnetic field noise. Also, it is difficult to control the systematic error resulting from a slight polarisation of the trapping light, as discussed by Romalis and Fortson [45].

Researchers at JILA are constructing an experiment to use HfF^+ molecular ions

in an rf Paul trap to measure the eEDM [46] [47]. This molecule has a number of metastable $^3\Delta$ states that could be used in the measurement, and it has a reasonably large effective field in these states of around 37GVcm^{-1} [48]. The experiment combines low sensitivity to magnetic field noise (because of its large effective field and $^3\Delta$ state) with the long integration times available to trapped samples. However, measuring the interaction energy between an electric field and the electron dipole moment at the same time as trapping the molecules in a rotating electric field presents its own challenges. One of the most significant will be making sure that the geometric phase in the molecular wavefunction due to the rotating field does not mimic the eEDM signal.

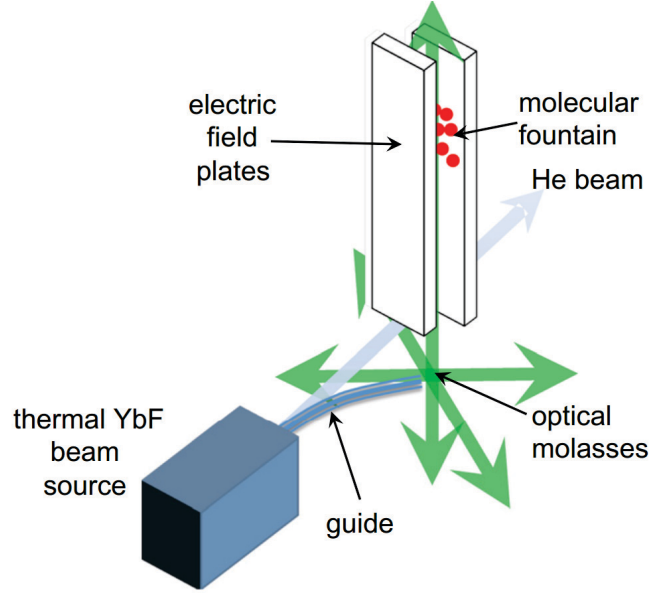


Fig. 1.4: Diagram of the YbF fountain, taken from Ref. [21]

The final experiment we mention here is a molecular fountain also being developed in our group at Imperial, in parallel with the work submitted in this thesis. This fountain will use a helium buffer gas source of YbF to produce 170 m s^{-1} molecules. These will be Zeeman slowed and guided into a region where they can be laser cooled and trapped in a molecular magneto optical trap (MOT). Once a group of

molecules have been accumulated in the trap, they will be launched between a pair of electric field plates, and they will be prepared with lasers, rf or microwaves into a state sensitive to the eEDM. The molecules will fly upwards, slow down and then turn around and fall back down, whereupon a second field will detect the amount of spin rotation the molecules have experienced. This machine should be capable of measuring the eEDM with an uncertainty of $6 \times 10^{-31} e \text{ cm}$ with 8 hours of integration. This will be a complex and difficult experiment, requiring a reliable buffer gas source of YbF molecules, the successful laser cooling of YbF, its trapping in a MOT and then a way to get the molecules into the electric field plates and transfer them into a state sensitive to the eEDM. However, the outcome will be a phenomenally sensitive experiment capable of an exquisitely precise measurement of the electron EDM.

1.4 Thesis overview

The remainder of this thesis is divided into two halves. The first half discusses the data that I collected between September 2011 and May 2014, with the aim of making a new measurement of the eEDM. When I joined the group, the experiment had been established for 10 years, and had recently been used to set a new upper limit on the eEDM [36]. After this measurement, it had been upgraded by the previous PhD student, Joe Smallman [49]. My first task was to learn how to operate the experiment and analyse the data it produced—this is discussed in Chapter 3. Working with Joe Smallman, I performed a number of tests for known systematic errors which are summarised at the start of Chapter 2. I also discovered and characterised three new systematic effects which are also discussed in this chapter. Finally, Chapter 4 presents my analysis of the origin of the statistical uncertainty in the data we gathered.

The second half of the thesis describes and analyses a series of improvements to the experiment which will allow a much more accurate measurement of the value the eEDM. In collaboration with other members of the group, I was responsible for

deciding which of the many possible ways of improving the experimental sensitivity would be most effective and practical to carry out. The improvements, presented in Chapter 5, use additional laser, rf and microwave fields to increase the number of molecules that can participate in the experiment and detect the molecules more effectively. These improvements are currently being incorporated into the experiment. In this chapter, I also present a simple rate equation model to estimate how YbF will respond to the additional fields.

In order to understand more fully how YbF interacts with the laser, microwave and rf fields that will be used in the improved experiment, Chapters 6–7 derive and solve the optical Bloch equations, first for some simple systems and then for all possible transitions between $X^2\Sigma^+(v = 0; N = 0, 1, 2)$, $X^2\Sigma^+(v > 0)$, and $A^2\Pi_{1/2}(J' = 1/2)$ levels in YbF. At each stage the results are compared to the simple rate model, to understand how the true behaviour of the molecule differs from a classical picture. Chapter 8 is the conclusions of my thesis, where I summarise the progress discussed in this thesis, and set out the next steps towards a new measurement of the electron electric dipole moment.

2. OVERVIEW OF THE EXPERIMENT

2.1 *The fundamental principle behind the experiment*

Consider a classical electric dipole \mathbf{d} placed in an electric field \mathbf{E} . This experiences a torque which acts to orientate the dipole parallel to the field. If the dipole is spinning about an axis which lies along \mathbf{d} , and \mathbf{E} is applied perpendicular to \mathbf{d} then the torque causes \mathbf{d} to rotate about \mathbf{E} at a rate proportional to $\mathbf{d} \times \mathbf{E}$. This phenomenon is called the precession of the angular momentum. Similar behaviour can be seen when a spinning gyroscope precesses in the earth's gravitational field, three drawings of which are shown in Fig. 2.1 (a). If the dipole is initially prepared along some particular direction, allowed to precess in a known field for a given time, and its final direction is observed, then the magnitude of \mathbf{d} can be calculated from the change in orientation of the dipole.

The classical picture of spin precession discussed in the previous chapter captures the essence of how the YbF eEDM experiment measures the size of the electron electric dipole moment. We choose a stable state of the ytterbium fluoride (YbF) where the outermost electron's spin and electric dipole moment are orientated with respect to the laboratory x axis with laser and radio-frequency fields. The molecule's internal electric field along the internuclear axis \mathbf{n} between the Yb and F atoms is aligned to the laboratory z axis by applying an external field to polarise the molecule. The polarisation is not perfect, with $\eta = \langle \mathbf{n} \cdot \mathbf{z} \rangle = 0.61$, and the direction of the internal electric field is anti-parallel to the applied field. If the eEDM is non-zero, there will be a slight precession in the orientation of the initially prepared

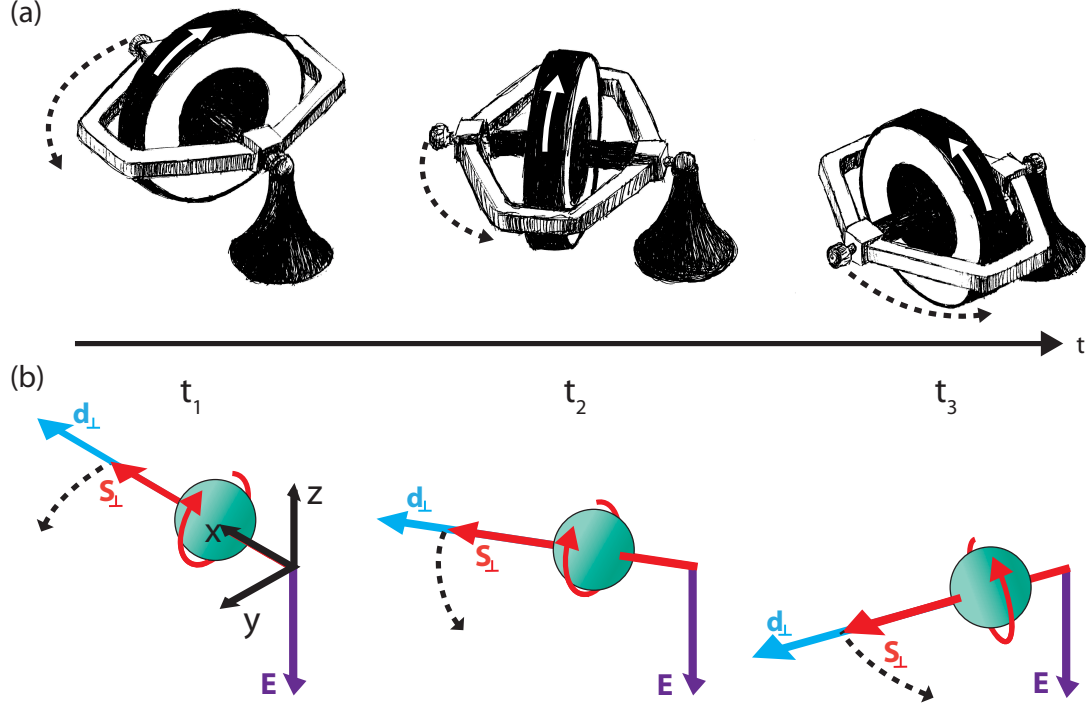


Fig. 2.1: (a) Three drawings of a spinning gyroscope precessing in the earth's gravitational field, courtesy of Sherena Corfield. (b) An electron with spin \hat{S} (projection S_{\perp} into a plane perpendicular to E) and eEDM d (projection d_{\perp} into a plane perpendicular to E) precesses over time in an electric field E .

state, caused by the $d_e \eta E_{\text{eff}}$ interaction between the electron electric dipole and the effective intermolecular field E_{eff} experienced by the electron, reduced by the fact that the molecule is not completely polarised. An illustration of this precession is shown in Fig. 2.1 (b). The change in orientation after some interaction time τ can be detected with more laser and radio-frequency fields, from which the size of d_e can be calculated.

The rest of this chapter explains how we make this spin precession measurement in practice. We start by explaining the energy level structure of YbF in section 2.2. We then set out a brief overview of the apparatus in section 2.3, before moving on to discuss the sequence of data taking in section 2.4. Finally, in section 2.5 we discuss how the gathered data is analysed to extract a value for the eEDM.

2.2 The structure of YbF

This section describes the energy levels of a YbF molecule and the transitions that can occur between them. Our interest in the structure of YbF is quite pragmatic: we would like to know how to manipulate the molecules into a state sensitive to the eEDM and then detect the evolution of that state. To understand the basic operation of the eEDM experiment, we do not need to know very much about YbF's structure or the character of its energy levels, so the reader who would like to get straight to the heart of the experiment can skip to section 2.2.5 on p. 43 and carry on from there. However, a fuller understanding of the structure of YbF is crucial to find ways to improve the experiment, described from Chapter 5 onwards, so we spend a few pages here exploring the energy levels and possible transitions in more detail.

We measure the eEDM with ^{174}YbF , a diatomic molecule consisting of a ytterbium-174 atom bonded to a fluorine atom. Like an atom, its electrons can occupy bound states of different energies and orbital angular momenta. In addition to these electronic energy levels the molecule has two nuclei that can vibrate about the centre of mass and rotate about the centre of inertia, adding additional rotational and vibrational energy levels. ^{174}YbF also has a number of electronic spins and one nuclear spin $1/2$ belonging to the fluorine nucleus.

We start the discussion of YbF's structure by ignoring the rotational and vibrational degrees of freedom and explain how the electronic structure of YbF can be treated. We then return to the rotational and vibrational degrees of freedom in the ground state, and give the basic form of the ground state eigenvectors. We then repeat this for the excited state. We round off the section with a discussion of the possible transitions between energy levels.

2.2.1 Electronic structure

When Yb (configuration [Xe] $4f^{14}6s^2$) bonds to F (configuration $1s^2 2s^2 2p^5$), one of its $6s$ electrons is accepted by the fluorine. The bond thus formed is basically ionic, leaving a positively charged Yb^+ and negatively charged F^- . All atomic orbitals are filled apart from the single electron in a $6s$ orbital. It is these lone unpaired $6s$ electrons whose spin precession will be measured in the experiment.

The electronic structure of this outer electron in YbF is very similar to that of an alkali atom. In atoms, for every value of the principal quantum number that the outermost electron can take, it is possible to define a set of terms, labelled by the total spin S and orbital angular momenta¹ L by a symbol of the form ^{2S+1}L . Each term will in general have a different energy. Since the electronic spin $\hat{\mathbf{S}}$ couples to the orbital angular momentum $\hat{\mathbf{L}}$ via the $\hat{\mathbf{L}} \cdot \hat{\mathbf{S}}$ spin orbit interaction, each term will be split into *levels* according to the possible values of $\hat{\mathbf{J}} = \hat{\mathbf{L}} + \hat{\mathbf{S}}$. To distinguish between levels, the term symbol is usually written in the form

$$^{2S+1}L_J. \quad (2.1)$$

It is also possible to label the terms and levels within a molecule with a molecular term symbol. For a molecule each term symbol starts with a capital letter, which labels whether the term is the ground electronic state or an electronically excited state. The electronic ground state is labelled with an X, and the excited states are labelled {A,B,C...} depending on whether they are the {first, second, third ...} excited state.

If we work in the molecular fixed frame, defined so that the \mathbf{z} axis lies along the internuclear axis \mathbf{n} , we see that the Hamiltonian does not have spherical symmetry. The total angular momentum is therefore not conserved and quantum number L cannot be used to label the term symbol. However, the cylindrical symmetry around

¹ Following the usual convention the eigenvalues of the operator \hat{X} are labelled X . Vector quantities are written in bold font.

the bond implies that m_L will be a good quantum number, so we can label the molecular term symbols with its eigenvalues. To make the distinction between the molecular fixed coordinates and the lab coordinates clear, the projection of $\hat{\mathbf{L}}$ along the internuclear axis is renamed $\hat{\Lambda}$.

Just like an alkali atom, terms with $\Lambda > 0$ will be split according to the spin orbit interaction. The cylindrical symmetry of the problem ensures that the projection of $\hat{\mathbf{J}}$ along the internuclear axis, labelled $\hat{\Omega}$, commutes with the Hamiltonian, so its eigenvalues Ω are good quantum numbers. Approximately speaking, the energy of terms with $\Lambda = \pm|\Lambda|$, which correspond to the orbital angular momentum being clockwise or anti-clockwise about the internuclear axis, are equal. The same goes for the energy of levels with $\Omega = \pm|\Omega|$, so the molecular term symbol for a level can be written as

$$\text{letter } ^{2S+1}|\Lambda|_{|\Omega|}. \quad (2.2)$$

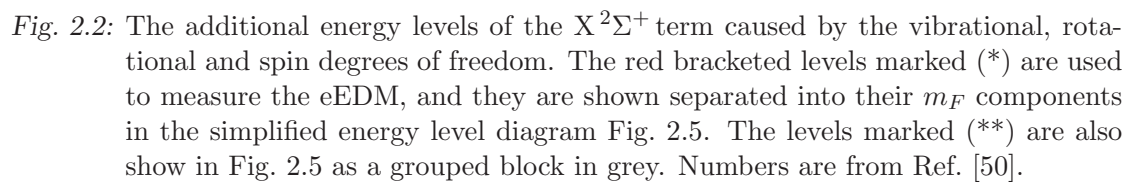
Similarly to the atomic case, the value of $|\Lambda|$ is specified using a spectroscopic notation, but rather than using S,P,D,... for $|\Lambda| = 0, 1, 2, \dots$ instead $\Sigma, \Pi, \Delta, \dots$ are used.

In this experiment, we are only interested in the ground electronic state² $X^2\Sigma^+$ and the $|\Omega| = 1/2$ component of the first electronically excited state $A^2\Pi_{1/2}$.

2.2.2 Vibrational, rotational and other structure of $X^2\Sigma^+$

Now we move from looking at the electronic structure to considering the vibrational and rotational structure of the $X^2\Sigma^+$ ground electronic state. This additional structure is shown in the energy level diagram 2.2. For our purposes, the eigenfunctions of the effective molecular Hamiltonian \hat{H}_0 for this electronic state can be considered

² The + superscript is included by convention to indicate the symmetry of the Σ state's electronic wavefunction under reflection in any plane containing the internuclear axis. This is not the same as the parity of the state.


$$|\psi_{GS}\rangle = |X, \Lambda = 0\rangle |v\rangle |N, F^{(+/-)}, m_F\rangle, \quad (2.3)$$
$$\hat{H}_0 |\psi_{GS}\rangle = E_{X,v,N,F} |\psi_{GS}\rangle, \quad (2.4)$$
$$E_{X,v,N,F} = E_X + E_v + E_{N,F(+/-)} . \quad (2.5)$$

The first of these factors, $|X, \Lambda = 0\rangle$, corresponds to the electron wavefunction for the orbital motion, its energy is the term energy E_X . The next term $|v\rangle$ is the state

vector for the vibrational motion of the Yb and F nuclei in the molecular bond. Its eigenvalues (to a first approximation) are those of a harmonic oscillator

$$E_v = hf(v + \frac{1}{2}), \quad f = 15.1894 \pm 0.0002 \text{ THz [51]}. \quad (2.6)$$

The splitting of $X^2\Sigma^+$ caused by this vibrational motion for $v = 0$ and $v = 1$ is shown in Fig. 2.2.

The third factor accounts for both the rotational motion of the nuclei (operator \hat{N}) and the couplings of the electron spin \hat{S} to the fluorine nuclear spin \hat{I} . The energies of these state vectors are basically those of a rigid rotor

$$E_{\text{rotation}} = hB_0N(N+1), \quad B_0 = 7233.8007 \pm 0.0010 \text{ MHz [50]}, \quad (2.7)$$

as can be seen by the large gigahertz-sized splitting between the $N = 0, 1, 2$ levels in Fig. 2.2. There are also small additional contributions caused by the spin-rotation and hyperfine interactions. The good quantum numbers for these states are N and F , the quantum number associated with the total angular momentum operator $\hat{F} = \hat{N} + \hat{S} + \hat{I}$. The lowest energy rotation state, $N = 0$, has no rotational angular momentum, so only the fluorine nuclear spin and electron spin contribute to the total angular momentum. The hyperfine interaction between the nuclear and electron spin causes the 170.254 MHz splitting between the $F = 0$ state where the two spins are anti-parallel and the $F = 1$ state where the two spins are aligned. In states with $N > 0$, the rotational angular momentum can combine with the two spins to give four possible values of F , corresponding to $F = N + 1$, $F = N - 1$ and two states with $F = N$. The two states with $F = N$ have different energies and are labelled with the superscript $+/-$ depending on whether they are the higher/lower energy state. The splitting of the levels into states labelled by N and F is shown in Fig. 2.2.

The magnetic sub-levels of the $F = 1$ and $F = 0$ levels of $N = 0$ will be frequently referred to in this thesis, so when we talk about these states we will exclude all of

the quantum numbers and refer to these levels by their F and m_F values only

$$|F, m_F\rangle \equiv |X, \Lambda = 0\rangle |0\rangle |0, F, m_F\rangle . \quad (2.8)$$

Finally, we note that as solutions of the molecular Hamiltonian, the ground states $|\psi_{GS}\rangle$ must have definite parity, given by

$$\hat{\mathcal{P}} |\psi_{GS}\rangle = (-1)^N |\psi_{GS}\rangle . \quad (2.9)$$

For the remainder of this thesis we are only interested in the full structure of the states where $v = 0$ and $N = 0, 1, 2$.

2.2.3 $A^2\Pi_{1/2}$ wavefunction

Now we move on to look at the structure of the $A^2\Pi_{1/2}$ electronically excited level in more detail. In this level we are only interested in the ground vibrational and ground rotational state

$$|\psi_{ES}\rangle = |A, J' = \tfrac{1}{2}, \mathcal{P}'\rangle |v' = 0\rangle |F', m'_F\rangle . \quad (2.10)$$

This has energy

$$\hat{H}_0 |\psi_{ES}\rangle = E_{A,\mathcal{P}',F'} |\psi_{ES}\rangle , \quad (2.11)$$

where

$$E_{A,\mathcal{P}',F'} = E_A + E_{v'} + E_{\mathcal{P}'} + E_{F'} . \quad (2.12)$$

By convention we label the eigenvalues of the excited state with a prime. We start with the first term of Eq. (2.10), the spin orbit wavefunction $|A, J' = \tfrac{1}{2}, \mathcal{P}'\rangle$. This has two possible parities, $\mathcal{P}' = \pm 1$. These correspond to the symmetric and anti-symmetric combinations of the $\Omega' = \pm 1/2$ wavefunctions for the electron spin and orbital motion. These two parity components have different energies because they

mix differently with neighbouring electronic levels, chiefly the $N = 0$ rotational level of the $B^2\Sigma^+$ second electronically excited level which is an isolated positive parity state. This lifting of the degeneracy is called Ω -doubling [52]. In molecular spectroscopy the components of the Ω -doublet are also sometimes labelled with an ‘e’ or ‘f’: for $A^2\Pi_{1/2} (J' = \frac{1}{2})$, $\mathcal{P}' = 1$ is the ‘e’ state and $\mathcal{P}' = -1$ is the ‘f’ state. In YbF, the separation between the positive and negative parity levels of $A^2\Pi_{1/2} (J' = 1/2)$ is 11.8 GHz [51], as illustrated in Fig. 2.3.

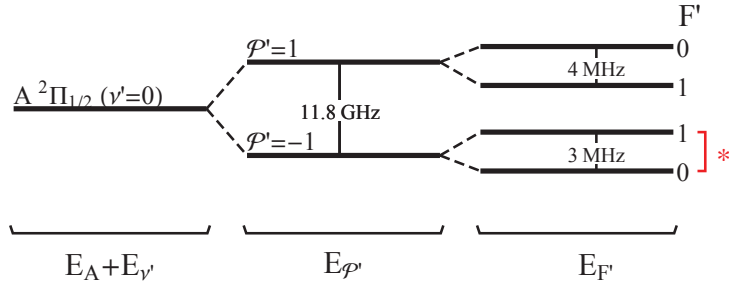


Fig. 2.3: Ω -doubling and hyperfine splitting in the $A^2\Pi_{1/2} (J' = 1/2)$ term [52]. The red bracketed levels marked (*) are used to detect the eEDM, and they are shown separated into their m_F components in the simplified energy level diagram, Fig. 2.5.

An important point to note about the second factor in expression (2.10), the vibrational wavefunction for the ground vibrational level in the A-state $|v' = 0\rangle$, is that it is not identical to the ground vibrational level in the X-state $|v = 0\rangle$. This is because exciting the outermost electron into a higher orbit changes the potential in which the nuclei oscillate. As we shall see, this allows the vibrational state to change when the molecule scatters light.

Finally, as with the ground state the hyperfine interaction leads to a slight splitting of the excited state into an $F' = 1$ and $F' = 0$ component, represented by the last vector $|F', m'_F\rangle$. The small splittings are shown in Fig. 2.3. As we are only interested in the ground vibrational and rotational levels of $A^2\Pi_{1/2}$, we will frequently drop the reference to the vibrational and J quantum numbers of the excited state and write $A^2\Pi_{1/2} (v' = 0, J' = 1/2, \mathcal{P}' = \pm 1) \equiv A^2\Pi_{1/2} (\mathcal{P}' = \pm 1)$.

2.2.4 Transitions

We are also interested in the optical, microwave and radio-frequency transitions between the states of YbF. The mathematical theory to quantitatively model how the molecule responds to this range of driving fields is developed more fully in Chapter 6, but it is helpful at this stage to simply describe the possible transitions.

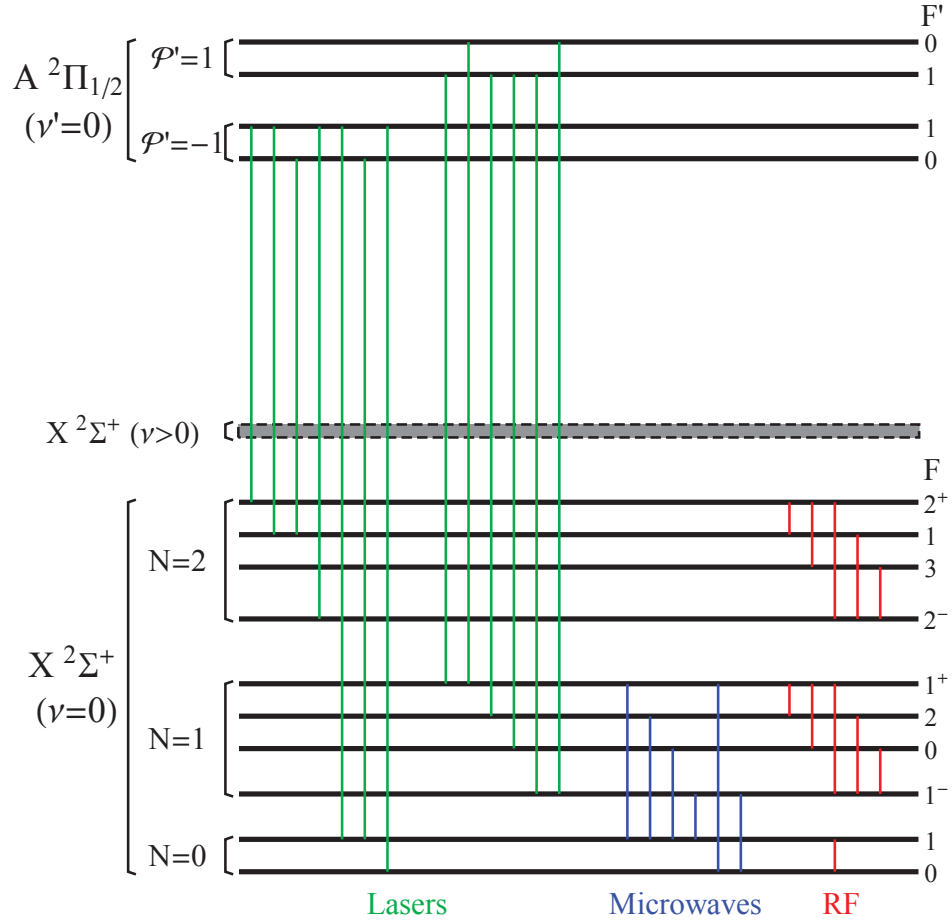


Fig. 2.4: A few relevant transitions between YbF energy levels. Microwave transitions between $N = 1$ and $N = 2$ are not shown.

Optical Transitions

States belonging to $X\ ^2\Sigma^+$ can be optically excited to $A\ ^2\Pi_{1/2}$, and $A\ ^2\Pi_{1/2}$ states decay by fluorescence into $X\ ^2\Sigma^+$. The transitions are all in the green region of the

visible spectrum; the wavelength for transitions from $v = 0$ to or from $v' = 0$ is around 552 nm. The selection rules that govern these optical transitions are simply

$$\Delta\mathcal{P} = \pm 1, \quad (2.13)$$

$$\Delta F = 0, \pm 1, \quad (2.14)$$

$$\Delta m_F = 0, \pm 1 \text{ but not } \Delta m_F = 0 \text{ if } \Delta F = 0. \quad (2.15)$$

Since optical transitions must change parity (rule (2.13)), transitions between $A^2\Pi_{1/2}$ and $X^2\Sigma^+$ ($N = 0, 1, 2$) form two groups. The positive parity $N = 0$ and $N = 2$ are both driven to the $\mathcal{P}' = -1$ excited state, whereas $N = 1$, which has negative parity, is driven to the positive parity $\mathcal{P}' = 1$ excited state. These are shown as two slightly separated groups of green lines on the left hand side of Fig. 2.4. Since each rotational level of $X^2\Sigma^+$ can only be driven to one parity component of the excited state, we will frequently drop the \mathcal{P}' label of the excited state and take it as read that the allowed transition is being driven.

The decays of $A^2\Pi_{1/2}$ states excited by laser light follow the selection rules (2.13)–(2.15). As discussed above, the X and A state vibrational state vectors are not the same, so the vibrational quantum number can change in an optical transition. However, the overlap is high: $|\langle v = 0 | v' = 0 \rangle|^2 = 0.928$ [53], which means that $A^2\Pi_{1/2}(v' = 0)$ will decay into $v > 0$ only 7.2% of the time. Rule (2.13) continues to apply, so molecules in $A^2\Pi_{1/2}(\mathcal{P}' = 1)$ can only decay to the $N = 1$ state, and molecules excited to the negative parity state can only decay into $N = 0$ or $N = 2$.

Notice that the requirement that F only change by at most one unit of angular momentum means that the $X^2\Sigma^+(N = 2, F = 3)$ state cannot be optically excited to $A^2\Pi_{1/2}(J' = \frac{1}{2})$, nor can decaying molecules from $A^2\Pi_{1/2}(J' = \frac{1}{2})$ fall into $X^2\Sigma^+(N = 2, F = 3)$. Consequently, if we are only interested in optical transitions, we can safely ignore this state.

Microwave transitions

Microwaves play no part in the current experiment but they will be used in the improvements to the experiment discussed in the second half of the thesis. For the microwave transitions between $N = 0$ and $N = 1$ levels of $X^2\Sigma^+(v = 0)$, the electric dipole selection rules are the same as for optical transitions (Eqs. (2.13)-(2.15)), but the frequencies are around 14.5 GHz. The possible transitions are shown in blue in Fig. 2.4.

RF transitions

Magnetic dipole radio-frequency transitions between the hyperfine states are used to manipulate the YbF spin, both in the completed experiments and in the new scheme discussed in Chapter 5. The selection rules for these transitions are

$$\Delta\mathcal{P} = 0, \quad (2.16)$$

$$\Delta F = 0, \pm 1, \quad (2.17)$$

$$\Delta m_F = 0, \pm 1 \text{ but not } \Delta m_F = 0 \text{ if } \Delta F = 0. \quad (2.18)$$

These transitions are shown in red in Fig. 2.4, and have frequencies between 30 and 190 MHz.

2.2.5 Simplified energy level structure

Having gone into some detail about the structure of the energy levels of YbF, now we concentrate on the levels relevant for the basic operation of the experiment, shown in Fig. 2.5. The most important levels shown are the two hyperfine components $F = 0$ and $F = 1$ of the ground electronic, rotational and vibrational state $X^2\Sigma^+(N = 0, v = 0)$. When we need to refer to the magnetic sub-levels individually, we use the notation: $|F, m_F\rangle$. We also show the lowest-energy electronically excited states into which these ground states can be excited, namely

$A^2\Pi_{1/2}(\mathcal{P}' = -1, v' = 0)$ $F' = 0$ and $F' = 1$. Finally, a grey box indicates all the other states into which the electronically excited states can decay.

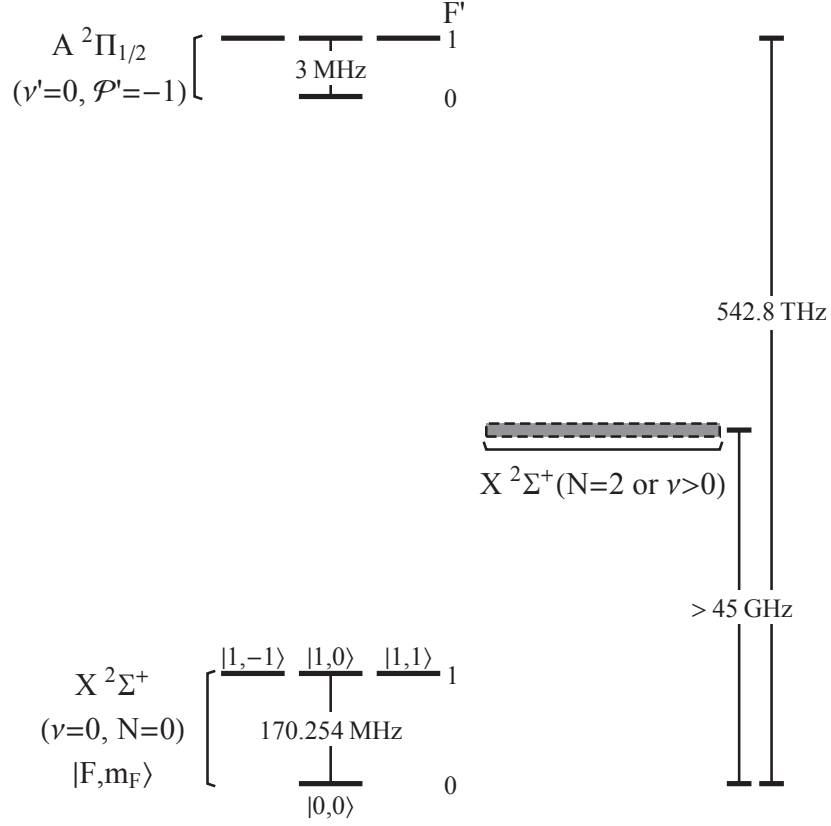


Fig. 2.5: A simplified energy level structure for YbF.

2.3 The experimental apparatus

Now that the structure of YbF has been discussed, we move on to present an overview of the apparatus, before describing how we use it to measure the size of the eEDM. This equipment is described in more detail in the thesis of Joe Smallman [49].

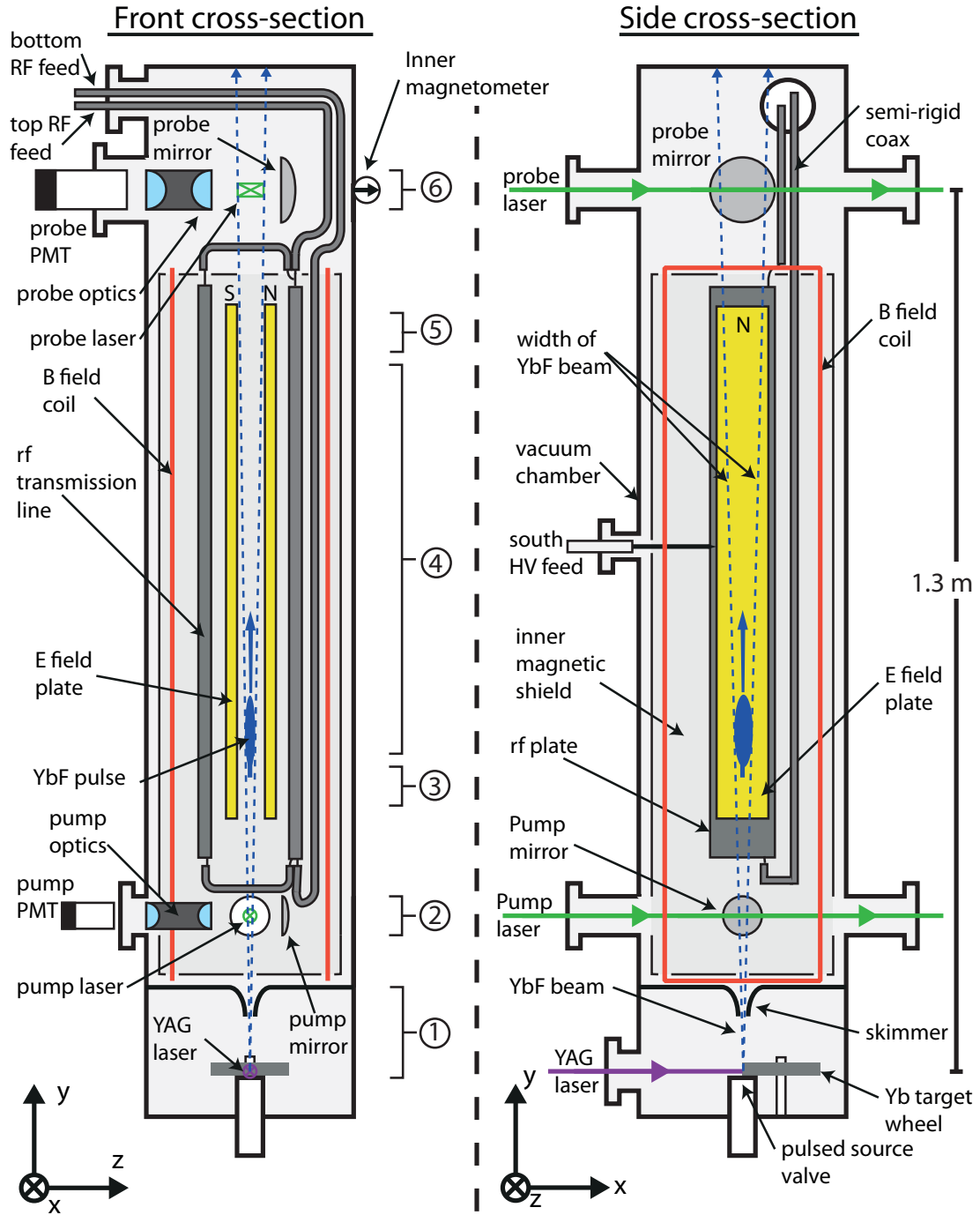


Fig. 2.6: The YbF beam machine. A YbF pulse shown in dark blue, is produced at the bottom of the machine and flies upward, expanding transversely as it goes (width indicated by the blue dashed line).

2.3.1 YbF beam machine

The core of the experiment is a ~ 2 m tall cylindrical vacuum chamber, shown in two cross-sections in Fig. 2.6 and in the photograph of Fig. 2.7. In normal operation, the vacuum chamber is surrounded by two layers of mu-metal magnetic shields which can be seen in Fig. 2.7 (b), but are not shown in Fig. 2.6. To explain the parts of the vacuum chamber it easiest to start at the bottom of the machine and work upwards. The circled numbers refer to Fig. 2.6.

In the bottom of the chamber, section ①, there is a supersonic source of YbF [54] [55], which functions as follows. First a solenoid valve opens for 160 μs releasing a gas mix of 98% argon and 2% SF_6 into the vacuum. After 350 μs , a YAG laser ablates a strip of ytterbium target in the presence of this gas mix, producing some YbF. The gas and molecules supersonically expand in the vacuum, cooling to a translational temperature between 3–15 K and a rotational temperature of 1–5 K. This produces $\sim 3 \times 10^9$ YbF molecules per steradian per pulse in the $X^2\Sigma^+(v=0, N=0, F=1, 0)$ states, flying upwards at 590 m s^{-1} . Any other products of the ablation or molecules that occupy other states of YbF play no part in the experiment and are ignored. The pulse passes up through a 2 mm diameter skimmer whose aperture is 94 mm above the source. This produces a collimated beam travelling towards the ceiling (along the y axis). The outline of this beam is shown in dotted blue in Fig. 2.6.

The next region of interest, ②, is the pump laser region. Here the beam passes through a pump laser and fluorescence scattered by the YbF molecules is imaged by a lens and mirror arrangement onto a photomultiplier tube (PMT). Regions ③–⑤ are the core of the experiment, and are located within a 1mm thick mu-metal shield (diameter 170 mm, height 985 mm with end caps). These contain a pair of 750 mm long, gold coated aluminium, high-voltage electric field plates, spaced by 12 mm and shown in yellow. These electric field plates are charged to $\pm 7.5\text{kV}$, producing a 12.5 kV cm^{-1} electric field between them. The field is either orientated along $+z$ or $-z$, depending on whether the plate labelled ‘N’ is positively charged and

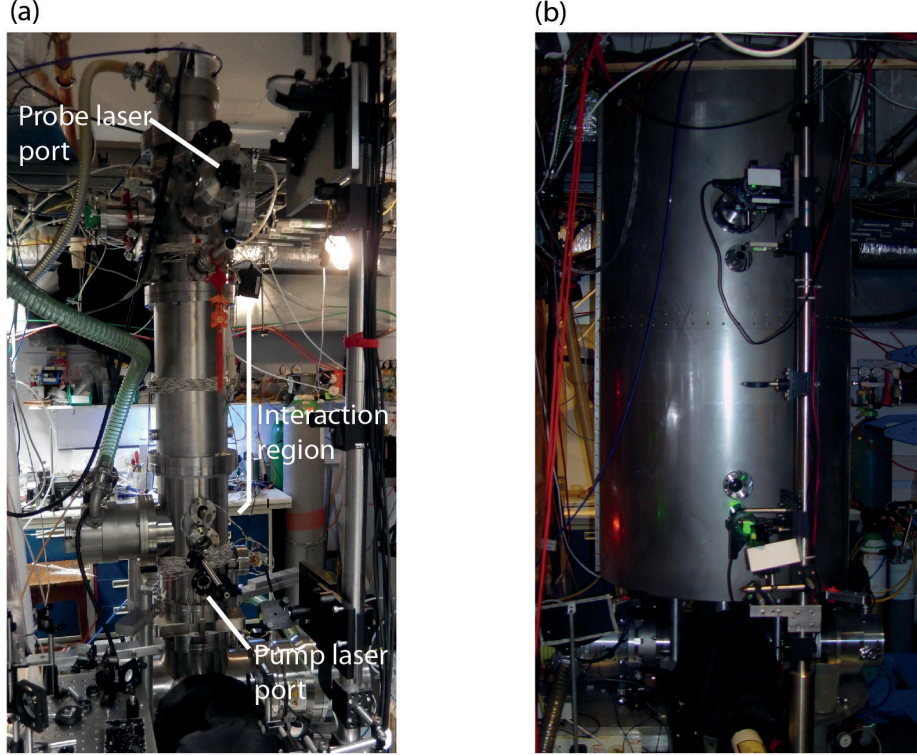


Fig. 2.7: Two pictures of the main eEDM vacuum chamber (a) without and (b) with the two outer mu-metal shields

‘S’ is negatively charged, or vice versa. A pair of magnetic field coils, shown in red, produce an adjustable magnetic field in the region of 10 nT, also along $\pm z$, depending on the direction in which current flows. Finally there is an rf, TEM, parallel plate transmission line (long grey rectangles in the diagram), designed to support 170 MHz rf waves. The rf enters the machine through a semi-rigid coax feed at the top, and is coupled into the transmission line. At the other end it is coupled out again into another length of semi-rigid coax. The rf can be fed in either direction and can therefore travel up or down the machine. In either case the magnetic field of the radiation, which drives rf transitions, lies along the machine x axis.

The last region of interest is ⑥, the probe region. Here the molecules fly through a probe laser beam and scatter probe light according to their internal state. Around

6% of the photons emitted by the molecules are imaged onto a PMT, which has a quantum efficiency of 0.1, so the total detection efficiency is 0.6%.

Having examined the beam machine, we now briefly discuss how the laser, high voltage, magnetic and radio-frequency fields that are fed into the machine are produced.

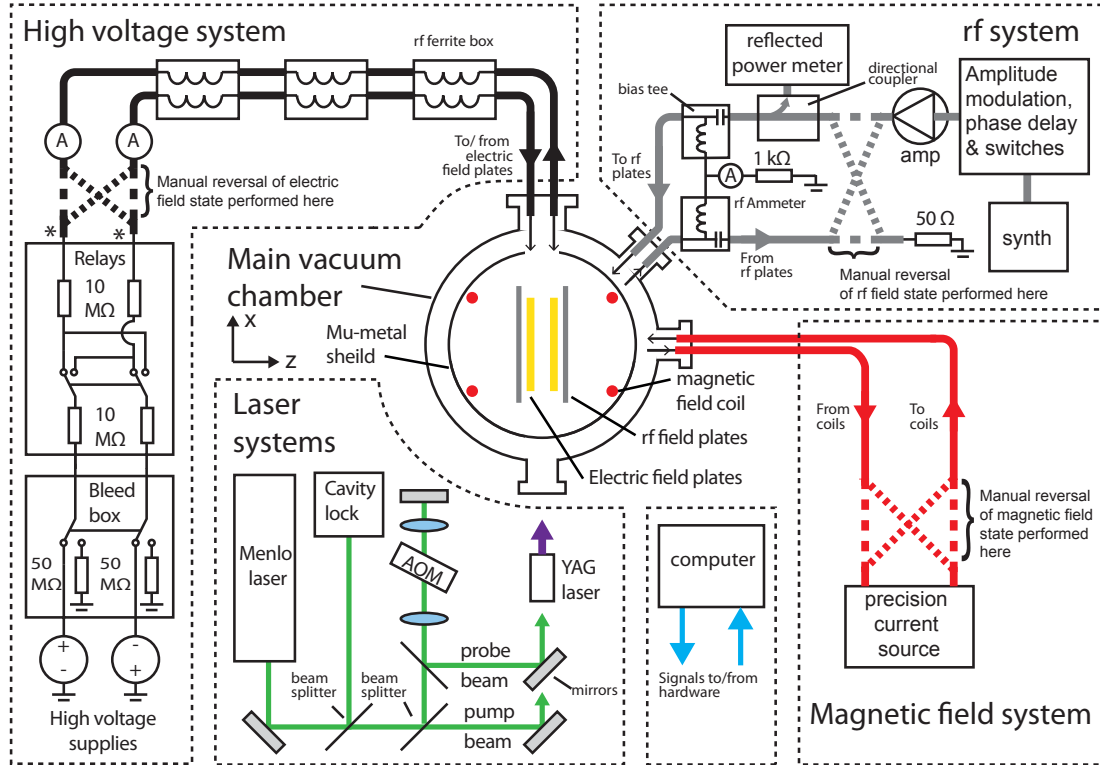


Fig. 2.8: The apparatus used to generate the high voltage, laser, rf and magnetic fields used in the experiment.

2.3.2 Laser beam generation

The pump and probe lasers are both derived from the same frequency-doubled solid state fibre laser, a *Menlo Orange One* with NTT doubler head. The laser is tuned to the $X^2\Sigma^+ (v = 0, N = 0, F = 1) \rightarrow A^2\Pi_{1/2}$ transition at 542,811,000 MHz by adjusting the *Menlo's* internal piezo and is actively frequency stabilised to a frequency

stable HeNe laser using a transfer cavity lock [56].

Some of the light is expanded to a 5mm-radius Gaussian beam and used to excite $X^2\Sigma^+ (F = 1) \rightarrow A^2\Pi_{1/2}$ in the pump region (2). The total power into the machine is approximately 5 mW. The remaining light is doubled-passed through an acousto-optic modulator (AOM) which blue shifts the light by 170.25 MHz so that it can excite $X^2\Sigma^+ (F = 0) \rightarrow A^2\Pi_{1/2}$ in the probe region (6). This beam is expanded to a size of 10×5 mm and around 2 mW cm^{-2} (approximately half the saturation intensity of 4.4 mW cm^{-2}) drives the $X^2\Sigma^+ (v = 0, N = 0, F = 0) \rightarrow A^2\Pi_{1/2}$ transition. Both the pump and probe beams are linearly polarised before entering the machine with orientation that we can adjust in the x - y plane. A schematic summary of the probe laser system can be seen in Fig. 2.8.

2.3.3 High voltage generation

The equipment used to generate and control the high voltages applied to the electric field plates is shown in the left hand side of Fig. 2.8. The high voltages are generated by positive and negative *Applied Kilovolts* supplies, set to produce $\pm 7.5 \text{ kV}$. The connection between the supplies and the high voltage plates can be reversed automatically using a high voltage relay system described in D M Kara’s thesis [57]. This means that either positive or negative voltages can be applied to the North or South plates, labelled ‘N’ and ‘S’ in Fig. 2.6. There is also a “bleed box” that can ground the plates between switches. The connections between the supplies and the plates can also be reversed manually by changing the way the cables to the machine are plugged into the relays. They can either be connected directly (vertical dashed thick black lines in Fig. 2.8) or crossed over (diagonally crossed thick black dashed lines in Fig. 2.8). We call these two manual configurations of the electric field ‘true’ and ‘false’ respectively. Each of the cables contains a nano-ammeter [58] which measures the leakage current flowing from the plates during eEDM data taking, and can also be used to measured the charging currents. High voltage cables go from the rack

to the high-voltage feedthroughs on the eEDM machine, running through three sets of rf ferrites to isolate the high voltage system from any radio-frequency fields. The feed to the South plate is shown on the right hand cross-section of Fig. 2.6.

2.3.4 Radio frequency generation

The radio-frequency equipment used in the experiment is shown in the top right hand side of Fig. 2.8. The rf is generated by a *HP 8657A* synthesiser, which is switched on throughout the experiment. Short pulses of rf can be made by opening a pair of *Minicircuits ZASWA-2-50DR* switches on the output of the synthesiser. The frequency of these pulses can be quickly tuned by adjusting the synthesiser's Direct Current Frequency Modulation (DCFM) input, and their amplitude can be independently controlled with an external amplitude modulator. The relative phase of two pulses can be adjusted by changing the DCFM voltage in between the pulses, and also by means of a *Minicircuits PAS-1* bi-phase modulator which can add an optional 180° phase delay to the second rf pulse. The exact configuration of all these rf components is described in much more detail in Ref. [49].

Once pulses of the correct amplitude, frequency, phase and duration are created, they are amplified by a *CPC MRI Plus* amplifier and are sent into the vacuum chamber. The cables into the machine can either be connected so that the rf is sent into the top rf feed or the bottom rf feed. The two possible ways of connecting the cables are shown at the top left of Fig. 2.8, where the horizontal, thick grey dashed lines correspond to rf being sent into the bottom of the transmission line (travelling up through the machine), and the diagonally crossed thick grey dashed lines correspond to rf being sent into the top of the machine (travelling down through the machine). We call these rf manual states 'true' and 'false' respectively. In either case, the rf is coupled out of the machine and dumped into a $50\ \Omega$ load.

2.3.5 Magnetic field generation

The magnetic fields are generated by a home build precision current source, described in Ref. [49] and indicated on the right hand side of Fig. 2.8. It is capable of producing currents up to a few milliamperes with a fractional stability of 5×10^{-3} . The manual state of the magnetic fields can also be swapped by reversing the cables on the output of the magnetic field supply. The vertical dashed red lines correspond to manual state “true” and the crossed red lines correspond to manual state “false”.

2.4 The experimental sequence

Having described the structure of the YbF molecule and given an overview of the experimental set-up, we now describe the main practical steps when we make a measurement of the size of the eEDM.

The experiment makes measurements on a pulsed supersonic beam of YbF. The sequence from the creation of a YbF packet to its destruction as it flies into the top of the machine is called a *shot*. The machine fires a shot approximately every 40 ms at a rate which is phase locked to half the mains frequency. It takes 2.6 ms for the shot to be completed. We start by following the sequence of events in one of these shots.

In between shots, some of the settings of the experiment can be changed. These could be the size or the direction of the applied magnetic field \mathbf{B} , and/or the direction of the applied electric field \mathbf{E} , for instance. Below, we describe how a measurement of the the eEDM involves taking several shots where the size and direction of \mathbf{B} and \mathbf{E} are varied.

We then go on to discuss the normal operation of the eEDM machine, where 9 parameters can be varied between two values each, giving $2^9 = 512$ distinct states of the machine. A collection of 4096 shots where each state of the machine is visited 8 times is called a *block*. This is the smallest amount of data that gives an

eEDM measurement; each block contains a value of the eEDM alongside many other measurements.

2.4.1 A shot

We now follow the sequence of actions during a single shot of the interferometer. To recap, the sequence of events is as follows: we first prepare the YbF spin and internuclear electric field along orthogonal axes, then allow the spin to precess in the presence of the internuclear field, before measuring the change in orientation caused by the electric field.

The numbers in this section indicate roughly where the events described take place in the machine, as shown in Fig. 2.6.

① *Make some YbF*

The source valve opens and the YAG laser fires, creating a pulse of YbF travelling upwards at 590 m s^{-1} . Only the molecules which thermalise to the ground vibrational and rotational state of $X^2\Sigma^+$ are used in the experiment.

② *Clear out the $F=1$ level with a pump beam*

The YbF molecules fly through the pump laser tuned to the $X^2\Sigma^+(v=0, N=0, F=1) \rightarrow A^2\Pi_{1/2}$ transition. The nearly degenerate spacing of the $F'=0$ and $F'=1$ levels in the excited state means that a single laser can drive transitions from $F=1$ to both levels. The intensity of the laser beam and flight time of the molecules through the beam are sufficient to pump molecules out of the $F=1$ state. Because of the allowed decays from the excited electronic state to the $X^2\Sigma^+(v=0, N=2)$ and $X^2\Sigma^+(v>0)$ levels, only 1/3 of molecules excited to $A^2\Pi_{1/2}$ will end up decaying into the $F=0$ ground state, roughly doubling its population. The optical pumping scheme is shown in Fig. 2.9 (a). The fluorescence caused by these decays is detected by a photomultiplier tube (PMT).

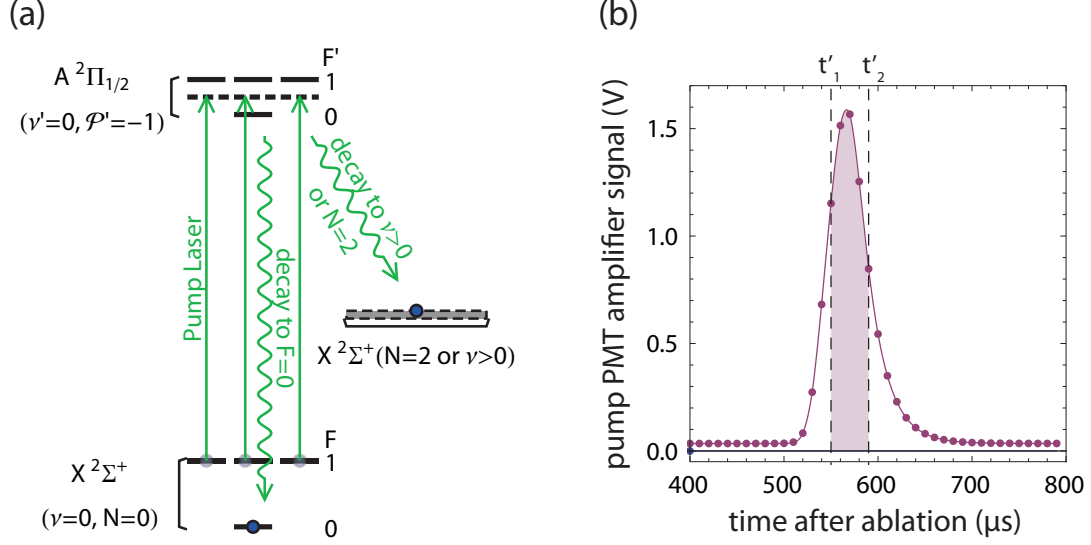


Fig. 2.9: (a) A pump laser beam addresses the three magnetic sub-levels of $F = 1$, removing any molecules which happen to be in this level. (b) The fluorescence signal detected by the pump PMT (red dots), with an accompanying interpolation function (red line). The dashed lines at t'_1 and t'_2 indicate the usual region over which the pump PMT signal is integrated (giving the shaded red region), as described on page 67.

The time-dependent fluorescence signal is recorded as the molecular pulse flies through the beam; since the source produces a spread of velocities, the signal lasts for around 150 μs while molecules with different velocities pass through the pump beam. The signal recorded by the pump PMT for a shot is shown in Fig. 2.9 (b).

③ Prepare the YbF into a superposition of $|1, -1\rangle$ and $|1, 1\rangle$

In between regions ② and ③ the molecules enter the space between the rf and dc field plates. The 12.5 kV cm^{-1} field polarises the YbF molecules, aligning their axis \mathbf{n} with the axis of the applied electric field z . For our choice of field, the polarisation factor $\eta = \langle \mathbf{n} \cdot \mathbf{e}_z \rangle$ is 0.61, where \mathbf{e}_z is a unit vector along z . This causes a Stark shift of the m_F components of the $F = 1$ energy levels, shown in Fig. 2.10 (a).

When the molecules are approximately in section ③, a first pulse of rf radiation ($\omega_{\text{rf}} = 2\pi \times 173.6 \text{ MHz}$, pulse length 9 μs) is sent down the rf transmission

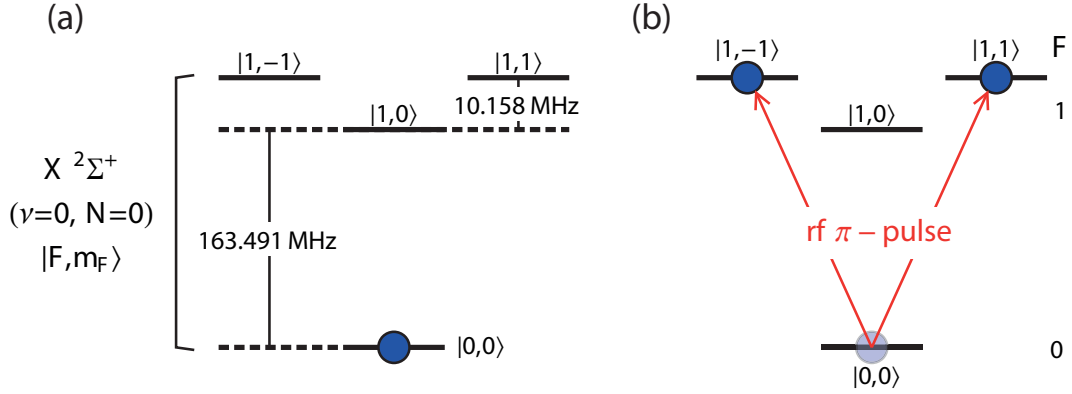


Fig. 2.10: (a) The Stark shifting of the $X^2\Sigma^+$ ($v = 0, N = 0$) levels in a 12.5 kV cm^{-1} electric field. (b) The excitation of $|0,0\rangle$ into a superposition $\frac{i}{\sqrt{2}}(|1,1\rangle - |1,-1\rangle)$ using an rf pulse.

line. The rf magnetic field \mathbf{B}_{rf} field is linearly polarised along x : $\mathbf{B}_{\text{rf}} = B_{\text{rf}}\mathbf{e}_x$. This can be rewritten as a sum of left and right circularly polarised magnetic fields: $\mathbf{e}_x = (\boldsymbol{\epsilon}_{-1} - \boldsymbol{\epsilon}_1)/\sqrt{2}$, where $\boldsymbol{\epsilon}_{\pm 1}$ are the unit vectors for radiation that drives σ^{\pm} transitions respectively, taking the quantisation axis to be along the z axis. The rf therefore drives the state $|0,0\rangle$ up to a superposition of $|1,-1\rangle$ and $|1,1\rangle$. We set the amplitude of B_{rf} such all the population is coherently transferred up to $F = 1$, (a π -pulse) then the system ends up in the superposition³ of the excited states

$$|0,0\rangle \rightarrow \frac{i}{\sqrt{2}}(|1,1\rangle - |1,-1\rangle). \quad (2.19)$$

The process is shown graphically in Fig. 2.10 (b).

④ Let the YbF spin evolve in electric and magnetic fields

Now we allow the molecules to evolve in the electric and magnetic fields while they fly upwards through the machine for a time $\tau = 980 \text{ } \mu\text{s}$. The Zeeman and eEDM interaction Hamiltonians $\hat{H} = -\hat{\boldsymbol{\mu}} \cdot \mathbf{B} - \eta d_e E_{\text{eff}}$ cause a perturbation to the $|1,-1\rangle$ and

³ To remove some global phase factors that multiply the states that follow, we define the energy scale so that the Stark shifted $|1, \pm 1\rangle$ levels have zero energy.

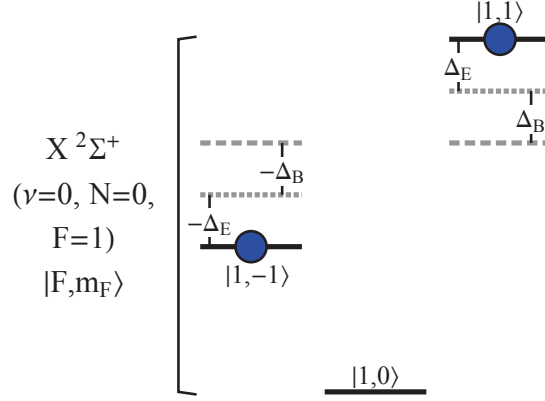


Fig. 2.11: The splitting of the states $|1,1\rangle$ and $|1,-1\rangle$ due to the Zeeman and electric dipole interactions. The splittings are given by $\Delta_B = \mu_B B$ and $\Delta_E = -\eta d_e E_{\text{eff}}$. Typical values are $|\Delta_B/\hbar| = 2\pi \times 125$ Hz, $|\Delta_E/\hbar| < 2\pi \times 1.2$ mHz

$|1,1\rangle$ levels, shifting their energy by $\mp(\Delta_B + \Delta_E) = \mp(B\mu_B - \eta E_{\text{eff}} d_e)$ respectively.⁴ If the electric and magnetic fields are both applied in the positive z direction, and the electron electric dipole has the same sign as the magnetic dipole ($d_e = -|d_e|$), then the Zeeman interaction will cause the $m_F = -1$ level to shift down in energy, whereas the eEDM interaction shifts the level up slightly in energy. This is a consequence of the fact that the internuclear electric field always opposes the applied field, so in this case $\eta E_{\text{eff}} = -0.61 \times 26$ GV cm⁻¹.

It follows from the Schroedinger equation that an eigenstate $|E\rangle$ of the system's Hamiltonian with energy E evolves after a time τ into the state $e^{-iE\tau/\hbar} |E\rangle$. Thus, the molecules evolve from the state on the right of Eq. (2.19) according to

$$\frac{i}{\sqrt{2}} (|1,1\rangle - |1,-1\rangle) \rightarrow \frac{i}{\sqrt{2}} (e^{-i(\phi_B + \phi_E)} |1,1\rangle - e^{i(\phi_B + \phi_E)} |1,-1\rangle), \quad (2.20)$$

where $\phi_B = \Delta_B \tau / \hbar$ and $\phi_E = \Delta_E \tau / \hbar$. This evolution has a simple interpretation as a precession of system's angular momentum about the z axis. In this picture, the

⁴ We adopt the convention used in the 2010 CODATA [59] that dipole of a system is positive if aligned with the angular momentum, and negative if antialigned. Thus $\hat{\mu} = -\mu_B \hat{F}$ for the $F = 1$ level with $g_F = -1$.

initial vector is acted on by the operator

$$\hat{\mathcal{R}}(\phi) = e^{-i\phi} |1, 1\rangle \langle 1, 1| + |1, 0\rangle \langle 1, 0| + e^{i\phi} |1, -1\rangle \langle 1, -1|, \quad (2.21)$$

which rotates a quantum state anticlockwise by an angle ϕ about the z axis. This operator can be derived using the results in Appendix A. Applying the operator to the state prepared by the rf gives

$$\hat{\mathcal{R}}(\phi) \frac{i}{\sqrt{2}} (|1, 1\rangle - |1, -1\rangle) = \frac{i}{\sqrt{2}} (e^{-i\phi} |1, 1\rangle - e^{i\phi} |1, -1\rangle) \quad (2.22)$$

In other words, the electric and magnetic fields apply a torque to the YbF molecule, causing it to rotate with a constant angular frequency $\dot{\phi} = (\Delta_B + \Delta_E) / \hbar$ clockwise about the z axis.

⑤ Drive population in $|1, 1\rangle - |1, -1\rangle$ back to $|0, 0\rangle$ with a second rf pulse

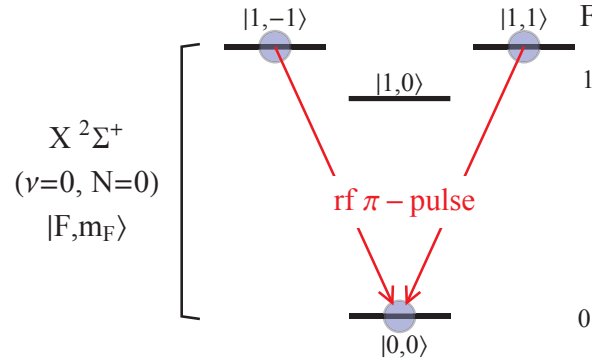


Fig. 2.12: A second RF pulse maps the state $\frac{i}{\sqrt{2}} (|1, 1\rangle - |1, -1\rangle)$ down to $|0, 0\rangle$. Because the phase of the superposition has evolved, some population is left in $F = 1$ and some is transferred to $F = 0$.

At ⑤, when the evolution time reaches $\tau = 980 \text{ } \mu\text{s}$, a second rf pulse is sent through the transmission line. The polarisation of the rf is still along x , but now all the population is in the $F = 1$ state. The overlap of the final state in Eq. (2.20) with the state $(|1, 1\rangle - |1, -1\rangle) / \sqrt{2}$ is transferred coherently down to the state $ie^{i\phi_{\text{rf}}} |0, 0\rangle$

with another π -pulse. Here $\phi_{\text{rf}} = \omega_{\text{rf}} \times 9 \text{ } \mu\text{s}$. Since the excited state has precessed from the originally prepared state (2.19) to the state (2.20), the overlap is not perfect, and so the amplitude to be in the state $|0, 0\rangle$ after the second rf pulse is

$$-\frac{1}{2}e^{i\phi_{\text{rf}}}(\langle 1, 1| - \langle 1, -1|)(e^{-i(\phi_B + \phi_E)}|1, 1\rangle - e^{i(\phi_B + \phi_E)}|1, -1\rangle) = -e^{i\phi_{\text{rf}}} \cos(\phi_B + \phi_E). \quad (2.23)$$

⑥ Count the number of molecules in $|0, 0\rangle$ with laser induced fluorescence

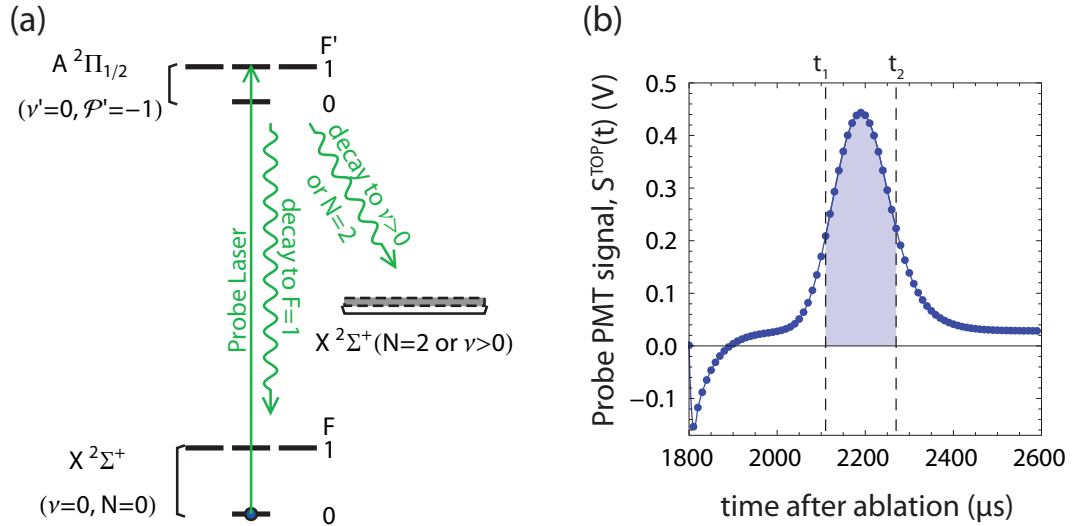


Fig. 2.13: (a) The population in $|0, 0\rangle$ is measured using a probe laser. There is still population remaining in $X^2\Sigma^+ F=1$ and $N=2$, which is not shown. (b) The fluorescence signal detected at the probe PMT as a function of time through the shot. The dip at $1800 \text{ } \mu\text{s}$ is caused by electrical pickup from the second rf pulse on the PMT electronics. By analysing the eEDM signal at different molecular arrival times, we conclude that the rf pickup does not influence our measurement of the eEDM.

The population of the $|0, 0\rangle$ state is read out by a probe laser tuned to the $X^2\Sigma^+(v=0, N=0, F=0) \rightarrow A^2\Pi_{1/2}$ transition, as shown in Fig. 2.13 (a). The fluorescence photons emitted when the molecules decay are measured using a PMT. The photoelectrons produced by the PMT generate a voltage pulse across a sense resistor, which is amplified to produce a time dependent voltage, $S^{\text{TOP}}(t)$. A typical

pulse is shown in Fig. 2.13 (b). This signal is a measure of the rate at which photons land on the detector, and hence its integral gives the total number of photons counted. Laser light is also scattered from surfaces and off-resonantly from other molecules, making a background $\mathcal{G}(t)$, so we write the top PMT signal as

$$S^{\text{TOP}}(E, B; t) = \mathcal{A}(t) \cos^2(\phi_B + \phi_E) + \mathcal{G}(t). \quad (2.24)$$

The spread in molecular velocities leads to a range of arrival times, with the most intense part of the beam crossing the probe laser shortly before 2200 μs . This time dependence in the intensity of the molecules is captured by the pre-factor $\mathcal{A}(t)$. The term of interest is the \cos^2 coming from the right hand side of Eq. (2.23). By considering how $S^{\text{TOP}}(E, B; t)$ varies when E and B are changed from shot to shot, we can extract the value of the eEDM as described next.

2.4.2 Simplified eEDM experiment

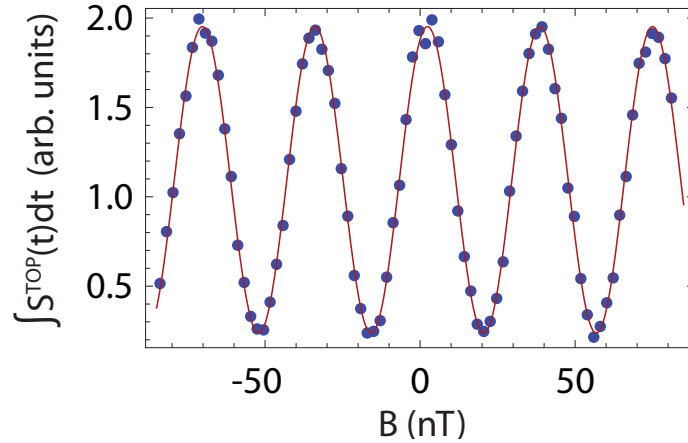


Fig. 2.14: Integrated signal in the top detector as a function of applied magnetic field.

If we take several shots with different values of B for a fixed electric field E pointing along z , we can scan out the \cos^2 interference curve $\int_{t_a - \Delta t/2}^{t_a + \Delta t/2} S^{\text{TOP}}(E, B; t) dt$ shown in Fig. 2.14 for molecules that are detected in a narrow window of length Δt

around the time t_a . Now suppose we reverse the direction of the electric field, then we can scan out a second interference curve $\int_{t_a-\Delta t/2}^{t_a+\Delta t/2} S^{\text{TOP}}(-E, B; t) dt$ where

$$S^{\text{TOP}}(-E, B; t_a) = \mathcal{A}(t_a) \cos^2(\phi_B - \phi_E) + \mathcal{G}(t_a). \quad (2.25)$$

The phase difference between these curves, shown greatly exaggerated in Fig. 2.15, is directly proportional to the EDM: $2\phi_E = 2\Delta_E \tau / \hbar = \frac{2}{\hbar} \eta E_{\text{eff}} d_e \tau$.

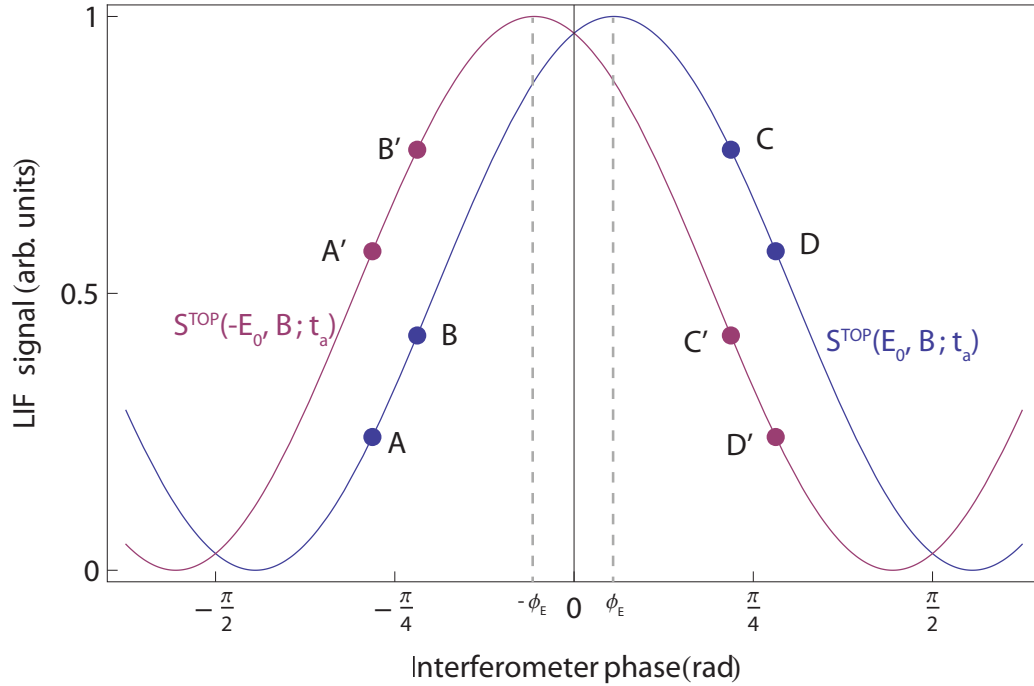


Fig. 2.15: A graph illustrating the phase shift in the interferometer when the direction of E relative to B is reversed. The phase is greatly exaggerated. Also shown are the 8 points on the two interference curves which we use during normal eEDM data-taking to measure the eEDM

We could scan and fit interference curves for both directions of E to determine this phase shift. However, it is a more efficient⁵ use of the measurement time to sample each curve at four different points, using four different values of the magnetic field for each value of the electric field. The signal measured at these four points is labelled

⁵ In this context, efficient means that this method gives a lower statistical uncertainty on the eEDM for a given number of shots.

$\{A, B, C, D\}$ for $S^{\text{TOP}}(+E, B; t_a)$ and $\{A', B', C', D'\}$ for $S^{\text{TOP}}(-E, B; t_a)$, as shown in Fig. 2.15. These values of the magnetic field are chosen to apply phase shifts of $\{-9\pi/32, -7\pi/32, 7\pi/32, 9\pi/32\}$, so that we work in the linear regions of the interference curves, around the $\pm\pi/4$ points. In these regions, the experiment is maximally sensitive to phase shifts caused by the eEDM interaction. The value of the eEDM is given by the combination of these eight points in Eq. (2.26) [60]

$$d_e = \frac{\pi/32}{\eta E_{\text{eff}} \tau} \left(\frac{A + B - C - D - A' - B' + C' + D'}{-A + B + C - D - A' + B' + C' - D'} \right). \quad (2.26)$$

This combination of points may look a little opaque, but we can straightforwardly check that it gives the correct result by inserting Eqs. (2.24) and (2.25) into (2.26) to find that the term in brackets in Eq.(2.26) is equal to $\phi_E/(\pi/32)$, and then use the previous definition of ϕ_E to write the result in terms of d_e . Notice that the amplitude of the interference curve, $\mathcal{A}(t_a)$, and the signal background $\mathcal{G}(t_a)$ do not have to be separately measured if we use this combination of points.

To increase our signal, rather than just use molecules that arrive at a single arrival time t_a , we can repeat this measurement for all the arrival times between $t_1 = 2110 \mu\text{s}$ and $t_2 = 2270 \mu\text{s}$. The integration gates and region of interest are shown in Fig. 2.13.

2.4.3 A more comprehensive eEDM experiment: A block

We have seen how to make a simple measurement of the eEDM by taking groups of 8 shots with suitable values of electric and magnetic fields. We can think of this as the modulation between beam shots of 3 parameters, each having two discrete values; namely the direction of the applied E field (labelled E), the direction of a large applied magnetic field (labelled B), chosen such that $\phi_B = \pi/4$ and a smaller magnetic field (labelled δB) chosen such that $\phi_{\delta B} = \pi/32$. During normal data taking we switch these three parameters and six more, to give 9 modulated parameters, each of which is stepped between two distinct values. This gives rise to 2^9 distinct states of

the machine, specified by the signs of all 9 parameters. We define a block of data as a set of $8 \times 2^9 = 4096$ measurements, in which each of these machine states is visited 8 times. At the start of each block certain settings are fixed. Some of these fixed settings are listed in Table 2.1. The 9 modulated parameters are listed in Table 2.2.

Parameter name	Description	Typical value
ν_{rf1}	Centre frequency of the first rf pulse	173.6 kHz
ν_{rf2}	Centre frequency of the second rf pulse	173.6 kHz
ν_{LF1}	Centre frequency of the probe AOM	170.25 kHz
a_{rf1}	Centre amplitude of the first rf pulse*	0 dBm
a_{rf2}	Centre amplitude of the second rf pulse*	-1.5 dBm
B_0	Bias z field to cancel any stray fields in machine	<2 nT
θ_{probe}	Probe polarisation angle	0-360°
θ_{pump}	Pump polarisation angle	0-360°
Φ_0	Relative phase between rf pulses	0-10 π rad

Tab. 2.1: Parameters held constant during a block. * indicates that this is measured before the rf amplifier.

Each parameter named X is modulated according to a waveform W_X , which is nothing more than a vector with 4096 entries, each either 1 or -1. There are equal numbers of 1 and -1. If the n^{th} entry in the waveform code $(W_X)_n$ is 1, then in the n^{th} shot the step in parameter X is positive, and if the n^{th} entry is -1, the step is negative. The waveforms are also orthogonal: $\sum_i (W_X)_i (W_Y)_i = 0$. They are randomly generated using the methods described in Ref. [61], and chosen to reject low frequency noise and systematic drifts of experimental parameters over the course of the block.

The block begins with the generation of a new set of random waveforms. Once this is complete the machine randomly sets and records θ_{pump} and θ_{probe} , the polarisation

Parameter name	Description	Stepped between
E	Electric field along z	$\pm 12.5 \text{ kVcm}^{-1}$
B	Large step in the magnetic field. Equivalent to stepping between $(A+B)/2$ and $(C+D)/2$ on Fig. 2.15. Causes the molecules to precess by an angle $\phi_B = \pm\pi/4$ as defined by Eq.(2.22).	$B_0 \pm 8.8 \text{ nT}$
δB	Small step in the magnetic field. Equivalent to stepping between A and B. Causes the molecules to precess by an angle $\phi_B = \pm\pi/32$ as defined by Eq.(2.22)	$\pm 1.1 \text{ nT}$
RF1F	Frequency of the first rf pulse	$\nu_{\text{rf1}} \pm 2 \text{ kHz}$
RF2F	Frequency of the second rf pulse	$\nu_{\text{rf2}} \pm 2 \text{ kHz}$
RF1A	Amplitude of the first rf pulse	$a_{\text{rf1}} \pm 5\%$
RF2A	Amplitude of the second rf pulse	$a_{\text{rf2}} \pm 5\%$
LF1	Frequency of the probe laser AOM	$\nu_{\text{LF1}} \pm 300 \text{ kHz}$
PI	Fixed phase shift between rf pulses	$\Phi_0 \pm \pi/2 \text{ rad}$

Tab. 2.2: Parameters switched during a block. The total magnetic field is the sum of the B and δB parameters.

direction of pump and probe laser beams, and Φ_0 , the phase difference between the two rf pulses. The machine then runs through each of the 9 stepped parameters listed in Table 2.2, applying first the positive step and then the negative step and recording the value of the parameter in each state as follows: the electric field is measured by measuring the voltage across a sense resistor in the switching apparatus. The magnetic field steps B and δB and the bias field B_0 are measured by recording the current applied to the magnetic field coils. The size of the rf frequency steps RF1F and RF2F and central frequencies ν_{rf1} and ν_{rf2} are measured with a frequency

counter, as is the size of the laser frequency step $\Delta\nu_{\text{LF1}}$ and the centre frequency ν_{LF1} . The amplitude of the rf pulses is measured with an rf power meter. This process takes around 40 s to complete.

Once these preliminary measurements are complete, the machine begins to fire the 4096 shots, switching the parameters in between shots according to the waveform codes so that the machine is in the correct state for each shot. The shots are taken at a rate of 25 Hz, which gives a total time of 40 ms for each shot. The molecules are only flying through the machine for 2.6 ms, and the remaining time is sufficient to switch all of the parameters apart from the electric field. The E switch is deliberately slow, taking 16 s to switch the electric field direction. This is done to ensure that the charging currents are limited to a few μA , low enough to avoid magnetising the magnetic shields. The details of these charging currents are discussed in more detail in section 3.5.2.

After all shots have been taken the data from the block is automatically analysed using the techniques discussed in the following section 2.5 and the parameters in Table 2.1 can be adjusted based on the results. These adjustments ensure that the rf and laser frequencies are kept on resonance and any stray magnetic fields along z are trimmed away by the bias field B_0 . The machine is now ready to take another block.

2.4.4 Clusters

A collection of blocks is taken autonomously by the eEDM machine without human intervention over the course of a single day in what we call a *cluster*. In between clusters we check the alignment of the laser beams, de-magnetise the shields if necessary and every 10 or so clusters we have to break vacuum in the source chamber to clean the YbF target wheel. Otherwise, the experiment can run continuously even over the weekend without intervention.

In between clusters we can also change the ‘manual state’ of the machine by

reversing the cable connections between the electric field rack and the vacuum chamber as described in section 2.3.3 (changing the E manual state), or by swapping the cables on the output of the rf generation apparatus and the machine as described in 2.3.4 (changing the rf manual state) or swapping the connections between the machine and the current supply which drives current around the magnetic field coils (changing the B manual state). Each of these three manual states is either ‘true’ or ‘false’ depending on which way round the cables are connected, so for each cluster we associate a three letter code such as {T,T,T} which indicates the manual state of the machine during that cluster. The convention is that the manual states are in the order {E,B,rf}. By understanding how the signals in our detectors change with manual reversals we can learn much about the source of any signals we see in the detectors, including systematic errors that might masquerade as an eEDM.

2.5 Data acquisition and analysis

2.5.1 Detectors

The detectors that gather data during each shot can be grouped into two types. Single point detectors produce one value for every shot of the block, whereas time dependent (TD) detectors produce several values as a function of time during a shot. We have already come across two TD detectors in section 2.3.1, namely the pump and probe PMTs. Here we list the remaining detectors in Tables 2.3 and 2.4. We will encounter many of these detectors again in the sections and chapters to come, but two that deserve a special mention are the ‘short’ and ‘9V battery’. These are plugged straight into the analogue-to-digital converter (ADC) card which samples the TD detectors and are useful for checking that the data acquisition electronics and signal processing algorithms give the right results when provided with these well-defined inputs.

Detector	Short name	Measures
Pump photodiode	NPD	Power of the pump laser beam
Probe photodiode	TPD	Power of the probe laser beam
MiniFlux 1 magnetometer	M1	Magnetic field along z axis close to the high voltage supplies
MiniFlux 2 magnetometer	M2	Magnetic field along z over the optical table, half way between MiniFlux1 and MiniFlux3
MiniFlux 3 magnetometer	M3	Magnetic field along z axis on top of the computer control rack
North leakage monitor	NL	Leakage current on the cable connected to the North plate (see Fig. 2.8 for location)
South leakage monitor	SL	Leakage current on the cable connected to the South plate (see Fig. 2.8 for location)
rf1 reflected power	R1	Power of the rf reflected out of the machine during first rf pulse (see Fig. 2.8 for location)
rf2 reflected power	R2	Power of the rf reflected out of the machine during second rf pulse (see Fig. 2.8 for location)
Pi flip monitor	PF	Phase of second rf pulse with respect to the first

Tab. 2.3: Single point detectors that record a single value each shot.

Detector	Short name	Measures	Records between (μs)	Resolution (μs)	Typical gates (μs)
Pump PMT	NORM	Laser induced fluorescence from pump beam	1800–2590	10	549–591
Probe PMT	TOP	Laser induced fluorescence from probe beam	400–780	10	2110–2270
Inner magnetometer	MAG	Magnetic field along z next to vacuum chamber (see Fig. 2.6 for location)	400–2400	200	400–2400
Short	GND	Voltage across a 50 Ω resistor; dummy input	400–2400	200	400–2400
9V battery	BAT	Voltage of a 9V battery; dummy input	1800–2590	10	1800–2590
RF Ammeter	RFC	DC current flowing onto rf plates (see Fig. 2.8)	400–2400	100	400–2400

Tab. 2.4: Time dependent detectors that record several values over a shot.

2.5.2 Extracting channels from a block

Once the block is completed, we have a set of detected quantities from the detectors listed in Tables 2.4 and 2.3 for each of the 4096 shots within the block. Let $S_i^D(t)$ label the (possibly time-dependent) quantity with short name D on the i^{th} shot of the interferometer. During each of these shots the machine was in one of the 512 possible states corresponding to each of the possible switched parameters either being in the ‘plus’ switch state or the ‘minus’ switch state.

We would like to analyse the data not only to extract the eEDM signal, but also to investigate the effect on all the detected quantities of stepping parameters or combinations of parameters. This allows us to check that the experiment is running correctly, and in particular to search for systematic errors in the determination of the eEDM. To that end, for a waveform W_X , we define a signal *channel* for detector D as

$$\{X\}_D(t) = \frac{1}{N} \sum_{i=1}^N (W_X)_i S_i^D(t) , \quad (2.27)$$

where $N=4096$. We most frequently want to consider channels in the top (probe) PMT detector, divided (normalised) by the integrated signal on that shot from the pump PMT. We call this composite detector the ‘Top Normed’. This normalisation reduces the effect of shot-to-shot variations in the number of molecules, since these variations scale both S^{TOP} and S^{NORM} by the same factor. These frequently-used channels are denoted by dropping the subscript D that identifies the detected quantity

$$\{X\}(t) = \frac{1}{N} \sum_{i=1}^N (W_X)_i \frac{\tilde{\mathcal{N}}}{\mathcal{N}_i} S_i^{\text{TOP}}(t) , \quad (2.28)$$

where the constant \mathcal{N}_i is the integrated signal in the pump PMT detector

$$\mathcal{N}_i = \int_{t'_1}^{t'_2} S_i^{\text{NORM}}(\tau) d\tau . \quad (2.29)$$

The integration bounds t'_1 and t'_2 give the range over which the pump PMT is normalised, as shown in Fig. 2.13 (b). They determine the fastest and slowest molecules whose signals will play a part in the experiment. Finally $\tilde{\mathcal{N}}$ is the mean of all the integrated pump signals in the entire block

$$\tilde{\mathcal{N}} = \frac{1}{N} \sum_{j=1}^N \int_{t'_1}^{t'_2} S_j^{\text{NORM}}(\tau') d\tau'. \quad (2.30)$$

The set of analysis waveforms W_X can include the modulation waveforms for a given block but is not restricted to those. For instance, the waveform that consists of the number ‘+1’ 4096 times, called W_{SIG} , gives the average signal at time t for that detector and block, $\{\text{SIG}\}_D(t)$. Other frequently-used analysis waveforms are the product of two or more modulation waveforms. These are signified by a slightly confusing dot product notation $W_{X.Y}$. In this waveform the i^{th} element is

$$(W_{X.Y})_i = (W_X)_i \times (W_Y)_i. \quad (2.31)$$

The method we use to generate the modulation waveforms ensures that they are orthogonal to each other and to any product of waveforms, so it is possible to extract the linear responses of the system to arbitrary combinations of the switched parameters.

To give the reader a feel for the signal channels, Table 2.5 presents a selection of a few channels and combinations of channels that we encounter frequently in the analysis of eEDM data, together with their interpretation.

Channel	Interpretation
$\{\delta B\}$	Proportional to the amplitude of the interference curve
$\{\text{SIG}\}$	Average signal detected by the probe PMT.
$\{\text{SIG}\}_{\text{NORM}}$	Average signal detected by the pump PMT.
$\frac{\{\delta B\}}{\{\text{SIG}\}}$	Proportional to the contrast of the interference curve.
$\frac{\{B\}}{\{\delta B\}}$	The signal change when the direction of the magnetic field is reversed normalised to the amplitude of the interference curve. A non-zero value indicates that there is an ambient magnetic field in the machine along z.
$\{E \cdot \delta B\}$	A correlation between the direction of the applied electric field and the amplitude of the interference fringe.
$\{E\}_{\text{MAG}}$	Magnetic field detected by the inner magnetometer which is correlated with the reversal of the electric field direction.
$\{E\}_{\text{NL}}$	Leakage current correlated with the direction of the applied electric field. A non-zero value may indicate currents flowing in machine which could mimic an eEDM.
$\frac{\{E \cdot B\}}{\{\delta B\}}$	The leading contribution to the eEDM signal, proportional to the eEDM phase and the size of d_e . For a set of shots all in an identical machine state apart from the switch states of E, B and δB this combination of points is the term in brackets in Eq.(2.26).
$\{\text{RF1F}\}$	The change in molecular signal when the frequency of the first rf pulse is stepped, if it is non-zero then the first rf pulse may be detuned.
$\{E \cdot \text{RF1F}\}$	The part of $\{\text{RF1F}\}$ that correlates with the reversal of the electric field; if non-zero it may indicate that the electric field is changing size upon reversal and causing the rf pulses to become detuned via a change in the Stark shift of the $ 1, \pm 1\rangle$ levels.

Tab. 2.5: A few interesting channels.

When considering simple algebraic combinations of different channels, we will usually write them out in full, as in Table 2.5. However for more complicated combinations of channels we will write the name of the combination of channels in square

brackets. The most often used combination of channels is [EDM], the combination gives the value of the eEDM in the presence of an uncanceled bias field and an electric field which changes size on reversal [60]

$$[\text{EDM}] = \frac{g_F \mu_B B_{\delta B} \tau}{\eta E_{\text{eff}} \tau} \left(\frac{\{E \cdot B\}}{\{\delta B\}} - \frac{\{B\}\{E \cdot \delta B\}}{\{\delta B\}\{\delta B\}} + \frac{\{\text{SIG}\}}{\{\delta B\}} \left(\frac{\{B \cdot \delta B\}\{E \cdot \delta B\}}{\{\delta B\}\{\delta B\}} - \frac{\{E \cdot B \cdot \delta B\}}{\{\delta B\}} \right) \right), \quad (2.32)$$

where $B_{\delta B}$ is the difference in magnetic fields between the two switch states of the small magnetic field step δB , chosen such that $g_F \mu_B B_{\delta B} \tau / \hbar = \pi/32$.

Often we want to integrate the detector signals between a start time t_1 and end time t_2 . We denote these signals using a pair of angle brackets

$$\langle \{X\}_D \rangle = \int_{t_1}^{t_2} \{X\}_D dt. \quad (2.33)$$

Note that here the angle brackets denote the integral, not an average. If the channel being integrated is the Top Normed, then we normally relate the integration bounds on the pump and probe detectors according to $t_1 = \kappa t'_1$ and $t_2 = \kappa t'_2$, where κ is the ratio of the source to pump detector distance to the source to probe detector. This means that we analyse the molecules with the same velocities in both the pump and probe detectors.

2.5.3 Blind

To prevent our analysis from being influenced by any preconceived ideas about the value of the eEDM, a hidden artificial blind is added to the eEDM signal, $\langle [\text{EDM}] \rangle$ by the computer during the data analysis. The value of this blind was chosen randomly by the computer after the last published measurement from a normal distribution with zero mean and $5 \times 10^{-27} e \text{ cm}$ standard deviation.

2.5.4 Statistical analysis of channel values

The channel values from several blocks can be combined to give an average value and associated confidence intervals for that channel. To perform the analysis we would like to choose statistical measures of the centre of the distribution of channel values which are:

1. *Robust*: they are not affected by spurious outlying points
2. *Efficient*: they place as narrow as possible a bound on the centre of the underlying distribution from which the channel values are drawn.

As a compromise between these two conflicting requirements, we use the 5% trimmed mean as the estimator for the centre of our distributions. This is the mean of the channel values with the largest 5% and smallest 5% of the data dropped.

To estimate the error on the value of the mean, we adopt the bootstrap method [62][63]. This has the great advantage of not assuming anything about the underlying distribution from which the channel values are a sample. This is necessary because our underlying distributions are complicated and certainly not Gaussian. An illustration of this can be seen in Fig. 2.16 (a) where the distribution of the $\langle[\text{EDM}]\rangle$ channel values for a collection of 2740 blocks is shown and compared to a Gaussian distribution of the same variance with a Q-Q plot in Fig. 2.16 (b). The deviation of the distribution from the Gaussian is noticeable; there are more points in the centre of the distribution, slightly fewer in the region between $\pm(1-7) \times 10^{-26} e \text{ cm}$ and a great many outliers from about $\pm 10 \times 10^{-26} e \text{ cm}$.

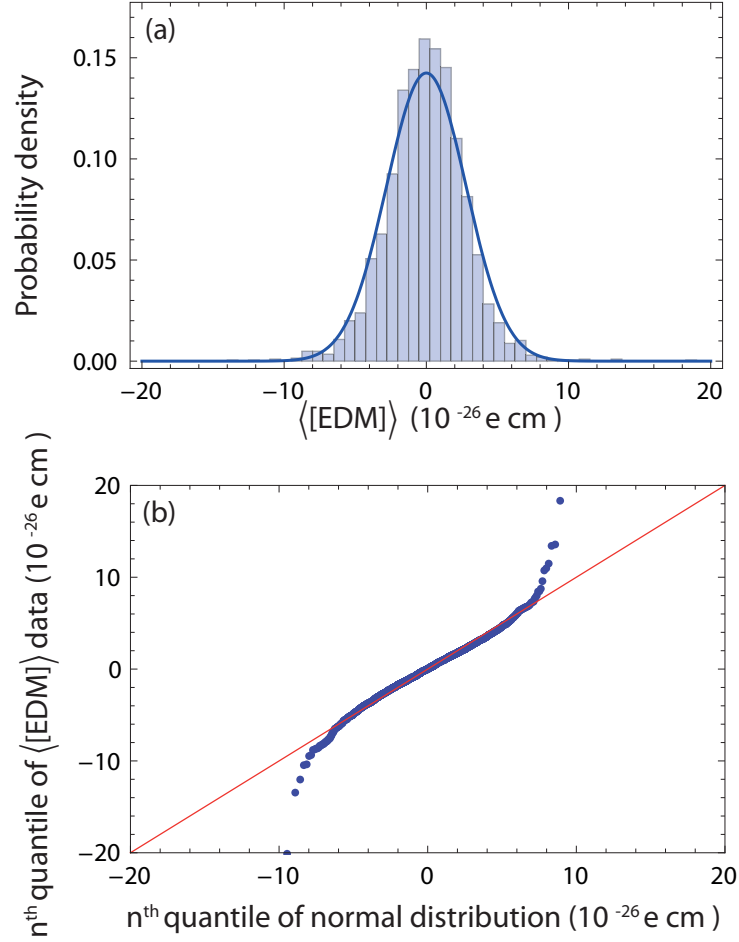


Fig. 2.16: (a) a histogram of $\langle[\text{EDM}]\rangle$ from 2740 blocks taken in July 2013. The mean of the distribution has been subtracted. The blue solid line is the probability density function for a normal distribution with the same standard deviation as $\langle[\text{EDM}]\rangle$. (b) A quantile-quantile plot of the normal distribution shown in (a) (x-axis) versus the $\langle[\text{EDM}]\rangle$ data (y-axis).

To calculate the error by the bootstrap, we first make a large number of *replicates* of the set of channel values. Each replicate is made by drawing a list of points randomly (with replacement) from the original (untrimmed) data set. The list is the same length as the original data set. The replicates form a collection of new data sets, which sample the underlying distribution as well as the the original data set did. We now calculate the 5% trimmed mean for each of the replicates, and histogram the results. The $n\%$ confidence intervals on the mean can be found by calculating the upper and lower bounds of the region of the histogram which contains $n\%$ of the trimmed means. An example of this process is shown in Fig. 2.17.

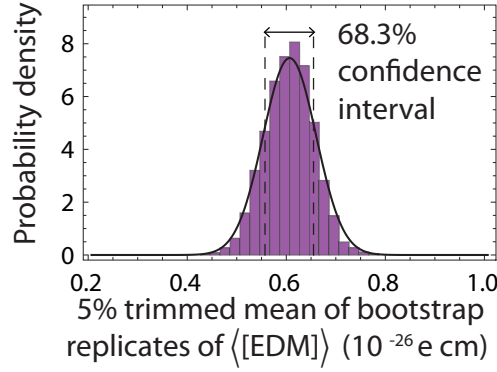


Fig. 2.17: A histogram of the 5% trimmed mean of 5000 replicate data sets made from the $\langle [EDM] \rangle$ block data shown in Fig. 2.16. The mean is the eEDM plus an unknown blind. The lines show the confidence interval that contains 68.3% of the trimmed means. The solid black line is a normal distribution with standard deviation equal to half the 68.3% confidence interval.

The distribution of bootstrap means, 2.17, is closer to a Gaussian, and its standard deviation is well approximated by s/\sqrt{N} where N is the total number of blocks and s is the average sensitivity of the machine in one block. When the machine is running well $s \simeq 2.5 \times 10^{-26} e cm$. In Chapter 4, I will discuss how this sensitivity is dominated by photon shot noise. The datasets which are discussed in this thesis are listed in Table 2.6.

This concludes the explanation of how we use the experiment to make a measurement of the eEDM. However, strictly speaking all we have shown so far is how to

Date	Cluster number(s)	Number of blocks	Notes
4/3/13–1/4/13	125, 127	3129	March 2013 dataset containing rf rotation systematic.
19/7/13–7/8/13	137, 140, 142	2740	July 2013 dataset where high voltage supplies systematic was discovered.
3/6/13–6/6/13	133	523	Shorter spin precession time (first rf pulse at 1260 μ s), old high voltage cabling.
9/7/13–12/7/13 & 11/10/13–13/10/13	136, 154	768	Shorter spin precession time (first rf pulse at 1260 μ s) with ferrites and improved high voltage cabling.
16/8/13–23/10/13	146, 156, 158	877	<i>Applied Kilovolt</i> supplies at ± 2.44 kV, no overshoot
1/11/13–5/11/13	162	611	<i>Bertan</i> supplies at ± 12 kV, no overshoot.
5/11/13–12/11/13	164	657	<i>Bertan</i> supplies at ± 7.5 kV, no overshoot.
13/11/13–19/11/13	165	991	<i>Applied Kilovolt</i> supplies at ± 7.5 kV, no overshoot.
21/11/13–27/11/13	166	1575	<i>Bertan</i> supplies at ± 7.5 kV with overshoot.
16/11/14	173	80	<i>Bertan</i> supplies at ± 7.5 kV with three times overshoot factor.

Tab. 2.6: Summary of datasets discussed in this thesis. Cluster numbers refers to the numbering of our datasets in the “Database control” *Mathematica* notebook. The first two dataset were measurements of the eEDM, but were subsequently discovered to contain systematic errors discussed in Chapter 3. The middle two datasets were taken to characterise the rf rotation systematic error, and the last six datasets were taken to investigate the high voltages supplies systematic error.

measure an interferometer phase correlated with the relative direction of the applied electric and magnetic fields. To be sure that this phase shift is being caused by an eEDM, and not something more mundane like a magnetic field correlated with the direction of the electric field, we need to investigate the systematic errors associated with our measurement. This will be the subject of the next chapter.

3. NEW SYSTEMATIC ERRORS

3.1 Introduction

Many effects can mimic the eEDM signal. Most of our time on the experiment is spent tracking down and characterising these potential sources of systematic error. In this chapter we describe the systematic errors associated with the measurement. We are able to measure many of the systematic errors by deliberately exacerbating an imperfection in the machine, and then looking to see the effect that this has on the value of the eEDM. Our ability to characterise the error is then limited by how much we can exacerbate the imperfection, and the statistical sensitivity of the experiment which, as we will discuss in Chapter 4, is limited by photon shot noise.

We begin by briefly describing the systematics which are presented in greater depth in Refs. [60] and [49]. We then discuss three new systematic errors that I have found. The first of these is associated with an rf-induced current in the machine that could potentially lead to magnetic fields correlated with the direction of the electric field. We call this the *RF discharge systematic error*. The second of these followed the surprising discovery that the rf polarisation direction in the machine can depend on the state of the high voltage switches, an effect we call the *RF rotation systematic error*. The final systematic effect in this chapter has an origin as yet unknown, but it seems to depend on which type of high voltage supplies we use. The effect is unimaginatively called the *High voltage supplies systematic error*.

Systematic Error	Upper limit ($10^{-28} e \text{ cm}$)	Reference
Un-corrected E-asymmetry*	0.5	[49]
Voltage offset	0.063	[49]
Residual rf1 detuning*	0.6	[49]
Leakage currents	0.2	[60]
dc shield magnetization [†]	0.25	[60]
Geometric phase	0.01	[60]
Motional magnetic field	0.0005	[60]
Stray magnetic field along y*	0.3	[60]
Stray magnetic field along x	0.2	[49]
Off-resonant $F = 1$ probing*	0.8	[49]
Probe beam ellipticity*	0.5	[49]
Pump beam ellipticity*	0.3	[49]
Pump detuning*	0.6	[49]
Sum of all terms in quadrature	1.48	
Sum of first seven terms in quadrature	0.85	

Tab. 3.1: Upper limits of various systematic errors described in detail in other work. The tests from Ref. [49] were all performed with 2 μs pulses at 12.5 KVcm^{-1} electric field. *Indicates an upper limit dictated by statistical sensitivity of the machine. [†]Indicates an upper limit dictated by the integration time on an auxiliary measurement.

3.2 Previous systematic errors

Table 3.1 summarises the systematic errors in the last published measurement [60], and from the tests described in the thesis of Joe Smallman [49]. Here we briefly discuss the nature and size of these errors.

We start with the first seven entries in this table. These represent imperfections in the experiment which are known to shift the value of the eEDM channel thus we include them in our final systematic error.

The first term, the un-corrected E-asymmetry, is the systematic shift that may arise if the electric field differs in magnitude by δE between the two electric field switch states. An asymmetry δE will lead to a change in the Stark shift between the $F = 0$ and ($F = 1, m_F = \pm 1$) levels when the electric field is reversed, and hence lead to an E-state dependent detuning of the rf pulses. This can be measured during normal data taking using the $\langle \{RF1F \cdot E\} \rangle$ and $\langle \{RF2F \cdot E\} \rangle$ channels. By reversing the manual connections between the high voltage generation equipment and the machine, we render ourselves sensitive only to the part of the asymmetry that is associated with the high voltages lines and plates. The typical size of this asymmetry over the whole interaction region is 0.1 Vcm^{-1} . To estimate the size of the systematic error associated with this asymmetry, we deliberately reverse the fields asymmetrically, increasing (or decreasing) the voltages on the plates by 10 V. Within the experimental errors, this asymmetric reversal had no effect on the value of the eEDM, with a slope of $(2.1 \pm 2.0) \times 10^{-28} e \text{ cm(Vcm}^{-1})^{-1}$ [49, p.137]. However, this effect has led to shifts in the eEDM value in the past, and there are known phenomena that can allow an asymmetry to cause a false eEDM, so we still associate a systematic error with this imperfection. Combining the worst case gradient with the estimated size of the electric field asymmetry gives the upper limit shown in Table 3.1.

Ideally, the voltages applied to the plates should both be equal and opposite, so

that the sum of the voltages is zero. However, it is possible that there is an additional voltage \bar{V} which is inadvertently applied to both plates, so that the average plate voltage with respect to earth is not zero. This leads to the second error in the table, the voltage offset error. To measure the size of the systematic effect arising from this worst case voltage offset, we deliberately bias both plates to between $\bar{V} = +500$ V and $\bar{V} = -500$ V. This test does lead to a measurable linear shift in the eEDM value, with a gradient of $(6.3 \pm 2.0) \times 10^{-30} e \text{ cmV}^{-1}$ [49]. Multiplying this by the upper limit of $|\bar{V}| < 1$ V, measured with a high voltage probe, provides the systematic error.

In the 2011 measurement, it was found that when $|\bar{V}| \gg 1$ V, the eEDM value depended on the detuning of the first rf pulse from resonance. When $|\bar{V}| < 1$ V, there was no measurable correlation between the eEDM and the detuning of the first rf pulse, the slope of the correlation being $(2.3 \pm 2.8) \times 10^{-28} e \text{ cm/kHz}$ of rf1 detuning. However, to be conservative we multiply this null gradient with the average rf1 detuning of 0.1 kHz to give the final worst case systematic error shown in the third row of the table.

The next two systematic errors, the leakage currents and shield magnetisations, are discussed in the context of the rf discharge and high voltage supplies systematic errors in the following sections, so we postpone the discussion of these errors until then.

The electric field between the plates, away from the edges, is supposed to always lie along z . However, in reality the plates are slightly bowed, which causes the electric field to rotate in the x - y plane. By mapping the electric field magnitude we limit the rotation to be no larger than ± 0.5 mrad. The motion of the molecules in a polarising electric field like this leads to additional phases, the magnitude of which is equal to the solid angle swept out by the molecules as they adiabatically follow those fields [64]. By itself, the bowing of the plates is not sufficient to cause a systematic error. However if combined with a patch potential which only covers one quarter of

a single plate, this can lead to a systematic error. Assuming a 1 V patch potential and making a calculation of the solid angle swept out by the molecules gives the systematic error listed in the table.

The motional magnetic field is a tiny effect in a molecular eEDM experiment; it is included here so that it can be compared to the atomic beam experiments, where it poses the most challenging systematic difficulty.

The next six entries in Table 3.1 are upper limits which we do not include in the total systematic error to the experiment. In the case of the stray magnetic field along y , the pump and probe beam ellipticity and the pump detuning, these effects have never been shown to shift the value of the EDM, and it is not clear how they could do so. We do not discuss these errors any further here. The stray magnetic field along x has been shown to shift the value of the eEDM channel, but in a way which is expected to be quadratic in the applied magnetic field. The error here is very conservative because it instead assumes a linear scaling. Probing on $F = 1$ was shown in the thesis of D. Kara [57, p. 96] to lead to a systematic shift of the eEDM. However, this may well have been attributable to the large voltage offset that was present when the data was acquired. Probing on $F = 1$ without a voltage offset [49, p. 141] and with the new rf structure now no longer leads to a systematic error, and the error quoted here is a conservative upper limit, based on a small off resonant probing of $F = 1$ by the probe laser, which is tuned to $F = 0$.

Adding the first seven systematic errors together in quadrature, we find that the total systematic error arising from previously known systematic effects is $0.85 \times 10^{-28} e \text{ cm}$. Now we move on to discuss the new systematic errors that I have discovered.

3.3 RF discharge systematic error

After our group's last published measurement of the eEDM [36], the apparatus was upgraded with a new rf amplifier to allow the rf π -pulses to be driven with shorter, higher powered rf. The goal was to broaden the rf linewidth, which is proportional to the inverse of the π -pulse duration. The broader linewidth desensitises the experiment to systematic errors arising from shifts in the rf line centre, such as the E-asymmetry and RF1 detuning systematic errors.

When we started to take data with the new amplifier, we reduced the rf pulse length from 18 μ s to 2 μ s. We then noticed some strange behaviour in the high voltage ammeters, which now seemed to be able to pick up some of the rf signal. To investigate this further, we attached a home built nano-ammeter to the bias tees that connect the rf sources (Fig. 2.8(b)) to the the rf feeds on the eEDM vacuum chamber, Fig. 2.6. This ammeter, marked A in Fig. 3.1 (a), reads the dc current that flows from the RF plates to earth. The bandwidth of the ammeter is 210 Hz and the calibration is 10 V μ A⁻¹.

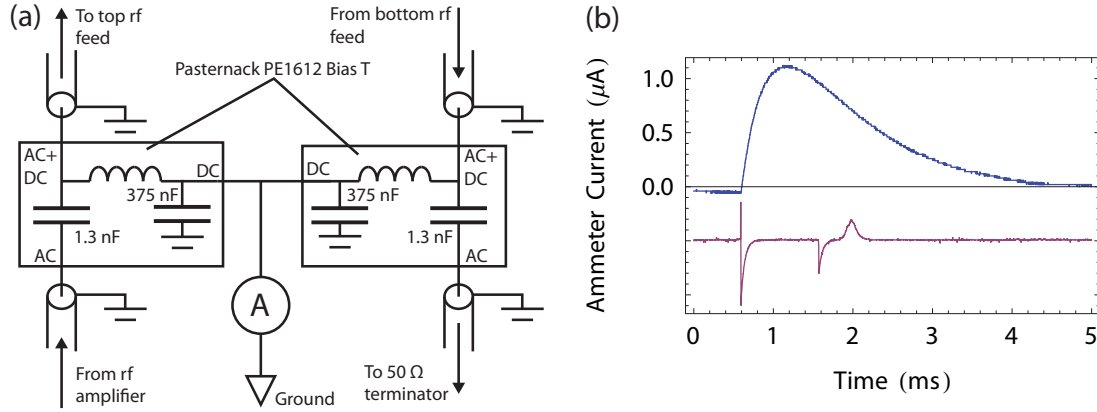


Fig. 3.1: (a) A circuit diagram showing the location of the rf ammeter on the rf cables, see Fig. 2.8 for the location position in the rf system. (b) The signature of an rf discharge is shown in blue, with a probe PMT trace underneath in red.

When the machine is operating abnormally, with rf pulses shorter than around

9 μs , we see bursts of current flowing through the ammeter. These appear intermittently: one such burst is shown in Fig. 3.1 (b). The trace in blue is the signal from the nano ammeter, and the trace in red is the recording of the signal from the probe PMT detector, scaled so that its features are visible on the same graph. The two sharp dips in the probe signal are electrical pickup from the two rf pulses, the third peak is due to molecules flying through the probe laser beam and fluorescing. The current spike in the blue trace starts simultaneously with the first rf pulse, rises to a maximum 0.5 ms later and then slowly decays. We interpret this graph as follows: a process that occurs during the first rf pulse deposits charge on the rf plates, which then charges the pair of 375 nF capacitors, before these are slowly discharged through the ammeter to ground.

These current spikes are not observed when: 1) the solenoid that opens the source valve is unplugged, 2) the YAG laser is not fired, 3) the YbF molecular signal is poor or 4) the RF power is low. They occur less often when the rf plates are biased to a few tens of volts either positive or negative, or the the rf power is too high. If the electric field plates are grounded, the spikes occur less frequently but they are larger when they do take place.

This behaviour suggests that we have *multipactor* discharges taking place [65]. These are frequently seen in particle accelerators and high power rf equipment. The process is as follows: a charged particle strikes a metal or dielectric surface within an rf field, causing secondary electrons to be emitted. These electrons are accelerated by the field into a second surface, where more secondary electrons are emitted. Since the rf field is continually changing direction, this can repeat many times, causing a sizeable current to flow in the process, as illustrated in Fig. 3.2 (a). When the avalanche finishes, the negative charge is deposited on one of the plates. We can estimate the size of gap that will support a multipactor discharge by assuming that the secondary electrons are created at rest, and that the oscillating electric field is the one we have (5 kV m^{-1}) when the rf drives a π -pulse in 2 μs . This gives $d = 3$

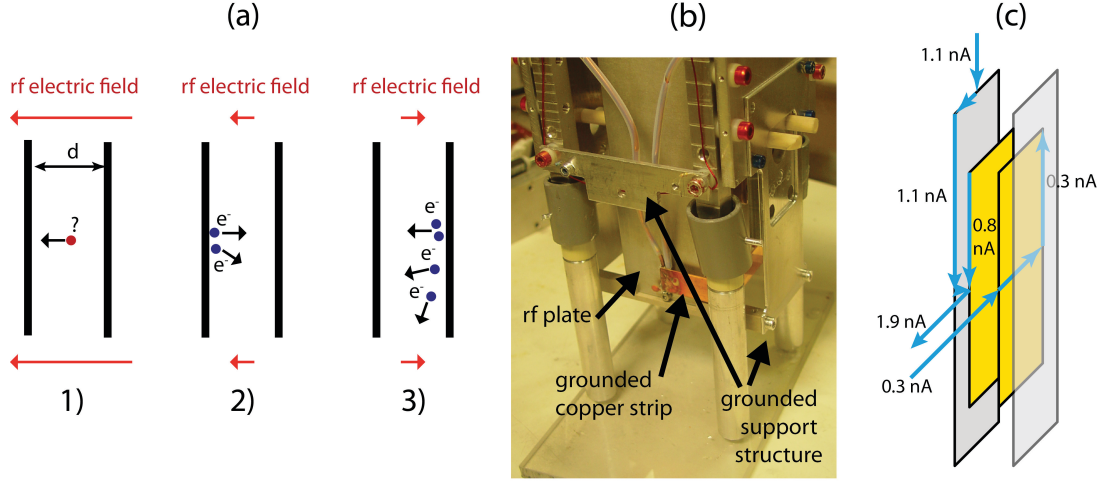


Fig. 3.2: (a) A sequential picture showing the growth of a multipactor discharge. (b) The bottom of the rf and electric field plates, showing the available locations for discharges to occur. (c) Worst case dc leakage paths used to estimate the leakage systematic error

mm as the gap, which is exactly the type of gap that exists between the rf plate structure and other ground planes in the apparatus.

The initial impact to start the discharge must come from charged particles created either in the source or by rf ionisation of neutral particles within the beam. If the rf powers are turned up much higher than is necessary in the experiment, it is also possible to initiate a multipactor discharge without any molecular beam.

It is likely that the discharge is happening close to the start of the machine since if the rf pulse is delayed so that most of the molecular packet is well within the electric field plates when the pulse is fired, the rate of rf discharges decreases. One possible location where the discharges could be taking place is shown in Fig. 3.2 (b). This shows the bottom part of the rf plates (long aluminium plate in the centre of

the picture). Two semi-rigid coaxial cables connect to the bottom of the plate. The grounded outer shell of the cables is soldered to a copper strip that is also indicated in the photo. The gap between this strip and the rf plates is the right size to support the discharge. Having said this, it is perfectly possible that the discharge can be taking place at some other location in the plate structure.

These multipactor discharges could result in a current flowing in the machine whose magnitude depends on the direction of the applied electric field. The direction of the electric field could influence the size of the current because fringe electric fields in one switch state might reduce the discharge process while the other might enhance it. Alternatively, we could imagine that one electric field switch state was better at deflecting ions towards the rf plates, thus leading to larger discharges. A current whose magnitude depends on the direction of the applied electric field can produce a magnetic field, and hence a spin precession, correlated with the sign of the electric field. That would be interpreted as an eEDM. In the next section we will discuss how we solved the multipactor discharge problem and how we assign a systematic uncertainty associated with any residual discharge.

3.3.1 *Suppressing the discharges and assigning a systematic error*

We tried a number of measures to reduce the multipactor discharges including:

1. Installing a pair of additional electric field plates in the source chamber to act as an ion deflector.
2. Electrically isolating and charging up the skimmer to prevent any ions from the source chamber from reaching the field plates.
3. Biasing the field plates by applying 30 V to the dc inputs of the bias tees.
4. Further shortening the rf pulses, so that their power was higher and thus the discharge gap length was longer, thus taking the process out of resonance with whatever part of the apparatus was sustaining the discharge.

While these measures reduced the discharges, in the end most blocks would still contain several shots with visible discharges in them. Increasing the rf pulse length to 9 μs finally stopped the discharges altogether, and this is the solution we adopted because it was the least disruptive at the time. However, we could have gone further in our investigations by opening up the main interaction region and placing insulators between the surfaces we suspected were discharging to determine where exactly the discharge was taking place. We could then have solved the problem by coating the rf structure or choosing different materials to reduce the probability of secondary electron emission, or by placing insulating barriers between any locations where discharges could take place. We will return to this topic in Chapter 5.

To guard against rf discharges in the future, the rf ammeter is now left in place during normal eEDM data taking, and its signal is recorded alongside the others. Each block is inspected for any obvious rf discharges and discarded if they are present. This has so far not been necessary with 9 μs pulses. For the remaining blocks, the average rf leakage current for each shot is recorded, and the part correlated with E is calculated for each block.

To see how large this residual discharge is, we can look at the set of 3129 blocks taken in March 2013. In this data run the currents correlated with the electric field directions were 1.9 nA, -0.3 nA and -1.1 nA for north plate, south plate and rf plate leakage monitors respectively. A positive current indicates current flowing out of the machine. All the leakage currents are of the same size as those during the last published measurement [57], and interestingly the average rf leakage current correlated with E flows into the machine, whereas the leakage spikes, when they take place, flow out. This suggests that the currents we see are primarily caused by dc leakage inside the machine, not multipactor discharges.

To turn these currents into magnetic fields seen by the molecules, we need a model for how they might flow inside the machine. Following the approach in Ref. [57], we imagine a worst case, in which the 0.3 nA current flows up one edge of the south plate

from the south feedthrough up to the top of the plate, the 0.8 nA flows down the opposite edge of the north plate and into the north feedthrough and 1.1 nA flows down the edge of the rf plate and discharges into the north feedthrough. These currents are shown in Fig. 3.2 (c). Summing their contributions to the field at centreline of the YbF beam, we find an average field of 5fT over the molecular interaction region correlated with the direction of the electric field. This would cause a fake eEDM no larger than 2×10^{-29} e cm.

3.4 RF rotation systematic

3.4.1 Diagnosing the problem

When we analysed the first data run taken in March 2013, shown in Fig. 3.3 (a), we discovered a significant $(1.1 \pm 0.1) \times 10^{-26}$ e cm difference in $\langle[\text{EDM}]\rangle$ between rf manual state true, (rf propagates from the bottom of the machine to the top), and rf manual state false (rf travels from top to bottom). We therefore decided to investigate the properties of the rf system in more detail.

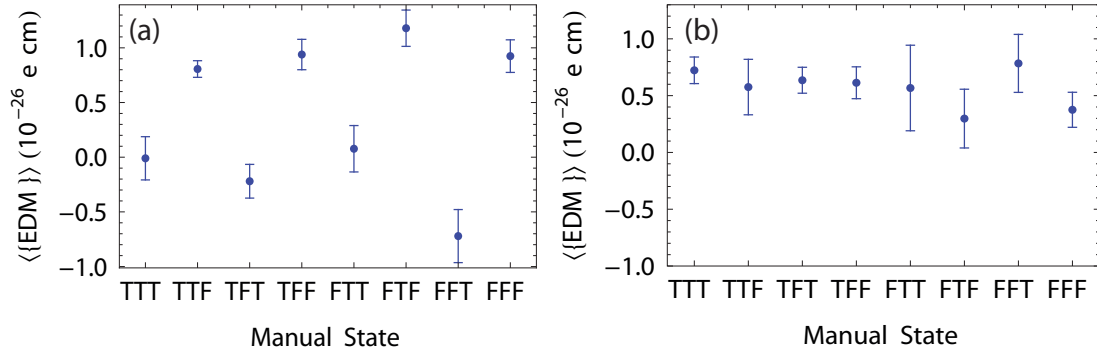


Fig. 3.3: Values of $\langle[\text{EDM}]\rangle$ in the eight different manual states for (a) the March 2013 data set before the high voltage lines were fixed and (b) the July 2013 data set after high voltage lines were fixed.

We started by monitoring the rf-power reflected back out of the machine by installing a directional coupler on the rf line, as shown in the top right hand side of

Fig. 2.8. A crystal detector on the coupler output detected significant differences in the back-reflected rf power between electric field switch states, with more rf being reflected when the machine was in rf manual state true. The values of these differences for the various manual states are shown in Table 3.2.

{E,B,rf} manual state	Reflected rf amplitude correlated with E-switch state (μV_{RMS})	
	Before improvements	After improvements
{F, F, F}	1031 ± 10	10 ± 9
{F, F, T}	1787 ± 7	6 ± 5
{T, F, F}	57 ± 13	7 ± 9
{T, F, T}	388 ± 4	2 ± 4

Tab. 3.2: Measurements of the E-switch dependent amplitude of the reflected rf field taken with a short interferometer before and after rf chokes were installed on the HV feeds.

We hypothesised that some of the rf in the transmission line was being coupled onto the RG213/U 50 Ω coaxial high voltage cables and travelling down to the high voltage (HV) equipment. The rf was then being reflected and re-emitted back into the machine. The HV feeds would now act as an rf antenna, and the re-emitted rf would combine with the travelling wave in the transmission line to slightly rotate the rf polarisation. A diagram showing the approximate polarisation of this unwanted rf can be seen in Fig. 3.4.

The exact degree of rotation would vary depending on the position within the transmission line, but it was likely to be largest closest to the HV feedthrough. If this is the case, then when the first rf transition is driven, the state prepared is no longer given by expression (2.19), but is rather

$$\frac{i}{\sqrt{2}} (e^{-i\theta_1} |1, 1\rangle - e^{i\theta_1} |1, -1\rangle) , \quad (3.1)$$

where θ_1 is the azimuthal angle of the rf magnetic field, being defined by the static

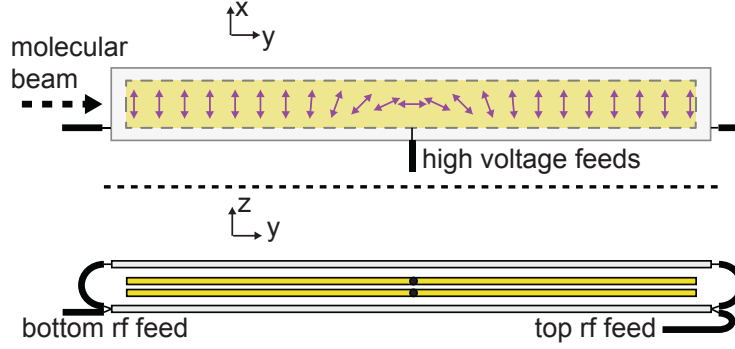


Fig. 3.4: Approximate polarisation of the rf magnetic field (indicated by purple arrows) generated when rf couples into the side of the machine through the high voltage feedthroughs.

E field. This is the relevant angle because we are exciting the state by $\Delta m_F = \pm 1$ transitions from $|0, 0\rangle$. Expression (3.1) is formally identical to the right hand side of Eq. (2.22), so if θ_1 depends on the direction of the electric field, the resulting phase shift may be misinterpreted as an eEDM. The second rf pulse can also be rotated by the unwanted radiation by an angle θ_2 , so the experiment is actually sensitive to the difference $\theta_{21} = \theta_1 - \theta_2$ between them. A fixed θ_{21} is indistinguishable during normal operation from a small static background magnetic field and is cancelled by our bias magnetic field B_0 (see p. 61 for more details). But if θ_{21} changes when E is reversed, this produces a false eEDM. For example a $10 \mu\text{rad}$ change is equivalent to an eEDM of $4.2 \times 10^{-28} e \text{ cm}$. We therefore need to be certain that the unwanted rf polarisation that changes with the electric field state is at least less than one part in a 10^6 at the start and end of the rf transmission line where we drive our pulses.

One way in which the amount of emitted rf could change when the electric field direction was reversed would be if the impedance of the electric field supplies was different in the two switch states. To test for this, we monitored the rf power immediately before the high voltage relays, at the location marked * in Fig. 2.8. In both rf manual states we found that rf did indeed couple onto the HV feeds, and in one particular rf manual state (true) the amount of rf in the lines depended significantly

upon the state of the electric field relays. Changing the rf manual state changes rf field distribution within the machine, so it is not surprising that there should be some rf manual state dependence in the amount of rf coupled onto the high voltage lines.

Having established that the amount of rf field coupled onto the HV cables depended upon the E-field relay switch state, it remained to show that this variation in power caused a rotation of the rf field in the machine. We achieved this by disconnecting one electric field plate from the HV supplies and deliberately coupling rf onto the HV vacuum feedthrough. Remarkably we were able to drive rf transitions along the whole length of the beamline using this side injected rf, indicating that it worked quite well as an antenna. To map out how the amplitude of the rf field produced by the side injected rf varied inside the eEDM machine, we scanned out the power required to drive a π -pulse from $F = 0$ to $F = 1$ as the timing of the first rf pulse was changed. Changing this timing changed the location of the molecules in the machine when they experience the radiation, and so allows the local field to be mapped. The results are shown in the top half of Fig. 3.5, where the rf amplitude needed to drive a π -pulse is plotted as a function of position through the machine. The power required to drive a π -pulse using this side injected rf varied quite considerably over the length of the machine, indicating that the rf field arising from the antenna coupling to the existing rf plate structure is predominantly concentrated in the top half of the machine.

We were also able to map the polarization direction of the rf field produced via side injection through the HV feed. We did this by recording interference curves of the type shown in Fig. 2.15, driving the first rf pulse with side injected rf, and the second pulse with rf fed in along the usual parallel plate transmission line. The phase of these curves was compared to normal interference curves where both rf pulses were sent down the normal transmission line. The phase shift between the curves gives the angle between the rf emitted from the HV feedthroughs and the

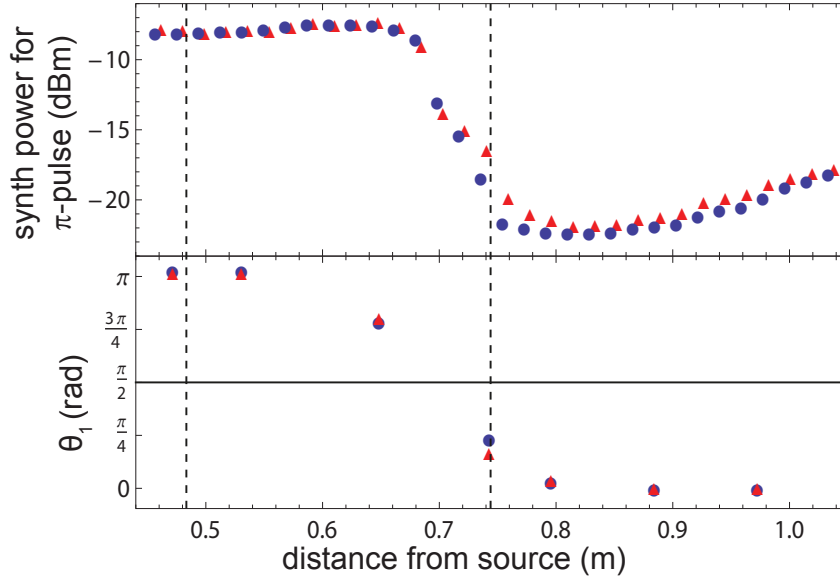


Fig. 3.5: Top: the amplitude needed to drive a π -pulse $F = 0$ to $F = 1$ at various points along the machine using side-injected rf. Bottom: the angle of the rf field due to side injected rf as a function of position along the machine, inferred from the phase shift of the interferometer curves. The dashed lines show the location of the centre of the molecular packet when the first rf pulse is fired in the long and short machine data. The experiment was performed for both rf manual state false (red triangles), and rf manual state true (blue circles).

regular rf radiation. By changing the timing of the first rf pulse, and so changing the point in the machine where the molecules interact with the rf radiation, it is possible to map out the local polarisation of the rf radiation in much the same way as the amplitude of the rf was mapped out. This is shown in the bottom section of Fig. 3.5. Towards either end of the electric field plates, the rf field polarization is largely along x , but it becomes more and more aligned to y as the rf transitions are driven closer to the feedthrough, 0.74 m downstream from the source. If the feedthrough to the electric field plate (shown in Fig. 2.6) were behaving like a dipole antenna, then we might expect the rf polarisation at the closest point to the feedthrough to be along y ($\theta_1 = \pi/2$). However, the rf becomes y polarised slightly earlier, 0.7 m downstream from the source. This may be because part of the rf is being carried on a grounded

braid which connects the outer core of the rf cable to the machine at this point, and so the feedthrough is not behaving as a simple antenna. Nevertheless, the point to stress is that we have confirmed experimentally that any rf coupling between the rf plates and the high voltage lines can rotate the polarisation inside the machine.

3.4.2 Amplifying the systematic

The results of section 3.4.1 suggest that potential systematic error due to relay-state-dependent rf field rotations could be amplified by changing the timing of the first rf pulse so that the molecules would be close to the HV feedthrough when the rf transition was driven. At this point, the polarisation of the unwanted rf is predominately orthogonal to the desired polarisation in the transmission line, and hence any small changes in its amplitude will cause large rotations of the local rf polarisation. This enhances the influence of unwanted rf compared to the normal operation of the machine, when the first rf pulse is at 820 μs , and the polarisation is predominately along x , and hence largely parallel to the x polarised rf in the transmission line. The effect of any E correlation in unwanted rf will be predominately to increase the amplitude of the rf slightly in one E switch state, rather than to change its polarisation. Timing the first pulse to occur at 1260 μs so that the centre of the molecular packet is 0.74 m from the source, as shown by the dashed line in Fig. 3.5 is called *short machine* data.

Cycling through the four electric and rf manual states, we obtained four independent measurements of the total E-switch dependent phase, which we denote β^{short} . Explicitly, this is the sum of the EDM phase, ϕ_E^{short} and the polarization rotation phase, $\theta_{21}^{\text{short}} = \theta_1 - \theta_2$, measured using a short length interferometer. We also obtained *long machine* measurements of $\beta^{\text{long}} = \phi_E^{\text{long}} + \theta_{21}^{\text{long}}$, with the first rf pulse occurring at 820 μs , when the molecular packet is centred around 0.48 m, the usual position for our first rf pulse during normal data taking.

The aim of this exercise is to extract a value of θ_1^{short} . Assuming that θ_1^{short} is

{E,B,rf} manual state	θ_1^{short} without chokes (mrad)	θ_1^{short} with chokes (mrad)
{false, false, false}	-1.00 ± 0.03	0.08 ± 0.04
{false, false, true}	-5.94 ± 0.07	0.05 ± 0.04
{true, false, false}	-0.35 ± 0.05	-0.01 ± 0.04
{true, false, true}	0.47 ± 0.04	-0.16 ± 0.03

Tab. 3.3: Measurements of the E-switch dependent component of the polarization rotation angle, θ_1 , taken with a short interferometer before and after rf chokes were installed on the HV feeds.

much larger than any other fixed phases that switch with E, and that there are no other large and uncontrolled systematic errors which vary between the taking of long and short machine data, this can be written as $\theta_1^{\text{short}} = \beta^{\text{short}} - R \beta^{\text{long}}$. Here R is the ratio of the evolution time in the short machine compared to the long machine. Our measured values of θ_1^{short} for each of the four manual states are given in the central column in Table 3.3. Note that the values are all significantly non-zero, and that in state {false, false, true}, the rotation is on the order of 1000 times larger than we can tolerate.

To reduce the rf systematic effect we inserted rf-chokes into the high voltage cables. Six Ferroxcube - TN14/9/5-4C65 rf ferrites were spaced along the high voltage cables. The total suppression on each line was measured to be > 35 dB. The ferrite chokes ensured that as little rf as possible could travel down the HV cables and become modulated by the relays. Fig. 3.6 shows a picture of two of pairs of rf ferrites enclosed in a metal box. The connections between the rf ferrite boxes and the cables were made with 10 kV SHV connectors (Kings 1065-1), and all the RG213/U coaxial cable was replaced by RG58 75 Ω cable, which was compatible with these connectors. We also improved the grounding of the electric field supplies so that electric field manual reversals could not change the impedance proprieties of the supplies. As a result we now no longer measure an E-state dependent variation in the reflected

rf power, in any of the manual states. This is shown in Table 3.2.

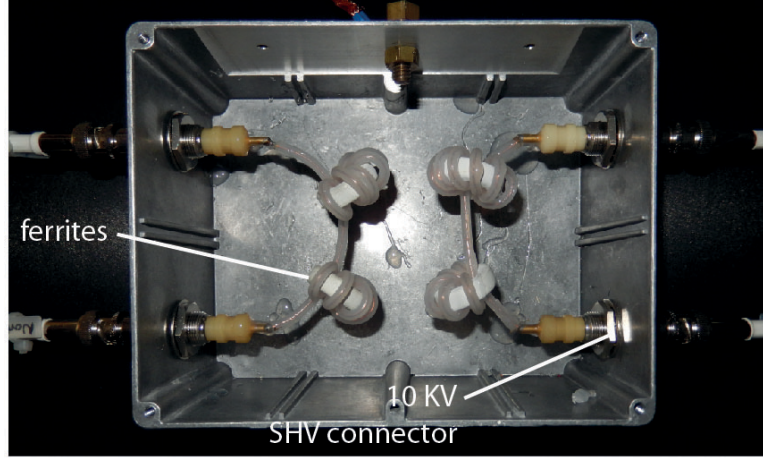


Fig. 3.6: A photograph showing a box containing two pairs of rf ferrites installed onto to each of the HV lines. In total there are 3 such boxes.

To quantify the reduction in the unwanted rf polarization rotation phase, we took more data with the shortened interferometer. As shown in Table 3.3, after placing chokes on the HV cables we find that the four values of θ_1^{short} are much reduced. The two manual states $\{\text{false}, \text{false}, \text{true}\}$ and $\{\text{true}, \text{false}, \text{false}\}$ are now consistent with zero, and $\{\text{false}, \text{false}, \text{false}\}$ is nonzero only at the two σ level. It is concerning that $\{\text{true}, \text{false}, \text{true}\}$ does have a much more significant non-zero value of θ_1^{short} even after the chokes have been installed. We have yet to understand whether this phase is related to the rf field rotation or another systematic error whose effect is magnified when transitions are driven close to the HV feedthrough. One indication that the origin of the phase may not be an rf rotation is that the reflected rf amplitude has been reduced by a factor of almost 200. It would be reasonable to assume that the amplitude of the unwanted rf polarisation inside the machine has also been reduced by a similar level, which would imply that θ_1^{short} should be reduced to a value smaller than the experimental errorbar. Instead, we only see a threefold reduction in its size.

With the chokes installed, we now also find that the value of the $\langle[\text{EDM}]\rangle$ (with

the first rf pulse back to its normal timing) is now consistent for all manual states, as shown in Fig. 3.3 (b).

The measurements discussed in this section suggest that we have greatly reduced the E-state dependent rf rotation. However, it is difficult to extract an upper limit by appropriately scaling the short machine data because of the anomalous {true, false, true} point. Instead, we plan to adopt a different approach to assign a final systematic error, as discussed in the following section.

3.4.3 Final systematic error

The signs are promising that we have fixed the rf rotation problem, but to assign a final systematic error we need to perform further tests on the experiment. The first step will be a comprehensive map of the rf polarisation inside the machine now that chokes have been installed. This can be achieved by driving rf transitions in the presence of magnetic fields along x , y and z . The fields will be of a sufficient magnitude that the m_F sub-levels of $F = 1$ can be resolved and individually addressed with different frequencies of rf radiation. By measuring the amplitude needed to drive transitions from $F = 0$ to each of these components in each of the applied magnetic fields, we can determine how much of each polarisation of rf is present. In the regions where the rf pulses are driven, we know that the rf is predominantly linearly polarised along x . Given that the rf and electric field plates are symmetric in the z - y plane, we can make the simplifying assumption that any component of the rf radiation along y is caused by reflections from the high voltage feedthroughs. As the bottom graph of Fig. 3.5 shows, this is a very pessimistic model because most of the rf that comes from the feedthroughs is actually predominantly polarised along x , not y , close to the edge of the plates. These polarisation maps will be undertaken when the improvements discussed in the second half of this thesis are completed, since these may change the distribution of rf radiation inside the machine.

Before these measurements are undertaken, we can get a very pessimistic upper

limit for the ratio of y polarised rf to x polarised rf, $r_{y/x}$, by looking at the bias magnetic field B_0 needed to centre the interferometer phase. Normally, we think that this field needs to be applied to cancel external magnetic fields, but if instead we think that it corrects for a fixed angle between the two rf pulses, we can place an upper limit on $r_{y/x}$. Using the data from the July 2013 data set taken after the chokes were installed we find that $r_{y/x} < 0.15$.

If the y polarised rf changes in size when E reverses, then this will lead to a rotation in the rf direction. Since the amplitude of the y polarised rf is directly proportional to the amplitude of rf on the high voltage lines in this pessimistic model, we can measure the size of this effect by injecting rf into the high voltage supplies, and monitoring how the fraction of back reflected rf changes when E is reversed. Preliminary tests indicate that we can measure fractional changes in the rf field $\Delta B_{\text{rf, line}}$ on the lines in this way to a few parts in a million when the relays are switched. Thus, either with the current set-up or with additional chokes if necessary, we could hope to limit the fractional change in the y polarised rf to one part in a million.

Provided the x polarised rf component is much larger than the y polarised rf component (as we expect it to be), small changes in the y component of the rf will cause a rotation in the direction of the rf polarisation in each rf region given by $|\theta_{1(2)}| = r_{y/x} \Delta B_{\text{rf, line}}$. In the worst case, given the location of the high voltage feedthroughs and the radiation pattern shown in Fig. 3.5, we could expect the two E -state dependent rotation angles to be opposite in sign, so that the total difference in rf polarisation angle between electric field switch states would be

$$\theta_{21} = 2r_{y/x} \Delta B_{\text{rf, line}} . \quad (3.2)$$

At an applied electric field of 12.5 KVcm^{-1} this gives a false eEDM of

$$d_{e,\text{rf}} = 8.4 \times 10^{-23} r_{y/x} \Delta B_{\text{rf, line}} . \quad (3.3)$$

If we can suppress the back reflected rf to one part in a million ($\Delta B_{\text{rf, line}} < 10^{-6}$), and we can limit the ratio $r_{y/x} < 0.1$, then the upper limit for the systematic error will be less than $8.4 \times 10^{-30} e \text{ cm}$.

3.5 High voltage supplies systematic

3.5.1 Discovery

After we installed the improved high voltage cables in the summer of 2013, we took the data shown in Fig. 3.3 (b) to check that the eEDM values reported for the various manual states were now all consistent. A mistake half way through this data run led to the high voltage cables between the vacuum chamber and the first set of ferrites being reversed (see Fig. 2.8 for the location of this switch), effectively performing an unintentional manual reversal. The value of the eEDM we were measuring also changed sign at this point. This implied that we were measuring a very large value for the eEDM, consistently across all the manual states, equivalent to $\langle [\text{EDM}] \rangle = (5.0 \pm 0.6) \times 10^{-27} e \text{ cm}$ with the blind removed. This equates to a phase shift correlated with the direction of the electric field relative to the magnetic fields of $(120 \pm 10) \mu\text{rad}$. To confirm whether or not we really had measured a non-zero eEDM, we reduced the voltage on each plate from $\pm 7.5 \text{ kV}$ to $\pm 2.44 \text{ kV}$. This decreased the polarisation factor of the molecule from $\eta = 0.61$ to $\eta = 0.32$, 1.87 times smaller. The un-blinded eEDM channel value for these blocks was $\langle [\text{EDM}] \rangle = (-0.3 \pm 2.5) \times 10^{-27} e \text{ cm}$, inconsistent at the 2.1σ level with the previous $\pm 7.5 \text{ kV}$ dataset. This suggests that the cause of the $\langle [\text{EDM}] \rangle$ channel in the $\pm 7.5 \text{ kV}$ dataset is not a genuine eEDM signal, but rather some other systematic effect which depended on voltage. We can also express $\langle [\text{EDM}] \rangle$ for the low voltage data as an E, B correlated phase of $(3 \pm 30) \mu\text{rad}$. If we think that the fake eEDM is being caused by an E switch state dependent rf rotation as we observed in the previous section, then we would expect the high and low voltage data to give the

same E,B correlated phases. The 3.5σ inconsistency between these phases means we can confidently rule out the rf rotation systematic causing the fake eEDM.

We were able to discount leakage currents from causing the systematics: using the data from the nano-ammeters the size of the leakage currents would imply an eEDM no larger than $7 \times 10^{-29} e \text{ cm}$. In more tests, we ruled out the possibilities that voltage asymmetry or offset systematics (entries 1 and 2 in Table 3.1) were responsible for this error.

Given that the fake eEDM is inconsistent with the 2011 published measurement, which reported an eEDM of $(2.4 \pm 5.7_{\text{stat}} \pm 1.5_{\text{syst}}) \times 10^{-28} e \text{ cm}$, we concentrated on the parts of the experiment which were changed between 2010-11 when those data were taken and 2013 when we noticed the large eEDM. Since the fake eEDM seems to be related to voltage, suspicion quickly fell on the high voltage supplies.

In the 2011 data set we used two different high voltages supplies: a *Bertan 602C-150N* negative supply and a *Bertan 602B-150P* positive supply. In case electrical differences between these supplies might somehow produce a false eEDM, these were subsequently replaced by an identical pair of *Applied Kilovolts HP010* 10 kV supplies. In order to test whether the change of supplies had actually caused a systematic error, we went back to using the *Bertan* supplies. The value of the eEDM channel then dropped to $\langle [\text{EDM}] \rangle = (0.7 \pm 1.4) \times 10^{-27} e \text{ cm}$ at $\pm 7.5 \text{ kV}$ and $\langle [\text{EDM}] \rangle = (1.0 \pm 1.1) \times 10^{-27} e \text{ cm}$ when the plates were charged at $\pm 12 \text{ kV}$. These two results are respectively 2.8 and 3.2 σ inconsistent with the $\pm 7.5 \text{ kV}$ data taken with the *Applied Kilovolts* supplies. Thus it seemed that these supplies might be causing the problem. Unfortunately, when we returned to the *Bertan* supplies, we also changed the way the electric field was switched, which I now describe.

The 2011 data set, taken with the *Bertan* supplies, and the March and July data sets taken with the *Applied Kilovolts* supplies, used the switching sequence illustrated for the case of $\pm 7.5 \text{ kV}$ in the top graph of Fig. 3.7. The control voltages start at $\pm 7.5 \text{ V}$, so that the high voltage supplies, which supply $1000\times$ the voltage,

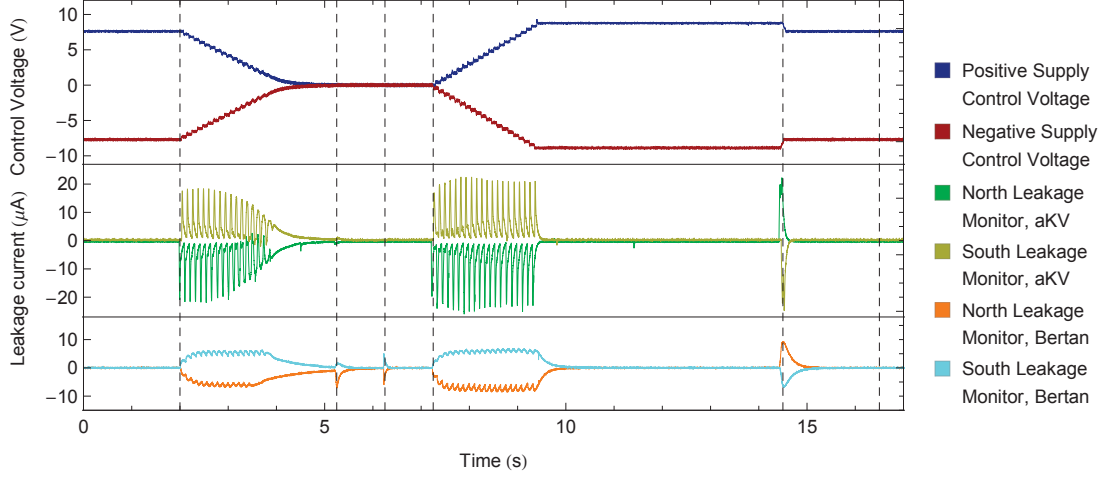


Fig. 3.7: Control voltages and charging currents for *Bertan* and *Applied Kilovolts* supplies. The dashed lines show when control signals are sent to the supplies and the relays, the action is explained in the text

are at ± 7.5 kV. At the first dotted line the E-switch sequence starts, and the control voltages are stepped down to zero over 2 s. At the second dotted line, a switch is thrown to ground the plates, then at the third line the relays are switched and each supply is connected to the opposite plate. Starting at the fourth dotted line the plate voltages are ramped up to 1.15 times their operating value and held at this voltage for 5 seconds before being reduced at the fifth dashed line to the values for eEDM data taking. There is then a 2 s settling time before eEDM data taking begins again. When we returned to the *Bertan* supplies the 15% overshoot was not applied, because we wanted to run at ± 12 kV and the overshoot caused sparking. To ensure that the plates had fully charged, the settling time after the switch sequence was increased to 3 s. Because of this, we could not say whether it was the change of supplies or the change of switching pattern that had caused the eEDM to go away.

In an effort to elucidate this, we took data with the *Applied Kilovolts* supplies without an overshoot, and with the *Bertan* supplies with an overshoot. They are shown in the bottom two rows of Table 3.4. Also shown are the results of the 2011 measurement, the July 2013 data set taken with the *Applied Kilovolts* supplies

and the data taken with the *Bertan* supplies and no overshoot in rows 1,2 and 3 respectively.

Date	Plate voltage (kV)	Supplies used	Overshoot applied ?	eEDM (10^{-27} e cm)
2011	± 6.0	<i>Bertan</i>	Yes	$0.24 \pm 0.57_{\text{stat}} \pm 0.15_{\text{syst}}$
07/2013	± 7.5	<i>Applied Kilovolts</i>	Yes	$5.0 \pm 0.6_{\text{stat}}$
11/2013	± 7.5	<i>Bertan</i>	No	$0.7 \pm 1.4_{\text{stat}}$
11/2013	± 7.5	<i>Applied Kilovolts</i>	No	$2.9 \pm 1.1_{\text{stat}}$
11/2013	± 7.5	<i>Bertan</i>	Yes	$2.8 \pm 0.8_{\text{stat}}$

Tab. 3.4: Some measurements of $\langle [\text{EDM}] \rangle$ made with the *Applied Kilovolt* and *Bertan* supplies with and without the overshoot. The error from other systematic effects is not included in the data taken in 2013 but it is smaller than the systematic error associated with the 2011 measurement, $\pm 0.15 \times 10^{-27}$ e cm.

Unfortunately, the results of these tests (rows 4 and 5) were inconclusive, since they both equally support the hypothesis that the supplies were responsible for the problem, or that the overshoot was causing the problem.

Since we could not distinguish between these two changes to the machine, we started by focusing on a systematic error that both changes could influence: magnetisation caused by charging currents that flow into the machine during the E-switch sequence. Reducing the operating voltage should also affect the size of the charging currents that flow, so all the signs pointed to this as a possible explanation. In discussing the results, it is helpful to consider dc charging currents and ac charging currents separately, which we do in the following two sections.

3.5.2 dc charging currents

Direct current (dc) charging currents are what we commonly think of when the electric field plates are charged: current flows out of the high voltage supplies, through

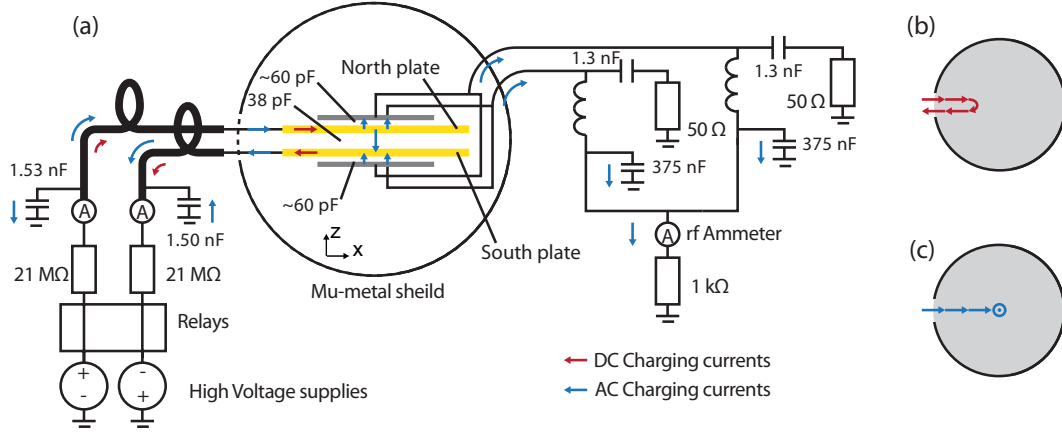


Fig. 3.8: (a) A circuit diagram of the components in the electric field and rf system necessary to understand the charging currents. The arrows indicate the currents that flow when the voltages to the North plate are increased and the South plate decreased simultaneously. (b) The current path for the dc shield magnetisation test. (c) The current path for the ac shield magnetisation test.

the current limiting resistors and the ammeters and onto the high voltage plates. The direction of this current when the magnitudes of the supply voltages are increased is shown by the red arrows in Fig. 3.8 (a). Charging currents could cause a magnetisation of any magnetically permeable material close to where they flow. The experiment is designed so that there are no ferromagnetic materials inside the main vacuum chamber, so the chief material that could be magnetised is the mu-metal shield. To avoid this, we limit the dc charging currents using 20 MΩ resistors on the high voltage lines after the supplies (the ammeters on the high voltage lines also add a 1 MΩ series resistance to the lines), and we also put the high voltage feedthroughs close together on one side of the machine (see Fig. 3.8 (a) again) so that the magnetic fields generated by the charging currents largely cancel.

Nevertheless, one can imagine that dc charging currents might magnetise the shields. To estimate the eEDM signal we could expect from a dc leakage current a test was performed in July 2009 before I joined the group, as follows: a loop of wire was passed through the high voltage hole in the side of a copy of the inner

shields and 350 μA current was sent along this wire. The path of the current is indicated in Fig. 3.8 (b). The current was applied for 7 s through this loop. The field inside the shield along what would be the machine z axis was then measured using a Bartington fluxgate magnetometer. The current was then reversed and the field re-measured. The change in the magnetometer reading of (0.39 ± 0.43) pT was consistent with zero magnetization. If we assume that the magnetisation is at worst linear in the applied current then the systematic error from dc shield magnetisation is no larger than 0.5×10^{-29} e cm/ μA of current flowing. It should be noted that the dc charging currents all flow for much less than 7 s, but we do not additionally scale the systematic error to account for this.

The charging currents running through the high voltage cables when the *Applied Kilovolts* and *Bertan* supplies are used can be seen in Fig. 3.7. While there are obvious differences in the fast response, neither has a dc charging current that is sufficient to magnetise the shields to produce a fake eEDM on the scale that we see: taking the worst peak current that flows when the *Bertan* supplies are used (10 μA) only gives an eEDM of 5×10^{-29} e cm, doing the same for the *Applied Kilovolts* supplies are used only gives an eEDM of 1.6×10^{-28} e cm, far smaller than the shift we have to account for.

3.5.3 ac charging currents

The ac component of the charging current offers a different possibility. This current can be transmitted capacitively from the high voltage lines, as illustrated by the blue arrows in Fig. 3.8 (a). Currents flowing in this way through the shields are more likely to magnetise them because the magnetic fields they generate do not cancel at the feedthrough.

To quantify how much magnetic field we could expect for a given current flowing in this way, we performed another test on the spare copy of the inner magnetic shields. We passed a loop of wire through the electric feedthrough hole and out of

the top of the shields, a current path indicated by Fig. 3.8 (c). A current was applied for 500 μA through this wire for 7s, followed by a 7s pause and then the magnetic field along the z axis was measured. The current was then applied in the opposite direction and the field was re-measured. We recorded a magnetic field change of 0.8 ± 1.9 pT along z , implying an upper limit to the size of any ac magnetisation systematic error of 1.3×10^{-29} e cm/ μA .

Now all we need to know is how much current actually follows this path for each of the different supplies, with and without the overshoot. The *Bertan* and *Applied Kilovolts* supplies differ significantly in their potential for ac charging currents. Looking at Fig. 3.7, we can see that the *Applied Kilovolts* respond rapidly to the steps in the control voltage, producing large transient currents whose ac component could flow as shown in Fig. 3.8 (c). In contrast, the *Bertan* supplies respond much more slowly to the voltage steps, only showing very small transients in the charging and discharging currents in the periods between 2–4 s and 7–9 s. Using these charging currents and a circuit model of the electric and rf plates, we can use *SPICE*, a free circuit simulation software package, to estimate the size of the transient currents. We have to resort to simulating these currents because the capacitor on the output of the bias tees reduces the ability of the rf ammeter to see such fast current changes.

For a net ac current to flow in the leakage path indicated by 3.8 (c), one of two things must be true: either the capacitance between the North plate and nearest rf plate must differ from the capacitance between the South plate and its neighbouring rf plate, or the timing of the voltage steps must not be synchronised. We can actually see evidence that our voltage steps are not synchronous in the *Applied Kilovolts* charging graphs in Fig. 3.7: the current that flows through the north leakage monitor when the voltages are reduced at around 14.5 s clearly happens before the corresponding current spike on the south leakage monitor. Using *SPICE* and the leakage currents shown in this Fig. 3.7 we can estimate the maximum peak currents flowing along the leakage path illustrated in Fig. 3.8 (c). These are listed in Table 3.5.

Supplies used	Peak ac charging current without overshoot and associated eEDM (μA , $e\text{ cm}$)		Peak ac charging current with overshoot associated eEDM (μA , $e\text{ cm}$)	
<i>Applied Kilovolts</i>	<1.0	1.3×10^{-29}	<1.1	1.4×10^{-29}
<i>Bertans</i>	<0.27	0.35×10^{-29}	<0.35	0.46×10^{-29}

Tab. 3.5: ac charging current with and without overshoot for *Bertan* and *Applied Kilovolt* supplies.

The figures in this table illustrate that while there may be quite large transient currents on the high voltage lines, most of these flow capacitively from the core of the high voltage lines to the cladding, and very little of the current is transmitted through the ac charging path shown in Fig. 3.8 (c). The upper limits on the shield magnetisation systematics caused by these currents are two orders of magnitude too small to explain the shifts in the $\langle\{\text{EDM}\}\rangle$ channel we actually see. Thus we conclude that like dc magnetisation, ac magnetisation effects are not sufficient to produce a large enough systematic error to account for the shift we see.

3.5.4 Other explanations

We have yet to discover what the cause of the systematic error is, but the following are possible lines of enquiry:

Magnetisation of something other than the mu-metal shields

The discussion and tests on the magnetic shields show that we can be confident that the charging currents caused by the overshoot or the *Applied Kilovolts* supplies are not magnetising the mu-metal shields. It is still possible that another item is being magnetised, for instance the outer vacuum chamber which is made from steel, or some tiny magnetic impurity close to the experiment. When we dismantled part of the machine in 2015 we also noticed that there were some $1\text{ M}\Omega$ resistors with some

slight magnetic permeability inside the main vacuum chamber. We will investigate to ensure that the currents flowing during the shield charging cannot magnetise these components either.

Other effects of the overshoot

Having ruled out magnetisation, it is difficult to know how else the overshoot could produce a systematic error. To accentuate any effects related to the settling of the electric fields, we took data with the *Applied Kilovolts* supplies at ± 7.5 kV but removed the 2 second settling time after the supplies are reduced from their overshoot value. The un-blinded eEDM value is consistent with the value taken with the 2 second settling time, $\langle \{ \text{EDM} \} \rangle = (4.0 \pm 2.0) \times 10^{-27} \text{ e cm}$. This strongly suggests that we can discount the overshoot as being in any way responsible for the fake eEDM signal we see.

Other differences between the two sets of high voltage supplies

It is possible that some difference between the two sets of supplies, other than the charging currents, is responsible for the systematic error. We compared the 50 Hz and 100 Hz ripple and found some slight differences, but it is difficult to know how this could lead to a systematic error. It is also possible that the *Applied Kilovolt* supplies, with their much larger bandwidth, are in some way picking up control signals from our experimental computer and varying the potentials on the plates in an unexpected way. We will continue to investigate to see if any other important differences become apparent.

3.6 Conclusion and next steps

We struggled from November 2012 to May 2014 to understand the systematic errors presented in this chapter. In the course of that, we learned that any error from rf

discharge is small, and that the rf rotation systematic can be controlled and quantified. However, we have yet to establish what is causing the electric field supplies systematic. At the end of May 2014 we decided that we should improve the sensitivity of the experiment so that it would be easier to find what exactly was causing this last systematic error. In the next chapter, the current limit on the experimental sensitivity is analysed, paving the way for the remainder of the thesis, where the ways of improving the experiment are laid out.

4. SENSITIVITY ANALYSIS

4.1 *Introduction*

In the previous chapter, we described some new systematic errors that have been discovered. We were left at the end of the chapter with a systematic error whose origin could not be determined. We resolved to improve the sensitivity of the experiment to make it easier to track down the origin of the systematic error. In order to do this most effectively, we had to understand what the major contributions to our statistical uncertainty were. This is the subject of the current chapter.

4.2 *Shot noise limit*

When we take a cluster of B blocks of eEDM data and work out the 5% trimmed mean and bootstrap error, as introduced in Chapter 2, we generally find that the 68.3% confidence interval on the mean is $\pm 2.5/\sqrt{B} \times 10^{-26} \text{ e cm}$. Roughly speaking then, we can think of the $1\text{-}\sigma$ uncertainty on a single block of eEDM data as being $\sigma_{d_e} = 2.5 \times 10^{-26} \text{ e cm}$. We refer to this as the sensitivity of the machine. It is instructive to investigate why the eEDM experiment has this sensitivity, since the answer will elucidate how we can improve the experiment.

Three quantities will be important in our discussion of the eEDM sensitivity. The first two are $\mathcal{P}^{\text{NORM}}$ and \mathcal{P}^{TOP} the average number of photons detected by the pump and probe PMT detectors, respectively. These can be extracted from the following channels:

$$\mathcal{P}^{\text{TOP}} = \frac{\langle \{\text{SIG}\} \rangle}{0.1} \quad \mathcal{P}^{\text{NORM}} = \frac{\langle \{\text{SIG}\}^{\text{NORM}} \rangle}{0.02}. \quad (4.1)$$

Here 0.1 and 0.02 are the appropriate conversion factors to turn the signals in $\text{V } \mu\text{s}$ into numbers of photons counted. The last quantity is the contrast, \mathcal{C} , defined as amplitude of the interference curve ($\mathcal{A}/2$ in Eq. (2.24)) divided by its mean value ($\mathcal{A}/2 + \mathcal{G}$ in Eq. (2.24)) for the block, averaged over all molecular arrival times. This can also be extracted from the block values as follows:

$$\mathcal{C} \simeq \frac{1}{t_{\text{gate}}} \frac{\frac{16}{\pi} \langle \{\delta B\} \rangle}{\langle \{\text{SIG}\} \rangle}, \quad (4.2)$$

where $t_{\text{gate}} = t_2 - t_1$ is the total length of the integration gate, defined by Eq. (2.33).

Having defined these useful quantities, we turn now to look at the combination of channels defined in Eq. (2.32), $[\text{EDM}]$, which gives the size of the eEDM. Integrating over all molecular arrival times, the dominant term in $\langle [\text{EDM}] \rangle$ is $\left\langle \frac{\{E \cdot B\}}{\{\delta B\}} \right\rangle$. The other terms inside the brackets of that equation only make small contributions to the central value and error of $\langle [\text{EDM}] \rangle$ and can be ignored in the present discussion. Making this approximation, the value of the eEDM is then

$$d_e = \frac{\hbar\pi}{32\eta E_{\text{eff}}\tau d_e t_{\text{gate}}} \left\langle \frac{\{E \cdot B\}}{\{\delta B\}} \right\rangle. \quad (4.3)$$

For estimating the uncertainty on d_e in one block, we further assume that the $\frac{\{E \cdot B\}}{\{\delta B\}}$ channel is constant over the integration gate, in which case we can write

$$d_e \simeq \frac{\hbar\pi}{32\eta E_{\text{eff}}\tau d_e t_{\text{gate}}} \frac{\langle \{E \cdot B\} \rangle}{\langle \{\delta B\} \rangle}. \quad (4.4)$$

We can use equations (2.28) and (2.33) to write out $\langle \{E \cdot B\} \rangle$ and $\langle \{\delta B\} \rangle$ channels as

$$\langle \{E \cdot B\} \rangle = \sum_{i=1}^N (W_{E \cdot B})_i \frac{\tilde{N}}{\mathcal{N}_i} \int_{t_1}^{t_2} S_i^{\text{TOP}}(t) dt, \quad (4.5)$$

$$\langle \{\delta B\} \rangle = \sum_{i=1}^N (W_{\delta B})_i \frac{\tilde{N}}{\mathcal{N}_i} \int_{t_1}^{t_2} S_i^{\text{TOP}}(t) dt. \quad (4.6)$$

Each of these equations represents the sum of 4096 terms, and the sign of the i^{th} or j^{th} term is given by the waveform value at that term $(W_{\delta B})_j$ or $(W_{E \cdot B})_i$. Each term represents the value of the top detector on the i^{th} shot, registered at the detector at a time t_k , normalised to the pump PMT signal for the same group of molecules. These two signals are shown on pages 57 and 53 respectively, where it should be noted that the gain of the pump PMT amplifier is 5×10^7 counts/V and the probe PMT amplifier is 1×10^7 counts/V.

Let us now consider a single term in one of these sums. Expanding Eq. (2.24) about the linear part of the interference curve where we always work, and using the fact that $\phi_B = (W_{\delta B})_i \frac{\pi}{32} + (W_B)_i \frac{\pi}{4}$, we can rewrite the i^{th} term of the sum as

$$\frac{\tilde{N}}{\mathcal{N}_i} \int_{t_1}^{t_2} S_i^{\text{TOP}}(t) dt = \frac{\tilde{N} \int_{t_1}^{t_2} (\mathcal{A}_i(t)(W_B)_i \left(\frac{1}{2} + (W_{\delta B \cdot B})_i \frac{\pi}{32} + (W_E)_i \phi_E \right) + \mathcal{G}_i(t)) dt}{\int_{t_1/\kappa}^{t_2/\kappa} S_i^{\text{NORM}}(\tau) d\tau}. \quad (4.7)$$

Here κ is the ratio of pump and probe distances discussed below Eq. (2.33) on p. 70. Now each of these terms may have some variability which could lead to an uncertainty in measuring $S_i^{\text{TOP}}(t)$. For instance, the pre-factor $\mathcal{A}_i(t)$ might vary because of frequency noise on the probe laser. Notice, however, that fluctuations in the molecule number, which would scale \mathcal{A} and S^{NORM} by the same factor do not lead to noise on the quantity $\int_{t_1}^{t_2} S_i^{\text{TOP}}(t) dt / \mathcal{N}_i$ (because $\mathcal{A}/2 \gg \mathcal{G}$ in our experiments). However, even if we stabilise all the experimental parameters, there is a fundamental lower limit on the uncertainty with which we can measure $\int_{t_1}^{t_2} S_i^{\text{TOP}}(t) dt / \mathcal{N}_i$ because each signal is made up of a discrete number of photon counts.

If some Poissonian process produces counts in a detector at a rate R , the mean number of counts during a time t will be Rt , with a standard deviation of \sqrt{Rt} . That is called shot noise. At best our signals are Poissonian and we can hope to reach the shot noise limit. Now each shot records (on average) \mathcal{P}^{TOP} photons at the top detector, and $\mathcal{P}^{\text{NORM}}$ at the pump. Assuming that the uncertainties in these two counts are just given by the shot noise, and both the pump and probe detectors measure the same group of molecules¹, then the uncertainty in the normalised count of Eq. (4.7) is

$$\sigma_i = \langle \{\text{SIG}\} \rangle \sqrt{\frac{1}{\mathcal{P}^{\text{TOP}}} + \frac{1}{\mathcal{P}^{\text{NORM}}}}. \quad (4.8)$$

In the ideal case, there are no other noise sources from shot to shot apart from these photon counting uncertainties. Hence, we can treat each shot as independent measurement of the quantity $\int_{t_1}^{t_2} S_i^{\text{TOP}}(t) dt / \mathcal{N}_i$, and the fractional error in N such shots is just σ_i / \sqrt{N} . We now have the values for the errors $\sigma_{\langle \{E \cdot B\} \rangle}$ and $\sigma_{\langle \{\delta B\} \rangle}$ associated with the quantities $\langle \{E \cdot B\} \rangle$ and $\langle \{\delta B\} \rangle$. The error in the ratio $\langle \{E \cdot B\} \rangle / \langle \{\delta B\} \rangle$ is just found using standard error propagation

$$\sigma_{\langle \{E \cdot B\} \rangle / \langle \{\delta B\} \rangle}^2 = \frac{\sigma_{\langle \{E \cdot B\} \rangle}^2}{\langle \{\delta B\} \rangle^2} + \frac{\langle \{E \cdot B\} \rangle^2}{\langle \{\delta B\} \rangle^4} \sigma_{\langle \{\delta B\} \rangle}^2. \quad (4.9)$$

Since $\langle \{E \cdot B\} \rangle \ll \langle \{\delta B\} \rangle$ we can neglect the second term. Inserting this result into Eq. (4.4) and using the definition for \mathcal{C} we find the error on Eq. (4.4) to be

$$\sigma_{d_e} \simeq \frac{\hbar}{\eta E_{\text{eff}} \tau^2 2\mathcal{C} \sqrt{N}} \sqrt{\frac{1}{\mathcal{P}^{\text{TOP}}} + \frac{1}{\mathcal{P}^{\text{NORM}}}}. \quad (4.10)$$

Eq. (4.10) agrees with Eq. (5) of Ref. [66] if $\mathcal{P}^{\text{NORM}} \gg \mathcal{P}^{\text{TOP}}$.

Finally then, we can look to see how the actual experimental sensitivity compares to Eq. (4.10). We do this for two large datasets that we took in March 2013 and July 2013; the results are shown in Table 4.1. The data for March 2013 has been divided

¹ A full correlation analysis between the pump and probe signals can in principle be performed to investigate the relationship between these two detector signals more fully.

into rf manual true and false data and analysed separately, because otherwise the rf rotation systematic error, shown in Fig. 3.3 (a), broadens the distribution of eEDM values and affects the measurement of the sensitivity.

Date	rf	Blocks	\mathcal{C}	\mathcal{P}^{TOP}	$\mathcal{P}^{\text{NORM}}$	Sensitivity (10^{-26} e cm/ $\sqrt{\text{block}}$)	
						Shot noise limit	Measured
03/13	T	973	0.63	697 ± 5	3390 ± 30	2.04 ± 0.01	2.56 ± 0.01
03/13	F	2156	0.65	722 ± 3	3168 ± 20	1.97 ± 0.01	2.39 ± 0.01
07/13	both	2740	0.60	651 ± 2	3390 ± 20	2.21 ± 0.01	2.61 ± 0.02

Tab. 4.1: Parameters relating to the eEDM statistical sensitivity for the July and March datasets. The March data set has been split into blocks in rf manual state true and rf manual state false. The July data set contains both rf manual states.

We see that the expected sensitivity is very close indeed to the sensitivity predicted by the shot noise limit. It is instructive to peer within the datasets to look a little more closely at the relationship between the measured sensitivity and the predicted sensitivity according to shot noise. To do this, we determine for each block the measured eEDM and the eEDM shot noise given by Eq. (4.10). These pairs are ordered according to the size of the shot noise, then collected into groups of 50. For each group we calculate the eEDM sensitivity defined above and plot it against the corresponding shot noise, as shown in Fig. 4.1.

There are several important points to note. First, for both datasets, the measured sensitivity for the group of blocks generally tracks the predicted sensitivity; that is to say, blocks where the molecular signal was higher and where the interferometer contrast was better were also better at measuring the value of the electron EDM. Also, if we look at the July dataset, it seems that photon counting noise is the dominant noise source, and the sensitivity of a block to the eEDM is close to Eq. (4.10). For the March dataset, the sensitivity is generally a little poorer than the shot noise level, indicating that there may be additional noise sources.

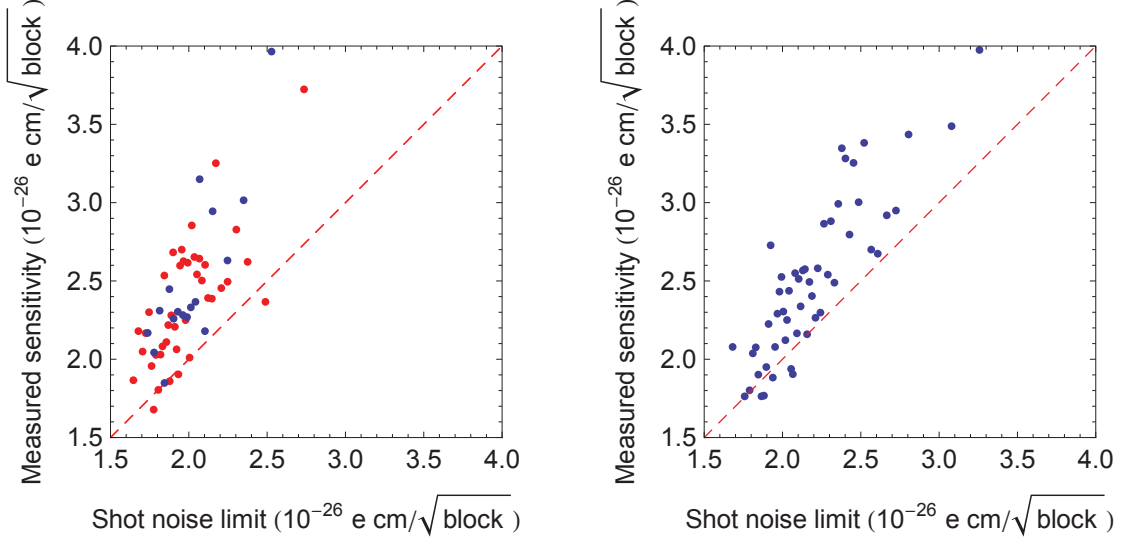


Fig. 4.1: Comparison of measured sensitivity to shot noise limit for March 2013 data run (left, red dots rf state false, blue dots rf state true) and July 2013 data run (right). The dashed red line is $y=x$.

In conclusion, it seems that noise in eEDM interferometer is currently dominated by photon shot noise, and the uncertainty that we could hope to achieve with one block of eEDM data taking is given to a good approximation by Eq. (4.10). That is interesting because one might have expected magnetic noise to be troublesome. However, the next section shows explicitly that we are still far from being limited by external magnetic field noise.

4.3 Magnetic field noise

The eEDM interaction affects the molecules like a magnetic field that changes sign with the electric field direction. A field of 1 pT along the z axis, switching synchronously with the electric field, would produce a signal in the eEDM channel of $3.6 \times 10^{-27} e \text{ cm}$. Therefore, any magnetic field fluctuations have the potential to increase the error in the eEDM channel. Since the direction of the electric field is modulated, magnetic field noise below the frequency of electric field switch is heavily suppressed. We take great care to minimise our exposure to higher frequency noise

by shielding the experiment within three layers of magnetic shielding and also by phase locking the experiment to the mains frequency.

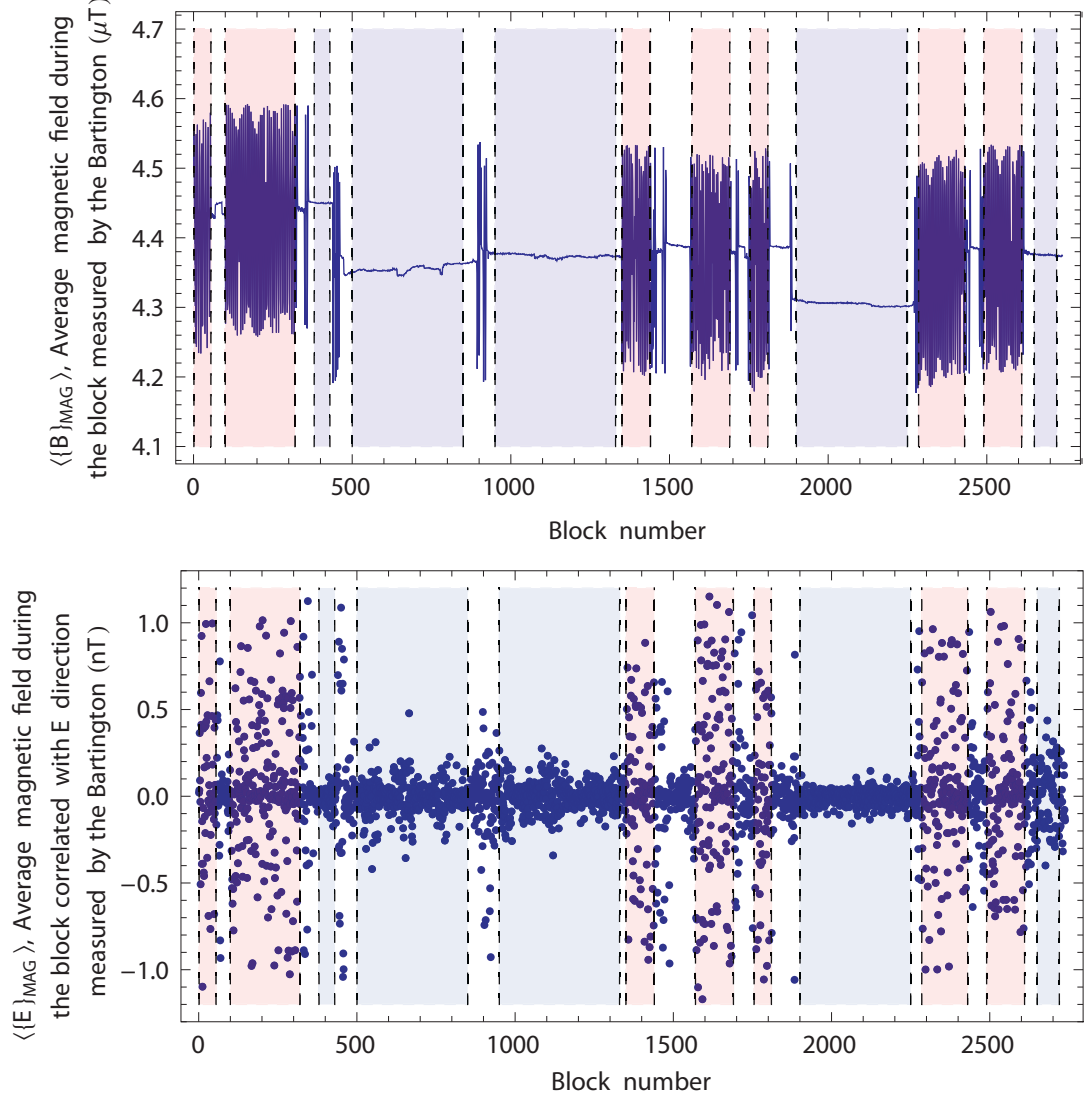


Fig. 4.2: Top: Average magnetic field, $\langle \{B\}_{\text{MAG}} \rangle$ detected by *Bartington* magnetometer during July 2013 data run. Bottom: Component of magnetic field detected by the *Bartington* magnetometer correlated with the direction of the applied electric field, $\langle \{E\}_{\text{MAG}} \rangle$. In both graphs the red shaded blocks make up the *noisy blocks* and the blue shaded blocks make up the *quiet blocks*. The unshaded blocks have some ambiguity over whether or not the magnetic field was ramping and so are not included in the analysis discussed in this section.

In the previous section, we saw that the error from magnetic field noise must be significantly smaller than the photon counting shot noise. In this section we assess how large it is. We do so by looking at the magnetic field using a *Bartington* magnetometer placed between the innermost and middle magnetic shields, at a location indicated in Fig. 2.6. We expect that if the *Bartington* detects a large magnetic field correlated with the electric field direction, i.e. if $\langle\{E\}_{\text{MAG}}\rangle$ is large, then the value of $\langle[\text{EDM}]\rangle$ for that block should also be shifted. Because the Bartington does not measure the magnetic field along the path of the molecules, but rather samples a particular place some distance away, the conversion between $\langle\{E\}_{\text{MAG}}\rangle$ to a false $\langle[\text{EDM}]\rangle$ depends crucially on the origin of the noise.

We stress this point because while both the March and July datasets were taken, we were able to detect a ramping magnetic field from a solid state laboratory two floors above the eEDM experiment. We concentrate now on the first half of the July data set, data from which are shown in Fig. 4.2. Blocks taken when the magnet was operating, shown shaded in red in the top half of Fig. 4.2, had an additional ambient field of up to a few hundred nT. We call these the *noisy blocks*. In other blocks, shown shaded in blue in Fig. 4.2, the field was not ramping and the magnetic field was stable. These are the *quiet blocks*.

Some Fourier components of the ramping magnetic field coincide by chance with the E switch, so the value of $\langle\{E\}_{\text{MAG}}\rangle$ during the noisy blocks is on average larger than during the quiet blocks, as shown in the bottom graph of Fig. 4.2. However, it is very gratifying to see that the eEDM sensitivity is not affected by these ramping fields: it is $(2.56 \pm 0.01) \times 10^{-26} e \text{ cm}/\sqrt{\text{block}}$ for both the quiet and the noisy blocks. Even so this field is far from ideal and we prefer not to have it when taking eEDM data. That magnet has now been moved, so it will not feature as a noise source in future eEDM experiments.

Let us therefore concentrate on the correlation between $\langle\{E\}_{\text{MAG}}\rangle$ and $\langle\{\text{EDM}\}\rangle$ in the quiet blocks, which is more representative of the magnetic field noise that

molecules will experience in the future. In Fig. 4.3 we plot the values of $\langle\{E\}_{\text{MAG}}\rangle$ and $\langle\{\text{EDM}\}\rangle$ against each other. To determine the relationship between these quantities, we use a bootstrapped linear regression. First, we make 1000 replicates of the data shown in the graph by sampling the dataset with replacement, as described at the end of Chapter 2. We then fit a straight line to each replicate dataset using linear regression. However, standard linear regression does not account fully for the errors in the x-direction, and the effect of this is to underestimate the slope. We correct this using the reliability ratio (see Ref. [49], p. 87). Finally, we calculate the mean and standard deviation of the replicate gradients, which gives us our estimate for the gradient and error on the gradient of $(10 \pm 2) \times 10^{-26} \text{ e cm/nT}$. The gradient is shown in Fig. 4.3.

As might be expected from a dataset where the spread in the x coordinate (standard deviation 0.085 ± 0.003) is almost identical to the error in measuring the x coordinate (0.053 ± 0.001), those points with the largest absolute values for $\langle\{E\}_{\text{MAG}}\rangle$ are the most powerful in determining the relationship between $\langle\{E\}_{\text{MAG}}\rangle$ and $\langle\{\text{EDM}\}\rangle$. If we drop the largest and smallest 5% of the points, the determination of the gradient becomes more uncertain, giving $(10 \pm 4) \times 10^{-26} \text{ e cm/nT}$. The adjusted R^2 for the fitting procedure is 0.08 ± 0.02 , which indicates that the points are spread very far from the regression line, however, this spreading results from the uncertainty in measuring $\langle\{E\}_{\text{MAG}}\rangle$ and $\langle\{\text{EDM}\}\rangle$, rather than indicating that a more complicated model should be used.

Using the 5% trimmed gradient and the spread in the $\langle\{E\}_{\text{MAG}}\rangle$ channel, we can estimate the RMS shift in the $\langle\{\text{EDM}\}\rangle$ channel (the error) due to the fields detected by the *Bartington* to be $\sigma_B = (9 \pm 3) \times 10^{-27} \text{ e cm}/\sqrt{\text{block}}$. If this error is added in quadrature to the shot noise limits shown in Table 4.1, the result is to increase the eEDM error per $\sqrt{\text{block}}$ by $2 \times 10^{-27} \text{ e cm}$. This leaves around $2 \times 10^{-27} \text{ e cm}$ excess noise to be accounted for.

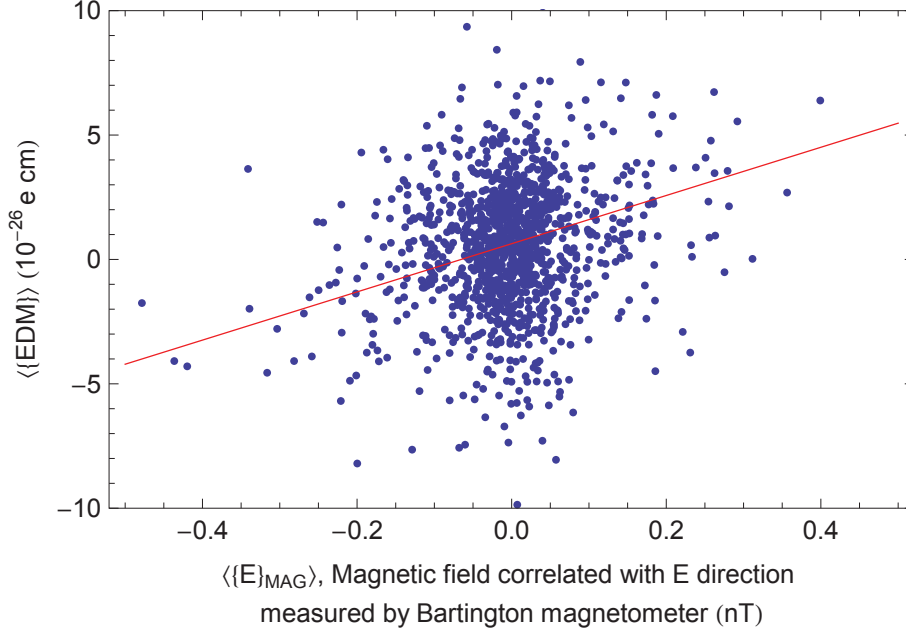


Fig. 4.3: Correlation between $\langle\{E\}_{\text{MAG}}\rangle$ and $\langle\{\text{EDM}\}\rangle$ for quiet blocks in the July 2013 data run. For blocks taken in electric field manual state false, the value of $\langle\{E\}_{\text{MAG}}\rangle$ has been multiplied by -1, to correct for the fact that the manual reversal effectively inverts the E-switch waveform.

4.4 Conclusion

In this section, we showed that the sensitivity of the YbF electron eEDM experiment can be largely explained by the uncertainty in the number of photons counted, and we can understand how to improve the experiment by trying to minimise the expression shown in Eq. 4.10. We also made an estimate for the size of the magnetic field noise, which is difficult given that it is much smaller than the shot noise. We measure a correlation between eEDM values and the magnetic field at the external magnetometer which shows that the magnetic field noise on the eEDM is $\sigma_B = (6.0 \pm 0.2) \times 10^{-27} e \text{ cm}/\sqrt{\text{block}}$. With the present shot noise level of approximately $2.1 \times 10^{-26} e \text{ cm}/\sqrt{\text{block}}$, this magnetic noise is negligible. When the shot noise is reduced to a comparable level, we will have to revisit this magnetic noise if it is not to become the dominant noise source.

5. OVERVIEW OF IMPROVEMENTS TO THE EXPERIMENT

5.1 *Increasing sensitivity by increasing signal*

In the last chapter, we showed that the statistical error on each block of eEDM data in 2013/4 was close to the shot noise limit given by Eq. (4.10), which we reproduce here

$$\sigma_{d_e} \simeq \frac{\hbar}{\eta E_{\text{eff}} \tau 2\mathcal{C} \sqrt{N}} \sqrt{\frac{1}{\mathcal{P}^{\text{TOP}}} + \frac{1}{\mathcal{P}^{\text{NORM}}}}. \quad (5.1)$$

Now we investigate how to reduce this quantity, so that we can make an improved eEDM measurement. The effective field $E_{\text{eff}} = 26 \text{ GV cm}^{-1}$ is a fixed property of the $X^2\Sigma^+(N=0, F=1)$ level in YbF. However, we can slightly increase η , the polarisation factor, by working at higher static electric fields. A side benefit of improving the high voltage cabling as described in section 3.4.2 was that by changing the connectors on the HV lines to 10 kV SHV connectors, we were able to operate at $\pm 12 \text{ kV}$ without too much difficulty. If we could run the experiment like this permanently, that would increase the polarisation factor from 0.61 to 0.69, a modest but useful reduction in σ_{d_e} .

Increasing the free evolution time τ is a long term goal of the experiment. The first step along this path is to develop a buffer gas source which will provide an intense beam of molecules travelling slowly (between $100\text{--}200 \text{ m s}^{-1}$) with 1.9×10^{10} YbF molecules per steradian per pulse in $X^2\Sigma^+(v=0, N=0)$ [67] [68]. This source will be incorporated into the experiment when it is completed. Looking even further into the future, the group is currently working to build a laser-cooled fountain of

YbF molecules [21], where the molecules would interact with the fields for 300 times longer than at present.

The contrast \mathcal{C} of the interferometer can be improved by reducing the pulse length of the rf used to drive the π -flips. With shorter pulses, the molecules sample less of the inhomogeneity in the rf field, and so can be more efficiently π -flipped. Using 2 μ s pulses gives an average contrast of $\mathcal{C} = 0.76 \pm 0.02$, compared to the average contrast of $\mathcal{C} = 0.61 \pm 0.01$ shown in Table 4.1. As discussed in Chapter 3, shorter rf pulses can lead to multipactor discharges. At the time when we were dealing with the discharges, we did not want to break vacuum in the main chamber and interfere with the interaction regions. However, while we install the improvements discussed in this section, we can take additional steps such as coating the rf plates or placing insulating barriers to disrupt the multipactor discharges and allow us to return to shorter length rf pulses.

While these improvements are being perfected, our parallel goal is to increase the factor \mathcal{P}^{TOP} . This will be achieved both by increasing the number of molecules pumped into the $X^2\Sigma^+ (v=0, N=0, F=0)$ state, and by detecting these molecules more effectively. We will also incorporate a way of detecting molecules left in both $X^2\Sigma^+ (F=0)$ and $(F=1)$, which will remove the need for a normalising detector and further improve our sensitivity.

We present a series of proposals to do this in this chapter, and expand upon them in the following chapters. If all the improvements discussed in this section can be successfully implemented, there should be an order of magnitude improvement in the sensitivity of the experiment.

5.2 New experimental apparatus

The improvements to the experiment are shown in diagram 5.1 in the sections marked with a blue shaded circle, and in the photographs of Fig. 5.2. In the pump region (2) and Fig. 5.2 (a)–(c), three resonant rf coils shown in red and a microwave horn deliver more pumping fields to the molecules. In addition, the pump laser light has been elongated slightly along the y axis, and more frequencies have been added. These changes are to increase the number of molecules pumped into the $|0, 0\rangle$ starting state, as we discuss below. The probe region, (6) has been completely re-designed in order to improve detection, also discussed below. Now in section (6.1) the molecules fly through a parallel plate microwave transmission line, designed to support TEM microwaves whose electric field is along the x axis. Two views of this transmission line are shown in the Figs. 5.2 (d)–(e). They then interact with the first probe beam in section (6.2). Once again, scattered photons are imaged onto a PMT. The molecules then fly through a second transmission line in section (6.3), and interact with a second probe laser beam in section (6.4). To understand how all these improvements increase the molecular signal, we now describe the new experimental sequence. Steps (1) and (3)–(5) are unchanged from the previous experimental sequence, section 2.4.1 on p. 52, and so we just include the title of the action here; the reader can refer back to that section if necessary.

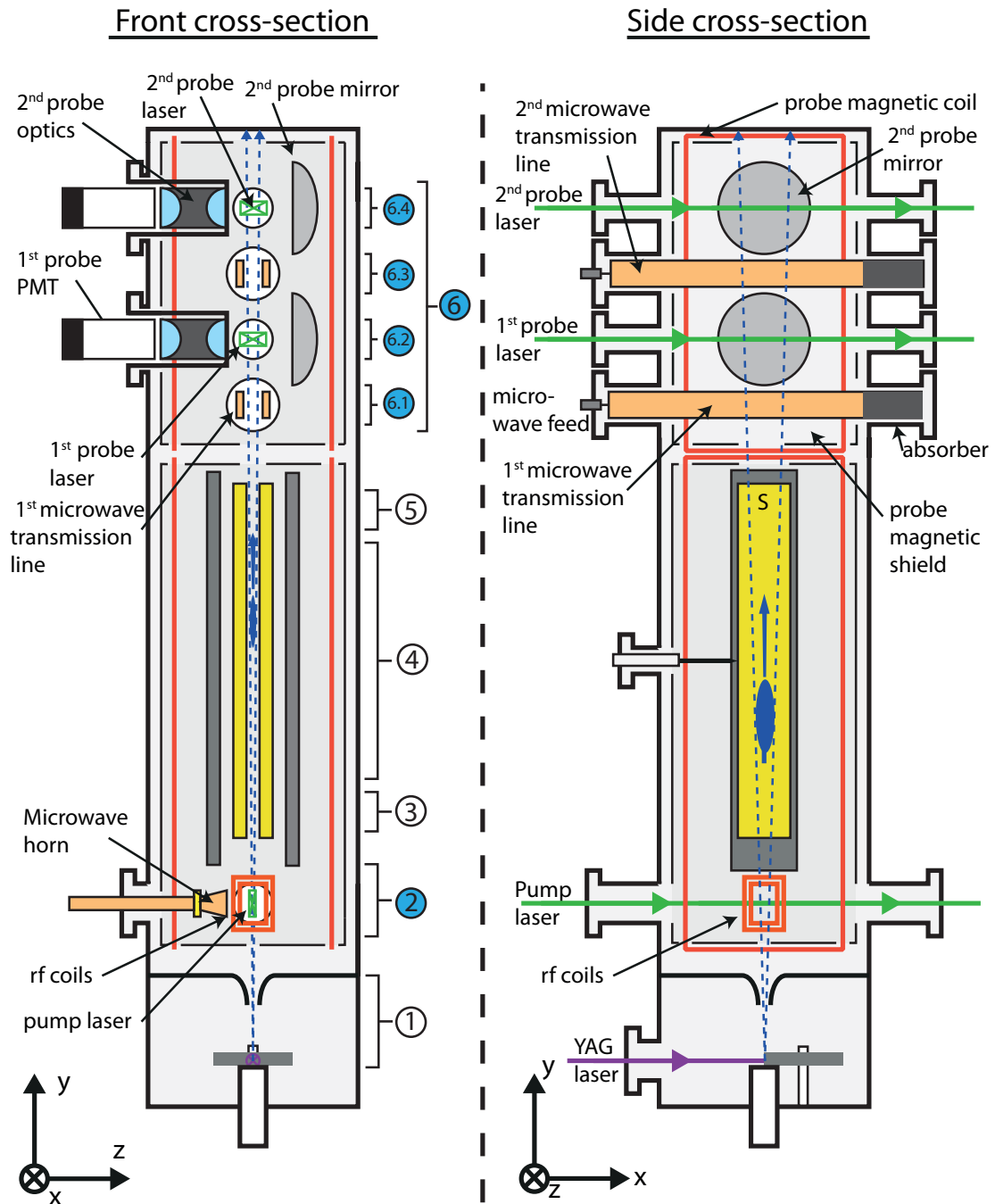


Fig. 5.1: The improved pumping and detection regions. The changes to the machine are in the regions ② and ⑥, shaded in blue. The remaining regions are unchanged from Fig. 2.6, p. 45.

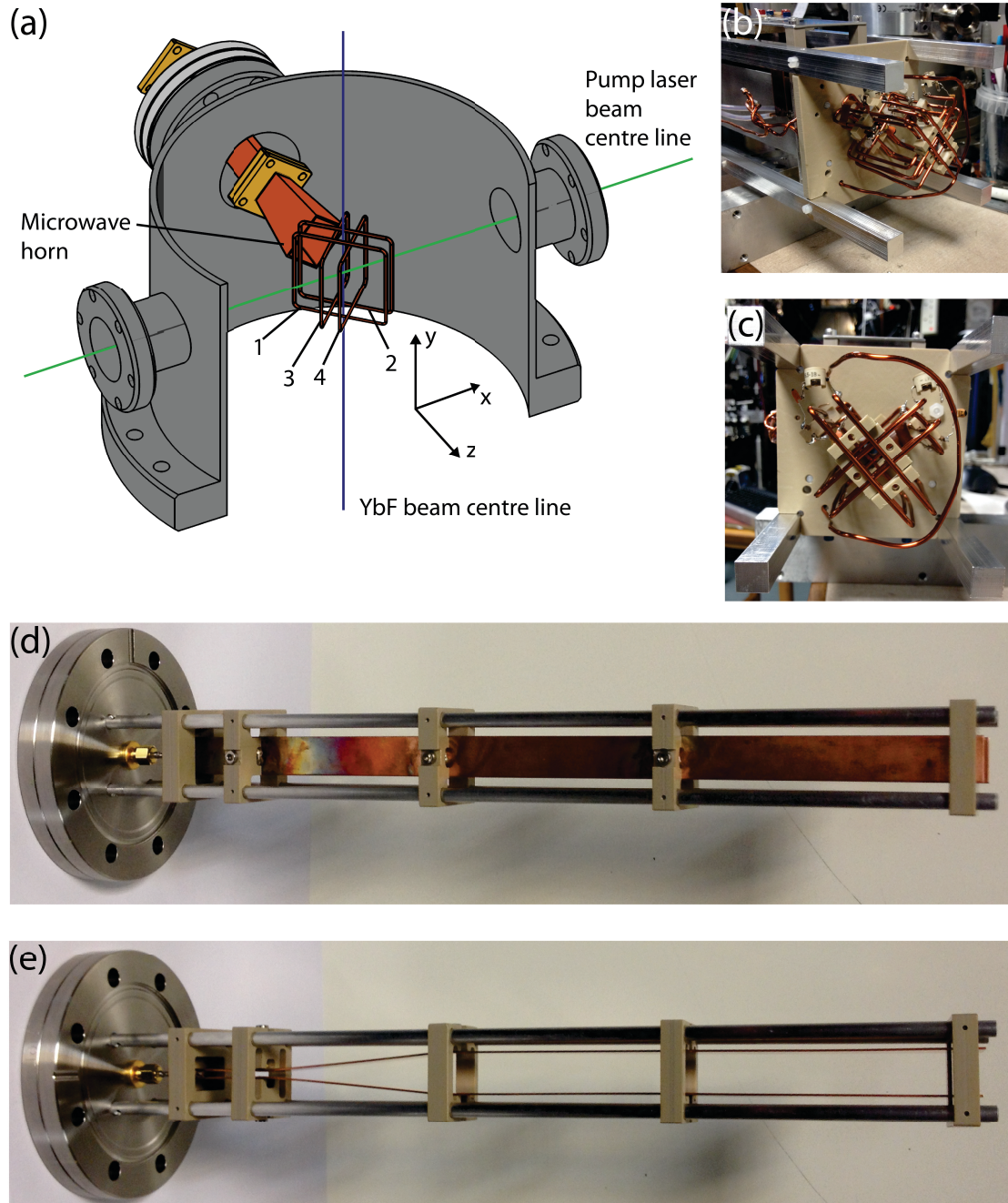


Fig. 5.2: (a) A view of the new pumping region (2), showing the four rf coils and microwave horn, the centre lines of the molecular beam and laser beam. The resonance frequencies of the coils are 1) 155.7 MHz, 2) 36.4 MHz, 3) 161.2 MHz and 4) 30.9 MHz. (b)–(c) Two pictures of the resonant rf coils, mounted on the plate support structure. (d)–(e) Two views of the microwave transmission line, sections (6.1) and (6.3). The absorber is not shown.

5.3 The new experimental sequence

5.3.1 A shot

- ① Make some YbF
- ② Pump system into $|0, 0\rangle$ using lasers, microwaves and rf radiation

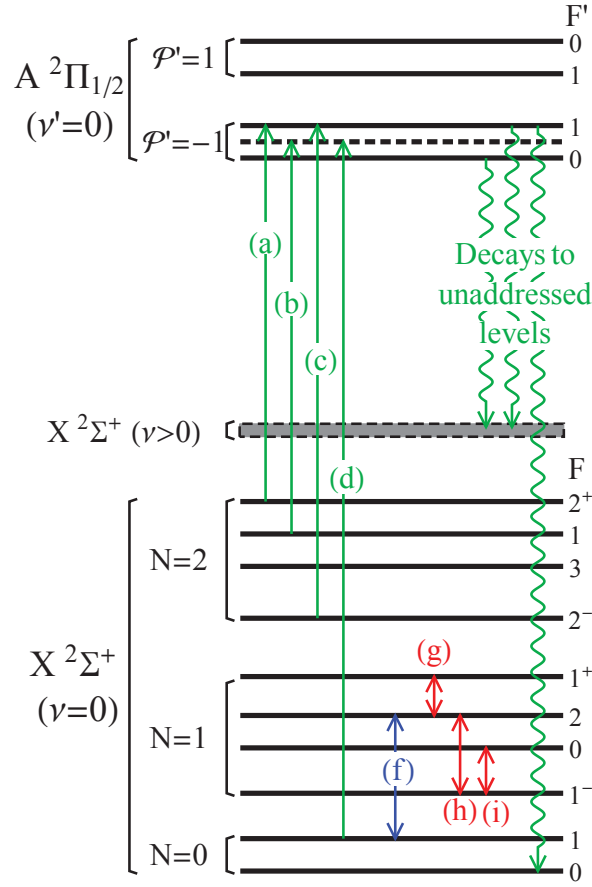


Fig. 5.3: The transitions driven in the new pumping region. Microwave radiation (f) and rf radiation (g)–(i) mix the rotational population in $N = 1$ into the state ($N = 0, F = 1$). The population in ($N = 0, F = 1$) is pumped to the excited state using a laser beam (d). Any decays into $N = 2$ are re-pumped using lasers (a)–(c), collectively called the $N = 2$ lasers. As well as decays to any of the $N = 0$ or $N = 2$ states addressed by laser beams (not shown), the excited state can decay into $|0, 0\rangle$ or $X \ ^2\Sigma^+ (v > 0)$, as indicated by the wiggly lines.

Pumping region ② is designed to transfer as much as possible of the thermal

population from $X^2\Sigma^+(v=0, N=0, 1, 2)$ into $X^2\Sigma^+|0, 0\rangle$ by optical pumping. To do this, the molecules are subjected to laser fields tuned to the four frequencies labelled (a)–(d) in Fig. 5.3. The polarisation of these fields will need to be modulated to excite all the components of the two $F=2$ levels of $X^2\Sigma^+(N=2)$. Microwaves tuned to the $X^2\Sigma^+(N=0, F=1) \rightarrow (N=1, F=2)$ transition (transition (f)) are applied by a horn. Radio-frequency fields drive magnetic dipole transitions $F=1^+ \rightarrow F=2$ (30.9 MHz, transition (g)), $F=2 \rightarrow F=1^-$ (161.2 MHz, transition (h)) and $F=0 \rightarrow F=1^-$ (155.7 MHz, transition (i)) in the $X^2\Sigma^+(N=1)$ level. These fields, produced by a set of resonant coils shown in the Figs. 5.2 (a)–(c), are linearly polarised at $\pm 45^\circ$ to the x axis. The microwave horn is rotated about the x axis so that the linearly polarised field it produces lies in the z - y plane at 50.5° to the y axis. With these fields it should be possible to mix all the $N=1$ levels with the $(N=0, F=1)$ level and hence to optically pump them into $|0, 0\rangle$ (with some losses to $X^2\Sigma^+(v>0)$). In section 5.4.1 we discuss exactly how much population is available to be pumped and how well we can expect to do in transferring this population into $|0, 0\rangle$.

③ *Prepare the YbF into a superposition of $|1, -1\rangle$ and $|1, 1\rangle$*

④ *Let the YbF spin evolve in electric and magnetic fields*

⑤ *Drive population in $|1, 1\rangle - |1, -1\rangle$ back to $|0, 0\rangle$ with a second rf pulse*

⑥ *Count the number of molecules left in $X^2\Sigma^+ F=1$ and $F=0$*

After the second rf pulse (step ⑤), the new detection region aims to count the molecules in $F=0$ and the number in $F=1$. The detection scheme has four steps:

(6.1) *Transfer $|0,0\rangle$ into $X^2\Sigma^+$ ($N=1, F=1^-, m_F=0$)*

The first step is to move molecules from the $|0,0\rangle$ state into the $(N=1, F=1^-, m_F=0) = |1, 1^-, 0\rangle$ state with a microwave π -pulse at 14,467,158 kHz.¹ The only allowed transitions of $|0,0\rangle$ into $N=1$ are to the $F=1^-$ and $F=1^+$ levels. Of these transitions, the transition matrix element to $F=1^+$ state is 20 times smaller than the matrix element to $F=1^-$, so we choose the more favourable transition. (see Chapter 6 and Appendix B for details of how to calculate these matrix elements).

(6.2) *Detect ($N=0, F=1$) population using cycling detection*

Now the population left in $(N=0, F=1)$ is detected by the first probe beam. This is made up of four laser frequencies already used in the pumping section, plus an additional beam resonant with the $X^2\Sigma^+ (v=0, N=0, F=0) \rightarrow A^2\Pi_{1/2}$ transition and labelled (e) in Fig. 5.4. The polarisation of the beams is modulated so that all the magnetic sub-levels of the $F=2^-$ and $F=2^+$ states are addressed. By applying these five beams (instead of one) we enable each YbF molecule to scatter many photons (instead of one) before decaying to $X^2\Sigma^+ (v>0)$ and becoming dark. This increases the detection efficiency by more than ten times, as we calculate in section 5.4.2. These fluorescence photons are imaged onto a PMT. The signal in this detector, named P_1 , measures the population left behind in the $F=1$ state after the second rf pulse

$$S^{P_1}(E, B; t) = \mathcal{A}(t) \sin^2(\phi_B + \phi_E) + \mathcal{G}(t). \quad (5.2)$$

¹ We choose to shelve $|0,0\rangle$ rather than the superposition left in $(N=0, F=1)$ because the orientation of the latter may vary in a way that is sensitive to the relative direction of the electric and magnetic fields in the region between the electric field plates and the microwave transmission line. This has potential to cause a signal which contributes to the $\langle\{\text{EDM}\}\rangle$ channel. Instead, we shelve the scalar state $|0,0\rangle$.

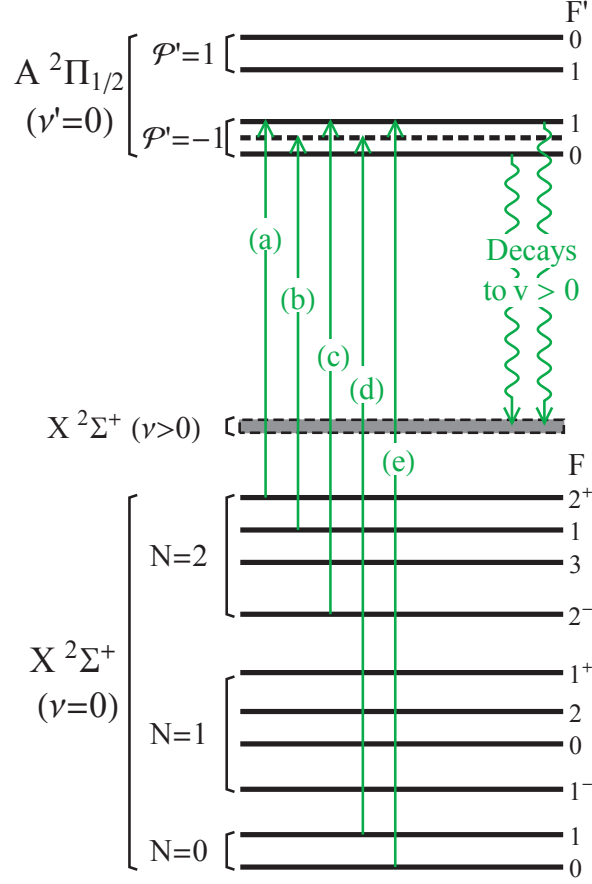


Fig. 5.4: The transitions driven in the new probing regions. The population in $N = 0$ and $N = 2$ is driven to the excited state using lasers (a)–(e). The excited state can decay to any of the $N = 0$ or a $N = 2$ states addressed by laser beams, from which it is re-pumped to the excited state, or to $X\ ^2\Sigma^+$ ($\nu > 0$).

6.3 Transfer $|1, 1^-, 0\rangle$ back into $|0, 0\rangle$

While the $(N = 0, F = 1)$ population was being detected, the population that had been shelved in $|1, 1^-, 0\rangle$ was flying through the machine. We transfer it back to $|0, 0\rangle$ with a second microwave π -pulse as it flies through the second microwave transmission line region. Any population in the states $|1, 1^-, \pm 1\rangle$ remains shelved after the second π -pulse because the microwave field is polarised along x , so it is important to stop the $|1, 1^-, 0\rangle$ state rotating about the x or y axis and thus gaining some amplitude in these states. To this end, we suppress stray magnetic fields

using a probe inner shield shown in Fig. 5.1, and two outer shields which will be elongated versions of the shields shown in Fig. 2.7 (b). In the main experimental chamber, which has approximately the same level of shielding, we are able to reduce the ambient fields to below 10 nT. If we are able to achieve a similar level of control of the fields in the new chamber, then the rotation of the $|1, 1^-, 0\rangle$ spin direction due to magnetic fields will be less than 2×10^{-2} rad and the microwave transition back to $|0, 0\rangle$ can be very efficient.

(6.4) *Detect $|0, 0\rangle$ population using cycling detection*

Now we detect the population in $|0, 0\rangle$ as it passes through the second set of probe beams. The frequencies used are the same as in step (6.2). The signal in this detector, labelled P_2 is given by

$$S^{P_2}(E, B; t) = \mathcal{A}'(t) \cos^2(\phi_B + \phi_E) + \mathcal{G}'(t). \quad (5.3)$$

5.3.2 Extracting a signal proportional to the *eEDM* phase in the new scheme

As well as increasing the signal, the improvements described in the previous section will change how the data is analysed at the end of the experiment. The pump PMT and optics have been removed, so there is no normalisation signal, but it is still possible to reject noise associated with shot-to-shot fluctuations of the molecular beam intensity. To do this we construct the following composite signal out of the signals from the new detectors

$$S^A(t) = \frac{S^{P_1}(t) - S^{P_2}(t)}{S^{P_1}(t) + S^{P_2}(t)}, \quad (5.4)$$

which cancels out the molecular beam fluctuations provided $\mathcal{G}', \mathcal{G} \ll \mathcal{A}$ and $\mathcal{A} \simeq \mathcal{A}$.

We can then use $S^A(t)$ directly to calculate the value of the eEDM

$$d_e = \frac{\hbar}{2\tau\eta E_{\text{eff}}} \{E \cdot B\}_A + \text{small correction terms}. \quad (5.5)$$

5.4 Rough calculations of the increase in signal

Having described the proposed improvements to the experiment, we now make some crude calculations of the increase in signal that we might expect. For the pump and probe regions in turn, we first present simple arguments for the maximum possible increase in signal, then get a rough idea of how the signal increase depends on the powers and durations of the applied fields by applying a simplified rate equation model. We then compute what intensity laser, rf and microwave fields we will need. In later chapters we repeat this process using a full quantum mechanical treatment, but a very simple model is useful to see if the proposal seems plausible, and to validate the more complicated treatment.

5.4.1 New pumping scheme

Theoretical maximum

The increase in $|0, 0\rangle$ population from the new pumping scheme depends on collecting molecules from the states $X^2\Sigma^+ (N = 0, F = 1)$, $(N = 1, F = 2, 1^-, 1^+, 0)$ and $(N = 2, F = 2^-, 2^+, 1)$ into $|0, 0\rangle$. Ideally each YbF molecule that starts in one of these states should be excited to $A^2\Pi_{1/2}$. Once in the excited state it would decay to $|0, 0\rangle$, or back to one of these states, or to $X^2\Sigma^+ (v > 0)$. The maximum possible increase should be when no population remained in those states after pumping. The fraction of the excited population that ends up in $|0, 0\rangle$ is then

$$\frac{\sum_{F', m'_F} P(|F', m'_F\rangle \rightsquigarrow |0, 0\rangle)}{\sum_{F', m'_F} \left[P(|F', m'_F\rangle \rightsquigarrow |0, 0\rangle) + P(|F', m'_F\rangle \rightsquigarrow X^2\Sigma^+ (v > 0)) \right]} \simeq 0.69, \quad (5.6)$$

where $P(|F', m_F'\rangle \rightsquigarrow Z)$ the probability of the excited state $|F', m_F'\rangle$ decaying to the state Z and the sums are over the four $m_{F'}$ sub-levels of the excited level. We have evaluated this using the results of Table B.1. We therefore conclude that 69% of molecules that are initially in a pumped level can ideally be transferred to the state $|0, 0\rangle$ using the new scheme, with the remaining 31% being lost to $X^2\Sigma^+(v > 0)$. In the current experiment where only $X^2\Sigma^+(N = 0, F = 1)$ is pumped, we should expect only 29% of the $X^2\Sigma^+(N = 0, F = 1)$ population to be transferred to $|0, 0\rangle$, and that is in good agreement with what we observe.

The new pumping scheme not only allows the $X^2\Sigma^+(N = 0, F = 1)$ population to be more efficiently pumped to $|0, 0\rangle$, but also brings in molecules from many other levels. Now we consider how far the $|0, 0\rangle$ population can be enhanced by these additional molecules. For a beam of rotational temperature T in the ground vibrational state, the probability of occupying a state of energy $E_{N,F(+/-),m_F} \simeq N(N+1)Bh$ is given by the Boltzmann distribution as

$$P(N|T) = \mathcal{N}(T)e^{-N(N+1)hB/k_B T}, \quad (5.7)$$

where $\mathcal{N}(T)$ is a normalising constant, $B = 7.234$ GHz is the rotational constant and h is Planck's constant. The maximum possible fractional increase in population in the state $|0, 0\rangle$ under the new pumping scheme for a beam of temperature T , compared to the current pumping scheme is therefore

$$f(T) = \frac{P(N = 0|T) + 0.69 [3P(N = 0|T) + 12P(N = 1|T) + 13P(N = 2|T)]}{P(N = 0|T) + 0.29 \times 3P(N = 0|T)}. \quad (5.8)$$

Here the numbers multiplying the probabilities in Eq. (5.8) are just the number of m_F sub-levels being addressed in each of the rotational levels.² The factor $f(T)$ is plotted as a function of T in Fig. 5.5. This factor is rather large for the typical

² Recall that $(N = 2, F = 3)$ cannot be excited to $A^2\Pi_{1/2}(J' = 1/2)$, so the factor multiplying $P(N = 2|T)$ is 13 not 20.

rotational temperatures of our beam (1.5–6 K), giving between 5 and 9 times more signal.

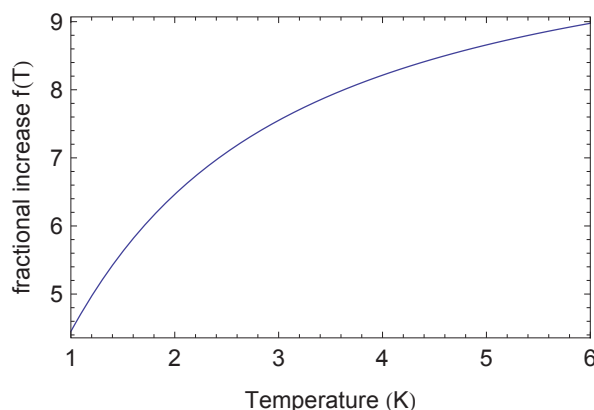


Fig. 5.5: Fractional increase in $|0,0\rangle$ if new pumping scheme is applied to a beam of rotational temperature T .

The average value for the rotational temperature of our beam is around 3 K, which implies we should expect the number of molecules to increase by a factor of up to 7.6 with the new pumping scheme.

Simple Rate Model

The almost 8-fold increase in signal predicted by the previous section only applies in the limit of very long interaction times and high powers. Unfortunately, our molecular beam is flying at 590 m s^{-1} upwards, so taking into account the dimensions of the ports in our vacuum chamber the molecules are never going to have more than around $50 \text{ }\mu\text{s}$ to interact with the light. In this section, we estimate how complete the pumping could be, given this interaction time and a reasonable laser power. In Chapters 6 and 7 we will develop a more rigorous model to handle the difficulties associated with various types of dark states, but for now we adopt a very simple rate equation model to get a feel for whether the scheme stands any practical chance of working.

Since this simple model will be used at various places in the rest of this thesis, we

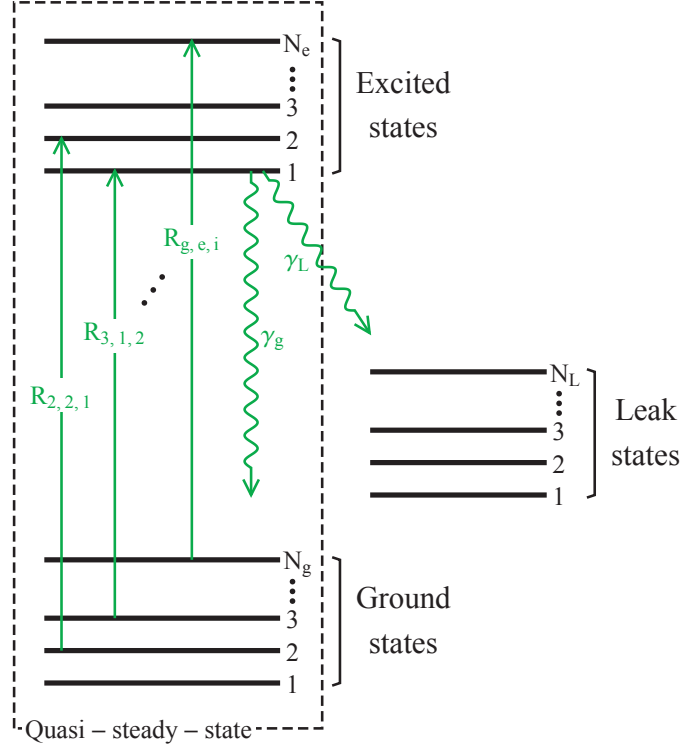


Fig. 5.6: Levels and transitions in the simple rate model.

start by describing the model in a more general way before focusing on the specific details of the new pumping scheme. The situation we have in mind is shown in Fig. 5.6. There are N_g ground states, N_e excited states and N_L ‘leak’ states, those to which population can be lost. We treat the distribution of population among those states as a classical probability distribution, having no quantum coherences. Each excited state decays at a rate γ_g into the collection of ground states, and γ_L into the collection of leak states, with a total decay rate $\gamma_g + \gamma_L = \Gamma$. Also, certain pairs of ground (g) and excited states (e) are linked by real classical driving fields with rates $R_{g,e,i}$. Here i is an index which labels the driving fields, and we call the sum of the rates $R_{\text{tot}} = \sum_i R_{g,e,i}$.

We additionally assume that there are other mechanisms not included in this model which ensure that the populations of the ground states are all equal, and the

populations of the excited states are all equal. These mechanisms could be additional fields which mix the population among the levels (such as the rf and microwave fields of the new pumping scheme), or they could be transverse magnetic fields. They could also be a modulation of the laser polarisation if the ground and excited states were the magnetic sub-levels of some angular momentum state. The major caveat in this model is that we assume that the mixing of all the populations has no effect on the rates $R_{g,e,i}$ at which population is driven to the excited state.

Let n_g be the probability of occupying one of the ground states, and n_e and n_L be the probability of occupying one of the excited and leak states respectively. The rate equations for this system are then

$$N_e \dot{n}_e = -\Gamma N_e n_e + R_{\text{tot}}(n_g - n_e), \quad (5.9)$$

$$N_g \dot{n}_g = \gamma_g N_e n_e - R_{\text{tot}}(n_g - n_e), \quad (5.10)$$

$$N_L \dot{n}_L = \gamma_L N_e n_e, \quad (5.11)$$

together with the normalisation condition

$$1 = N_e n_e + N_g n_g + N_L n_L. \quad (5.12)$$

We can substitute Eq. (5.12) into Eq. (5.9) to get

$$N_e \dot{n}_e = -\Gamma N_e n_e + \frac{R_{\text{tot}}}{N_g} (1 - N_e n_e - N_L n_L - N_g n_e). \quad (5.13)$$

Now we finally assume that $\gamma_g \gg \gamma_L$, so that the system of levels g and e can stay in a quasi-steady state, while their populations gradually leak into the levels L. This is equivalent to assuming that over the time-scales in which it takes the g and e levels to come into equilibrium, n_L remains constant. Solving Eq. 5.13 for this quasi steady state by setting $\dot{n}_e = 0$ and $\dot{n}_L = 0$, we find that the total excited state population

is given by

$$N_e n_e = \frac{N_e}{N_e + N_g} \left(\frac{(1 - N_L n_L)}{\Gamma N_e N_g / (R_{\text{tot}}(N_e + N_g)) + 1} \right). \quad (5.14)$$

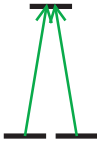
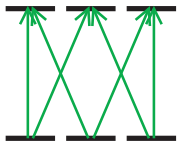
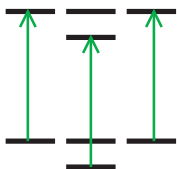
We now insert Eq. (5.14) into Eq. (5.11) to see how n_L varies over longer times. Assuming that there are initially no molecules in any of the leak states, the probability to be in these states grows over time according to

$$N_L n_L(t) = 1 - \exp \left[\frac{-\gamma_L N_e t}{\Gamma N_e N_g / R_{\text{tot}} + N_e + N_g} \right]. \quad (5.15)$$

Equations (5.14) and (5.15) will be frequently used in the second half of this thesis.

It is useful to rewrite the pumping rates $R_{g,e,i}$ in terms of some more convenient quantities. Section II of Ref. [69] gives many useful formulae to do this. In particular, the rate of the transition driven on resonance between an upper and lower state in a system of atomic rate equations is given as $R_{g,e,i} = |\Omega_{g,e,i}|^2 / \Gamma$. The Rabi rates $\Omega_{g,e,i}$ can be related to the transition strengths by $f_{g,e,i} s_i = 2|\Omega_{g,e,i}|^2 / \Gamma^2$, where $s_i = I_i / I_{\text{sat}}$ is the saturation parameter, I_i is the intensity of radiation and for the optical transitions, $I_{\text{sat}} = \pi \hbar c \Gamma / 3 \lambda^3$ is the saturation intensity. The transition strengths can be written as $f_{g,e,i} = \frac{|\langle g | \hat{\mathbf{d}} \cdot \boldsymbol{\epsilon}_i | e \rangle|^2}{\sum_k |\langle k | \hat{\mathbf{d}} | e \rangle|^2}$, where $\hat{\mathbf{d}}$ is the dipole operator, $\boldsymbol{\epsilon}_i$ is the polarisation of vector of the light and the sum over k includes all states to which the upper state e can decay. For the YbF transitions we will consider, these can be found by squaring the projection factors found in Tables B.1 and B.2 as appropriate. Other transition strengths for rf or microwave transitions can also be found by squaring the relevant projection factors given in Appendix B.

The values of R_{tot} for a few frequently encountered cases are shown in Table 5.1. Here it is assumed that the intensities of the driving fields are all equal, and their frequencies are close enough that we use a single saturation intensity I_{sat} for all the transitions.

Case	Example level diagram	R_{tot}	Notes
1) $N_e = 1, N_L = 0$,		$\frac{\Gamma I}{2I_{\text{sat}}}$	This is the situation described in appendix A of Ref. [21]
2) $N_e > 1, N_L = 0$, all possible decays paths from excited levels addressed with equal intensity.		$\frac{N_e \Gamma I}{2I_{\text{sat}}}$	Follows from the definition of $f_{g,e,i}$
3) $N_e > 1, N_L = 0$, Each upper level with quantum number F' linked to a lower level F with radiation of a single polarisation.		$\frac{N_e \Gamma I}{6I_{\text{sat}}}$	Must be 1/3 of 2) by isotropy of space
4) New pumping scheme with linear polarisation on all beams	See Fig. 5.3	$\frac{0.515\Gamma I}{I_{\text{sat}}}$	Calculated with Table B.1
5) New probing scheme with linear polarisation on all beams	See Fig. 5.4	$\frac{0.619\Gamma I}{I_{\text{sat}}}$	Equal to $\frac{4f_{00}\Gamma I}{6I_{\text{sat}}}$, f_{00} is the Franck-Condon factor

Tab. 5.1: Evaluation of the total pumping rate for a selection of relevant cases. The intensity driving each transition is always equal to I

Many situations involving laser cooling or cycling detection with diatomic molecules [70] [21] correspond to case 3) in Table 5.1, where typically the number of ground states addressed by laser beams N_g greatly outnumbers the number of excited states N_e . In these cases, using Table 5.1 and Eq. (5.14), the total excited state population can be written as

$$N_e n_e = \frac{N_e}{N_e + N_g} \left(\frac{N_g 6 I_{\text{sat}}}{(N_e + N_g) I} + 1 \right)^{-1}. \quad (5.16)$$

This equation is very close to the steady state behaviour predicted when the full time dependent rate equations are solved for YbF, given in Ref. [21]. It is helpful to compare this with the familiar two level-system, (case 1) with $N_g = 1$), for which

$$n_e = \frac{1}{2} \left(\frac{I_{\text{sat}}}{I} + 1 \right)^{-1}. \quad (5.17)$$

As $I/I_{\text{sat}} \rightarrow \infty$, the population in both systems is becomes equally distributed over all the levels, so that in the two level system $n_e \rightarrow 1/2$, whereas in the multilevel system $N_e n_e \rightarrow N_e/(N_g + N_e)$. This limits the maximum possible scattering rate to $\Gamma N_e n_e$. Now compare the dependence on I/I_{sat} . Both equations have the same form, but the I/I_{sat} of the 2-level formula is replaced in the multilevel case by

$$\frac{I}{I_{\text{sat}}} \rightarrow \frac{(N_e + N_g)}{2N_g} \frac{I}{3I_{\text{sat}}}. \quad (5.18)$$

The change from two levels to many levels reduces the intensity in two ways. First, through the factor $\frac{(N_e + N_g)}{2N_g}$, and second because of the an extra factor of $1/3$. The first factor has appeared because the number of ground and excited states has increased, and the second appears because the transition is only being driven with one laser polarisation, while the decays can be to any polarisation. Notice that in the limit $N_g \gg N_e$, the right hand side of expression (5.18) becomes $I/(6I_{\text{sat}})$.

The conclusion is clear: in our new pumping and detection schemes, the saturated

scattering rate is going to be small compared with Γ , and we will need high intensity to approach saturation.

Solution of the rate model for new pumping scheme and required laser, microwave and rf intensities

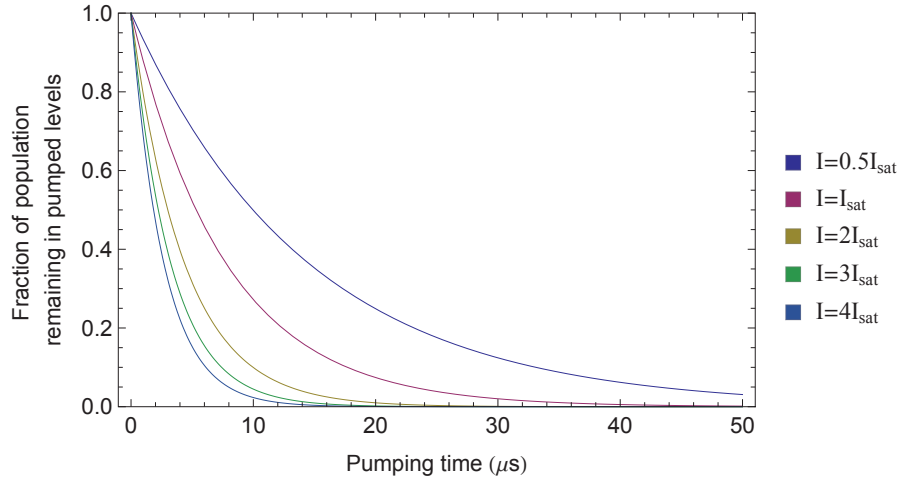


Fig. 5.7: Fraction of population left in the pumped levels as a function of interaction time for a variety of laser intensities. The intensity here is the value of the intensity driving each transition.

Now we apply this simple rate model to the new pumping scheme. We imagine driving resonantly each of the transitions from $X^2\Sigma^+(N=0, F=1)$ and $X^2\Sigma^+(N=2, F=2^+, 1, 2^-)$ up to $A^2\Pi_{1/2}$ using linearly polarised light, as shown in Fig. 5.3. In this case, using the results of Table 5.1 and the parameters $\{\gamma_L = 0.22\Gamma, \Gamma = 2\pi \times 5.7 \text{ MHz}, N_e = 4, N_g = 28\}$, we calculate the evolution for the population shown in Fig. 5.7, for a selection of laser intensities. This indicates that an intensity on each of the laser frequencies of around I_{sat} should be enough to complete the pumping in 50 μs .

The area of the pump laser beam should be 3 cm by 0.4 cm to cover the width of the beam and give a 50 μs interaction time. Using this with the value for the saturation intensity for our transitions, $I_{\text{sat}} = 4.4 \text{ mW cm}^{-2}$, gives a required power

of around 5 mW on each sideband, or 20 mW in total. This should not be too difficult to produce.

At this point in the discussion, we have not yet calculated the field strengths needed for the rf and microwave transitions marked (f)–(i) in Fig. 5.3. As a rough estimate, though, we can expect that the Rabi rates of these fields should be comparable to or larger than the laser Rabi rate. There is no single laser Rabi rate, because the differing oscillator strengths for each transition give different Rabi rates, but if each transition is driven at $I = I_{\text{sat}}$, then the Rabi rates are all similar and lie between $2\pi \times 0.6$ MHz and $2\pi \times 1.8$ MHz. The microwave intensity required to produce this Rabi rate on transition (f) is of the order of a few hundred micro-watts per square centimetre, and is easily accessible with commercial microwave frequency sources and a microwave horn. The rf field will need to be much higher because this drives the magnetic dipole transitions (g), (h), and (i). However, we know that the amplifier driving our 170 MHz transmission line in the present eEDM experiment can produce Rabi rates of up to $2\pi \times 0.25$ MHz. With the resonant rf coils shown in Fig. 5.2 (b)–(c) we achieve a quality factor of around $Q = 200$, which if used in combination with a similar amplifier to our current rf systems should give Rabi rates of up to $2\pi \times 3.5$ MHz.

We will also need to modulate the laser polarisation to avoid dark states, and the ideal rate for that is also yet to be determined. This too optimises at a rate similar to the Rabi frequency, and modulating the laser polarisation at this frequency should not be too challenging using a Pockels cell.

5.4.2 New detection scheme

We now turn our attention to the new detection scheme, which aims to produce a large increase in the numbers of photons scattered by each molecule. After shelving the $F = 0$ population ($\textcircled{6.1}$ in Fig. 5.1), we detect the $F = 1$ molecules by exciting them into $A^2\Pi_{1/2}$ with the probe lasers shown and (a)–(e) in Fig. 5.4. The only states

they can fall into that will not be re-excited are $X^2\Sigma^+(v > 0)$. The probability of such a decay from $A^2\Pi_{1/2}$ is $1 - f_{00}$, where $f_{00} = 0.928$ is the branching ratio to the $v = 0$ [53]. Therefore, the average number of photons that each molecule will scatter if the interaction time is long enough and the powers are high enough is

$$\langle N_{\text{photons}} \rangle = \frac{1}{1 - f_{00}} = 13.9 \text{ photons.} \quad (5.19)$$

The same analysis with the current detection schemes shows a yield of only 1.3 photons, so there is potentially an 11-fold increase in signal at the first detector((6.2) in Fig. 5.1). The net detection efficiency of our collection optics is 0.6% (including the quantum efficiency of the PMT), so the probability of detecting a given molecule will be 5%. This means that the shot noise will still be dominated by the number of photons counted, rather than the number of molecules that make it through the experiment. The shelved molecules are then recovered in section (6.3) in Fig. 5.1 and detected in section (6.4) in Fig. 5.1. If the shelving and recovery work perfectly, then taking both detectors together we could expect a 22-fold increase in signal compared with the present detection scheme.

5.4.3 Rate equation calculations

In the previous section we found that the average molecule only scatters 13.9 photons when there is an unlimited interaction time. Now we consider how many photons we can practically scatter in a limited interaction time.

The average number of photons scattered is just $\langle N_{\text{photons}} \rangle \times$ fraction pumped to $X^2\Sigma^+(v > 0)$, and that fraction can be approximately calculated with the help of Eq. (5.15). The relevant constants are $\{\gamma_L = 0.07\text{T}, N_e = 4, N_g = 17\}$. The results for various laser intensities are shown in Fig. 5.8. To ensure that the photons scattered by the molecules are successfully imaged onto the PMT detectors, we will need to restrict the size of the probe laser beams to be around 15 mm in length, and 16 mm in width. This will provide an interaction time of 25 μs for the detection to

take place. From Fig. 5.8, we can see that with $I = I_{\text{sat}}$ we scatter 12 photons in 25 μs , around 86% of the maximum possible. This requires about 10 mW on each sideband, or 50 mW of total laser power in each detection region.

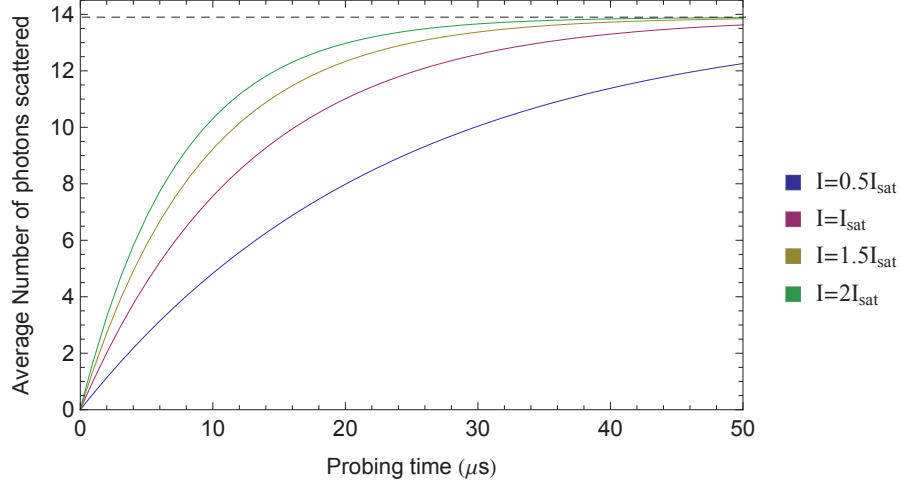


Fig. 5.8: Number of photons scattered during the improved detection scheme predicted by the simple rate equation model.

5.4.4 Microwave π -pulse efficiency

Another important consideration is the efficiency of the microwave pulse in shelving and unshelving the $F = 0$ population. This is influenced by two main factors: the first is the velocity spread of the molecules, the second the homogeneity of the electric field.

The spread in velocities leads to the faster molecules spending less time traversing the microwave field, and so they receive a little less than a π -pulse, while slower molecules receive a little more than a π -pulse. The probability of Rabi flopping from one state to another after time τ is $\sin^2(\Omega\tau/2)$ [71, p.128]. For our typical timing gates, we sample molecules with velocities between 568 and 612 m s^{-1} . This means that the product $\Omega\tau/2$ varies by $\pm 3.7\%$ either side of $\pi/2$. However, as \sin^2 is quadratic around $\pi/2$, the population transfer only varies as the square of this

spread, in other words by $\pm 0.5\%$. Averaging over the velocity distribution leads to a maximum π -pulse efficiency more than 99%.

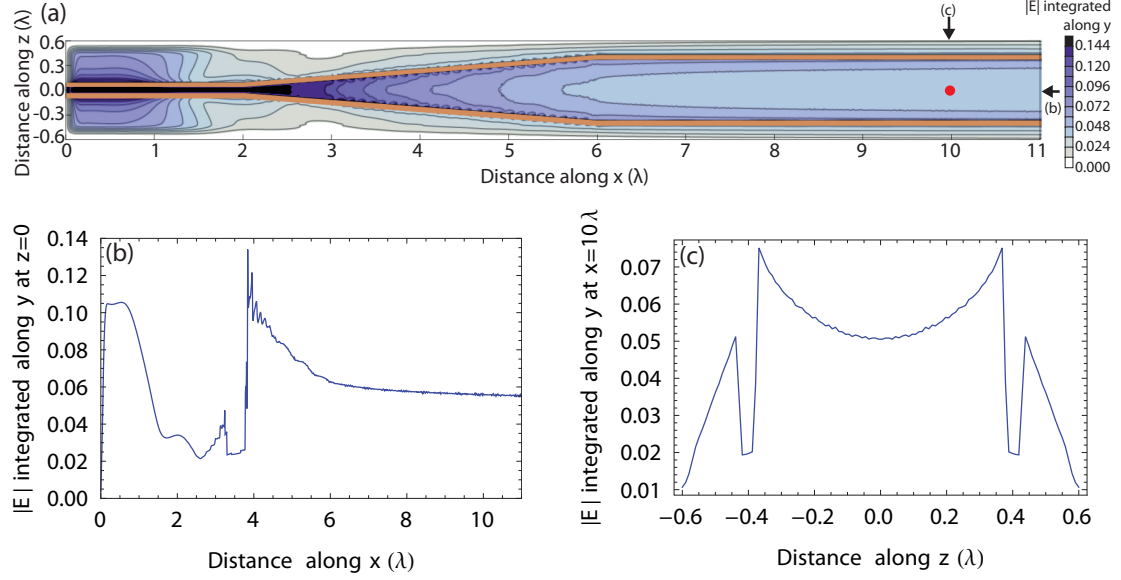


Fig. 5.9: MEEP Simulations of the microwave transmission line. (a) shows absolute value of the microwave electric field, integrated between $z = -\infty$ and $z = \infty$, which the molecules would experience as they fly through the transmission line, as a function of the x and z . The distances are plotted in terms of the microwave wavelength $\lambda = 20.7$ mm. The centreline of the molecular beam will be at the red dot. (b) and (c) are two slices through graph (a) at $z=0$ and $x = 10\lambda$ respectively.

The efficiency of the π -pulse will more critically be limited by variations in the microwave electric field over the waveguide. The flared parallel plate microwave transmission line shown in Fig. 5.2 (d)–(e) was chosen because computer simulations with *MEEP*, a finite-difference time-domain simulator, indicated that the microwave field homogeneity in the x - z plane (transverse to the molecular beam) should be good with this arrangement. That is because the TEM waveguide mode launched at the feedthrough is maintained as the waveguide is flared up, despite the fact that the parallel plates support higher modes. The design is also supposed to avoid unwanted lossy modes that reflect off the edges of the waveguide [72]. The results of the MEEP simulations are shown in Figs. 5.9 (a)–(c). In Fig. 5.9 (a), the integral of the absolute value of the microwave electric field $|E|$ along a line from $z = -\infty$ to $z = \infty$ is plotted

as a function of the x - y position of the molecules in the waveguide. Fig. 5.9 (b) shows a slice through the graph along x at $z = 0$, and (c) shows a different transverse slice along z at $x = 10\lambda$, where $\lambda = 20.7$ mm is the microwave wavelength. The centre of the molecular packet will be at $x = 0$, $z = 10\lambda$. It will be important to terminate the line correctly, or standing waves will affect the homogeneity. We plan to use a tapered termination wedge made from flaked graphite bonded with vacuum compatible resin, since this has good absorption properties at our microwave frequencies [73]. If the standing waves can be suppressed, then most of the molecules can receive almost a perfect π -pulse, as shown in Fig. 5.10. Averaging over the whole region that the molecule occupy (± 15 mm either side of the centre in x , ± 8 mm either side of the centre in z), the total π -pulse efficiency should be around 97%.

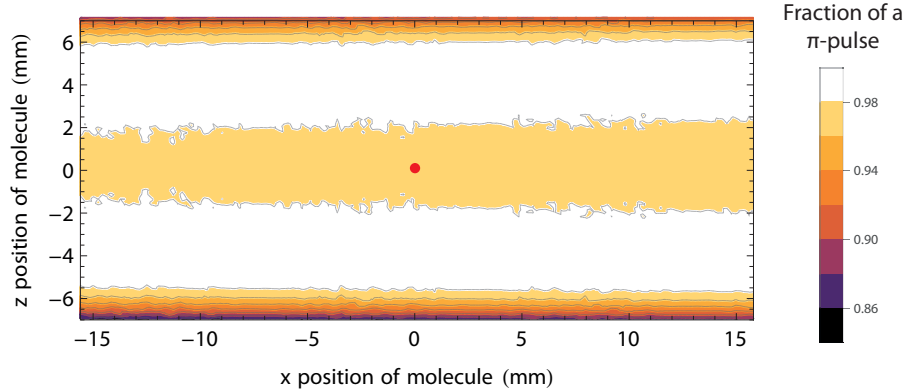


Fig. 5.10: Fraction of a π -pulse experienced by molecules travelling through the microwave transmission line. The overall amplitude of the microwave field has been adjusted to maximise the average efficiency of the π -pulse. The red dot shows the centre of the molecular beam.

5.5 Conclusion and overview of the next half of the thesis

In conclusion, it seems reasonable on the basis of these relatively simple calculations that we can realise a 9-fold increase in the eEDM signal using the new pumping scheme and a further 20-fold increase in signal from the new detection scheme.

In the next two chapters, we deal more fully with the proposed improvements to the experiment. This begins in Chapter 6 where we lay out the optical Bloch equations (OBEs) for the system. Then, in Chapter 7, we use these equations to calculate the true pumping times for the new detection and pumping regions.

6. DERIVATION OF THE OPTICAL BLOCH EQUATIONS FOR THE EVOLUTION OF YbF IN OPTICAL, MICROWAVE AND RF FIELDS

6.1 Overview

This chapter lays out the theory necessary to model the optical, microwave and radio-frequency transitions between the $X^2\Sigma^+(v=0, N=0, 1, 2)$, $A^2\Pi_{1/2}(\mathcal{P}' = \pm 1)$ and $X^2\Sigma^+(v > 0)$ states. Transitions between these states form the basis of the new pumping and detection schemes described in the previous chapter. By solving the optical Bloch equations, we are able to predict how any initial collection of YbF molecules will evolve under the applied fields and calculate important properties like the number of photons scattered per molecule.

6.2 Equation of motion

The evolution of a YbF molecule can be modelled by including a phenomenological relaxation term r in the Liouville-von Neumann equation

$$\dot{\hat{\rho}}^{(S)} = \frac{1}{i\hbar} [\hat{H}, \hat{\rho}^{(S)}] + r(\hat{\rho}^{(S)}) . \quad (6.1)$$

Here, $\hat{\rho}^{(S)}$ is the density operator for the molecular system written in the Schrödinger picture, \hat{H} is the Hamiltonian of the system and the operator r governs the incoherent evolution of the density matrix operator because of spontaneous emission from the electronically excited states. These equations are usually called the optical Bloch

equations (OBEs).

We will always evaluate the matrix elements of the density operator using a basis which is the set of molecular eigenstates of the internal Hamiltonian \hat{H}_0 , which we label $|i\rangle, |j\rangle$ and so on

$$|i\rangle \langle i| \hat{\rho}^{(S)}(t) |j\rangle \langle j| = \rho_{ij} |i\rangle \langle j|. \quad (6.2)$$

The diagonal entries in the density matrix ρ_{ii} are called the *populations*, and they give the probability of finding the molecule in that state $|i\rangle$. The off-diagonal elements ρ_{ij} , $i \neq j$ are called *coherences*: they represent some element of superposition between the states i and j .

Our approach will be to start with the first term in Eq. 6.1, which captures the coherent interactions of the system with the applied field. We then use the results of a full QED calculation [74] of the interaction between an atom and a light field to give the form of r .

6.3 Coherent interaction terms

We start by explicitly writing the Hamiltonian for the system

$$\hat{H} = \hat{H}_0 + \hat{H}_{\text{int}}, \quad (6.3)$$

here \hat{H}_0 is the internal Hamiltonian of the molecule, while \hat{H}_{int} describes the interactions of the molecules with laser, rf and microwave fields

$$\hat{H}_{\text{int}} = \hat{H}_{\text{laser}} + \hat{H}_{\text{microwave}} + \hat{H}_{\text{rf}}. \quad (6.4)$$

Fig. 2.4 summarises all the transitions that we will be considering. For a given simulation where there are a number of fields, labelled f , with frequencies ω_f , the

matrix elements of \hat{H} in terms of the set of molecular eigenstates of the field-free Hamiltonian \hat{H}_0 are

$$\left(\hat{H}_0\right)_{ij} = \hbar\omega_i\delta_{ij}, \quad (6.5)$$

$$\left(\hat{H}_{\text{Laser}} + \hat{H}_{\text{Microwave}}\right)_{ij} = \sum_{f \in \mathcal{F}} \langle i | - \sum_p \hat{\mathbf{d}} \cdot \boldsymbol{\epsilon}_p E_p^f \cos \omega_f t | j \rangle, \quad (6.6)$$

$$\left(\hat{H}_{\text{RF}}\right)_{ij} = \sum_{f \in \mathcal{F}} \langle i | - \sum_p \hat{\boldsymbol{\mu}} \cdot \boldsymbol{\epsilon}_p B_p^f \cos \omega_f t | j \rangle. \quad (6.7)$$

Here $\hat{\mathbf{d}} = -e\hat{\mathbf{r}}$ is the electric dipole operator and $\hat{\boldsymbol{\mu}} = -\mu_B (g_s \hat{\mathbf{S}} + g_l \hat{\mathbf{L}})$ is the magnetic dipole operator, neglecting the small contributions from nuclear spin and rotation and taking g_s as the absolute value of the electron g factor $g_e \simeq -2$. E_p^f (B_p^f) are the complex electric(magnetic) amplitudes of each component of the field labelled f , written in terms of the spherical basis unit vectors $\boldsymbol{\epsilon}_p$. In terms of the Cartesian unit vectors \mathbf{e}_x , \mathbf{e}_y and \mathbf{e}_z these are written as $\boldsymbol{\epsilon}_0 = \mathbf{e}_z$, $\boldsymbol{\epsilon}_{\pm 1} = \mp(\mathbf{e}_x \pm i\mathbf{e}_y)$. \mathcal{F} is the set of all applied oscillating fields being considered in a given simulation.

To keep the following section from becoming too cluttered, we rewrite the matrix elements in the following form

$$M_{ij}^f = \sum_p \frac{1}{2\hbar} \langle i | \hat{\mathbf{m}} \cdot \boldsymbol{\epsilon}_p A_p^f | j \rangle, \quad (6.8)$$

where if i and j are different electronic or rotational levels $\hat{\mathbf{m}} = \hat{\mathbf{d}}$ and $A_p^f = E_p^f$, and if i and j are in the same rotational level of the ground electronic level, then $\hat{\mathbf{m}} = \hat{\boldsymbol{\mu}}$ and $A_p^f = B_p^f$. An explicit evaluation of the M_{ij}^f for all relevant states is carried out in Appendix B.

Substituting Eq. (6.8) into (6.1) we find that the density matrix elements evolve according to Eq. 6.9.

$$\dot{\rho}_{ij}^{(S)} = -i(\omega_i - \omega_j) \rho_{ij}^{(S)} + \sum_{f,k} \left(iM_{ik}^f \rho_{kj}^{(S)} - \rho_{ik}^{(S)} iM_{kj}^f \right) (e^{i\omega_f t} + e^{-i\omega_f t}) + r_{ij}. \quad (6.9)$$

Now we want to make a substitution which will remove the first term on the left hand

side of Eq. (6.9). The replacement $\rho_{ij}^{(S)} = e^{-i(\omega_i - \omega_j)t} \rho_{ij}$, which transforms the density matrix operator into the interaction picture, achieves this. After some rearrangement and using $\omega_{ij} = \omega_j - \omega_i$ and $\Delta_{ij}^f = \omega_{ij} - \omega_f$ Eq. (6.9) can be rewritten

$$\begin{aligned} \dot{\rho}_{ij} = \sum_{f,k} \left\{ iM_{ik}^f \rho_{kj} \left(e^{-i\Delta_{ik}^f t} + e^{-i(2\omega_f + \Delta_{ik}^f)t} \right) - \rho_{ik} \left(e^{-i\Delta_{kj}^f t} + e^{-i(2\omega_f + \Delta_{kj}^f)t} \right) iM_{kj}^f \right\} \\ + e^{-i\omega_{ij}t} r_{ij}. \end{aligned} \quad (6.10)$$

Next, we discard a great many rapidly oscillating terms in Eq. (6.10). These include terms where the driving field is very far detuned from resonance, and also terms of the form $e^{-i(2\omega_f - \Delta_{ij}^f)t}$, provided of course that $2\omega_f - \Delta_{ij}^f$ is not close to resonance with any other transitions (as is the case for all the fields considered in this thesis). The effect of this “rotating wave” approximation (RWA) is to consider only the coarse-grained evolution of the density matrix elements in Eq. (6.10). The time interval $\Delta\tau$ over which the equations of motion are “smoothed” is set by the most rapidly oscillating terms retained in Eq. (6.10), which is now rewritten as

$$\dot{\rho}_{ij} = \sum_{f,k} iM_{ik}^f \rho_{kj} e^{-i\Delta_{ik}^f t} - \rho_{ik} e^{-i\Delta_{kj}^f t} iM_{kj}^f + e^{-i\omega_{ij}t} r_{ij}. \quad (6.11)$$

We typically retain terms where the detunings Δ_{ij}^f are up to around 5 times the natural line width of the excited state, $\Gamma = 2\pi \times 5.7$ MHz. For the simulation durations (up to 100 μ s) and Rabi rates (up to $2\pi \times 10$ MHz) we consider in our simulations, retaining higher frequency terms has a negligible effect on the final populations.

6.4 Relaxation terms

The relaxation terms we use for our system are derived in Ref. [74], which treats the interaction between an atomic or molecular system with multiple excited and ground states and a quantised light field using quantum electro-dynamics. Their

approach builds on the work of Ackerhalt *et al.* [75] [76] in two level systems. It allows both the (coherent) excitation of the atomic system by an applied field, and its relaxation, to be derived at the same time from the interaction between the electromagnetic vector potential and the atom or molecule. In our case, we only want to take those terms which account for the relaxation of the system. We add these terms phenomenologically to the coherent evolution of the system we derived in the previous section.

It is useful at this point to make a distinction between electronically excited and ground states, since the expressions for the relaxation of coherences between pairs of electronically excited states, pairs of electronic ground states and coherences between ground excited states are different in these different cases. We use the indices e and e' for electronically excited states and g and g' for ground states.

Taking the relaxation terms from equations (18) (a)–(c) and also using the expression for the total decay rate of an excited state (16c), all in Ref. [74], we find, in agreement with Ref. [77], that the elements of r are given by

$$r_{eg} = -\frac{\omega_0^3}{6\pi\epsilon_0\hbar c^3} \sum_{e',g',p} \langle e | \hat{\mathbf{d}} \cdot \boldsymbol{\epsilon}_p | g' \rangle \langle g' | \hat{\mathbf{d}} \cdot \boldsymbol{\epsilon}_p | e' \rangle \rho_{e'g}^{(S)}, \quad (6.12)$$

$$r_{ee'} = -\frac{\omega_0^3}{6\pi\epsilon_0\hbar c^3} \sum_{e'',g,p} \left(\langle e | \hat{\mathbf{d}} \cdot \boldsymbol{\epsilon}_p | g \rangle \langle g | \hat{\mathbf{d}} \cdot \boldsymbol{\epsilon}_p | e'' \rangle \rho_{e''e'}^{(S)} + \langle e'' | \hat{\mathbf{d}} \cdot \boldsymbol{\epsilon}_p | g \rangle \langle g | \hat{\mathbf{d}} \cdot \boldsymbol{\epsilon}_p | e' \rangle \rho_{e'e''}^{(S)} \right), \quad (6.13)$$

$$r_{gg'} = \frac{\omega_0^3}{3\pi\epsilon_0\hbar c^3} \sum_{e,e',p} \langle g | \hat{\mathbf{d}} \cdot \boldsymbol{\epsilon}_p | e \rangle \langle e' | \hat{\mathbf{d}} \cdot \boldsymbol{\epsilon}_p | g' \rangle \rho_{ee'}^{(S)}. \quad (6.14)$$

In writing the relaxation terms in this form it is assumed that the energy spacing between pairs of excited states or ground states is much much smaller than the energy difference between ground and excited states: $\omega_{ee'} \ll \omega_{eg}$ and $\omega_{gg'} \ll \omega_{eg}$. We have approximated the various optical frequencies ω_{eg} by their average ω_0 . The error in assuming this is only one part in 1000.

Sometimes, it is convenient to rewrite the pre-factor in equations (6.12)-(6.14) in terms of the excited state decay rate Γ using the following formula

$$\Gamma = \frac{\omega_0^3}{3\pi\epsilon_0\hbar c^3} \sum_{g,p} |\langle e | \hat{\mathbf{d}} \cdot \boldsymbol{\epsilon}_p | g \rangle|^2. \quad (6.15)$$

where the sum in p is over the three polarisations, and in g is over all electronic ground states. The quantity $\sum_{g,p} |\langle e | \hat{\mathbf{d}} \cdot \boldsymbol{\epsilon}_p | g \rangle|^2 = \mu^2$ is square of the transition dipole moment μ .

To reassure ourselves that these terms are correct, we can take a step back from the complicated YbF system and check that the terms they produce reduce to the expected form in a pair of simpler cases.

6.4.1 Relaxation terms in a two level system

Firstly, consider a two level system with only one ground and one excited state. Then, using Eq. (6.15) the four elements of r_{ij} are the familiar terms [71]:

$$r_{eg} = -\frac{\Gamma}{2} \rho_{eg}^{(S)}, \quad (6.16)$$

$$r_{ge} = -\frac{\Gamma}{2} \rho_{ge}^{(S)}, \quad (6.17)$$

$$r_{ee} = -\Gamma \rho_{ee}^{(S)}, \quad (6.18)$$

$$r_{gg} = \Gamma \rho_{ee}^{(S)}. \quad (6.19)$$

6.4.2 Relaxation terms in a $J' = 1 \rightarrow J = 1$ system

Now let us consider the slightly more complicated case with angular momentum $J' = 1$ in the excited state and $J = 1$ in the ground state, each having three projections $m_J = +1, 0, 1$. There are 6 states in total and 36 relaxation matrix elements. The requirement that the density matrix remain Hermitian when it evolves under the relaxation matrix means that the matrix must also be Hermitian ($r_{ij} =$

r_{ji}^*), which limits the unique entries to 21. We use the notation $\rho_{e/g m_F e'/g' m'_F}^{(S)} = \langle e/g, m_F | \rho^{(S)} | e/g, m_F \rangle$ and $r_{e/g m_F e'/g' m'_F} = \langle e/g, m_F | r | e/g, m_F \rangle$, so for instance the term in the relaxation matrix for the coherence between the excited $m_F = -1$ level and the ground $m_F = 0$ level is written as r_{e-1g0} . Where the result applies for all excited or ground m_F elements we drop the m_F subscripts and return to the previous subscript notation, so r_{eg} is the relaxation rate of the coherence between any excited state e and any ground state g .

Using the Wigner-Eckart theorem we can work out the matrix elements to be substituted into equations (6.12)-(6.14)

$$\langle e, m_F | \hat{\mathbf{d}} \cdot \boldsymbol{\epsilon}_p | g, m'_F \rangle = \mu(-1)^{1-m'_F} \begin{pmatrix} 1 & 1 & 1 \\ -m'_F & p & m_F \end{pmatrix} \sqrt{3}. \quad (6.20)$$

Pleasingly, the results of the simpler two level system carry over into this more complicated 6 level system. The excited-ground state coherence decay terms r_{eg} , and on diagonal excited-excited decay terms r_{ee} decay in exactly the same way as the two level case, obeying equations (6.16)–(6.18). The off-diagonal excited-excited state coherences also decay at a rate of Γ

$$r_{ee'} = -\Gamma \rho_{ee'}^{(S)}. \quad (6.21)$$

Also, we find that the ground state populations grow as follows:

$$r_{g-1g-1} = \frac{\Gamma}{2} \left(\rho_{e-1e-1}^{(S)} + \rho_{e0e0}^{(S)} \right), \quad (6.22)$$

$$r_{g0g0} = \frac{\Gamma}{2} \left(\rho_{e-1e-1}^{(S)} + \rho_{e1e1}^{(S)} \right), \quad (6.23)$$

$$r_{g1g1} = \frac{\Gamma}{2} \left(\rho_{e0e0}^{(S)} + \rho_{e1e1}^{(S)} \right). \quad (6.24)$$

Each excited state population, which decays at a rate Γ , equally decays into two ground states, filling each of these at a rate $\Gamma/2$.

The final terms that need to be considered are those which modify the ground state coherences, the $r_{gg'}$ terms. It might seem surprising that spontaneous emission can change the value of these terms, but consider the following example: suppose we start with a single atom in an excited pure state $|\psi\rangle = \frac{1}{\sqrt{2}}(|e, 1\rangle + |e, 0\rangle) \otimes |0 \text{ photons}\rangle$ of the atomic system, and the ground state of the vacuum, the states shown with slightly faded blue circles in Fig. 6.1.

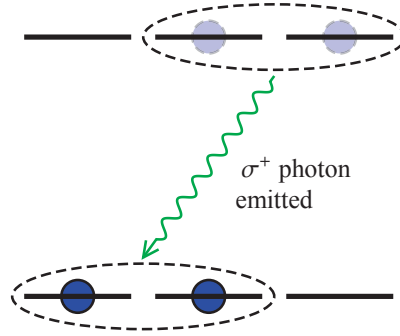


Fig. 6.1: An excited state superposition of an $F = 1$ upper level decaying into a ground state superposition via the emission of a single σ^+ photon

We know that if we leave this state for long enough, it must decay into the ground state by emitting a photon with an energy around the excited-ground state separation, so roughly speaking the state vector must evolve into

$$|\psi\rangle \rightarrow \frac{1}{2} (|g, 1\rangle \otimes |\pi \text{ photon}\rangle + |g, 0\rangle \otimes |\sigma^+ \text{ photon}\rangle) + \frac{1}{2} (|g, 1\rangle \otimes |\sigma^- \text{ photon}\rangle + |g, -1\rangle \otimes |\sigma^+ \text{ photon}\rangle) . \quad (6.25)$$

If we now transform the right hand side of expression (6.25) into the density matrix picture, then take the partial trace over the photonic part of the Hilbert space to recover the density matrix for the atomic part of the system, we find that not only have the ground state populations increased so that the $\rho_{g-1g-1}^{(S)} = \rho_{g0g0}^{(S)} = 0.25$, $\rho_{g1g1}^{(S)} = 0.5$, but so have the ground state coherences $\rho_{g0g-1}^{(S)} = \rho_{g-1g0}^{(S)} = 0.25$. Essen-

tially, the fact that either part of the upper state superposition can decay by emitting a σ^+ photon means that after a decay the state must retain part of its pure character, represented by the amplitude to be in the ground state superposition $|g, 0\rangle + |g, -1\rangle$. An illustration of such a decay is indicated in Fig. 6.1.

Returning to equations (6.12)-(6.14), the growth of the ground state coherences from spontaneous decays from the excited states are given by

$$r_{g-1g0} = \frac{\Gamma}{2} \rho_{e0e1}^{(S)}, \quad (6.26)$$

$$r_{g-1g1} = -\frac{\Gamma}{2} \rho_{e-1e1}^{(S)}, \quad (6.27)$$

$$r_{g0g1} = \frac{\Gamma}{2} \rho_{e-1e01}^{(S)}. \quad (6.28)$$

This form of the relaxation elements can also be found in Ref. [78] and Ref. [79], Appendix A.

We end this subsection on the $J' = 1 \rightarrow J = 1$ system with a brief note about transforming r_{ij} into the interaction picture. We need to use the transformed term $e^{-i\omega_{ij}t}r_{ij}$ at the end of Eq. (6.10). Conveniently, for any system in which the excited and ground states are just the m_F projections for a single J level, all of the exponentials cancel and we recover a set of relaxation terms in the interaction picture which are identical in form to the Schrödinger picture terms, but with every matrix element $\rho_{ij}^{(S)}$ replaced by its interaction picture equivalent ρ_{ij} . As we shall see, for more complicated systems like YbF where there the upper and lower electronic levels are manifolds with several values of J this simple interchangeability between the Schrödinger and Interaction picture matrix elements no longer holds.

6.4.3 Relaxation terms in the YbF System

Having gone some way in reassuring ourselves that the relaxation terms for decays between collections of ground and excited states reproduce the familiar terms in

two simple cases, we now proceed to evaluate them for the more complicated YbF system. In doing so, we can reuse much of the calculation performed in Appendix B to find the matrix elements M_{ij}^f in the case where f is an electric field. What we want is not r_{ij} but $\tilde{r}_{ij} = e^{-i\omega_{ij}t}r_{ij}$ where once again each Schrödinger picture density matrix element in r_{ij} has been transformed into the interaction picture using the transformation $\rho_{ij}^{(S)} = e^{i\omega_{ij}t}\rho_{ij}$. So, if we substitute the matrix elements from Appendix B into equations (6.12) and (6.13) we get the simple expressions

$$\tilde{r}_{eg} = -\frac{\Gamma}{2}\rho_{eg}, \quad (6.29)$$

$$\tilde{r}_{ee'} = -\Gamma\rho_{ee'}, \quad (6.30)$$

whereas Eq. (6.14) becomes

$$\tilde{r}_{gg'} = \frac{\Gamma}{|\mu_{A-X}|^2} \sum_{e,e',p} \langle g | \hat{\mathbf{d}} \cdot \boldsymbol{\epsilon}_p | e \rangle \langle e' | \hat{\mathbf{d}} \cdot \boldsymbol{\epsilon}_p | g' \rangle \rho_{ee'} e^{i(\omega_{ee'} - \omega_{gg'})t}. \quad (6.31)$$

Now Eq. (6.31) indicates that every electronic ground state coherence has the possibility of increasing as a result of excited state decays. This includes not only coherences between the different m_F components of the same level, but also the coherences between states in different hyperfine and/or rotational levels. The growth of coherences between states of significantly different energy should seem surprising given the physical mechanism for the coherence growth terms discussed in section 6.4.2. Conveniently, the exponential term at the end of Eq. (6.31) comes to our rescue. The basic idea is that for a large number of terms, this exponential will oscillate very quickly compared to any other terms in Eq. (6.11). Recall that after applying the rotating wave approximation to get Eq. (6.11), the fastest oscillating exponentials were any detuning terms, and those oscillated at a frequency of order $5 \times \Gamma$. We therefore retain only those terms in Eq. (6.31) which oscillate at a

frequency less than $5 \times \Gamma$. This is a version of the *secular approximation* [78].

The terms retained in Eq. (6.31) are as follows: starting with the sum over pairs of excited states e and e' , this is now restricted to pairs of states which belong to the same parity component of the Ω -doublet. Now turning to the pairs of ground states g and g' , these must be in the same rotational and vibrational state. Also, terms affecting coherences between any of the m_F states in the lower F level and the upper F level(s) in each rotational state are dropped.

Making these restrictions, we can use Eqs. (6.31) and (6.11) together with the results of appendix B to predict the pumping and scattering rates for our YbF system. To solve the equations, we use *Mathematica 9.0*, a computer package which supports the symbolic manipulation of algebraic expressions and the numerical solution of arrays of coupled complex differential equations. Each solution of the coupled differential equation takes between 1–10 seconds to complete, depending on the number of driving fields. In the following chapter we discuss some of these solutions.

7. SOLUTIONS OF THE OPTICAL BLOCH EQUATIONS FOR THE IMPROVED PUMPING AND DETECTION SCHEMES

7.1 Overview

In this chapter we use the optical Bloch equations introduced in Chapter 6 to numerically evaluate the new cycling detection and enhanced pumping schemes shown in Fig. 7.1.

In both the pumping and detection, we want all the population that we address in the ground electronic states to be excited up to the $A^2\Pi_{1/2}$ state and then undergo spontaneous decay, either to pump the molecules into $|0,0\rangle$ in the new pumping scheme, or to scatter photons repeatedly in the new detection scheme. In section 7.2 of this chapter, we explore the ways that this can go wrong as a result of population trapped in $X^2\Sigma^+$. These trapped states are called *dark states* of the system. Looking at a pair of simple example systems, we show how two classes of dark states can be destabilised by modulating the polarisation of the driving fields, and by detuning the driving fields from resonance. We compare the behaviour when this destabilisation is optimised with the prediction of the simple rate equations introduced in section 5.4.1, to see how closely the rate equations are able to model the full quantum mechanical treatment.

Having examined these simple systems, we move on to the full simulation of the new schemes. In section 7.3 we examine how to optimise the detection scheme with respect to the power, detuning and modulation rate of the driving light. We then do the same in section 7.4 for the new pumping scheme. These calculations allow us

to estimate with some confidence the enhancement in signal that the new pumping and detection schemes should provide.

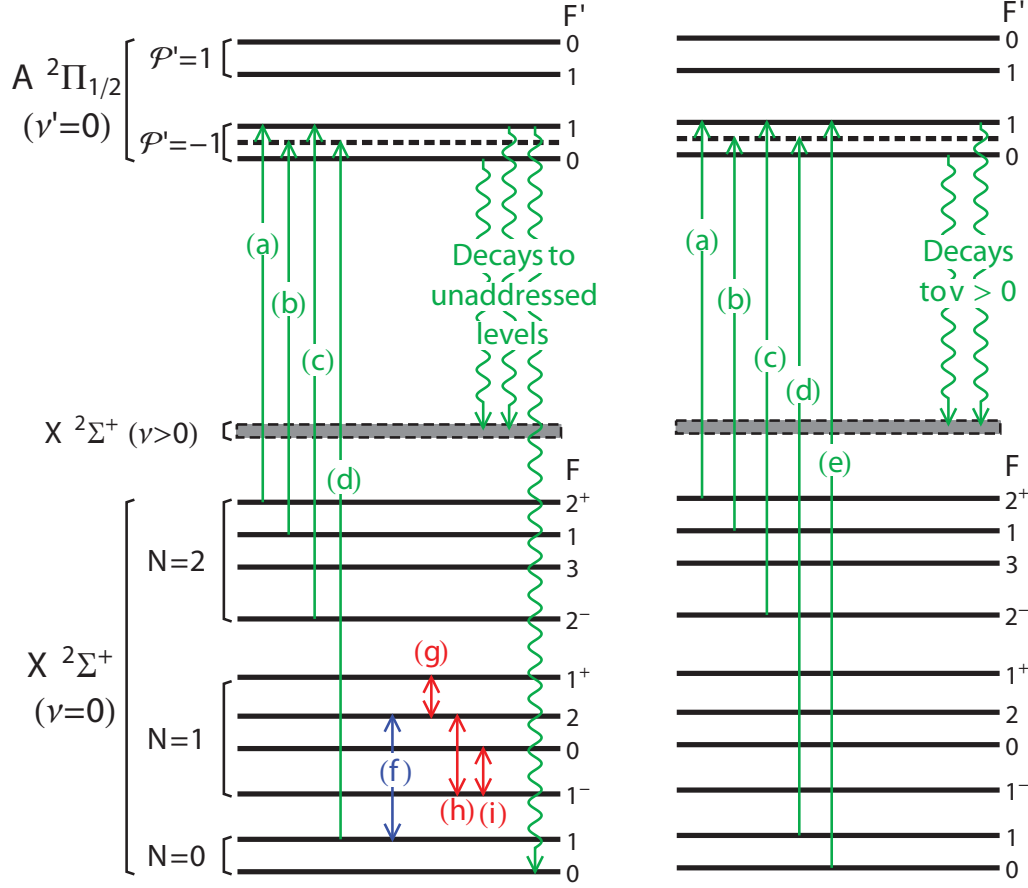


Fig. 7.1: Left: The new pumping scheme. Right: The new probing scheme. Decays to levels addressed by laser beams are omitted.

Our approach expands on work by Berkeland and Boshier [80] and Lindvall *et al* [81] in the destabilisation of dark states in atomic systems and J. Barry [82] in molecular systems in a number of ways. Firstly, we simulate a fully coupled molecular system which has many more levels (22 for the probe scheme and 41 for the pump scheme) than have previously been considered. In the work of J. Barry, only a simplified system is considered. Also, by comparing our results with the rate models throughout the discussion, we ascertain to what extent these much simpler models

can be applied in our case. Finally, in our simulations of the pumping scheme, we examine the interplay of radio-frequency, microwave and laser fields in a way which has not been considered before.

7.2 Dark States

It might seem that a molecule in one of the X-states addressed by laser beams (a)–(e) must surely be excited up to $A^2\Pi_{1/2}$ and undergo spontaneous emission. However, unless we are careful, there are dark states within these levels which stubbornly resist being driven up to $A^2\Pi_{1/2}$.

It is helpful to make a somewhat artificial distinction between two types of dark states: the first, discussed in the next subsection, are *angular momentum dark states* that arise from trying to drive the $(N = 2, F = 2^\pm)$ levels into the $F' = 1$ excited state. The second type are dark states that occur when two or more states are driven to a third state with equally detuned radiation. Since this phenomenon is called Coherent Population Trapping [83], we refer to these dark states as *CPT dark states*. The reason we make this distinction is because two different techniques must be used to destabilise each type of dark state. To understand how dark states of both these types arise and how they can be removed, we leave the YbF system for now and consider in the following two sections some simpler systems.

7.2.1 Angular momentum dark states and their destabilisation

When a level with total angular momentum F is driven up to an excited level with total angular momentum $F' = F - 1$, there are always states in the ground level which are not excited [80]. The specific example relevant to us is an $F = 2$ level being driven up to an $F' = 1$ level, shown in Fig. 7.2. This is the situation we encounter in both the pumping and detection schemes when we try to drive the $(N = 2, F = 2^\pm)$ levels into the $F' = 1$ excited state. When the light is purely

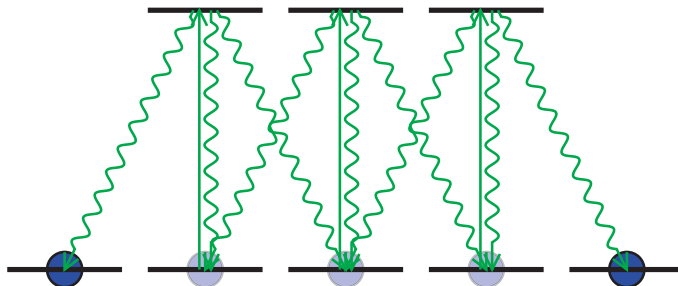


Fig. 7.2: Pumping a $F = 2 \rightarrow F' = 1$ transition in zero magnetic field with linear polarisation causes all the population to build up in the $m_F = \pm 2$ ground states

linearly polarised, it is clear that the $m_F = \pm 2$ components will be left un-pumped, as shown in Fig. 7.2. If the light is σ^+ polarised the two states will be $m_F = 1, 2$ and if the light is σ^- polarised they will be $m_F = -1, -2$. If the light is an arbitrary mixture of linear and σ^+, σ^- then there are still two dark states. These are now superpositions of the ground states such that the transition dipole moment is still orthogonal to the polarisation of the light.

If we apply the lasers shown in either scheme of Fig. 7.1, but do nothing to address these angular momentum dark states, then molecules leak into the dark states at a rate comparable with the Rabi frequency. This compromises the pumping scheme, and it reduces the number of fluorescence photons in the new detection scheme since it dramatically increases the probability of leaking out of the cycling scheme every time the excited state is visited.

There are several ways to solve this problem. The simplest way is to apply a static magnetic field, making the spin precess. This phase shifts the Zeeman components relative to each other, causing the dark states to be remixed into the pumping cycle at a rate determined by the Larmor frequency. The difficulty in our case is that the magnetic field would need to be fairly large, because the $(N = 2, F = 2^-)$ level has a g_F factor of only 0.023 (see Table B.3). The Larmor precession frequency will need to be comparable to the laser Rabi rates - around 1MHz. To achieve this Rabi

rate, we would need a field of 3 mT. This would be required in both the probe and pump region, and would completely dwarf the fields we currently apply (~ 10 nT) in the main eEDM interaction region. It would also make it difficult to drive clean microwave π -pulses in the two microwave transmission-line regions.

Instead, we opt for the next simplest solution: a modulation of the laser polarisation. This is achieved by passing the laser beam through an optically active lithium niobate (LiNbO_3) crystal, where the refractive index for one polarisation is electrically modulated (Pockels effect).

Alternating between σ^+ light, which pumps towards more positive m_F values, and σ^- which pumps back towards negative m_F , will stop the population from building up in the angular momentum dark states. Similarly, we may switch between vertically and horizontally polarised light, when the occupancy of the lower levels will be oscillate between states of low $|m_F|$ and high $|m_F|$.

Simple system being driven with polarisation modulated light

Our practical problem is to find out for a given laser electric field E what choice of parameters optimises the pumping rate out of the $F = 2$ level. Eventually we will answer this question for the full system of levels used in the pumping and detection, but for now we would like to solve the optical Bloch equations for a simpler system to get a feel for the physics. We follow the approach of Berkeland and Boshier [80] and solve the optical Bloch equations for a system with a lower $F = 2$ level and an upper $F' = 1$ level. The 8 sublevels are driven by an electric field of amplitude E , which propagates along z and has x and y components (in the rotating wave approximation) $E \exp[i\Phi_0 g(t, \tau)] \mathbf{e}_x \exp[i\omega_f t]/\sqrt{2}$ and $E \exp[i\phi] \mathbf{e}_y \exp[i\omega_f t]/\sqrt{2}$. The phase shift in the x component is the differential shift imposed by the electro-optic modulator, which varies with period τ between 0 and Φ_0 . The time-dependence is given by $g(t, \tau)$, which oscillates between 0 and 1. The phase shift ϕ in the y component allows us to change the ellipticity of the input field. The equations of

motion for this system are almost identical to those derived in Chapter 6

$$\dot{\rho}_{ij} = \sum_k iM_{ik}\rho_{kj}e^{-i\Delta_{ik}t} - \rho_{ik}e^{-i\Delta_{kj}t}iM_{kj} + r_{ij}, \quad (7.1)$$

where ρ_{ij} are the interaction picture elements of the density matrix, Δ_{ik} is the detuning of the laser field from the transition frequency, and since we have only one field we have dropped the f superscripts throughout. The matrix elements M_{ik} and the relaxation matrix r_{ij} can both be evaluated using equations (B.1) and (6.12)–(6.14) together with the following expression for the dimensionless matrix elements found in those equations

$$\langle 1, m' | \hat{\mathbf{d}} \cdot \boldsymbol{\epsilon}_p | 2, m \rangle = |\boldsymbol{\mu}|(-1)^{1-m'}\sqrt{3} \begin{pmatrix} 1 & 1 & 2 \\ -m' & p & m \end{pmatrix}. \quad (7.2)$$

Numerically solving Eq. (7.1) we find, without modulation, that the steady state has no population in $F' = 1$ because the molecules have pumped into a dark state. By contrast, with modulation the $F' = 1$ population reaches a quasi-steady oscillating state which allows the molecule to continue scattering. An example of this is shown in Fig. 7.3.

In Fig. 7.3, we have taken $\Phi_0 g(t, \tau)$ to be $\pi \sin^2(\pi t/\tau)$, we have set τ equal to the lifetime of the excited states, $1/\Gamma$, and the light field has intensity $2I_{\text{sat}}$. After an initial transient, caused by switching the light on suddenly, the system relaxes into its quasi-steady state with a relaxation time of order ten upper state lifetimes. This means it takes a few scatters to forget the initial condition.

In order to optimise the excited state population, and hence the scattering rate, I have repeated this calculation for a range of modulation depths Φ_0 , and for a range of periods τ , with modulation functions $g(t, \tau)$ that are square, sinusoidal and

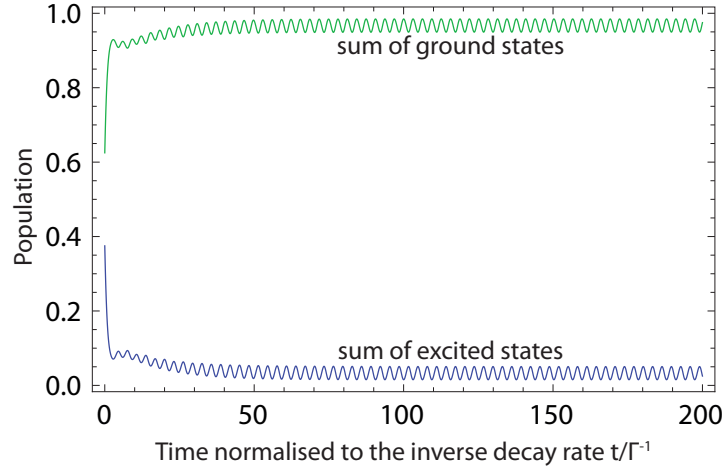


Fig. 7.3: The evolution of the ground and excited state populations calculated using Eq. (7.1). Parameters are $\phi = 0$, $\Phi_0 = \pi$, $g(t, \tau) = \sin^2(\pi t \tau)$, $\tau = 1/\Gamma$ and $I = 2I_{\text{sat}}$, and the population is initially evenly distributed over all levels. We see that the excited state population is sustained by modulating the polarisation.

triangular. We also use a fourth function $\Phi_0 g(t, \tau) = \Phi_0 t / \tau$ which can be pictured as a constant frequency difference between the two components of $\Phi_0 / (2\pi\tau)$. The results are shown in Fig. 7.4, which plots the mean excited state populations after a time equal to several hundred times the inverse natural linewidth. Again we take $I = 2I_{\text{sat}}$ and $\phi = 0$.

Starting with Fig. 7.4 (a) which shows the results for a square modulation, we see that the excited state population is periodic in the modulation depth parameter Φ_0 with period 2π . This is as expected, since jumping between 0 and Φ_0 has to be the same as jumping between 0 and $\Phi_0 + 2\pi$. The optimal modulation depth is π , indicating that switching between $+$ and -45° light achieves the highest scattering rate. Looking now at the dependence on the modulation rate for $\delta = 2\pi/\tau$, we see that the excited state population rises steeply to a maximum at $\delta = 0.27 \times \Gamma$ before slowly tailing off. The behaviour at low rates is straightforward: the molecules all pump into a dark state where they remain until the polarisation flips and hence the mean scattering rate is roughly proportional to the modulation rate δ . A natural way to characterise the pumping rate is $\bar{\Omega} = \Gamma \sqrt{I/(2I_{\text{sat}})}$. In the case of a 2-level

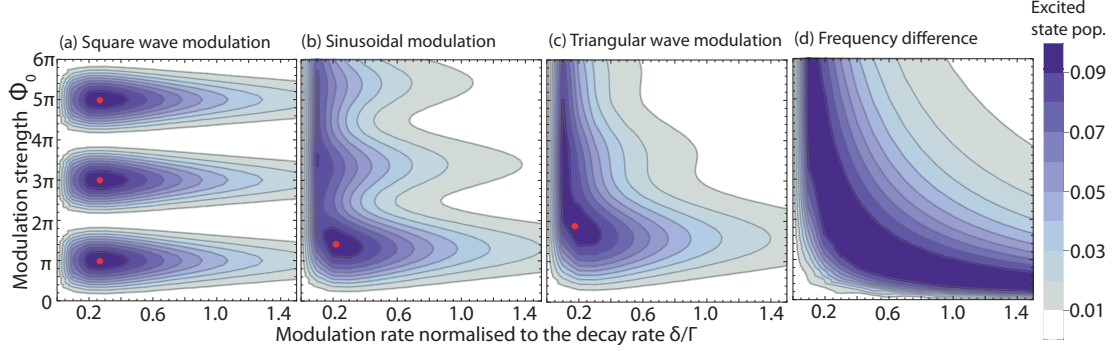


Fig. 7.4: The excited state population as a function of the modulation rate δ and the modulation strength B for a square, sinusoidal and triangular modulation. For the three graphs $\Omega = \Gamma$ and $\phi = 0$. The red dot indicates the choice of parameters which maximises the excited state population for this choice of Ω and $\phi = 0$

system $\bar{\Omega}$ is just the Rabi frequency, which determines how quickly the molecule is excited. In Fig. 7.4 $I = 2I_{\text{sat}}$ hence $\bar{\Omega} = \Gamma$. With many levels, the oscillator strength is shared across several transitions, and several excitations may be required to find a dark state, so the optical pumping rate is correspondingly several times slower than Γ . When the polarisation flips rapidly, the time available for excitation becomes short compared with the inverse of $\bar{\Omega}$. In this regime the depletion of the ground state (or growth in population of the excited state) is quadratic in the interaction time, and the polarisation switching becomes less and less effective with increasing frequency. To maximise the probability of population transfer taking place, therefore, it is important that the time spent at each polarisation state is sufficiently long so that the population transfer can leave the quadratic region.

Now we consider graph (d). Instead of jumping between two fixed phases as in graph (a), the phase in this graph is constantly modulated at a rate Φ_0/τ or $\Phi_0\delta/(2\pi)$. A phase modulation like this could be realised by applying a constant frequency difference equal to $\Phi_0\delta/(2\pi)$ between the two components by using an acousto-optic modulator. Given the symmetry in this phase modulation function between Φ_0 and δ , this graph must be symmetrical if reflected in the line $\Phi_0 = \delta$ and the contours of equal excited state population must be of the form $\Phi_0 = 2\pi a/\delta$.

Graphs (b) and (c) correspond to an intermediate case between the extremes of graphs (a) and (d). Turning first to graph (b), which corresponds to a sinusoidal modulation: this exhibits a residue of the periodicity in Φ_0 seen in graph (a), but also shows some symmetry between Φ_0 and δ seen in graph (d). This is because the sinusoidal modulation has some periods where the polarisation direction is modulated at a constant rate (like graph (d)), and other regions around the turning points of the modulation function g which are more like the static polarisation regions seen in graph (a). This last graph shows similar behaviour to that seen by Berkeland and Boshier [80, Fig. 5] for a sinusoidal polarisation modulation in an $F = 1 \rightarrow F' = 0$ system. For the triangular wave modulation shown in graph (c), the phase is always being modulated back and forth at a rate $2\Phi_0\delta/2\pi$, i.e $2\Phi_0/\tau$. We notice that this graph has largely lost its periodicity in the modulation strength Φ_0 , and the region of high excited state population has become increasingly boomerang shaped, corresponding more closely to the situation encountered in graph (d).

The corresponding graphs for circularly polarised input light ($\phi = \pi/2$) are almost identical with only slight variations in the location of the absolute maxima for the various modulation functions.

Dependence of the optimum modulation rate and strength on the Rabi rate

Fixing $\phi = 0$ and varying $\bar{\Omega}$, we now investigate the changes in the values of Φ_0 and δ which maximise the excited state population. At each value of $\bar{\Omega}$, the excited state population was maximised numerically with respect to Φ_0 and δ . The top row of Fig. 7.5 shows the variation with Rabi frequency of the optimised modulation rate. We see that for $\bar{\Omega} \gg \Gamma$, the optimum values of δ converge on a fixed fraction of $\bar{\Omega}$, which for this value of ϕ is ≈ 0.36 for the square modulation, $\approx 1/3$ for the sinusoidal modulation and ≈ 0.17 for the triangular modulation. As $\bar{\Omega}$ becomes comparable to or smaller than Γ , the optimum values diverge slightly from the large $\bar{\Omega}$ limiting fractions, tending to higher fractions of $\bar{\Omega}$. The modulation strength Φ_0 (bottom

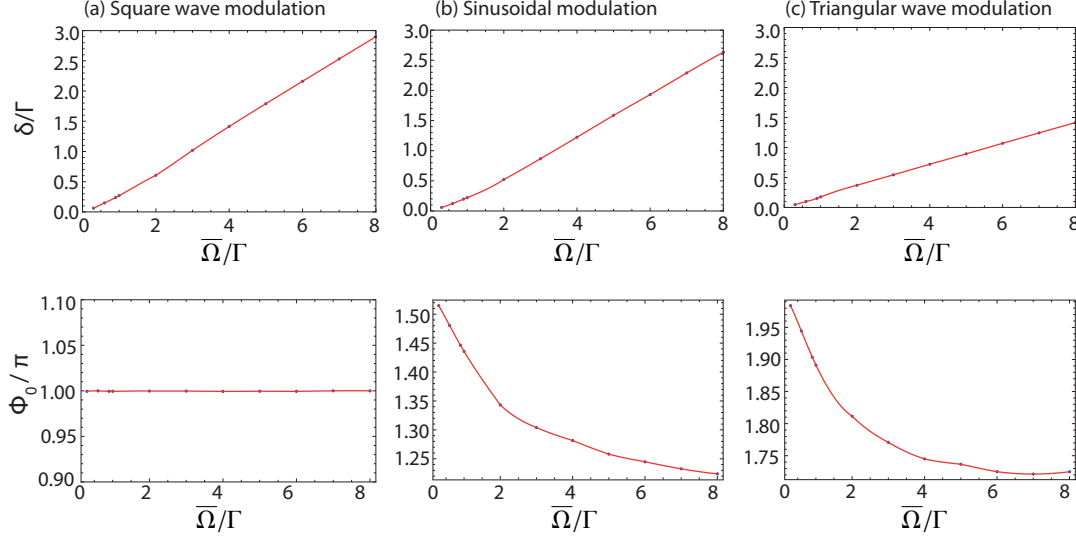


Fig. 7.5: The values of the modulation rate δ and modulation strength B which maximize the excited state population for a given choice of the Rabi frequency $\bar{\Omega}$. The effect of increasing $\bar{\Omega}$ relative to Γ on the excited state population is shown in Fig. 7.7.

row of Fig. 7.5) that maximises the excited state population is constant at π for the square modulation, but decreases for the sinusoidal and triangular waves as $\bar{\Omega}$ is increased.

Effect of detuning on the optimum modulation rate

There is one more important consideration when it comes to angular momentum dark states, namely how the optimum modulation rate is affected by detunings of the laser beams. To understand this problem, for a square modulation we fix the $\bar{\Omega} = \Gamma$, $\Phi_0 = \pi$, $\phi = 0$ and vary the laser detuning. The results are shown in Fig. 7.6.

As expected, positively or negatively detuning the driving lasers reduces the excited state population. However, notice that it also changes the optimum polarisation modulation rate, increasing it in proportion to the size of the applied detuning. The red line on the graph indicates the optimum polarisation modulation rate for a given detuning, its gradient for large detunings is 1. As the laser is detuned, it is advantageous to increase the modulation rate by exactly the same amount, since this acts to

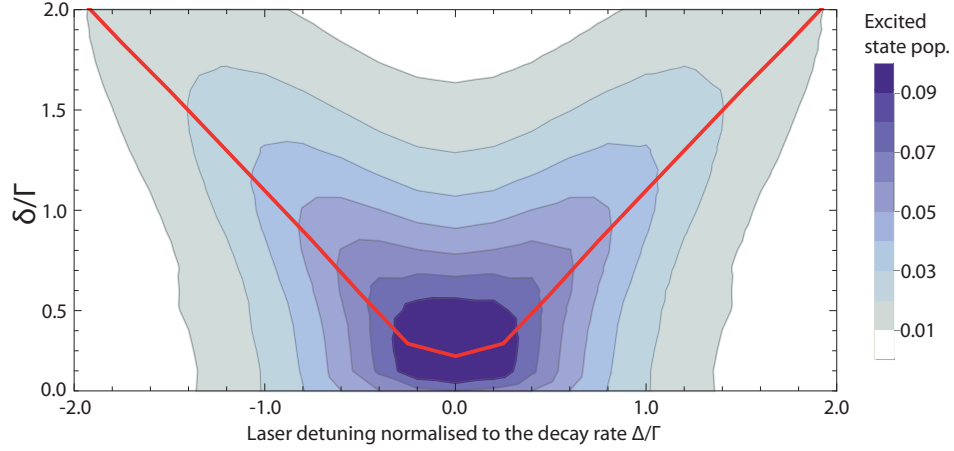


Fig. 7.6: The effect on the excited state population of simultaneously varying the detuning of the driving laser field Δ and the polarisation modulation rate δ . The modulation function is the square wave $\Phi_0 = 1$ and $\bar{\Omega} = \Gamma$. The red line shows the value of δ which maximises the excited state population for a given value of the laser detuning.

shift the frequency of the laser out to $\pm\delta$ thus partially decreasing the effect of the modulation. This is useful to know since we may try to address several transitions off resonantly with the same laser, some of which may be $F = 2$ levels.

Comparison with rate equations

We end this section on angular momentum dark states by seeing how the scattering rate at the optimum values of δ and Φ_0 depend on the Rabi rate $\bar{\Omega}$ for the three modulation functions, and comparing this to the simple rate equation model derived in section 5.4.1 on page 128. Of course, the comparison with the rate equation model is not really fair, because it cannot capture the fact that the driving fields are constantly addressing different levels, but we just ignore this difficulty and treat the laser beams as always being linearly polarised, and assume that the effect of the polarisation modulation is just to spread the population equally among the m_F sub-levels of the ground state and the m'_F sub-levels of the excited state. This corresponds to case 3) of Table 5.1, so that Eq. (5.14) for the total excited state population can

be written as

$$N_e n_e = 3 \left(8 + 15\Gamma^2 / \bar{\Omega}^2 \right)^{-1} . \quad (7.3)$$

Comparing this rate equation model to the results found from solving the optical Bloch equations for the optimum parameters (Fig. 7.7), we notice two things. Firstly, if B and δ are optimised, all of modulation functions produce nearly identical scattering rates, so we can choose whichever function is easiest to realise experimentally. This will usually be a sinusoidal modulation. Secondly, for the optimised parameters all of the functions only achieve between 80%–90% of the scattering rate we would naively expect if we just considered the levels as being linked by classical driving fields. Another way of putting this is that roughly speaking, the effect of dark states in this system is to modify Eq. (7.3) by replacing $\bar{\Omega} \rightarrow 0.69\bar{\Omega}$, or to say that the effective intensity driving the transitions is reduced by a factor of $0.69^2 \simeq 1/2$. Of course, if the rates are not optimised, then the occupation of the excited state and hence the overall scattering rate can be far lower.

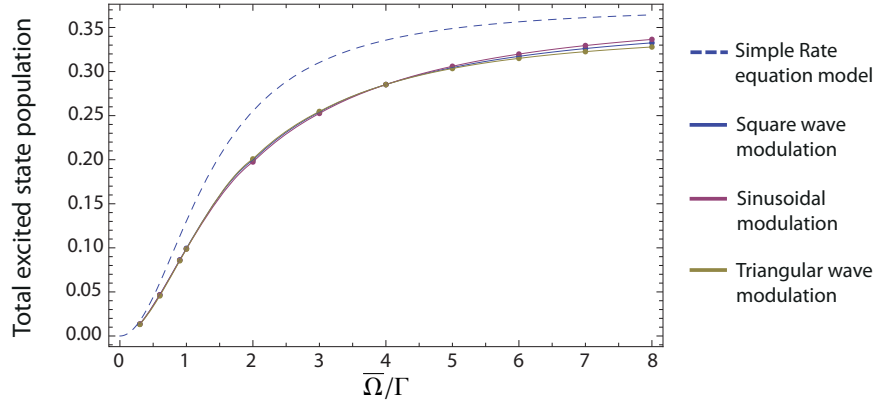


Fig. 7.7: The excited state population as a function of $\bar{\Omega}$ for the three types of modulation, with Φ_0 and δ set to their optimum values for each value of $\bar{\Omega}$. Also shown is the predicted excited state population from a simple rate equation model.

Summary of results

To summarise the practical conclusions from this section

1. Angular momentum dark states can be successfully destabilised by modulating the polarisation of the driving light.
2. For the optimum choice of parameters, the total excited state population follows the simple rate equation model (5.14) but with I replaced by $I/2$.
3. All three functions come to almost exactly the same maximum value for a given Ω , so we should choose the easiest to implement in the lab. This is a sinusoidal modulation.
4. The ideal modulation rate for a sinusoidal modulation is $\approx \bar{\Omega}/3$, and the ideal modulation depth is between $3\pi/2$ and π (see Fig. 7.5).
5. If the laser is detuned by Δ , the polarisation modulation rate should be also increased by Δ to optimise the scattering rate.

7.2.2 CPT dark states

We now move from discussing angular momentum dark states to a more general form of dark state that exists when several (possibly non-degenerate) m_F sub-levels are coupled together using coherent radiation. The specific case we will focus on is one where many ground electronic states are coupled up to the same excited state. This is a situation which occurs in both the pumping and detection schemes. We find that the lessons learnt above carry over into the more complex collection of inter-linked states that can be found in the new pumping scheme, where a great many levels are all linked together by coherent radiation.

To see that systems like these can have dark states, we start by considering a simple lambda-system with two levels $|1\rangle$ and $|2\rangle$ coupled to a third state $|e\rangle$ with laser fields resonant with the transition frequencies and with Rabi rates Ω_1 and Ω_2

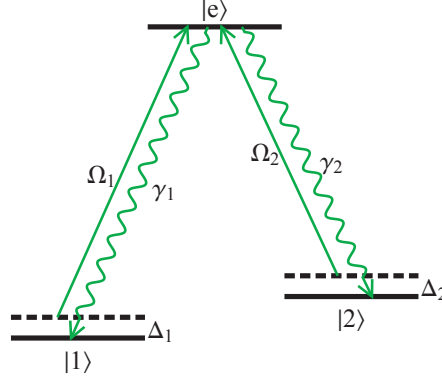


Fig. 7.8: A Lambda system

and detunings Δ_1 and Δ_2 respectively. The state $|e\rangle$ can decay spontaneously by emitting a fluorescence photon into the states $|1\rangle$ and $|2\rangle$, with partial rates γ_1 and γ_2 , but the states $|1\rangle$ and $|2\rangle$ are stable and do not decay. This is shown in Fig. 7.8.

If $\Delta_1 = \Delta_2 = 0$, then there is a dark state of this system given by

$$|\psi_D(t)\rangle = \frac{\Omega_2 e^{-i\omega_1 t} |1\rangle - \Omega_1 e^{-i\omega_2 t} |2\rangle}{\sqrt{\Omega_1^2 + \Omega_2^2}}. \quad (7.4)$$

We can check this state is dark by substituting it into the the Schroedinger equation for the system

$$i\hbar \frac{\partial}{\partial t} |\psi(t)\rangle = \hat{H} |\psi(t)\rangle, \quad (7.5)$$

where in the rotating wave approximation, the Hamiltonian can be written as

$$\begin{aligned} \hat{H} = & \hbar (\omega_1 |1\rangle \langle 1| + \omega_2 |2\rangle \langle 2| + \omega_e |e\rangle \langle e|) \\ & + \frac{1}{2} (e^{-i(\omega_1 + \Delta_1 - \omega_e)t} \Omega_1 |1\rangle \langle e| + e^{-i(\omega_2 + \Delta_2 - \omega_e)t} \Omega_2 |2\rangle \langle e|) + \text{H.C.} . \end{aligned} \quad (7.6)$$

The time evolution of this state never contains any amplitude to be excited to $|e\rangle$. This means that any population that starts in this state will not be excited to the upper level. Now suppose the system does not start in this dark state, then at some

time it will be excited up to $|e\rangle$ by the lasers. Once in $|e\rangle$, the state will sometimes spontaneously decay, falling into $|1\rangle$ with probability γ_1/Γ or $|2\rangle$ with probability γ_2/Γ . This means that after each spontaneous decay, the probability to be found in $|\psi_D(t)\rangle$ increases since $\langle\psi_D(t)|1\rangle \neq 0$ and $\langle\psi_D(t)|2\rangle \neq 0$. In other words, whatever state the systems starts in, eventually it will decay into $|\psi_D(t)\rangle$. Systems with more levels and more driving fields will experience CPT when two or more fields are equally detuned from a common excited state to which they are driving transitions.

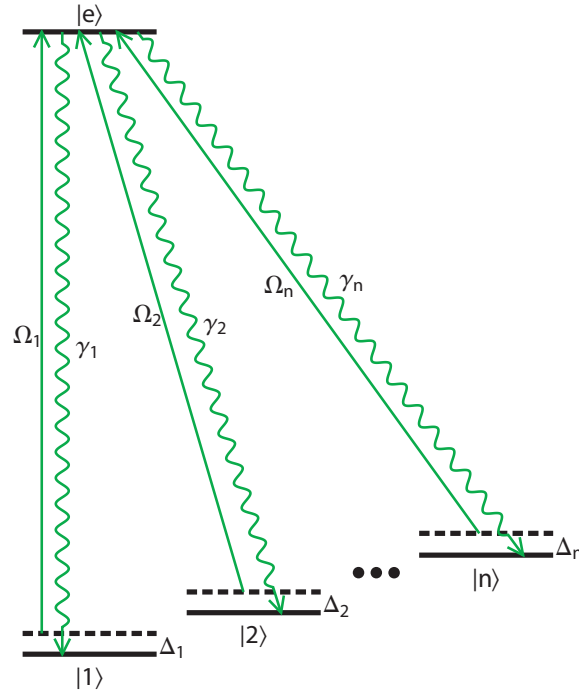


Fig. 7.9: A generalised lambda-system consisting of n stable ground states coupled to a single excited state $|e\rangle$

Luckily for us, the solution to destabilising CPT dark states is remarkably simple: just set $\Delta_1 \neq \Delta_2$, and then there is no state of the form (7.4) for the system to pump into. This then leads naturally to two questions:

1. What detunings and Rabi rates best optimise the excited state population?
2. How does the excited state population for the optimum parameters compare

with what we might expect from a simple rate equation model?

Once again, we turn to the trusty OBEs to answer these questions. We start by considering a simple system of n lower energy levels all coupled to a single upper level $|e\rangle$, illustrated in Fig. 7.9. Since each level is at most linked with one other by a driving field, we can again drop the f superscript and use the results from Chapter 6 to write the OBEs as

$$\dot{\rho}_{ij} = \sum_k iM_{ik}\rho_{kj}e^{-i\Delta_{ik}t} - \rho_{ik}e^{-i\Delta_{kj}t}iM_{kj} + r_{ij}, \quad (7.7)$$

where

$$M_{ij} = \frac{1}{2}\delta_{ie}\Omega_j + \frac{1}{2}\delta_{je}\Omega_i - \delta_{ie}\delta_{je}\Omega_e, \quad (7.8)$$

$$r_{ij} = (1 - \delta_{ie})\delta_{ij}\gamma_i\rho_{ee} - \frac{1}{2}\delta_{ie}\Gamma\rho_{ej} - \frac{1}{2}\delta_{je}\Gamma\rho_{ie}, \quad (7.9)$$

$$\Delta_{ij} = \Delta_j\delta_{ie} - \Delta_i\delta_{je}, \quad (7.10)$$

$$\Gamma = \sum_i^{N_g} \gamma_i. \quad (7.11)$$

The indices i, j and k run from $1 \dots N_g, e$ where $1 \dots N_g$ are the lower levels and e is the excited state, as does the sum in Eq. (7.7). δ_{ij} is the Kronecker delta symbol. In writing the relaxation terms, we have assumed that the energy spacing $E_i - E_j$ for any pair of levels is large compared to the quantity $\hbar\Delta_{ij}$. Recall also that $\Omega_i = \Gamma\sqrt{\gamma_i I_i / (\Gamma 2 I_{\text{sat}})}$, where I_i is the intensity driving the transition between the excited state and the i^{th} ground state.

Since each level couples to at most one other level, we can rewrite Eq. (7.7) to remove the time dependence of the right hand side via the substitution $\rho_{ij} = \tilde{\rho}_{ij}e^{-i\Delta_{ij}t}$. Now we can solve for the steady state by setting the left hand side derivatives to

zero, leading to

$$0 = i\Delta_{ij}\tilde{\rho}_{ij} + \sum_k iM_{ik}\tilde{\rho}_{kj} - i\tilde{\rho}_{ik}M_{kj} + \tilde{r}_{ij}, \quad (7.12)$$

$$\tilde{r}_{ij} = (1 - \delta_{ie})\delta_{ij}\gamma_i\tilde{\rho}_{ee} - \frac{1}{2}\delta_{ie}\Gamma\tilde{\rho}_{ej} - \frac{1}{2}\delta_{je}\Gamma\tilde{\rho}_{ie}. \quad (7.13)$$

These equations can be solved exactly so as to determine the excited state population $\tilde{\rho}_{ee}$, which once again is proportional to the number of florescences photons per second, given by $\Gamma\tilde{\rho}_{ee}$.

Solutions when all the partial decay rates are equal

Let us start with the simple case of two ground states, $N_g = 2$, shown in Fig. 7.8, and let us take $\gamma_1 = \gamma_2$ and $\Omega_1 = \Omega_2$. Our goal is to detune each laser from resonance so as to achieve the maximum scattering rate. Because of the symmetry of this problem with respect to the labelling of the states 1 and 2, we might reasonably expect the excited state population to maximise when the detunings Δ_1 and Δ_2 are equal in magnitude but opposite in sign: $\Delta_1 = -\Delta_2$. The excited state population as a function of detuning and Rabi rate subject to this constraint is shown in Fig. 7.10.

As expected, when $\Delta_1 = \Delta_2 = 0$, the steady state excited state population drops to zero, as the system pumps into the dark state $(|1\rangle - |2\rangle)/\sqrt{2}$ discussed at the start of this section. Also, we can see from this graph that the detuning which optimises the excited state population is always a fixed fraction of Ω_1 , given by $\Delta_1^{\text{opt}} = \pm\Omega/2$. This optimum detuning is illustrated by the red line in this figure.

How does the scattering rate in this optimised case compare with the scattering rates we hoped to achieve before we knew about the existence of CPT dark states? To answer this, we once again compare the excited state population with that predicted by the simple picture in section 5.4.1. We are considering case 1) of Table 5.1 with

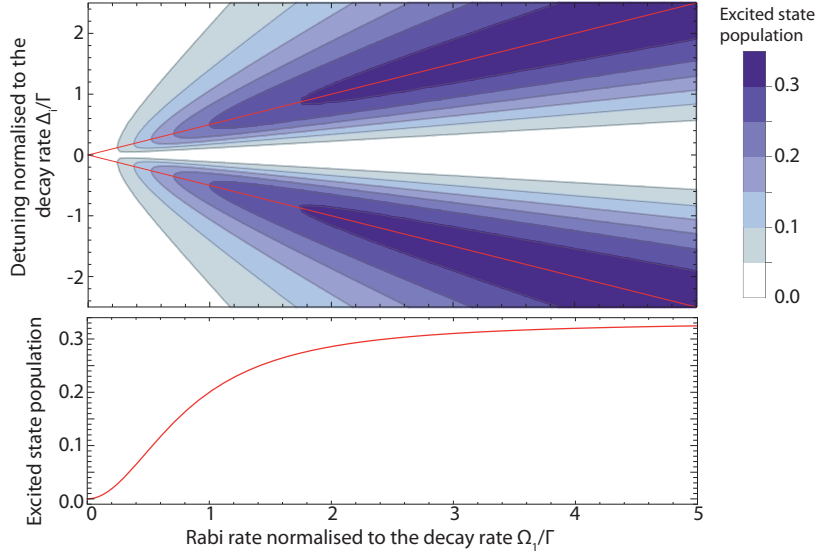


Fig. 7.10: Top: Excited state population for various values of the detuning $\Delta_1 = -\Delta_2$ and Rabi rate $\Omega_1 = \Omega_2$ for a three level lambda system. Bottom: Excited state population setting $\Delta_1 = \Omega_1/2$, identical to the rate equation model

$N_e = 1$, $N_L = 0$, for which Eq. (5.14) becomes

$$n_e = \frac{1}{(N_g + 1) + \Gamma^2/\Omega_1^2}. \quad (7.14)$$

Remarkably, this is also the excited state population that we get by solving the OBEs for the optimum detuning $\Delta_1^{\text{opt}} = \pm\Omega/2$. For $N_g = 2$ the excited state population exactly matches the curve at the bottom of Fig. 7.10. Detuning the driving fields to remove the dark states leads us back to exactly the same scattering rate as we would expect if we treated the problem as an entirely classical system of rate equations.

Now we consider what happens when we increase the number of ground states, while keeping all the partial decay rates equal. Surprisingly, we find that if the parameters are optimised to give the maximum scattering rate, Eq. (7.14) continues to give the correct excited state populations, at least up to $N_g = 7$ where we stopped checking. These optimum parameters are as follows. For a fixed total intensity of light, equal intensities should drive each transition, which results in equal Rabi rates. The frequencies should be chosen so that pairs of transitions have opposite detunings

$\pm\Delta_1, \pm\Delta_2$, etc and if there is an odd number of transitions, the unpaired one has zero detuning. These detunings are listed in Table 7.1 for systems having N_g up to 5.

Number of ground states, N_g	Optimum detunings
2	$\Delta_1^{\text{opt}} = \frac{\Omega}{2}$
3	$\Delta_1^{\text{opt}} = \frac{\Omega\sqrt{3}}{2}$
4	$\Delta_1^{\text{opt}} = \frac{\Omega\sqrt{3+\sqrt{6}}}{2}, \Delta_2^{\text{opt}} = \frac{\Omega\sqrt{3-\sqrt{6}}}{2}$
5	$\Delta_1^{\text{opt}} = \frac{\Omega\sqrt{5+\sqrt{10}}}{2}, \Delta_2^{\text{opt}} = \frac{\Omega\sqrt{5-\sqrt{10}}}{2}$

Tab. 7.1: The detunings that optimise the excited state population in a system of n lower levels coupled to a single upper level.

These solutions are not unique. Any way of pairing the transitions will do, since there is nothing to distinguish one ground state from another. Aside from this trivial relabelling, it is also possible that there may be other ways of arranging the detunings and intensities to match or exceed the excited state population given by Eq. (7.14), but I have not been able to find them.

In this symmetrical case with one excited state, we conclude that the scattering rate given by the simple rate equations can still be achieved, provided each transition is addressed with equal intensity radiation and the lasers are appropriately detuned from each transition.

Solutions when the partial decay differ

Now we consider what happens if the partial decay rates are not equal. The situation is more complex, and in some ways even more surprising. We start once again with the three level lambda system shown in Fig. 7.8, and for a range of values of the partial decay rate γ_1 we numerically vary Δ_1, Δ_2, I_1 and I_2 to maximise the excited

state population, subject to the constraint that the total intensity $I_{\text{tot}} = I_1 + I_2$ is fixed. We then repeat this process for a range of fixed total intensities and track how the parameters Δ_1 , Δ_2 , I_1 and I_2 that maximise excited state population vary. The results are shown in Fig. 7.11. In the previous section, we found that the optimum detunings were fixed fractions of the Rabi rate, so it is helpful to define a characteristic rate for a given total intensity $\bar{\Omega}_{\text{Av}} = \Gamma \sqrt{I_{\text{tot}}/(2N_g I_{\text{sat}})}$.

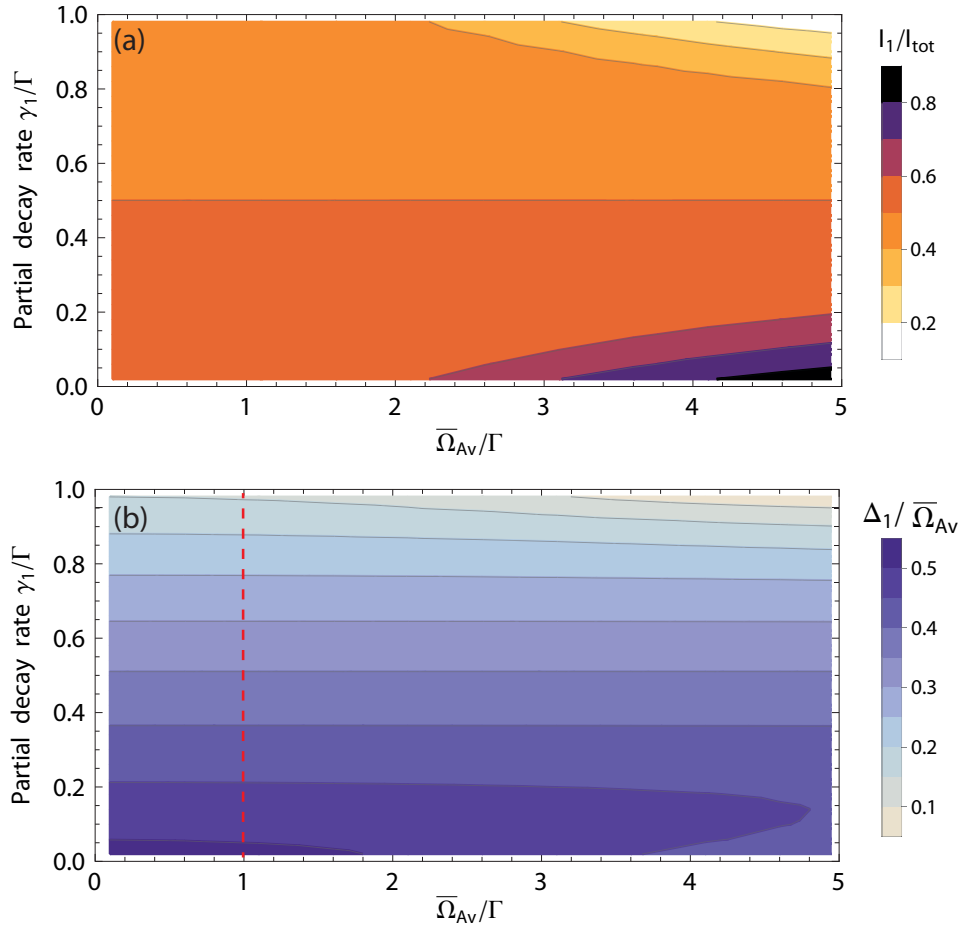


Fig. 7.11: (a) The fraction of the total intensity I_1/I_{tot} and (b) the decay rate $\Delta_1/\bar{\Omega}_{\text{Av}}$ that maximise the excited state population ρ_{ee} as a function of $\bar{\Omega}_{\text{Av}}$ and γ_1 . The red dashed line in (b) shows the location of the slice shown in Fig. 7.12.

To understand Fig. 7.11, we begin with the left hand side of (a), where $\bar{\Omega}_{\text{Av}}$ is small compared to Γ , or equivalently where $I_{\text{tot}}/2$ is small compared with $2I_{\text{sat}}$. In

this region, the best choice is still to set both intensities to be equal, irrespective of the value of γ_1 . Staying with Fig. 7.11 (a), we now move to the right hand side of the graph, where $\bar{\Omega}_{\text{Av}} > \Gamma$. In this region, it is no longer best to set all the intensities to be equal. Instead, if $\gamma_1 < \gamma_2$ (i.e. if $\gamma_1/\Gamma < 1/2$) it is better to use a higher fraction of the total light intensity on the $|1\rangle \rightarrow |e\rangle$ transition. The opposite is true if $\gamma_1 > \gamma_2$. This is quite surprising: if we have a lambda system driven far above saturation ($I_{\text{tot}} \gg I_{\text{sat}}$) and where the decay rate to one level is very low, the best strategy is to put a higher fraction of the total intensity into driving the weakly allowed transition.

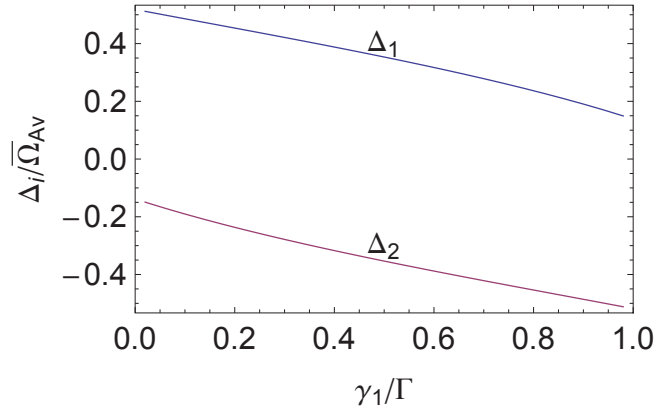


Fig. 7.12: The normalised detunings $\Delta_1/\bar{\Omega}_{\text{Av}}$ and $\Delta_2/\bar{\Omega}_{\text{Av}}$ that maximise the excited state population, as a function of the partial decay rate to state $|1\rangle$, γ_1 . $\bar{\Omega}_1 = \bar{\Omega}_2 = \Gamma/\sqrt{2}$.

Now consider Fig. 7.11 (b), which shows the optimum value of the detuning Δ_1 as a function of $\bar{\Omega}_{\text{Av}}$ and γ_1 . First of all, consider the behaviour of Δ_1 as γ_1 is varied, for fixed $\bar{\Omega}_{\text{Av}}$. When γ_1/Γ approaches 1 (or zero), it is favourable to reduce (or increase) the detuning of the laser driving the $|1\rangle \rightarrow |e\rangle$ transition. A slice through graph (b) at $\bar{\Omega}_{\text{Av}} = 0.4\Gamma$, indicated by the red dashed line, is shown in Fig. 7.12, which also includes the corresponding value of Δ_2 . Now we consider how the optimum value of Δ_1 changes as $\bar{\Omega}_{\text{Av}}$ is increased. In the region where $\bar{\Omega}_{\text{Av}} < \Gamma$, the optimum is always a fixed fraction of $\bar{\Omega}_{\text{Av}}$. This can be seen from the fact that the contours of Fig. 7.11 (b) are parallel to the x axis in the range $0 < \bar{\Omega}_{\text{Av}}/\Gamma \lesssim 1$. As we move

to the right hand side of the graph where $\bar{\Omega}_{\text{Av}} > \Gamma$, the contours at large and small values of γ_1 begin to curve. This indicates that the optimum detuning no longer scales linearly with $\bar{\Omega}_{\text{Av}}$

Having found the parameters that optimise the scattering rate, we move on to investigate what the excited state population is for these parameters. The most surprising feature of having unequal partial decay rates is that the excited state population can exceed the maximum available with $\gamma_1 = \gamma_2$. In other words, it is possible to achieve an excited state population that exceeds the steady-state solution (7.14) of the rate equation. This is shown in Fig. 7.13 (a), which plots the ratio of the excited state populations given by the OBEs and by the rate model, for the case where $I_{\text{tot}} = 4I_{\text{sat}}$. In both models, the detunings have been adjusted to maximise the excited state population. When $\gamma_1 \neq \gamma_2$, OBEs give slightly more population in the excited state than the rate model. This occurs because as $\gamma_1/\Gamma \rightarrow 1$ or 0, the population is no longer equally distributed between the ground states, but instead is concentrated in the state that is favoured by the decay from $|e\rangle$. This means that the system starts to behave more like a two level system and hence the excited state population increases. By contrast, the rate model gives equal ground state populations when constrained to maximise the scattering rate, even when the partial decay rates are not equal, as shown in the appendix of Ref. [21].

This unexpected enhancement of the scattering rate does not seem to be limited to the $N_g = 2$, case, as 7.13 (b) illustrates. This graph shows the ratio between the excited state population found by solving the OBEs, and that which is found from the simple rate model as a function of the two partial decay rates γ_1/Γ and γ_2/Γ for the case $N_g = 3$. The Rabi rates are equal to each other and to Γ , and the detunings have been adjusted to maximise the excited state population. The minimum possible excited state population occurs when $\gamma_1 = \gamma_2 = \gamma_3$, right at the centre of the graph. As one decay becomes more probable than the others (moving towards the in the corners of the graph) the excited-state population from the density matrix model

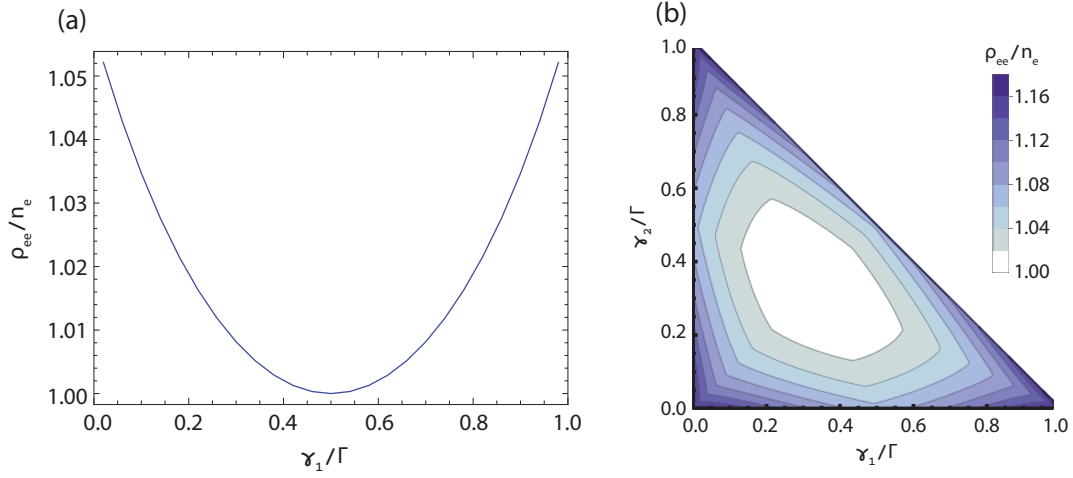


Fig. 7.13: Maximum steady excited population ρ_{ee} from solving the OBEs, divided by n_e from the rate equation model (Eq. (7.14)), plotted as a function of the partial decay rate(s). (a) Three level lambda system ($N_g = 2$) where $\Omega_1 = \Omega_2 = \Gamma$, (b) Four level lambda system ($N_g = 3$), $\Omega_1 = \Omega_2 = \Omega_3 = \Gamma$.

exceeds the excited state population n_e given by the rate model.

After this discussion, we tentatively conclude that CPT dark states should not stand in the way of achieving the scattering rates predicted by the simple rate equation model.

7.3 Simulations of the new detection scheme

We are now finally in a position to begin simulating the full YbF system, with a reasonable degree of confidence that the simple predictions of the rate equation model should be achievable, at least roughly, as long as proper efforts are made to destabilise the dark states. We begin with the new detection scheme, since this is simpler than the new pumping scheme and what we learn about the powers and detunings of the detection lasers can then be applied to the pumping lasers.

7.3.1 Dark states of the new detection scheme

The detection scheme we ultimately want to simulate is shown in the right hand side of Fig. 7.1. To check that our discussion of dark states in section 7.2 is valid for this more complex YbF system, we will start by making all the mistakes that we know should lead to dark states: we set the polarisation to be linear along the quantisation axis z , so allowing the population to build up in the $m_F = \pm 2$ states of $N = 2$, and we also set lasers (a), (c) and (e) to be resonant with their respective transitions, allowing the possibility of CPT dark states among the ground states. We also detune the lasers driving transitions (b) and (d) an equal 1.5 MHz from the $F' = 0$ and $F' = 1$ levels.

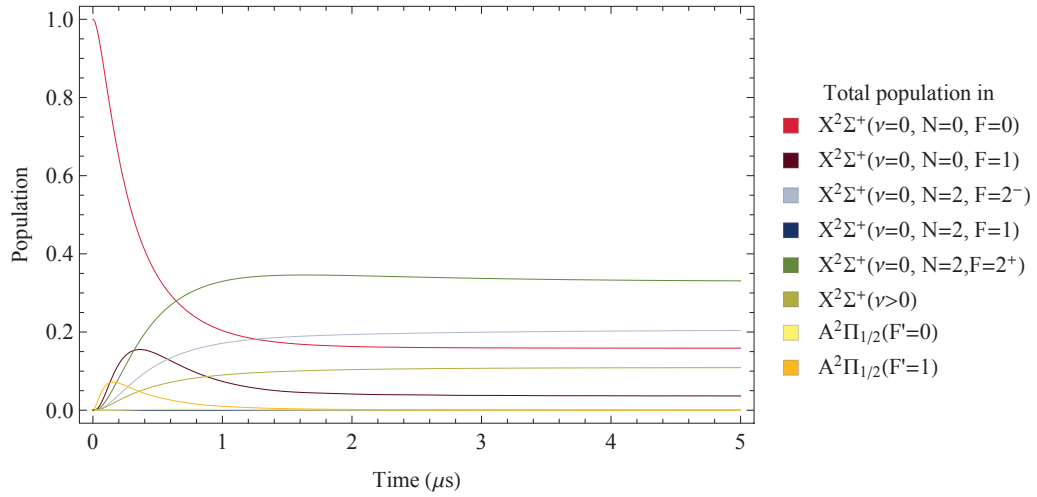


Fig. 7.14: Evolution of the populations of the new detection scheme shown on the right hand side of Fig. 7.1. Notice that the excited state populations drop to zero in the steady state, and only $\sim 10\%$ of the population is pumped to $X^2\Sigma^+ (v > 0)$.

We set the intensity of each laser beam to be equal to the saturation intensity, and solve the OBEs for this system (Eq. (6.11)) with all the population starting in the $|0, 0\rangle$ state. The evolution of the populations over time is shown in Fig. 7.14. After about 3 μs all the population that started in the absolute ground state has been

redistributed among the levels in $N = 0$ and $N = 2$, with about 10% being optically pumped into $X^2\Sigma^+(v > 0)$. This happens after each molecule has scattered 1.6 photons on average. The system then goes dark, the excited state populations drop to zero, and the populations enter a steady state. The system is now in a mixture of various angular momentum and CPT dark states. We can confirm this visually by looking at a matrix plot of the density matrix elements in the steady state, Fig. 7.15.

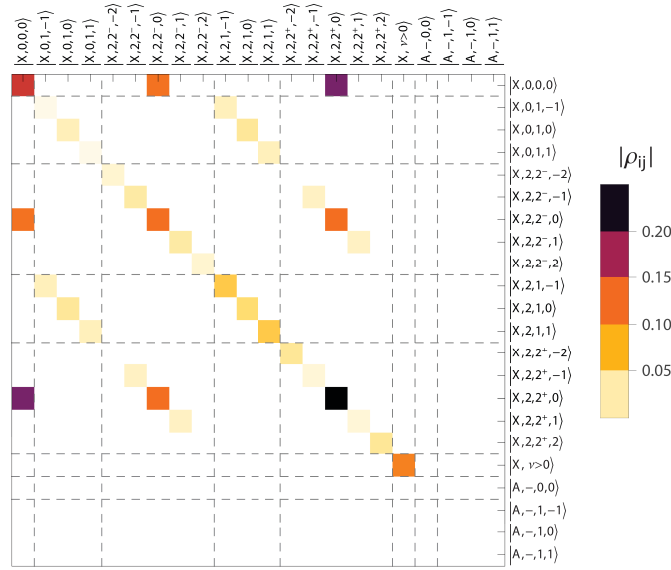


Fig. 7.15: Matrix plot of the steady state solution of the density matrix for the simulation shown in Fig. 7.14. Each entry in the grid represents the absolute value of the density matrix element $|\rho_{ij}| = |\langle i | \hat{\rho} | j \rangle|$, where the quantum numbers for $|i\rangle$ are shown along the right hand side of the grid and $|j\rangle$ along the top of the grid. The ground electronic, $v = 0$ states are labelled $|X, N, F^\pm, m_F\rangle$. The ground electronic, $v > 0$ states are collectively labelled $|X, v > 0\rangle$. The electronically excited states are labelled $|A, \mathcal{P}', F', m_F'\rangle$.

The shading of each square in this 22×22 grid represents the absolute value of the density matrix elements $|\rho_{ij}| = |\langle i | \hat{\rho} | j \rangle|$ indicated by the x and y labels of the grid. The diagonals indicate population, while we refer to the off-diagonals as “coherences”. So, the square in the top left hand corner indicates the population in

the absolute ground state, and the lighter shaded square in the top row, column 7 is the value of the coherence between the absolute ground state and $X^2\Sigma^+ (v=0, N=2, F=2^-, m_F=0)$. Following the notation of Eq. (2.3), page 37 these two states are $|X, \Lambda=0\rangle|0\rangle|0,0,0\rangle$ and $|X, \Lambda=0\rangle|0\rangle|2,2^-,0\rangle$, or $|X,0,0,0\rangle$ and $|X,2,2^-,0\rangle$ following the streamlined notation explained in the caption to the figure.

The matrix plot lets us visually confirm our diagnosis of the nature of the final state of the system. First of all, the diagonal shading tells us what we already knew from Fig. 7.14, there is some population left in the ground states. In Fig. 7.15, it is broken down into all of the m_F sub components, where as in Fig. 7.14 the sublevel populations within each F level are summed together. We can also see that for some states like $|X, v>0\rangle$ and $|X, 2, 2^\pm, \pm 2\rangle$, the only entries in Fig. 7.15 are those for populations; there are no coherences involving these states. Thus we can say that with respect to our chosen quantisation basis the system has pumped into each of of these states with some probability, given by the darkness of the diagonal entry. For all the other ground electronic states states like $|X, 0, 0, 0\rangle$ the situation is more complex. Taking this state as an example, it has coherences with $|X, 2, 2^\pm, 0\rangle$, which we might expect since these three states are all linked to a common excited state $|A, -1, 1, 0\rangle$ and so can be pumped into a CPT dark state.

In our experiment, two separate lasers will drive the transitions from $N=0$ and $N=2$ and these will not be phase locked to each other. Their phases will remain correlated only for a limited time—essentially the inverse laser line width. As these are in the range 10 kHz–1 MHz, the dark state will not be stable beyond about 100 μ s. However, the pumping and detection will take place over some tens of μ s, so we should not rely on the inherent instability of the lasers to destabilise the dark states. Instead, let us follow the lessons we learnt in section 7.2.2 and detune each laser from the central frequency of the transition by an amount of order 1 MHz, ensuring that no two detunings are equal. For the moment, we keep the polarisation of all the lasers fixed along the z axis, and maintain the intensity of all the beams at

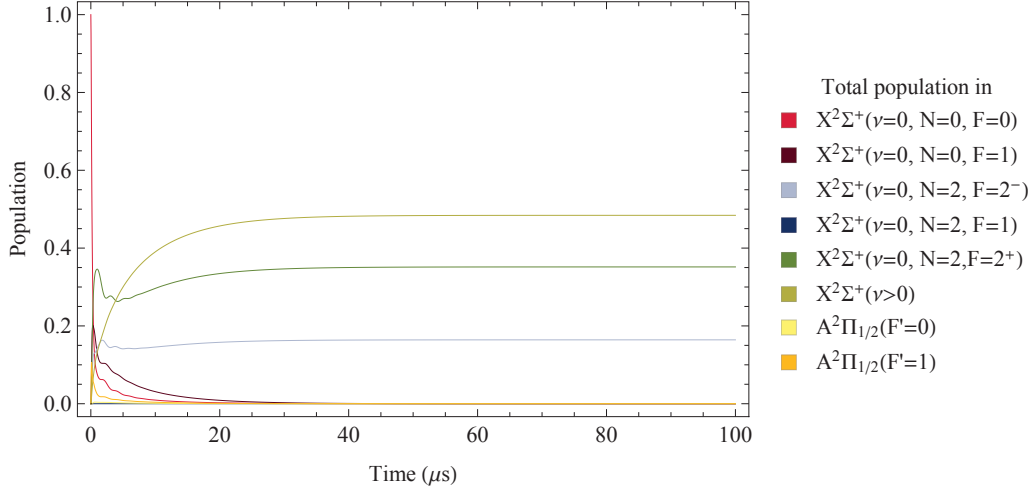


Fig. 7.16: Evolution of the populations of the new detection scheme shown on the right hand side of Fig. 7.1, where each beam is now slightly detuned from resonance

$$I = I_{\text{sat}}.$$

Now, as we can see from Fig. 7.16, almost half the population pumps out of the levels being addressed and into $X^2\Sigma^+(\nu > 0)$. This takes much longer than in the previous simulation- around 40 μs . As shown in Fig. 7.17, the molecules that remain are in the $F = 2^\pm$ levels of $N = 2$. These cannot be excited because the laser is linearly polarised along z , and the excited states have no $m_F = \pm 2$ sub-levels. This is shown in the matrix plot for the steady state of this simulation, Fig. 7.17.

Finally, to make sure we also address these angular momentum dark states, we modulate the laser polarisation by breaking the light into two components at $\pm 45^\circ$ to z and delaying the phase of one component with a sinusoidal modulation function, as discussed on page 158, where we set the modulation frequency somewhat arbitrarily to $2\pi \times 1 \text{ MHz}$, which is approximately the same size as the laser Rabi rates when $I = I_{\text{sat}}$, in keeping with what we learnt in section 7.2.1.

Now, at last, the entire population pumps into $X^2\Sigma^+(\nu > 0)$, as shown in Fig. 7.18, scattering on average 13.9 photons per molecule in the process. How-

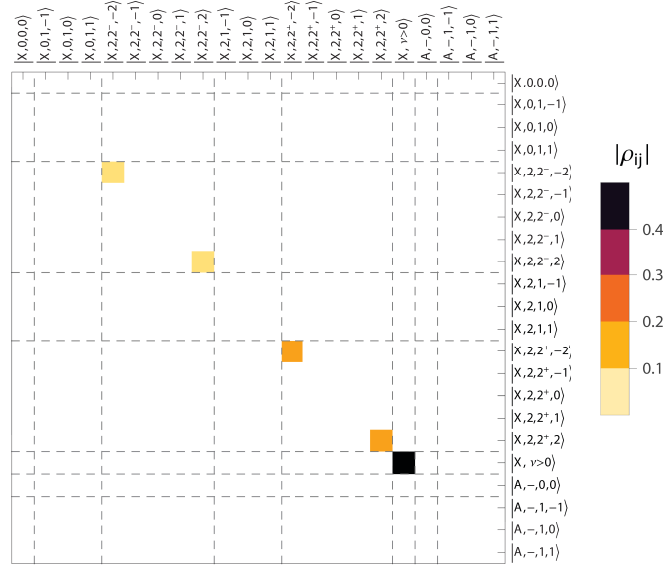


Fig. 7.17: Matrix plot of the steady state solution of the density matrix for the simulation shown in Fig. 7.16. See the caption for Fig. 7.15 for more information.

ever, notice how long it takes this scattering to happen: it takes $80 \mu\text{s}$ to pump 90% of the molecules to $X^2\Sigma^+(v > 0)$, compared with $30 \mu\text{s}$ in the simple rate equation picture (Fig. 5.8).

In the next section, we will optimise the detection by varying the detunings of the laser beams, the polarisation modulation rate, and the balance of intensities between the beams.

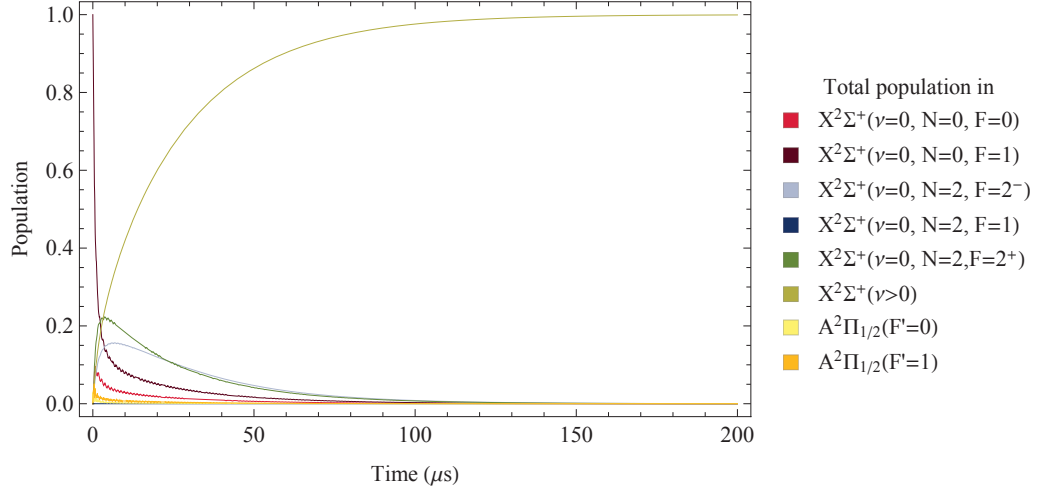


Fig. 7.18: Evolution of the populations of the new detection scheme shown on the right hand side of Fig. 7.1, where each beam is now slightly detuned from resonance and the laser polarisation is modulated at 1 MHz.

7.3.2 Optimising the parameters for the new detection scheme

In this section, our goal is to scatter as many photons as possible during our limited detection time. To restrict the problem to a manageable size, we vary 11 parameters which are: the detunings of the 5 beams, the fraction of the total laser intensity contained within each beam, and the frequency of the laser polarisation modulation. We use a sinusoidal function, but section 7.2.1 indicates that other functions will produce similar results. The modulation depth Φ_0 is fixed at $1.5 \times \pi$, which should maximise the excitation rate when the $\bar{\Omega} \lesssim \Gamma$, as will be the case in all the following simulations. We further assume that all the laser beams are combined together and propagate along the same axis. The polarisation of the light going into the polarisation modulation crystal is chosen as either $+$ or -45° to the modulated axis. The way they are generated in the laboratory means that beams (a) and (b) have the same polarisation. Because all the beams are combined using polarising cubes, one of the remaining beams has the same polarisation as (a) and (b) while the other two are orthogonal. We arbitrarily choose (d) to have the same linear polarisation

as (a) and (b) while (c) and (e) have the orthogonal polarisation.

For each set of parameters, we look at the fraction of molecules pumped into $X^2\Sigma^+(v > 0)$ after 25 μs . Since we know that it takes on average $1/(1 - f_{00}) = 13.9$ photon scatters before a molecule is pumped to $X^2\Sigma^+(v > 0)$ (Eq. (5.19)), the fraction in $X^2\Sigma^+(v > 0)$ after a certain time, multiplied by 13.9, gives the average number of photons scattered per molecule.

The number of photons scattered depends in a complicated way on the detunings and powers of each of the other laser beams. We optimise the scattering rate by maximising it with respect to each parameter in turn, then iterating several times. For a given starting condition this converges on a local maximum of the function, and we repeat it for a few different initial conditions to search for the global maximum. We then repeat this for four values of the total intensity which are $I_{\text{tot}} = 2.5I_{\text{sat}}, 4I_{\text{sat}}, 5I_{\text{sat}}$ and $7.5I_{\text{sat}}$.

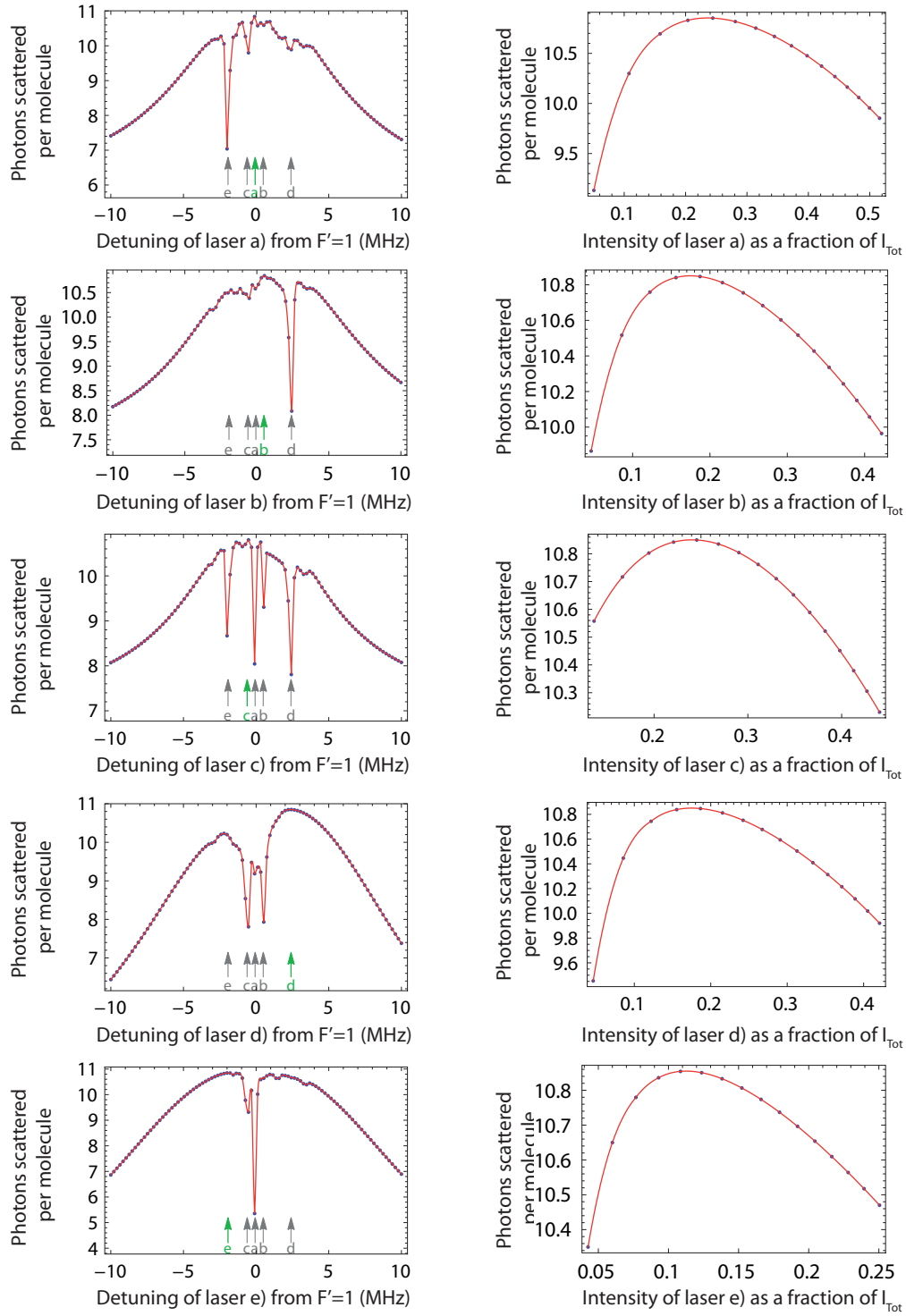


Fig. 7.19: Average number of photons scattered after $25\ \mu\text{s}$ with $I_{\text{tot}} = 5I_{\text{sat}}$ as a function of the detuning of each laser and the fraction of the total intensity in each beam. The red line is an interpolation function between the points. The labelled arrows indicate the optimum detunings.

To understand a bit more clearly how the number of scattered photons depends on the detunings, modulation rate and powers in each beam, we focus for the time being on the case where the total intensity of the lasers beams is fixed at $I_{\text{tot}} = 5I_{\text{sat}}$. We scan each parameter about its optimum value, keeping all the others fixed at their optimum values, and plot the effect this has on the number of photons scattered. The results for scanning the detunings and intensity ratios are shown in Fig. 7.19, while the effect of scanning the polarisation modulation rate is shown in Fig. 7.20.

Let us start by looking at how the pumped fraction depends on the detunings, which are the left hand graphs in Fig. 7.19. We see that each graph has a roughly Lorentzian lineshape, with a width of ten or twenty MHz, and some finer features. The broad line is associated with the (power-broadened) width of the scattering resonance associated with that particular transition. For the graphs (b) and (d), there are really two transitions as the laser excites both $F' = 1$ and $F' = 0$, which are separated by 3 MHz. The sharp dips occur when the detuning of the laser that is being scanned equals that of another laser addressing the same upper level. When this happens the molecule can pump into a CPT dark state, which may or may not be destabilised by other laser beams. On each of these graphs there are four grey and one green arrows. The green arrow shows the location of the optimum frequency for the transition that is being scanned, and the four grey arrows indicate the detunings of the other lasers, which match up with the locations of the dips. Clearly there is much more to be said about why the features take the form they do, but for our present purposes they are a nuisance since many numerical maximisation techniques get stuck in the local maxima next to these deep features. The graphs on the right hand side of Fig. 7.19 show how the scattering rate depends on the division of the laser intensity between the beams. This is much more benign, with each beam needing between 0.15 and 0.3 of the total intensity.

Fig. 7.20 shows that the polarisation modulation rate affects the the scattering rate in a similar way to the simpler case we simulated above, of an $F = 2$ system

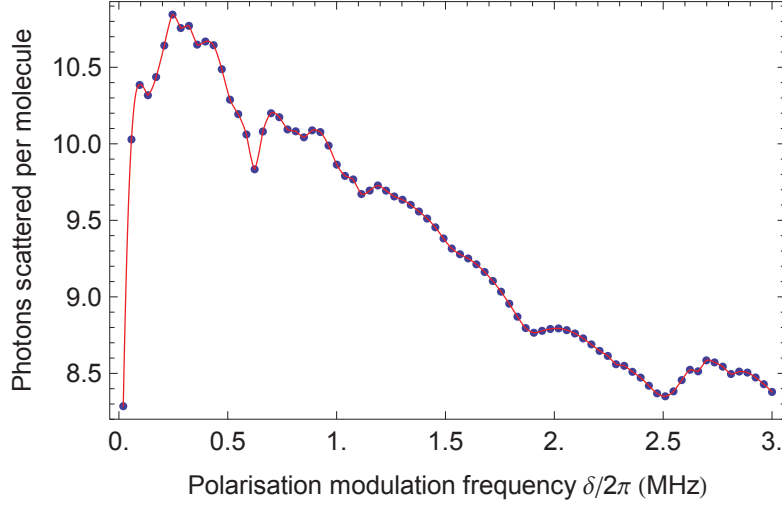


Fig. 7.20: Average number of photons scattered per molecule as a function of the polarisation modulation frequency.

being driven to $F' = 1$ (results in Fig. 7.4 on page 159). The scattering rate rises steeply to a maximum at about 0.25 MHz before tailing off slowly as the rate is increased above this frequency. This exactly mirrors the behaviour of the second graph of Fig. 7.4, if we take a section through the contour plot when $\Phi_0 = 3\pi/2$. The small features on this plot are a result of the interplay between the detunings and the polarisation modulation rate, which in section 7.2.1 page 161 we found should be matched to maximise the scattering rate. On both of the $F = 2 \rightarrow F' = 1$ transitions there is an intensity of $I = 1.2I_{\text{sat}}$; from our earlier discussions this would suggest that the polarisation modulation rate should be set at 1.5 MHz. The actual rate that maximises the scattering rate is somewhat lower than this at 0.25 MHz.

In Fig. 7.21 we compare the average number of photons scattered in a given interaction time when the parameters have been optimised in this way with the result predicted by the simple rate equations (p. 128). The four graphs show this for different total laser intensities. In each case, we see that the full density matrix solution gives a scattering rate that is only slightly below the rate equation result, indicating that we have indeed managed to destabilise the dark states, even though

the system is now much more complex than before. Roughly speaking, the results one finds by solving the OBEs for an average intensity I on each beam match the rate equation results one would expect if $0.7I$ – $0.8I$ is used instead—thus we can think of the dark states as effectively reducing the laser intensity by between 20% to 30%.

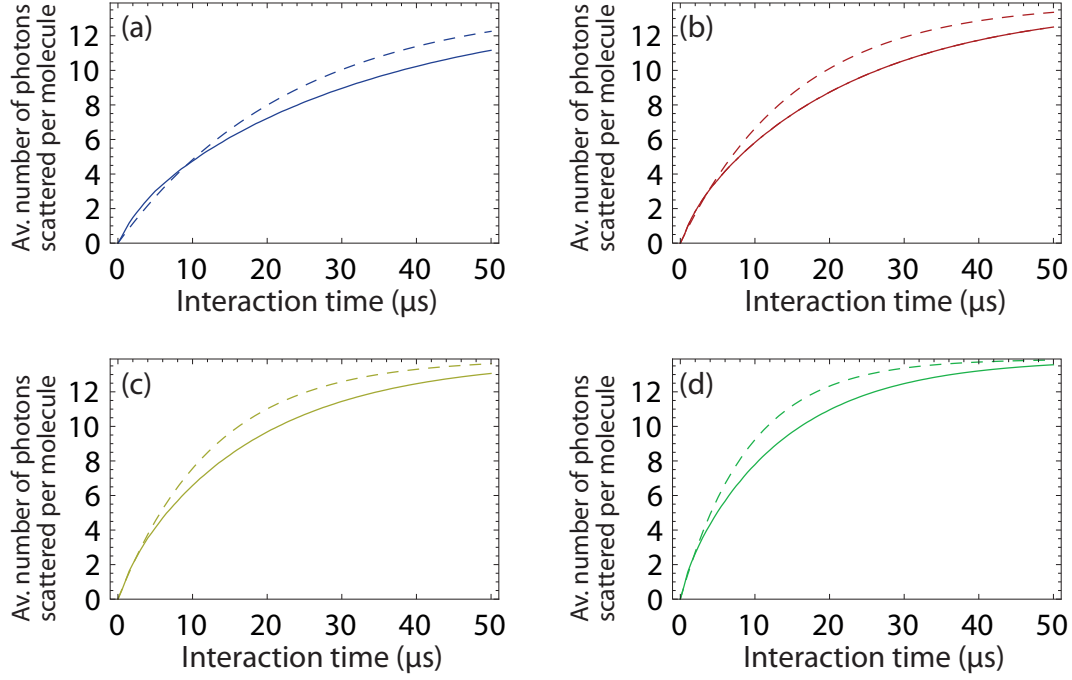


Fig. 7.21: Average number of photons scattered per molecule as a function of interaction time after some optimisation of the detunings, ratios of intensity between the beams and polarisation modulation frequency, for four different values of the total laser intensity, I_{tot} . These are: (a), $I_{\text{tot}} = 2.5I_{\text{sat}}$, (b) $I_{\text{tot}} = 4I_{\text{sat}}$, (c) $I_{\text{tot}} = 5I_{\text{sat}}$ and (d) $I_{\text{tot}} = 7.5I_{\text{sat}}$. The solid lines are the solutions of the OBEs, the dashed lines from the rate model, Eq. (5.15)

7.3.3 Transverse Doppler broadening

So far, we have assumed that the YbF molecules have no Doppler shift, being in a perfectly collimated beam, at a right angle to the laser beams. However, in reality the molecular beam is not perfectly collimated, so some of the molecules will have a small Doppler shift. Fig. 7.22 shows how the number of photons scattered per

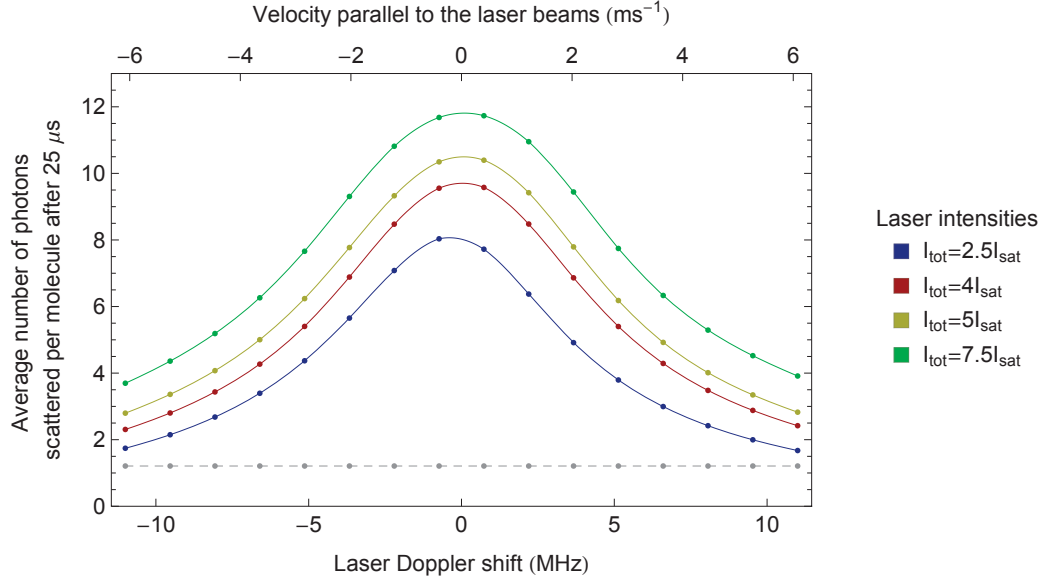


Fig. 7.22: Number of scattered photons as a function of laser Doppler shift and velocity parallel to the probe laser beam propagation direction.

molecule varies with a common detuning of the laser beams. Notice that only those molecules which have a Doppler shift smaller than the natural linewidth scatter close to the maximum number of photons. Those molecules with larger shifts scatter very few photons. For reference, the graph also shows a grey dashed line which represents the number of photons scattered under the old, single laser detection scheme with intensity set at $I_{\text{sat}}/2$. Here, all the molecules in this velocity range scatter 1.2 photons. This means that we can expect a factor of 10 increase in signal for molecules with Doppler shifts up to a few MHz, and a smaller improvement for those with higher Doppler shifts.

By taking spectra of our molecular beam at low laser power we have determined that the Doppler profile is well approximated by a Gaussian with a 15 MHz FWHM. This, together with the results shown in Fig. 7.22, gives the average number of photons we can expect each molecule to scatter in a 25 μs interaction time. The results are listed in Table 7.2 for a selection of total laser intensities. The middle column shows for comparison the number of photons that would be scattered in the

absence of any Doppler shift.

Total intensity of laser beams, I_{tot}	Number of photons scattered by molecules with no Doppler shift	Average photons scattered per molecule averaged over Doppler profile
$2.5 I_{\text{sat}}$	8.1	5.0
$4 I_{\text{sat}}$	9.7	6.4
$5 I_{\text{sat}}$	10.5	7.2
$7.5 I_{\text{sat}}$	11.8	8.6

Tab. 7.2: Average number of photons scattered per molecule in the new detection scheme with and without the effect of transverse Doppler shifts.

These numbers show that, given the laser power available, we should not expect to reach the ideal maximum of 13.9 photons per molecule, but we should expect a large improvement over the present detection efficiency.

7.3.4 Conclusion on the new detection scheme

If we aim for the modest goal of having the average intensity on each beam as I_{sat} ($I_{\text{tot}} = 5I_{\text{sat}}$), and an interaction time of 25 μs , then the total laser power required will be around 53 mW in each of the probe regions, and the beam area in each region will be 16×15 mm for the detection light to address the full molecular beam with and provide the necessary interaction time. Using the results of Table 7.2, and taking $I_{\text{tot}} = 5I_{\text{sat}}$ in each probe region, we expect a 6-fold increase over what we currently detect, giving in total a twelve-fold increase in detection efficiency.

A significant challenge will be working with large, intense laser beams close to the PMT optics, and not overwhelming the signal with scattered light. With our present detection optics and a somewhat smaller detection beam, we are able to achieve a background scattering rate of around 70 kHz/mW of laser light [84]. If we can do this well with the larger beam then we could hope to have a background scatter rate

of 4MHz. This would be very satisfactory as the photon count rate from molecules will be around 26 MHz in each detector, even without the improvement in the beam intensity from the proposed new pumping scheme. Once this is taken into account the signal to noise ratio will improve even further.

7.4 Simulations of the new pumping scheme

7.4.1 Preliminary considerations

Now we turn to the simulation of the new pumping scheme shown in the left hand energy level diagram of Fig. 7.1. Before we embarked on the simulations, we spent some time considering how we would actually be able to deliver the laser, rf and microwave fields to the molecules. The important design considerations were to make sure that the fields were large enough, that the potential interaction time with the molecules was long enough and that the polarisations of the rf magnetic fields were not parallel or perpendicular to the microwave electric field polarisation. This last requirement ensures that all the m_F components of $X^2\Sigma^+ (N = 1, F = 2)$ are mixed together by the rf fields and can be driven to $X^2\Sigma^+ (N = 0, F = 1)$ by the microwave radiation.

The solution we decided on is shown in diagram (a) of Fig. 5.2. The four laser beams propagate along the machine x axis. Before entering the machine, the light is polarised either along y or z , and is passed through the polarisation modulation crystal orientated at 45° to the y axis, so that the polarisation is modulated in the y - z plane. The rf coils generate fields which are nominally in the x - z plane, polarised at either $\pm 45^\circ$ to the x axis. There are four coils in the vacuum chamber, three are resonant with the transitions labelled (g)–(i) in Fig. 7.1, and an additional coil can drive the $F = 1^+ \rightarrow F = 0$ transition in $N = 1$ if needed. Finally, the microwave horn, shown in Fig. 5.2 launches microwaves which travel along the z axis. The horn is rotated so that two corners of the aperture (dimensions 21×25 mm) lie on the y

axis. Since the polarisation of microwaves is aligned to the short side of the horn, these microwaves are polarised in the y - x plane at 50.5° to the y axis. Of course, in reality the fields (especially the microwave field) are likely to be complicated by reflections from all the metallic structures in this region.

In the probe region, our goal was to maximise the scattering rate with respect to total intensity of the probe light. In the pump region, we do not have to worry about scattered laser light, so the laser power can be higher, the only limit being the powers we can produce with our lasers. Because the YbF beam is smaller in the pump region, the intensity of the laser beams will also be higher for a given laser power, so we can imagine using a total laser intensity of up to around $8I_{\text{sat}}$. The interesting question is to work out how big the rf and microwave fields need to be if they are to work well with this laser intensity.

7.4.2 Initial simulation

We start by picking some plausible parameters to check that the simulation works as expected. We know from the probe simulations that all the driving fields need to be suitably detuned slightly from resonance, and from each other, to prevent population being trapped in a CPT dark state. With that in mind we detune each of the rf and microwave fields a few hundred kHz from resonance. The magnetic field is chosen so that for each rf frequency, $\frac{\mu_B|B|}{\hbar} = 2\pi \times 1$ MHz, and the microwave electric field is chosen so that $\frac{\mu_e|E|}{\hbar} = 2\pi \times 1.5$ MHz, where $\mu_e = 3.91 \pm 0.03$ Debye is the YbF permanent dipole moment [50]. We set the total laser intensity to $8I_{\text{sat}}$ and the detunings, polarisation modulation rates and relative intensities in each beam to be those which maximised the probe scattering rate when $I_{\text{tot}} = 5I_{\text{sat}}$.

In the initial state of the molecular beam, the probability that a given m_F sub-level of rotational quantum number N is populated can be found from the Boltzmann distribution, Eq. (5.7). We normalise the probability distribution by restricting ourselves to molecules created in the first three rotational levels, $N \leq 2$, so that

$\sum_0^{N=2} 4(2N+1)P(N|T) \stackrel{!}{=} 1$. This means that the diagonal elements of the density matrix can be interpreted as the probability of occupying that energy level, given that the molecule was created with $N \leq 2$. For now, we will assume that the beam is at 3 K, the average rotational temperature of our source during normal operation. At this temperature, the probabilities of starting a given m_F level in $N = 0, 1, 2$ are in the ratio 1:0.79:0.5, which means that there is 23.5 times more YbF produced with $N \leq 2$ than in $|0, 0\rangle$.

The populations of the ground electronic states evolve under these conditions as shown in Fig. 7.23. We see that the population is pumped into the absolute ground state $X^2\Sigma^+(v=0, N=0, F=0)$, as desired, over the first 50 μs or so. The population also grows in the vibrationally excited states $X^2\Sigma^+(v>0)$. Population in $(N=2, F=3)$ is weakly mixed into the system of pumped levels by the rf field (h), which off-resonantly drives the transition $(N=2, F=2^-)$. Since the coupling is weak, we can ignore this level in our remaining calculations, but we should bear in mind that this level could also be accessed in future if we like. All the other remaining $v=0$ levels are pumped out, with a characteristic pumping time of order 10 μs . The excited state populations are shown in Fig. 7.24.

The results plotted in Fig. 7.23 are very promising. The probability of occupying $|0, 0\rangle$ after 50 μs has increased from 4.2% to 54.2%, a 13 fold increase in the ground state population. This is 7 times more signal than we have using the current pumping scheme. Of the remaining population, 25.0% is in $X^2\Sigma^+(v>0)$, 14.1% is in the $(N=2, F=3)$ level and the remaining 6.7% is distributed over the other ground states.

In the following section we will investigate how the pumping rate depends on the microwave and rf fields, so that we have a better idea what powers we should use, before repeating this calculation taking into account the Doppler shift of the laser beam.

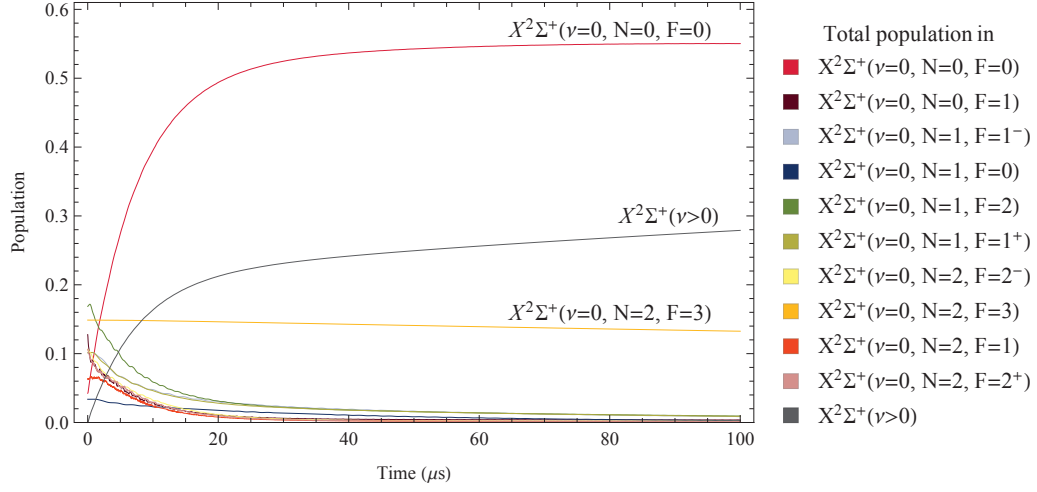


Fig. 7.23: Evolution of the ground state populations of the new pumping scheme shown on the left hand side of Fig. 7.1. The parameters for each beam are described in the accompanying text. We see that more than half the molecules are pumped into the ground state $X^2\Sigma^+(v=0, N=0, F=0)$.

7.4.3 Fraction pumped for various rf and laser powers

The fields in the pump region are not as well controlled as in the detection region; The variations in the power and direction of the microwave and rf fields are likely to be significant and complicated to determine. Therefore, it is a waste of time to painstakingly optimise the pumping rate for a given set of parameters. Instead, we just scan two parameters: the magnitude of the microwave electric field (f) and the magnitude of the three rf magnetic fields (g), (h) and (i), which we set to be equal. We do this for the same intensity as in the previous section, $I_{\text{tot}} = 8I_{\text{sat}}$. All other parameters are also left unchanged. For each simulation, we plot the gain in the $|0,0\rangle$ population after 50 μs , which is the maximum available interaction time in practice. The results of this simulation are shown in Fig. 7.25.

The important point to take away from this Fig. is that the microwave and rf Rabi rates have a definite optimum region: if too large or small a rate is used, the fraction of molecules pumped to $|0,0\rangle$ decreases. The microwave optimum happens

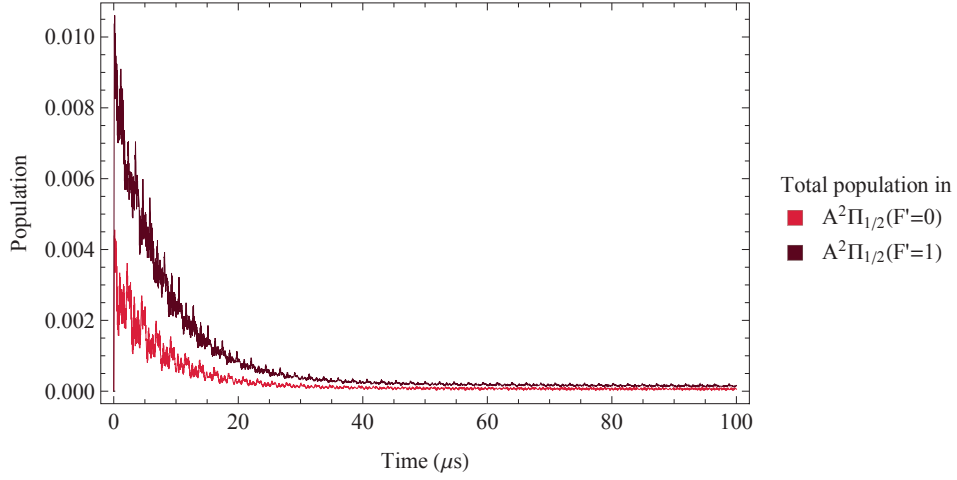


Fig. 7.24: Evolution of the excited state populations of the new pumping scheme shown on the left hand side of Fig. 7.1. The parameters for each beam are described in the accompanying text.

because the frequency of the microwave field (f) is only 9.1 MHz away from the transition $(N = 0, F = 0) \rightarrow (N = 1, F = 1^-)$. If the microwave power is too high this drives molecules out of $|0, 0\rangle$, redistributing the population among the electronic ground states before eventually it is lost to a vibrationally excited state. Similarly, if the rf radiation is too strong, the fields (h) and (i) off-resonantly drive population from $|0, 0\rangle$ into $(N = 0, F = 1)$, again reducing $|0, 0\rangle$ final population. Fig. 7.25 shows that the values used in the previous simulation, $\frac{\mu_B |B|}{\hbar} = 2\pi \times 1$ MHz and $\frac{\mu_e |E|}{\hbar} = 2\pi \times 1.5$ MHz are close to optimum.

7.4.4 Comparison of results with simple models in section 5.4.1

In section 5.4.1 we used a simple rate equation model to estimate the laser intensities needed to empty out all the levels being addressed. It is interesting now to see how coherences affect the pumping rate. This is illustrated in Fig. 7.26, which plots the fraction of the population that is pumped according to the OBEs (solid red line) and according to the rate equations (dashed red). Population in the weakly coupled

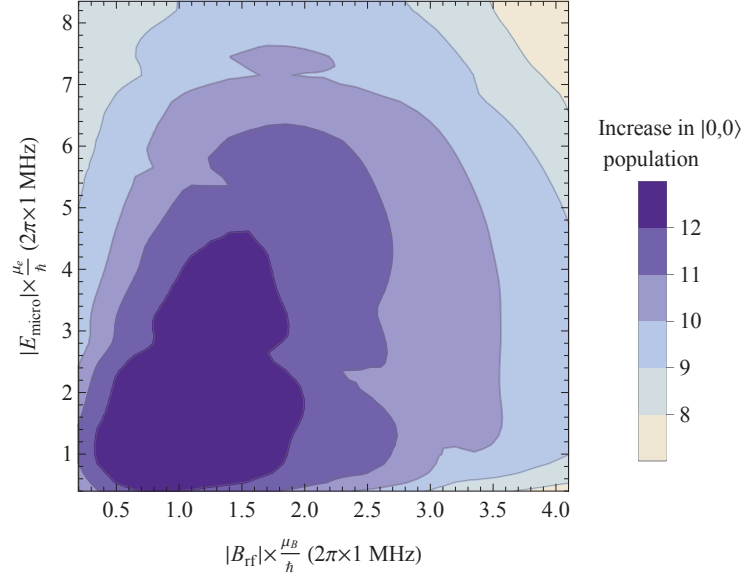


Fig. 7.25: Increase in $|0,0\rangle$ population as a function of microwave and rf Rabi rate. The total intensity is $I_{\text{tot}} = 8I_{\text{sat}}$.

$(N = 2, F = 3)$ state is neglected.

Initially, the classical model performs tolerably well, predicting that the levels are pumped at twice the rate given by the OBEs. However, after around $20 \mu\text{s}$ the two models diverge, as the pumping speed becomes limited by the rate at which the dark states can be destabilised. This slow decay rate was not correctly captured by the classical model, and underlines the importance of a full quantum treatment to correctly predict the effectiveness of the new scheme.

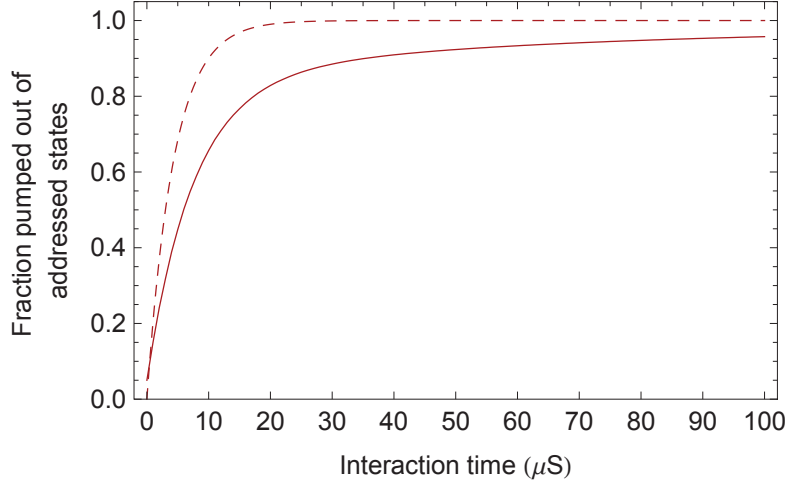


Fig. 7.26: The fraction of the population that is pumped according to the OBEs (solid red line) and the rate equations (dashed red) $I_{\text{tot}} = 8I_{\text{sat}}$.

7.4.5 Doppler broadening

Much as with the new probing scheme, it is also important to consider the distribution of transverse velocities. The relationship between the detuning of the laser beams and the final population pumped to the absolute ground state after 50 μs is shown in Fig. 7.27. Similarly to the situation for the probe region, those molecules with high transverse velocities will not be efficiently pumped to the ground state.

Using the measured Doppler profile (identical to the transverse Doppler profile used in section 7.3.3), and weighting the results of Fig. 7.27 accordingly, we find that the final population in the absolute ground state is increased by a factor of 10.5 when the total laser intensity is $8I_{\text{sat}}$, the interaction time is 50 μs and the microwave electric and rf magnetic fields are $\frac{\mu_e|E|}{\hbar} = 2\pi \times 1.5 \text{ MHz}$ and $\frac{\mu_B|B|}{\hbar} = 2\pi \times 1 \text{ MHz}$ respectively.

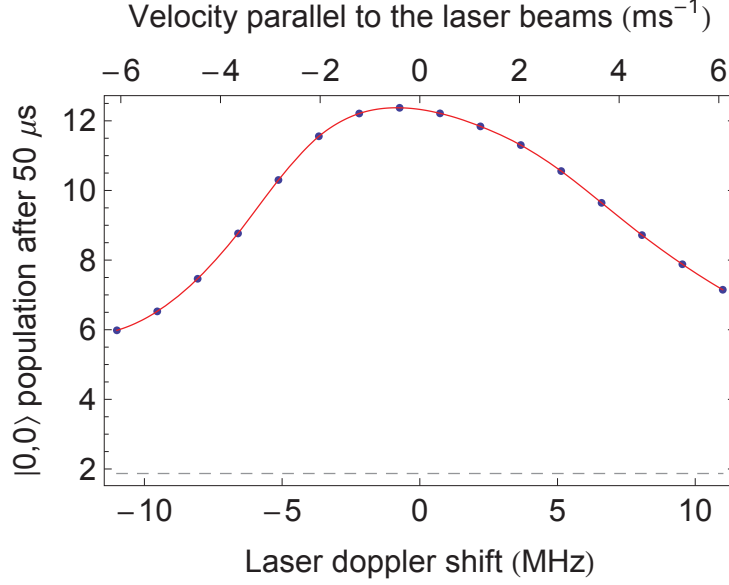


Fig. 7.27: The increase in the $|0,0\rangle$ population after 50 μs of the new pumping scheme, for various values of the laser Doppler shift. The grey dashed line at the bottom of the graph shows the population in $|0,0\rangle$ after the current pumping scheme.

7.4.6 Conclusion to the discussion of the new pumping scheme

The simulations in this section show that applying the laser, microwave and rf fields shown in Fig. 7.1 along the directions shown in Fig. 5.2 and with the polarisations described in 7.4.1 should result in an increase in the final population in the $|0,0\rangle$ state population of 10.5. Under the current, single frequency pumping scheme the increase is only 1.9, so the new pumping scheme should increase the population available to participate in the experiment by a factor of 5.6.

In order to achieve this, we need a total laser intensity of $8I_{\text{sat}}$, or 42 mW. We also a microwave electric field of $\frac{\mu_e|E|}{\hbar} = 2\pi \times 1.5$ MHz. If we ignore the effects of reflections from the rf coils and other metallic obstructions, this should require around 6 dBm of microwave power, which is easily achieved with a commercial synthesiser and amplifier. Finally, we need oscillating magnetic fields of $\frac{\mu_B|B|}{\hbar} = 2\pi \times 1$ MHz at each of the three rf frequencies. Even with the resonant coils, this may require a

high power amplifier.

7.5 Conclusions on OBE simulations

The goal of this chapter was to form a clear idea about how well the new pumping and detection schemes will work. In particular, we wanted to whether dark states would significantly compromise the scattering rates we hope to achieve.

We began by arguing that both angular momentum and CPT dark states could be remixed to avoid drastic reduction of the scattering rate, provided that the laser detunings and powers were optimised. We then moved on to the full YbF system. In our discussion of the new pumping scheme, we showed that our arrangements of fields can cause most of the population in the first three rotational levels to be pumped to $|0, 0\rangle$, the only exceptions being the $(N = 2, F = 3)$ state and those molecules with large transverse velocities. Compared with our current scheme, the overall increase in the number of molecules able to participate in the experiment should be around a factor of 5.6.

In our simulations of the new probing scheme, we found that for optimised laser detunings and modulation rates, the scattering rate predicted by the full solution to the OBEs is very close to the simple rate picture. However, it is important to emphasise how relatively low this scattering rate is; even though the radiative decay rate from the excited state is $2\pi \times 5.7$ MHz, the scattering rate from the excited state is only $2\pi \times 9$ kHz when each transition is driven at $I = I_{\text{sat}}$ because of the low probability for the molecule to occupy the excited state. Because of the Doppler shift it is likely that only those molecules with low transverse velocities will scatter the full 13.9 photons. Even so, we anticipate a large increase in the number of photons scattered per molecule, around 6 times more signal in each detection region.

One difficulty associated with the new detection scheme which we may need to address is that any signal left in the $N = 2$ or $N = 0$ by the first set of detection lasers

will be available to be detected again by the second set of lasers, reducing the contrast of the interferometer signal in the second detection region. Two effects will mitigate this. First, the new pumping scheme will be slightly velocity selective. It will narrow the transverse velocity spread and hence the Doppler width by preferentially pumping those molecules with low transverse velocities into $|0, 0\rangle$. Second, the molecules left in $N = 0, N = 2$ after the first set of detection lasers will be those with high Doppler shifts, and these will be excited less strongly by the lasers in the second detection region.

If the contrast in the second detection region still remains a problem, even taking these mitigating factors into account, there are a number of steps we could take.

1. We could attempt to work with higher power laser beams, but at some point the scatter from the lasers will overcome the gains from increased photon scattering.
2. We could use an additional “clean-up” laser beam between the first detection region and the second microwave transmission line to complete the pumping process, making sure that this was in a region where the scatter could not be detected by the PMTs.
3. We could introduce a slit to mask off the wings of the molecular beam, only allowing those molecules in the centre of the distribution with low Doppler shifts to participate in the experiment. This is obviously unattractive since it reduces the overall signal.
4. Alternatively, a drastic solution would be to leave the population transferred to $N = 1$ in place (i.e. not apply a second microwave pulse), and detect it with a different set of lasers tuned to the positive parity excited state. This measurement would not have any background signal from molecules left in $N = 0, 2$, but would require an additional laser system.

However things work in practice, we think it should be possible to dramatically increase the number of photons counted in each shot of the interferometer.

Improvement	Fractional improvement in sensitivity
Higher electric field	1.13
Higher contrast from shorter rf pulses	1.25
New pumping scheme	2.37
New probing scheme	3.46
Product	11.6

Tab. 7.3: Gains in sensitivity from improved experiment

This chapter suggests that it should be possible to increase the number of photon counts per shot by a factor of 70 in total (6 from beam intensity and 12 from detection efficiency). If the magnetic field noise continues to be well controlled, the operating voltages can be increased to ± 12 kV, and the contrast can be improved with shorter rf pulses, (as summarised in Table 7.3), then this should lead to a new sensitivity of $2.2 \times 10^{-27} \text{ e cm}/\sqrt{\text{Block}}$, more than a factor of 10 lower than our current statistical sensitivity.

8. CONCLUSION AND OUTLOOK

This thesis discussed the progress that has been made towards a new, more sensitive measurement of the eEDM using YbF. We can divide this progress into two main areas: First, we have increased our understanding of systematic errors affecting the measurement, and second, we have developed a comprehensive strategy to improve the experimental sensitivity.

8.1 *Systematic Errors*

Chapter 3 describes three new sources of systematic error with the measurement. The first involved rf discharge that could flow from the rf plates, potentially leading to a magnetic field which was correlated with the direction of the applied electric field. We showed that if the discharge is well controlled, this current, combined with the regular leakage currents from the high voltages plates, leads to a maximum systematic error no larger than $0.2 \times 10^{-28} e \text{ cm}$. The second systematic error was more troublesome: a rotation of the rf polarisation when the electric field direction was reversed. Improving the cabling between the electric field generation equipment and the machine greatly reduced this error, and we have formulated a good plan to associate a stringent error on the size of any residual effect. The final systematic error seems to be connected with a change in the high voltage supplies. So far, we have had more success in ruling out possible causes of the systematic than uncovering its exact origin, but we have discounted 1) the magnetisation of the shields through ac or dc currents 2) the rf rotation systematic error 3) any other previously known systematic error. Although this effect is at present unacceptably large

($\sim (5.3 \pm 2.6) \times 10^{-27} \text{ e cm}$) the fact that it can be made much smaller by exchanging the supplies suggests that with a little more persistence we can track down the origin of this systematic and remove it altogether.

8.2 Sensitivity

In Chapter 4 we showed that the statistical error in our measurement of the eEDM is dominated by shot noise, with a very small contribution from external magnetic field noise. This led us to propose in Chapter 5 that we could increase the statistical sensitivity of the machine by increasing the number of molecules able to participate in the experiment, and by detecting those molecules more efficiently.

We plan to increase the number of molecules participating in the experiment by pumping molecules produced by the source in $X^2\Sigma^+(N=0, F=1)$, $(N=1, F=2, 1^-, 1^+, 0)$ and $(N=2, F=2^-, 2^+, 1)$ into $F=0$. In Chapter 5 we calculated that with our beam's average rotational temperature (3K), we could expect a maximum of around 7.6 times more signal from this process. We then developed a simple rate model that predicted this increase should be attainable with the interaction times and laser powers at our disposal.

To detect the molecules more efficiently we plan to use a four part scheme. First the population in $F=0$ is transferred to $N=1$ with a microwave π -pulse, delivered with a microwave transmission line. This step can be close to 100% efficient. Second, the molecules remaining in $F=0$ are detected with lasers tuned to address all the decays from $A^2\Pi_{1/2}(\mathcal{P} = -1)$ to $X^2\Sigma^+(v=0)$. Each molecule in $F=0$ will scatter a maximum of 14 photons on average, more than ten times more signal than at present. Third, another microwave π -pulse will return the $N=1$ population to $F=0$. Fourth and finally, another set of lasers, tuned to address all the decays from $A^2\Pi_{1/2}(\mathcal{P} = -1)$ to $X^2\Sigma^+(v=0)$ will interact with the $F=0$ molecules. Each one of these molecules will also scatter a maximum of 14 photons on average before

decaying to $v > 0$.

To help us better understand the new pumping and detection schemes, we developed a more comprehensive density matrix model in Chapters 6 and 7 which could capture the effects of dark states on the pumping and probing schemes. We found that if sufficient care is taken to destabilise dark states, the scattering rates in the new probing scheme can be very close to the simple rate model, with the scattering rate given by Eq. 5.14, but with $I \rightarrow 0.7I$. The average number of photons scattered in 25 μs with a total intensity $I_{\text{tot}} = 5I_{\text{sat}}$ is 10.5, compared to the 12 photons predicted by the rate equation model. For the new pumping scheme, the effects of dark states show that the rate model does not give a good indication of the pumping rate, especially at longer interaction times. Even so, with a 50 μs interaction time and a total intensity of $I_{\text{tot}} = 8I_{\text{sat}}$, we achieve a fractional increase in the signal of 6.8 compared to our current pumping scheme, if the beam is at a rotational temperature of 3 K. This should be compared to a maximum possible increase of 7.6 at this rotational temperature. We find that for both the pumping and probing schemes, the transverse Doppler width decreases the effectiveness of the process, by 18% in the case of the pumping and 31% in the case of the new probing scheme. Taking this into account, we expect to increase the number of molecules participating in the experiment by a factor of 5.6 through the new pumping scheme, and increase the number of photons scattered per molecule by a factor of 6 in each detection region, for a total gain in signal of a factor of 12 in each shot. Combined with some other small improvements, we expect the total increase in sensitivity to be around a factor of 12.

8.3 Outlook

At the end of this thesis, we are left with a clear plan as to how to reduce the statistical uncertainty in our measurement of the eEDM by a factor of more than 10.

All of the apparatus to undertake the improved measurement has been constructed, and we anticipate that the new improved experiment will be operational by January 2016. Table 8.1 shows us how the parameters of the improved experiment compare to the 2014 ACME experiment. If we ran the experiment for around 100 days (about the length of last eEDM data run), we would achieve a statistical sensitivity of around $1.4 \times 10^{-29} e \text{ cm}$, a factor of 2.5 better than the current limit.

Property	ACME 2014	Imperial		
		2011	2015	Proposed
E_{eff} (GVcm $^{-1}$)	-81.5 ± 5.7^a	-26^b	-26^b	-26^b
W_S/E_{eff} ($e \text{ cm}$)	1.3×10^{-20c}	8.6×10^{-21c}	8.6×10^{-21c}	8.6×10^{-21c}
Polarisation factor $ \eta $	1	0.558	0.61	0.69
Magnetic moment g (μ_B)	0.0044^d	1	1	1
Interaction time (ms)	1.1	0.642	0.980	0.980
State lifetime (ms)	~ 2	∞	∞	∞
Molecules detected per pulse	$\sim 1000^e$	500	685	46,000
Contrast \mathcal{C}	0.94 ± 0.02^e	0.55^f	0.61 ± 0.01	0.76 ± 0.02
Sensitivity ($10^{-28} e \text{ cm}/\sqrt{\text{day}}$)	4^g	30	16	1.4

Tab. 8.1: A comparison of some relevant parameters associated with the ThO experiment in 2014, and the YbF experiment in 2011, 2015 and after the improvements described in this thesis. ^a Ref. [34], ^b Ref. [32], ^c Ref. [33], ^d Ref. [35], ^e Ref. [14], ^f Ref. [66], ^g Ref. [85]

The current upper limits on various systematic errors and their projected values

Systematic Error	Current upper limit ($10^{-28} e \text{ cm}$)	Projected upper limit ($10^{-28} e \text{ cm}$)
Un-corrected E-asymmetry	0.5*	0.05
Voltage offset	0.063*	0.063
Residual rf1 detuning	0.6*	0.06
dc and rf leakage currents	0.2**	0.2
dc shield magnetization [†]	0.5 (1.6)	0.25
ac shield magnetization [†]	0.05 (0.14)	0.05
rf rotation	-	0.084
Geometric phase	0.01	0.01
Motional magnetic field	0.0005	0.0005
Sum in quadrature	0.87	0.35

Tab. 8.2: Current and projected systematic errors. [†]numbers without brackets are for *Bertan* supplies and with brackets are for the *Applied Kilovolts* supplies. *taken with $2 \mu\text{s}$ pulses. **taken with $9 \mu\text{s}$ pulses.

are shown in Table 8.2. With the exception of the high voltage supplies systematics (not listed) the other systematic errors associated with the experiment are well controlled to less than $1 \times 10^{-28} e \text{ cm}$ at present. Looking forward to the size of those systematic errors in the improved experiment, we expect many errors to continue to reduce in size in line with the new statistical sensitivity. If this is the case, then the total systematic error-bar (again excluding the unknown high voltage systematic error) will be less than $0.35 \times 10^{-28} e \text{ cm}$. This error is dominated by the dc shield magnetisation and the leakage currents. There is considerable scope for more careful measurement of these effects with the current apparatus, and we are also buying improved optical magnetometers that can sit inside the vacuum chamber and make better direct measurements of both these errors.

Thus, we expect that in the near future, the YbF experiment will be able to

make a new, world leading measurement of the eEDM with a total uncertainty of a few $10^{-29} e \text{ cm}$ and we can continue the search for new T-violating physics with the apparatus described in this thesis.

APPENDIX

A. QUANTUM MECHANICAL ROTATION MATRICES

The operator $\hat{\mathcal{R}}(\boldsymbol{\alpha})$ that rotates a quantum mechanical state $|\psi\rangle$ by an angle α about the axis $\boldsymbol{\alpha}/|\boldsymbol{\alpha}|$ to leave it in the new state $\hat{\mathcal{R}}(\boldsymbol{\alpha})|\psi\rangle = |\psi'\rangle$ can be written as

$$\hat{\mathcal{R}}(\boldsymbol{\alpha}) = e^{-i\boldsymbol{\alpha}\cdot\hat{\mathbf{F}}}, \quad (\text{A.1})$$

where $\hat{\mathbf{F}}$ is the vector operator whose elements are the projection of the total angular momentum operator onto the three coordinate axes $\mathbf{F} = (\hat{F}_x, \hat{F}_y, \hat{F}_z)$ [86]. The rotated version of an operator \hat{A} is simply

$$\hat{\mathcal{R}}^\dagger(\boldsymbol{\alpha}) \hat{A} \hat{\mathcal{R}}(\boldsymbol{\alpha}). \quad (\text{A.2})$$

Often, we want to find the matrix elements $\hat{\mathcal{R}}_{ij} = \langle i | \hat{\mathcal{R}} | j \rangle$ of the rotation operator. When these are written in terms of the basis states of the total angular momentum F and the projections m, m' along a particular z axis then they form what is known as Wigner rotation matrix

$$\langle F, m' | \hat{\mathcal{R}} | F, m \rangle = \mathcal{D}_{m'm}^F. \quad (\text{A.3})$$

The values of $\mathcal{D}_{m'm}^F$ can be looked up and are useful in evaluating the various matrix elements found in the next appendix.

B. MATRIX ELEMENTS FOR YbF

This appendix explains how to calculate the matrix elements for magnetic and electric dipole transitions between the various states of the $X^2\Sigma^+(v=0, N=0, 1, 2)$ and $A^2\Pi_{1/2}(v=0, J=\frac{1}{2}, \mathcal{P}=\pm 1)$ levels. The starting point for these elements are the terms shown in Eq. (6.8). Because we make the dipole approximation, A_p^f is constant and can be factorised out of the inner product

$$M_{ij}^f = \sum_p \frac{A_p^f}{2\hbar} \langle i | \hat{\mathbf{m}} \cdot \boldsymbol{\epsilon}_p | j \rangle. \quad (\text{B.1})$$

The symbol f denotes that this element is for the field labelled f . If i and j are different electronic or rotational levels $\hat{\mathbf{m}} = \hat{\mathbf{d}}$ and $A_p^f = E_p^f$, and if i and j are in the same rotational level of the ground electronic level, then $\hat{\mathbf{m}} = \hat{\boldsymbol{\mu}}$ and $A_p^f = B_p^f$.

The remainder of this chapter is concerned with the calculation of the “projection factors” $\langle i | \hat{\mathbf{m}} \cdot \boldsymbol{\epsilon}_p | j \rangle$. First, we need to express the molecular states $|i\rangle$ $|j\rangle$ in terms of some convenient basis functions, which we do in the following sections. Then, to evaluate a given projection factor, we start by applying the Wigner-Eckart theorem to separate the orientation-dependent part of the projection factor from the rotationally invariant part, otherwise known as the reduced matrix element. We then uncouple the angular momenta back to a level that is common to both the bra and ket of the reduced matrix element. The specific formulae used to uncouple angular momentum can be found in many standard texts such as Zare [3] and Brown and Carrington [87]. In order to do this we need a more explicit form of the YbF wavefunctions which are given in Refs. [50] and [88], and reproduced here in section B.1. In the

specific case of the optical transitions, we follow an identical procedure to Wall *et al* in Ref. [88] but using the parameters for YbF not CaF. In all of these calculations I am indebted to M. Tarbutt for his *Mathematica* notebooks and assistance.

B.1 Form of the wavefunctions

B.1.1 $A^2\Pi_{1/2}$

As we discussed in section 2.2.3, the $A^2\Pi_{1/2}$ is an Ω -doublet, having positive and negative parity states. These excited states are not degenerate because there is a small (amplitude of order 0.01) mixture of the $B^2\Sigma^+$ state, but we ignore that here and take the state to be of pure $A^2\Pi_{1/2}$ character. We choose basis states which are eigenfunctions of $\hat{\Lambda}$, $\hat{\Sigma}$ and $\hat{\Omega}$, the projections of $\hat{\mathbf{L}}$, $\hat{\mathbf{S}}$ and $\hat{\mathbf{J}} = \hat{\mathbf{L}} + \hat{\mathbf{S}}$ respectively onto the internuclear axis. This scheme is known as Hund's case (a). The wavefunction (2.10) can now be written as symmetric and antisymmetric combinations of states with $|\Lambda| = 1$, $|\Omega| = 1/2$ and $J = 1/2$

$$\begin{aligned} |\psi_{\text{ES}}\rangle &= |A, J = \tfrac{1}{2}, \mathcal{P}\rangle |v' = 0\rangle |I = \tfrac{1}{2}, F, m_F\rangle \\ &= \frac{1}{\sqrt{2}} (|1, \tfrac{1}{2}, -\tfrac{1}{2}, \tfrac{1}{2}, \tfrac{1}{2}\rangle + \mathcal{P} |-1, \tfrac{1}{2}, \tfrac{1}{2}, \tfrac{1}{2}, -\tfrac{1}{2}\rangle) |0\rangle |\tfrac{1}{2}, F, m_F\rangle, \end{aligned} \quad (\text{B.2})$$

where the parity \mathcal{P} takes the values $+1$ (even) and -1 (odd).

Typically we will join the first and third kets in the above expression together so that the basis vectors for the non vibrational part of the excited state wavefunction are labelled by

$$|\Lambda, S, \Sigma, J, \Omega, I, F, m_F\rangle. \quad (\text{B.3})$$

B.1.2 $X^2\Sigma^+$

In the ground state, the situation is slightly more complicated because of the nonzero rotational angular momentum. We start by picking the basis

$$|N, S = \frac{1}{2}, J, I = \frac{1}{2}, F, m_F\rangle \quad (\text{B.4})$$

that specifies the quantum numbers for the three angular momenta $(\hat{N}, \hat{S}, \hat{I})$, defined on p. 38, that make up \hat{F} . In this basis, we first couple \hat{N} and \hat{S} to make $\hat{J} = \hat{N} + \hat{S}$, and then let $\hat{F} = \hat{J} + \hat{I}$. This is known as Hund's case $b_{\beta J}$ [87].

For $N = 0$, F has just two values, $F = 0$ and $F = 1$, arising from the coupling of \hat{S} and \hat{I} . For $N > 0$, there are four states, with F quantum numbers $F = N + 1$, $F = N$, $F = N$ and $F = N - 1$. The first and last of these states are just given by

$$|N, F = N \pm 1, m_F\rangle = |N, \frac{1}{2}, N \pm \frac{1}{2}, \frac{1}{2}, N \pm 1, m_F\rangle. \quad (\text{B.5})$$

The remaining states are mixtures of $J = N \pm \frac{1}{2}$ whose coefficients are given by Sauer *et al* [50]. For $N = 1$ and $N = 2$ the J-mixed states are

$$|1, 1^-, m_F\rangle = -0.536 |1, \frac{1}{2}, \frac{1}{2}, \frac{1}{2}, 1, m_F\rangle + 0.884 |1, \frac{1}{2}, \frac{3}{2}, \frac{1}{2}, 1, m_F\rangle, \quad (\text{B.6})$$

$$|1, 1^+, m_F\rangle = 0.884 |1, \frac{1}{2}, \frac{1}{2}, \frac{1}{2}, 1, m_F\rangle + 0.536 |1, \frac{1}{2}, \frac{3}{2}, \frac{1}{2}, 1, m_F\rangle, \quad (\text{B.7})$$

$$|2, 2^-, m_F\rangle = -0.564 |1, \frac{1}{2}, \frac{3}{2}, \frac{1}{2}, 2, m_F\rangle + 0.826 |2, \frac{1}{2}, \frac{5}{2}, \frac{1}{2}, 2, m_F\rangle, \quad (\text{B.8})$$

$$|2, 2^+, m_F\rangle = 0.826 |1, \frac{1}{2}, \frac{3}{2}, \frac{1}{2}, 2, m_F\rangle + 0.564 |2, \frac{1}{2}, \frac{5}{2}, \frac{1}{2}, 2, m_F\rangle. \quad (\text{B.9})$$

When we need to calculate matrix elements connecting $X^2\Sigma^+$ and $A^2\Pi_{1/2}$ levels, we need to write the states in terms of a common basis. The simplest way to do this

is to rewrite the states of $X^2\Sigma^+$ in terms of those of $A^2\Pi_{1/2}$, using¹ Eq. (23 a) of Ref. [89], which for a linear molecule is

$$|\eta, \Lambda, N, S, J, I, F, m_F\rangle = \sum_{\Omega, \Sigma} (-1)^{N-S+\Omega} \sqrt{(2N+1)} \begin{pmatrix} J & S & N \\ \Omega & -\Sigma & -\Lambda \end{pmatrix} \times |\eta, \Lambda, S, \Sigma, J, \Omega, I, F, m_F\rangle . \quad (\text{B.10})$$

Here η stands for any other quantum numbers. In our case for the electronic ground states with $\Lambda = 0$ and $S = 1/2$ this becomes

$$|N, S, J, I, F, m_F\rangle = \frac{1}{\sqrt{2}} |\Lambda, S, -\Sigma, J, -\Omega, I, F, m_F\rangle + \frac{(-1)^{N+J-1/2}}{\sqrt{2}} |\Lambda, S, \Sigma, J, \Omega, I, F, m_F\rangle . \quad (\text{B.11})$$

B.2 Calculating the projection factors

Now we can finally calculate the factors $\langle i | \hat{\mathbf{m}} \cdot \boldsymbol{\epsilon}_p | j \rangle$ that project the dipole onto the direction of the external field components. First we calculate the matrix elements for transitions between the basis states, which are given by expression (B.4) for the rf and microwave transitions, and expression (B.3) for the optical matrix elements. Then, we expand $|i\rangle$ and $|j\rangle$ on this basis to compute the projection factors.

B.2.1 Projection factors for the rf transitions

In the new pumping scheme, we drive rf transitions between F components in the same rotational state of the X-state.² The matrix elements between the basis states

¹ Note that Eq. (6.149) of Ref. [87] is incorrect because of the effect of anomalous commutation relations, see Ref. [89].

² It does not help to drive transitions within the A-state.

are of the form

$$-g_s\mu_B \langle N', S, J', I, F', m'_F | \hat{\mathbf{S}} \cdot \boldsymbol{\epsilon}_p | N, S, J, I, F, m_F \rangle \delta_{vv'} \delta_{XX'} . \quad (\text{B.12})$$

The spin operator does not act on the orbital electronic wavefunction and vibrational wavefunctions, hence they are contracted over and have been removed, leaving the two Kronecker delta functions. Now this matrix element can be evaluated by first applying the Wigner-Eckart theorem (Eq. (5.14) of Ref. [3]) to give

$$g_s\mu_B (-1)^{1+F'-m'_F} \begin{pmatrix} F' & 1 & F \\ -m'_F & p & m_F \end{pmatrix} \langle N', S, J', I, F' || \hat{\mathbf{S}} || N, S, J, I, F \rangle . \quad (\text{B.13})$$

The $\hat{\mathbf{S}}$ operator acts on the first angular momentum $\hat{\mathbf{J}}$ of the coupled system $\hat{\mathbf{F}} = \hat{\mathbf{J}} + \hat{\mathbf{I}}$, and acts on the second part of the coupled system $\hat{\mathbf{J}} = \hat{\mathbf{N}} + \hat{\mathbf{S}}$, so we twice use the equations for a rank-1 tensor acting on one part of a coupled system (Eqs. (5.72) and (5.73) of Zare [3]) to give

$$\begin{aligned} \langle N', S, J', I, F' || \hat{\mathbf{S}} || N, S, J, I, F \rangle = \\ (-1)^{2J'+N'+1+F} \sqrt{(2F'+1)(2F+1)(2J'+1)(2J+1)} \times \\ \left\{ \begin{matrix} J' & F' & 1/2 \\ F & J & 1 \end{matrix} \right\} \left\{ \begin{matrix} 1/2 & J' & N' \\ J & 1/2 & 1 \end{matrix} \right\} \langle N', S || \hat{\mathbf{S}} || N, S \rangle . \end{aligned} \quad (\text{B.14})$$

The last term is a standard expression which gives

$$\langle N', S || \hat{\mathbf{S}} || N, S \rangle = \delta_{N'N} \sqrt{(2S+1)S(S+1)} . \quad (\text{B.15})$$

Putting it all together we get that if f is an rf field³

$$\begin{aligned} \langle N, S, J', I, F', m'_F | \hat{\boldsymbol{\mu}} \cdot \boldsymbol{\epsilon}_p | N, S, J, I, F, m_F \rangle = \\ g_s \mu_B (-1)^{1+F'-m'_F+2J'+N+1+F} \sqrt{\frac{3}{2}(2F'+1)(2F+1)(2J'+1)(2J+1)} \times \\ \begin{pmatrix} F' & 1 & F \\ -m'_F & p & m_F \end{pmatrix} \begin{Bmatrix} J' & F' & 1/2 \\ F & J & 1 \end{Bmatrix} \begin{Bmatrix} 1/2 & J' & N \\ J & 1/2 & 1 \end{Bmatrix}. \end{aligned} \quad (\text{B.16})$$

B.2.2 Microwave projection factors

Microwave transitions can be driven between different rotational levels of the ground electronic state. The operator that does this is $\hat{\mathbf{d}} \cdot \boldsymbol{\epsilon}_p = \hat{\boldsymbol{\mu}}_e \cdot \boldsymbol{\epsilon}_p$, where $\hat{\boldsymbol{\mu}}_e$ is the permanent dipole moment of the molecule caused by the separated Yb⁺ and F⁻ ions in their ionic bond. In the molecule-fixed frame, this permanent dipole lies along the z -axis. The Wigner rotation matrix (Eq. (A.3)) allows us to project that onto the external field direction

$$\hat{\boldsymbol{\mu}}_e \cdot \boldsymbol{\epsilon}_p = \hat{\mu}_e \mathcal{D}_{0p}^1. \quad (\text{B.17})$$

The matrix elements of the projection factor are then

$$\langle X, \Lambda = 0 | \hat{\mu}_e | X, \Lambda = 0 \rangle \langle N', S, J', I, F', m'_F | \mathcal{D}_{0p}^1 | N, S, J, I, F, m_F \rangle \delta_{vv}. \quad (\text{B.18})$$

The first inner product just gives the expectation value of the molecular dipole moment $\mu_e = 3.91 \pm 0.03$ Debye [50]. The procedure to evaluate the second inner product is almost identical to that on p. 266 of Ref. [87] with the added complication of the fluorine nuclear spin. First we apply the Wigner-Eckart theorem to give the

³ This is similar to Eq. (9.95) in Ref. [87] but with the added complication of the fluorine spin in our case.

reduced matrix element just as with the rf elements

$$\mu_e(-1)^{F'-m'_F} \begin{pmatrix} F' & 1 & F \\ -m'_F & p & m_F \end{pmatrix} \langle N', S, J', I, F' \| \mathcal{D}_{.0}^1 \| N, S, J, I, F \rangle, \quad (\text{B.19})$$

where $\mathcal{D}_{.0}^1$ is the reduced rotation matrix operator. Now, we need to rewrite the reduced matrix elements in a basis where $\hat{\mathbf{N}}$ has been uncoupled from $\hat{\mathbf{S}}$ and $\hat{\mathbf{I}}$, because $\mathcal{D}_{.0}^1$ only act on the spatial degrees of freedom. As with the rf elements we notice that $\mathcal{D}_{.0}^1$ only acts on the first part of the coupled system $\hat{\mathbf{F}} = \hat{\mathbf{J}} + \hat{\mathbf{I}}$ and only acts on the first part of the coupled system $\hat{\mathbf{J}} = \hat{\mathbf{N}} + \hat{\mathbf{S}}$ so applying Eq. (5.72) of Ref. [3] twice we find

$$\begin{aligned} \langle N', S, J', I, F' \| \mathcal{D}_{.0}^1 \| N, S, J, I, F \rangle = \\ (-1)^{J'+J+N'+1+F} \sqrt{(2F'+1)(2F+1)(2J'+1)(2J+1)} \times \\ \begin{Bmatrix} J' & F' & 1/2 \\ F & J & 1 \end{Bmatrix} \begin{Bmatrix} N' & J' & 1/2 \\ J & N & 1 \end{Bmatrix} \langle N' \| \mathcal{D}_{.0}^1 \| N \rangle. \end{aligned} \quad (\text{B.20})$$

The final reduced matrix element is a standard result, given by Eq. (5.148) of Ref. [87]

$$\langle N' \| \mathcal{D}_{.0}^1 \| N \rangle = (-1)^{N'} \sqrt{(2N'+1)(2N+1)} \begin{pmatrix} N' & 1 & N \\ 0 & 0 & 0 \end{pmatrix}. \quad (\text{B.21})$$

Combining these results, the projection factors for the dipole matrix elements are

given by

$$\begin{aligned}
\langle N', S, J', I, F' | \hat{\mathbf{d}} \cdot \boldsymbol{\epsilon}_p | N, S, J, I, F \rangle = & \\
& (-1)^{J'+J+1+F+F'-m'_F} \\
& \times \sqrt{(2F'+1)(2F+1)(2J'+1)(2J+1)(2N'+1)(2N+1)} \\
& \times \begin{pmatrix} F' & 1 & F \\ -m'_F & p & m_F \end{pmatrix} \begin{pmatrix} N' & 1 & N \\ 0 & 0 & 0 \end{pmatrix} \\
& \times \begin{Bmatrix} J' & F' & 1/2 \\ F & J & 1 \end{Bmatrix} \begin{Bmatrix} N' & J' & 1/2 \\ J & N & 1 \end{Bmatrix}. \tag{B.22}
\end{aligned}$$

B.2.3 Optical projection factors

The final set of matrix elements that need to be calculated are those for the optical transitions between the $X^2\Sigma^+$ and $A^2\Pi_{1/2}$ levels. These are used both to calculate the matrix elements that arise when laser beams are applied to the molecules, and to evaluate the relaxation terms in the optical Bloch equations. As with the microwave transition, it is helpful to rewrite the operator $\hat{\mathbf{d}} \cdot \boldsymbol{\epsilon}_p$ in terms of the components of the angular momentum tensor in the molecule-fixed frame. Unlike the microwave transitions, however, the electric dipole in this case is the dipole operator for the optically active electron $\hat{\mathbf{d}} = -e\hat{\mathbf{r}}$ which does not have to lie along the z axis of the molecule-fixed frame. Using the Wigner rotation matrices this becomes

$$\hat{\mathbf{d}} \cdot \boldsymbol{\epsilon}_p = \sum_{q \in \{-1, 0, 1\}} \hat{d}_q \mathcal{D}_{qp}^1. \tag{B.23}$$

We choose to evaluate this operator using the basis states (B.3)

$$\sum_{q \in \{-1, 0, 1\}} \langle \Lambda', S', \Sigma', J', \Omega', F', m'_F | \hat{d}_q \mathcal{D}_{qp}^1 | \Lambda, S, \Sigma, J, \Omega, F, m_F \rangle \langle v' | v \rangle. \tag{B.24}$$

Unlike the rf and microwave transitions, the optical matrix elements connect different electronic states. These have slightly different vibrational wavefunctions which are not orthogonal, so the second inner product is not equal to one. For YbF $|\langle v' = 0 | v = 0 \rangle|^2 = 0.928$ [53]. After applying the Wigner-Eckart theorem and uncoupling $\hat{\mathbf{F}}$ back into $\hat{\mathbf{I}}$ and $\hat{\mathbf{J}}$ the first factor in expression (B.24) can be rewritten as

$$(-1)^{2F' - m'_F + J' + 3/2} \sqrt{(2F' + 1)(2F + 1)} \begin{pmatrix} F' & 1 & F \\ -m'_F & p & m_F \end{pmatrix} \begin{Bmatrix} J' & F' & 1/2 \\ F & 1/2 & 1 \end{Bmatrix} \times \sum_{q \in \{-1, 0, 1\}} \langle \Lambda', S', \Sigma', J', \Omega' | \hat{d}_q \mathcal{D}_q^1 | \Lambda, S, \Sigma, J, \Omega \rangle. \quad (\text{B.25})$$

The sum over reduced matrix elements in this last expression can be rewritten [88] as

$$\sum_{q \in \{-1, 0, 1\}} \langle \Lambda', S', \Sigma', J', \Omega' | \hat{d}_q \mathcal{D}_q^1 | \Lambda, S, \Sigma, J, \Omega \rangle = \sum_{q \in \{-1, 1\}} (-1)^{J' - \Omega'} \sqrt{(2J' + 1)(2J + 1)} \times \begin{pmatrix} J' & 1 & J \\ -\Omega' & q & \Omega \end{pmatrix} \mu_{\text{A-X}}, \quad (\text{B.26})$$

where $|\mu_{\text{A-X}}|^2 = \frac{3\pi\epsilon_0\hbar c^3\Gamma}{\omega^3}$ is the transition dipole moment, equal to 4.39 ± 0.16 Debye [53].

Thus, the projection factors for optical transitions between the basis states are

given by

$$\begin{aligned}
& \langle \Lambda', S, \Sigma, J', \Omega', I, F', m'_F | \hat{\mathbf{d}} \cdot \boldsymbol{\epsilon}_p | \Lambda, S, \Sigma, J, \Omega, I, F, m_F \rangle \langle v' | v \rangle = \\
& \mu_{A-X} \langle v' | v \rangle (-1)^{2F' - m'_F + 2J' - \Omega' + 3/2} \sqrt{(2F' + 1)(2F + 1)(2J' + 1)(2J + 1)} \\
& \times \sum_{q \in \{-1, 1\}} \begin{pmatrix} F' & 1 & F \\ -m'_F & p & m_F \end{pmatrix} \left\{ \begin{matrix} J' & F' & 1/2 \\ F & 1/2 & 1 \end{matrix} \right\} \begin{pmatrix} J' & 1 & J \\ -\Omega' & q & \Omega \end{pmatrix}. \quad (\text{B.27})
\end{aligned}$$

The real ground-state and excited-state eigenvectors $|\psi_{\text{GS}}\rangle$ and $|\psi_{\text{ES}}\rangle$ can be written out in terms of the basis vectors using Eqs. (2.3), (2.10), (B.2), (B.11) and (B.5)–(B.9). When we calculate the projection factors with these real states, we find as expected that the dipole operator only connects states of opposite parity, so there are two separate systems: $A^2\Pi_{1/2}(\mathcal{P} = 1)$ can only be excited from, and decay to $X^2\Sigma^+(N = 1)$ whereas $A^2\Pi_{1/2}(\mathcal{P} = -1)$ can transition to $X^2\Sigma^+(N = 0)$ and $X^2\Sigma^+(N = 2)$. The projection factors for these two closed systems are shown in the two Tables B.1 and B.2.

By squaring the elements in these two tables one obtains the relative probability that a given excited state $|F, m_F\rangle$ will decay into each of the ground states. This is also called the branching ratio.

		$A^2\Pi_{1/2}(\mathcal{P} = -1)$			
		$ 0, 0\rangle$	$ 1, -1\rangle$	$ 1, 0\rangle$	$ 1, 1\rangle$
$X^2\Sigma^+$ ($v = 0$)	$ 0, 0, 0\rangle$	0	-0.454	-0.454	-0.454
	$ 0, 1, -1\rangle$	0.454	0.454	0.454	0
	$ 0, 1, 0\rangle$	-0.454	-0.454	0	0.454
	$ 0, 1, 1\rangle$	0.454	0	-0.454	-0.454
	$ 2, 2^-, -2\rangle$	0	-0.222	0	0
	$ 2, 2^-, -1\rangle$	0	0.157	-0.157	0
	$ 2, 2^-, 0\rangle$	0	-0.091	0.181	-0.091
	$ 2, 2^-, 1\rangle$	0	0	-0.157	0.157
	$ 2, 2^-, 2\rangle$	0	0	0	-0.222
	$ 2, 1, -1\rangle$	0.321	-0.161	-0.161	0
	$ 2, 1, 0\rangle$	-0.321	0.161	0	-0.161
	$ 2, 1, 1\rangle$	0.321	0	0.161	0.161
	$ 2, 2^+, -2\rangle$	0	0.325	0	0
	$ 2, 2^+, -1\rangle$	0	-0.230	0.230	0
	$ 2, 2^+, 0\rangle$	0	0.133	-0.265	0.133
	$ 2, 2^+, 1\rangle$	0	0	0.230	-0.230
	$ 2, 2^+, 2\rangle$	0	0	0	0.325

Tab. B.1: Projection factors $\frac{1}{\mu_{A-X}} \langle \psi_{ES} | \hat{\mathbf{d}} \cdot \boldsymbol{\epsilon}_p | \psi_{GS} \rangle$ between the hyperfine levels $|F, m_F\rangle$ of $A^2\Pi_{1/2}(\mathcal{P} = -1)$ and the hyperfine levels $|N, F^{+/-}, m_F\rangle$ of $X^2\Sigma^+$. The sum of the squares of each column gives the branching ratio for decays to the $X^2\Sigma^+(v = 0)$ levels, $f_{00} = 0.928$.

		$A^2\Pi_{1/2}(\mathcal{P} = 1)$			
		$ 0, 0\rangle$	$ 1, -1\rangle$	$ 1, 0\rangle$	$ 1, 1\rangle$
$X^2\Sigma^+$ ($v = 0$)	$ 1, 1^-, -1\rangle$	0.028	-0.379	-0.379	0
	$ 1, 1^-, 0\rangle$	-0.028	0.379	0	-0.379
	$ 1, 1^-, 1\rangle$	0.028	0	0.379	0.379
	$ 1, 0, 0\rangle$	0	-0.454	-0.454	-0.454
	$ 1, 2, 2\rangle$	0	0.393	0	0
	$ 1, 2, -1\rangle$	0	-0.278	0.278	0
	$ 1, 2, 0\rangle$	0	0.161	-0.321	0.161
	$ 1, 2, 1\rangle$	0	0	0.278	-0.278
	$ 1, 2, 2\rangle$	0	0	0	0.393
	$ 1, 1^+, -1\rangle$	0.556	0.297	0.297	0
	$ 1, 1^+, 0\rangle$	-0.556	-0.297	0	0.297
	$ 1, 1^+, 1\rangle$	0.566	0	-0.297	-0.297

Tab. B.2: Projection factors $\frac{1}{\mu_{A-X}} \langle \psi_{ES} | \hat{\mathbf{d}} \cdot \boldsymbol{\epsilon}_p | \psi_{GS} \rangle$ between the hyperfine levels $|F, m_F\rangle$ of $A^2\Pi_{1/2}(\mathcal{P} = 1)$ and the hyperfine levels $|N, F^{+/-}, m_F\rangle$ of $X^2\Sigma^+$. The sum of the squares of each column gives the branching ratio for decays to the $X^2\Sigma^+(v = 0)$ levels, $f_{00} = 0.928$.

B.3 g factors

We also want to consider how the energy levels shift when a static magnetic field B is applied along a given axis. Taking that axis to be z , the shift in a ground state energy level $|N, F^{+/-}, m_F\rangle$ (which has no orbital angular momentum) for small applied fields is found via first order perturbation theory to be

$$\Delta E = g_s \mu_B B \langle N, F^{+/-}, m_F | \hat{\mathbf{S}} \cdot \boldsymbol{\epsilon}_0 | N, F^{+/-}, m_F \rangle, \quad (\text{B.28})$$

here g_s is once again the absolute value of the electron gyromagnetic ratio $g_e \simeq -2$. These energy shifts can be rewritten in terms of the Landé g -factors g_F for a given level

$$\Delta E = g_F \mu_B B m_F, \quad (\text{B.29})$$

where the g -factors $g_F = \frac{g_s}{m_F} \langle N, F^{+/-}, m_F | \hat{\mathbf{S}} \cdot \boldsymbol{\epsilon}_0 | N, F^{+/-}, m_F \rangle$ shown in Table B.3 can be calculated using the results in subsection B.2.1.

$ N, F^{+/-}\rangle$	$-g_F$
$ 0, 0\rangle$	0
$ 0, 1\rangle$	1
$ 1, 1^-\rangle$	0.071
$ 1, 0\rangle$	0
$ 1, 2\rangle$	1/2
$ 1, 1^+\rangle$	0.428
$ 2, 2^-\rangle$	0.023
$ 2, 1\rangle$	-1/2
$ 2, 2^+\rangle$	0.477

Tab. B.3: g_F factors of a few of the $X^2\Sigma^+ (v=0)$ states

Finding the g_F factors for the excited states is slightly more complicated because the magnetic dipole operator contains contributions from the orbital angular momenta and from smaller terms that arise from mixing between $\text{A } ^2\Pi_{1/2}$ and other neighbouring electronic states. To find the g_F factors one needs to evaluate Eq. (9.71) of Ref. [87], using the various constants given in Ref. [90]. This has been done by M. Tarbutt [69], giving the g_F factors for the $F' = 1$ levels of $\text{A } ^2\Pi_{1/2}(\mathcal{P})$ as $g_F = -0.268 \times \mathcal{P}$.

C. PERMISSIONS

Jack Devlin,
Research Assistant,
Department of Physics,
Blackett Laboratory,
Imperial College London,
Prince Consort Road,
London SW7 2BB,
United Kingdom.

APS Permissions,
One Physics Ellipse,
College Park,
MD 20740-3844,
USA.

26/6/2015

To Whom it May Concern,

I am completing my PhD thesis at Imperial College London entitled 'Progress towards a more sensitive measurement of the electron electric dipole moment with YbF'.

I seek your permission to reprint, in my thesis an extract from: T. Chupp and M. Ramsey-Musolf, "Electric dipole moments: A global analysis, " *Physical Review C*, vol. 91, no.3, p. 035502, Mar. 2015. The extract to be reproduced is: Figure 1.

I would like to include the extract in my thesis which will be added to Spiral, Imperial's institutional repository <http://spiral.imperial.ac.uk/> and made available to the public under a [Creative Commons Attribution-NonCommercial-NoDerivs licence](#).

If you are happy to grant me all the permissions requested, please return a signed copy of this letter. If you wish to grant only some of the permissions requested, please list these and then sign.

Yours sincerely,

Jack Devlin

Permission granted for the use requested above:

I confirm that I am the copyright holder of the extract above and hereby give permission to include it in your thesis which will be made available, via the internet, for non-commercial purposes under the terms of the user licence.

[please edit the text above if you wish to grant more specific permission]

Signed:

Name:

Organisation:

Job title:

From: Associate Publisher <assocpub@aps.org>
Sent: 08 July 2015 16:39
To: Devlin, Jack A
Subject: Response to Letter

Hi Jack,

Thank you for your letter. To request APS copyright permission please refer to the article abstract page with the figure you wish to republish. There you will find a button on the right-hand side listed 'Reuse & Permissions'. Please answer the series of questions to generate a letter of permission.

You may post your thesis on Imperial College's institutional repository, since you are a student. Proper bibliographic citation and notice of APS copyright must be included.

Just to clarify, only the APS figure in your thesis is permissible to publish. If you want to incorporate the entire APS article that will require more attention; please let me know.

Feel free to ask any other questions you may have.

Best Wishes,

Alex Menendez
APS

10/20/2015

RightsLink - Your Account

American Physical Society License Details

Oct 20, 2015

This is an Agreement between Jack A Devlin ("You") and American Physical Society ("Publisher"). It consists of your order details, the terms and conditions provided by American Physical Society, and the payment instructions.

License Number	3732691209875
License date	Oct 19, 2015
Licensed Content Publisher	American Physical Society
Licensed Content Publication	Physical Review C
Licensed Content Title	Electric dipole moments: A global analysis
Licensed copyright line	©2015 American Physical Society
Licensed Content Author	Timothy Chupp and Michael Ramsey-Musolf
Licensed Content Date	Mar 6, 2015
Volume number	91
I would like to...	Thesis/Dissertation
Requestor type	Student
Format	Electronic
Portion	image/photo
Number of images/photos requested	1
Portion description	Figure 1
Rights for	Main product
Duration of use	Life of current edition
Creation of copies for the disabled	no
With minor editing privileges	no
For distribution to	Worldwide
In the following language(s)	Original language of publication
With incidental promotional use	no
The lifetime unit quantity of new product	0 to 499
The requesting person/organization is:	Jack Devlin
Order reference number	None
Title of your thesis / dissertation	Progress towards a more sensitive measurement of the electron electric dipole moment with YbF
Expected completion date	Jul 2015
Expected size (number of pages)	226
Total	0.00 USD
Terms and Conditions	

BIBLIOGRAPHY

- [1] E. M. Purcell and N. F. Ramsey, “On the Possibility of Electric Dipole Moments for Elementary Particles and Nuclei,” *Physical Review*, vol. 78, no. 6, pp. 807–807, Jun. 1950, doi: 10.1103/PhysRev.78.807.
- [2] J. H. Smith, E. M. Purcell, and N. F. Ramsey, “Experimental Limit to the Electric Dipole Moment of the Neutron,” *Physical Review*, vol. 108, no. 1, pp. 120–122, Oct. 1957, doi: 10.1103/PhysRev.108.120.
- [3] R. N. Zare, *Angular Momentum*. John Wiley & Sons, 1988.
- [4] T. D. Lee and C. N. Yang, “Question of Parity Conservation,” *Phys. Rev.*, vol. 104, no. 1, pp. 254–258, 1956, doi: 10.1103/PhysRev.104.254.
- [5] C. S. Wu, E. Ambler, R. W. Hayward, D. D. Hoppes, and R. P. Hudson, “Experimental Test of Parity Conservation in Beta Decay,” *Physical Review*, vol. 105, no. 4, pp. 1413–1415, Feb. 1957, doi: 10.1103/PhysRev.105.1413.
- [6] J. H. Christenson, J. W. Cronin, V. L. Fitch, and R. Turlay, “Evidence for the 2π Decay of the K_2^0 Meson,” *Physical Review Letters*, vol. 13, no. 4, pp. 138–140, Jul. 1964, doi: 10.1103/PhysRevLett.13.138.
- [7] B. Aubert *et al.*, “Measurement of CP-Violating Asymmetries in B^0 Decays to CP Eigenstates,” *Physical Review Letters*, vol. 86, no. 12, pp. 2515–2522, Mar. 2001, doi: 10.1103/PhysRevLett.86.2515.
- [8] A. Abashian *et al.*, “Measurement of the CP Violation Parameter $\sin 2\varphi_1$ in B_d^0

- Meson Decays,” *Physical Review Letters*, vol. 86, no. 12, pp. 2509–2514, Mar. 2001, doi: 10.1103/PhysRevLett.86.2509.
- [9] R. Aaij *et al.*, “Measurements of Indirect CP Asymmetries in D^0 ,” *Physical Review Letters*, vol. 112, no. 4, p. 041801, Jan. 2014, doi: 10.1103/PhysRevLett.112.041801.
- [10] A. S. Streater, R F and Wightman, *PCT, Spin and Statistics, and All That*. Princeton University Press, 2000.
- [11] A. Angelopoulos *et al.*, “First direct observation of time-reversal non-invariance in the neutral-kaon system,” *Physics Letters B*, vol. 444, no. 1-2, pp. 43–51, Dec. 1998, doi: 10.1016/S0370-2693(98)01356-2.
- [12] J. P. Lees *et al.*, “Observation of Time-Reversal Violation in the B^0 Meson System,” *Physical Review Letters*, vol. 109, no. 21, p. 211801, Nov. 2012, doi: 10.1103/PhysRevLett.109.211801.
- [13] B. L. Roberts and W. J. Marciano, *Lepton Dipole Moments*. World Scientific, 2010.
- [14] J. Baron *et al.*, “Order of magnitude smaller limit on the electric dipole moment of the electron.” *Science (New York, N.Y.)*, vol. 343, no. 6168, pp. 269–72, Jan. 2014, doi: 10.1126/science.1248213.
- [15] Planck Collaboration *et al.*, “Planck 2015 results. I. Overview of products and scientific results,” p. 36, Feb. 2015. <https://arxiv.org/abs/1502.01582>
- [16] D. E. Morrissey and M. J. Ramsey-Musolf, “Electroweak baryogenesis,” *New Journal of Physics*, vol. 14, no. 12, p. 125003, Dec. 2012, doi: 10.1088/1367-2630/14/12/125003.

-
- [17] A. D. Sakharov, “Violation of CP in variance, C asymmetry, and baryon asymmetry of the universe,” *Soviet Physics Uspekhi*, vol. 34, no. 5, pp. 392–393, May 1991, doi: 10.1070/PU1991v034n05ABEH002497.
- [18] A. Riotto and M. Trodden, “Recent progress in baryogenesis,” *Annual Review of Nuclear and Particle Science*, vol. 49, no. 1, pp. 35–75, Dec. 1999, doi: 10.1146/annurev.nucl.49.1.35.
- [19] J. Engel, M. J. Ramsey-Musolf, and U. van Kolck, “Electric dipole moments of nucleons, nuclei, and atoms: The Standard Model and beyond,” *Progress in Particle and Nuclear Physics*, vol. 71, pp. 21–74, Jul. 2013, doi: 10.1016/j.pnpnp.2013.03.003.
- [20] N. Craig, “The State of Supersymmetry after Run I of the LHC,” p. 72, Sep. 2013. <http://arxiv.org/abs/1309.0528>
- [21] M. R. Tarbutt, B. E. Sauer, J. J. Hudson, and E. A. Hinds, “Design for a fountain of YbF molecules to measure the electron’s electric dipole moment,” *New Journal of Physics*, vol. 15, 2013, doi: 10.1088/1367-2630/15/5/053034.
- [22] J. L. Feng, “Naturalness and the Status of Supersymmetry,” *Annual Review of Nuclear and Particle Science*, vol. 63, no. 1, pp. 351–382, Oct. 2013, doi: 10.1146/annurev-nucl-102010-130447.
- [23] L. I. Schiff, “Measurability of Nuclear Electric Dipole Moments,” *Physical Review*, vol. 132, no. 5, pp. 2194–2200, Dec. 1963, doi: 10.1103/PhysRev.132.2194.
- [24] E. A. Hinds, “Testing time reversal symmetry using molecules,” *Physica Scripta*, vol. T70, no. T70, pp. 34–41, Jan. 1997, doi: 10.1088/0031-8949/1997/T70/005.
- [25] E. D. Commins, J. D. Jackson, and D. P. DeMille, “The electric dipole moment of the electron: An intuitive explanation for the evasion of Schiff’s

- theorem,” *American Journal of Physics*, vol. 75, no. 6, p. 532, Jun. 2007, doi: 10.1119/1.2710486.
- [26] P. Sandars, “The electric dipole moment of an atom,” *Physics Letters*, vol. 14, no. 3, pp. 194–196, Feb. 1965, doi: 10.1016/0031-9163(65)90583-4.
- [27] S. A. Murthy, D. Krause Jr., Z. L. Li, and L. R. Hunter, “New Limits on the Electron Dipole Moment from Cesium,” *Physical Review Letters*, vol. 63, no. 9, pp. 965–968, 1989, doi: 10.1103/PhysRevLett.63.965.
- [28] K. Abdullah, C. Carlberg, E. Commins, H. Gould, and S. Ross, “New experimental limit on the electron electric dipole moment,” *Physical Review Letters*, vol. 65, no. 19, pp. 2347–2350, Nov. 1990, doi: 10.1103/PhysRevLett.65.2347.
- [29] E. Commins, S. Ross, D. DeMille, and B. Regan, “Improved experimental limit on the electric dipole moment of the electron,” *Physical Review A*, vol. 50, no. 4, pp. 2960–2977, Oct. 1994, doi: 10.1103/PhysRevA.50.2960.
- [30] B. C. Regan, E. D. Commins, C. J. Schmidt, and D. DeMille, “New limit on the electron electric dipole moment,” *Physical Review Letters*, vol. 88, no. 7, p. 071805, 2002, doi: 10.1103/PhysRevLett.88.071805.
- [31] M. G. Kozlov and L. N. Labzowsky, “Parity violation effects in diatomics,” *Journal of Physics B: Atomic, Molecular and Optical Physics*, vol. 28, no. 10, pp. 1933–1961, May 1995, doi: 10.1088/0953-4075/28/10/008.
- [32] M. G. Kozlov, “Enhancement of the electric dipole moment of the electron in the YbF molecule,” *Journal of Physics B: Atomic, Molecular and Optical Physics*, vol. 30, no. 18, p. L607, 1997, doi: 10.1088/0953-4075/30/18/003.
- [33] T. Chupp and M. Ramsey-Musolf, “Electric dipole moments: A global analysis,” *Physical Review C*, vol. 91, no. 3, p. 035502, Mar. 2015, doi: 10.1103/PhysRevC.91.035502.

-
- [34] L. V. Skripnikov and A. V. Titov, “Theoretical study of thorium monoxide for the electron electric dipole moment search: electronic properties of $H\ ^3\Delta_1$ in ThO.” *The Journal of Chemical Physics*, vol. 142, no. 2, p. 024301, Jan. 2015, doi: 10.1063/1.4904877.
- [35] E. Kirilov *et al.*, “Shot-noise-limited spin measurements in a pulsed molecular beam,” *Physical Review A*, vol. 88, no. 1, p. 013844, Jul. 2013, doi: 10.1103/PhysRevA.88.013844.
- [36] J. J. Hudson, D. M. Kara, I. J. Smallman, B. E. Sauer, M. R. Tarbutt, and E. A. Hinds, “Improved measurement of the shape of the electron.” *Nature*, vol. 473, no. 7348, pp. 493–496, 2011, doi: 10.1038/nature10104.
- [37] W. C. Griffith, M. D. Swallows, T. H. Loftus, M. V. Romalis, B. R. Heckel, and E. N. Fortson, “Improved limit on the permanent electric dipole moment of ^{199}Hg ,” *Phys. Rev. Lett.*, vol. 102, p. 101601, Mar 2009, doi: 10.1103/PhysRevLett.102.101601.
- [38] S. Eckel, P. Hamilton, E. Kirilov, H. W. Smith, and D. DeMille, “Search for the electron electric dipole moment using Ω -doublet levels in PbO,” *Physical Review A*, vol. 87, no. 5, p. 052130, May 2013, doi: 10.1103/PhysRevA.87.052130.
- [39] N. R. Hutzler *et al.*, “A cryogenic beam of refractory, chemically reactive molecules with expansion cooling.” *Physical Chemistry Chemical Physics : PCCP*, vol. 13, no. 42, pp. 18976–85, Nov. 2011, doi: 10.1039/c1cp20901a.
- [40] Y. Kim *et al.*, “New experimental limit on the electric dipole moment of the electron in a paramagnetic insulator,” *Physical Review D*, vol. 91, no. 10, p. 102004, May 2015, doi: 10.1103/PhysRevD.91.102004.
- [41] S. Eckel, A. O. Sushkov, and S. K. Lamoreaux, “Limit on the Electron Electric Dipole Moment Using Paramagnetic Ferroelectric $\text{Eu}_{0.5}\text{Ba}_{0.5}\text{TiO}_3$,” *Physi-*

- cal Review Letters*, vol. 109, no. 19, p. 193003, Nov. 2012, doi: 10.1103/PhysRevLett.109.193003.
- [42] J. Lee *et al.*, “Optical spectroscopy of tungsten carbide for uncertainty analysis in electron electric-dipole-moment search,” *Physical Review A*, vol. 87, no. 2, p. 022516, Feb. 2013, doi: 10.1103/PhysRevA.87.022516.
- [43] F. Fang and D. S. Weiss, “Resonator-enhanced optical guiding and trapping of Cs atoms,” *Optics Letters*, vol. 34, no. 2, p. 169, Jan. 2009, doi: 10.1364/OL.34.000169.
- [44] H. Kawamura *et al.*, “Search for permanent EDM using laser cooled Fr atoms,” *Hyperfine Interactions*, vol. 214, no. 1-3, pp. 133–139, Feb. 2013, doi: 10.1007/s10751-013-0788-7.
- [45] M. V. Romalis and E. N. Fortson, “Zeeman frequency shifts in an optical dipole trap used to search for an electric-dipole moment,” *Physical Review A*, vol. 59, no. 6, pp. 4547–4558, Jun. 1999, doi: 10.1103/PhysRevA.59.4547.
- [46] A. Leanhardt *et al.*, “High-resolution spectroscopy on trapped molecular ions in rotating electric fields: A new approach for measuring the electron electric dipole moment,” *Journal of Molecular Spectroscopy*, vol. 270, no. 1, pp. 1–25, Nov. 2011, doi: 10.1016/j.jms.2011.06.007.
- [47] K. C. Cossel *et al.*, “Broadband velocity modulation spectroscopy of HfF^+ : Towards a measurement of the electron electric dipole moment,” *Chemical Physics Letters*, vol. 546, pp. 1–11, Sep. 2012, doi: 10.1016/j.cplett.2012.06.037.
- [48] L. V. Skripnikov and A. V. Titov, “Theoretical study of ThF^+ in the search for T,P-violation effects: Effective state of a Th atom in ThF^+ and ThO compounds,” *Physical Review A*, vol. 91, no. 4, p. 042504, Apr. 2015, doi: 10.1103/PhysRevA.91.042504.

-
- [49] I. J. Smallman, “A New Measurement of the Electron Electric Dipole Moment Using Ytterbium Fluoride,” Ph.D. dissertation, Imperial College London, 2013. <http://www3.imperial.ac.uk/ccm/publications/extra>
- [50] B. E. Sauer, J. Wang, and E. A. Hinds, “Laser-rf double resonance spectroscopy of ^{174}YbF in the $X^2\Sigma^+$ state: Spin-rotation, hyperfine interactions, and the electric dipole moment,” *The Journal of Chemical Physics*, vol. 105, no. 17, p. 7412, Nov. 1996, doi: 10.1063/1.472569.
- [51] K. Dunfield, C. Linton, T. Clarke, J. McBride, A. Adam, and J. Peers, “Laser Spectroscopy of the Lanthanide Monofluorides: Analysis of the $A^2\Pi-X^2\Sigma^+$ Transition of Ytterbium Monofluoride,” *Journal of Molecular Spectroscopy*, vol. 174, no. 2, pp. 433–445, Dec. 1995, doi: 10.1006/jmsp.1995.0014.
- [52] B. E. Sauer, S. B. Cahn, M. G. Kozlov, G. D. Redgrave, and E. A. Hinds, “Perturbed hyperfine doubling in the $A^2\Pi_{1/2}$ and $[18.6]0.5$ states of YbF ,” *The Journal of Chemical Physics*, vol. 110, no. 17, p. 8424, Apr. 1999, doi: 10.1063/1.478751.
- [53] X. Zhuang *et al.*, “Franck-Condon factors and radiative lifetime of the $A^2\Pi_{1/2}-X^2\Sigma^+$ transition of ytterbium monofluoride, YbF ,” *Physical Chemistry Chemical Physics : PCCP*, vol. 13, no. 42, pp. 19013–7, Nov. 2011, doi: 10.1039/c1cp21585j.
- [54] M. R. Tarbutt *et al.*, “A jet beam source of cold YbF radicals,” *Journal of Physics B Atomic Molecular and Optical Physics*, vol. 35, no. 24, pp. 5013–5022, 2002, doi: 10.1088/0953-4075/35/24/306.
- [55] P. C. Condylis, “Measuring the electron electric dipole moment using supersonic YbF ,” Ph.D. dissertation, Imperial College London, 2006. <http://www3.imperial.ac.uk/ccm/publications/extra>

-
- [56] S. Truppe, “New Physics with Cold Molecules: Precise Microwave Spectroscopy of CH and the Development of a Microwave Trap,” Ph.D. dissertation, Imperial College London, 2014. <http://www3.imperial.ac.uk/ccm/publications/extra>
- [57] D. Kara, “Towards an electron electric dipole moment measurement using Ytterbium Fluoride,” Ph.D. dissertation, Imperial College London, 2010. <http://www3.imperial.ac.uk/ccm/publications/extra>
- [58] B. E. Sauer, D. M. Kara, J. J. Hudson, M. R. Tarbutt, and E. A. Hinds, “A robust floating nanoammeter.” *The Review of Scientific Instruments*, vol. 79, no. 12, p. 126102, Dec. 2008, doi: 10.1063/1.3036985.
- [59] P. J. Mohr, B. N. Taylor, and D. B. Newell, “CODATA recommended values of the fundamental physical constants: 2010,” *Reviews of Modern Physics*, vol. 84, no. 4, pp. 1527–1605, Nov. 2012, doi: 10.1103/RevModPhys.84.1527.
- [60] D. Kara, I. J. Smallman, J. J. Hudson, B. E. Sauer, M. R. Tarbutt, and E. A. Hinds, “Measurement of the electron’s electric dipole moment using YbF molecules: methods and data analysis,” *New Journal of Physics*, vol. 14, no. 10, p. 103051, 2012, doi: 10.1088/1367-2630/14/10/103051.
- [61] J. J. Hudson, M. R. Tarbutt, B. E. Sauer, and E. A. Hinds, “Stochastic multi-channel lock-in detection,” *New Journal of Physics*, vol. 16, no. 1, p. 013005, Jan. 2014, doi: 10.1088/1367-2630/16/1/013005.
- [62] R. Brad, E and Tibshirani, *An introduction to the bootstrap*. Chapman & Hall/CRC, 1993.
- [63] A. C. Davison and H. D. V, *Bootstrap methods and their application*. Cambridge University Press, 1997.

-
- [64] M. R. Tarbutt, J. J. Hudson, B. E. Sauer, and E. A. Hinds, “Prospects for measuring the electric dipole moment of the electron using electrically trapped polar molecules,” *Faraday Discuss.*, vol. 142, pp. 37–56, 2009. doi:10.1039/B820625B
- [65] R. A. Kishek, Y. Y. Lau, L. K. Ang, A. Valfells, and R. M. Gilgenbach, “Multipactor discharge on metals and dielectrics: Historical review and recent theories,” *Physics of Plasmas*, May 1998, doi: 10.1063/1.872883.
- [66] B. E. Sauer *et al.*, “Time reversal symmetry violation in the YbF molecule,” *Hyperfine Interactions*, vol. 214, no. 1-3, pp. 119–126, Feb. 2013, doi: 10.1007/s10751-013-0803-z.
- [67] S. Skoff *et al.*, “Diffusion, thermalization, and optical pumping of YbF molecules in a cold buffer-gas cell,” *Physical Review A*, vol. 83, no. 2, Feb. 2011, doi: 10.1103/PhysRevA.83.023418.
- [68] S. Skoff, “Buffer gas cooling of YbF molecules,” Ph.D. dissertation, Imperial College London, 2011. <http://www3.imperial.ac.uk/ccm/publications/extra>
- [69] M. R. Tarbutt, “Magneto-optical trapping forces for atoms and molecules with complex level structures,” *New Journal of Physics*, vol. 17, no. 1, p. 015007, 2015, doi: 10.1088/1367-2630/17/1/015007.
- [70] E. S. Shuman, J. F. Barry, D. R. Glenn, and D. DeMille, “Radiative Force from Optical Cycling on a Diatomic Molecule,” *Physical Review Letters*, vol. 103, no. 22, p. 223001, Nov. 2009, doi: 10.1103/PhysRevLett.103.223001.
- [71] C. J. Foot, *Atomic Physics*. Oxford University Press, 2005.
- [72] A. Rushdi, R. Menendez, R. Mittra, and S.-w. Lee, “Leaky Modes in Parallel-Plate EMP Simulators,” *IEEE Transactions on Electromagnetic Compatibility*, vol. EMC-20, no. 3, pp. 443–451, Aug. 1978, doi: 10.1109/TEM.1978.303677.

-
- [73] Y. Fan, H. Yang, M. Li, and G. Zou, “Evaluation of the microwave absorption property of flake graphite,” *Materials Chemistry and Physics*, vol. 115, no. 2-3, pp. 696–698, Jun. 2009, doi: 10.1016/j.matchemphys.2009.02.010.
- [74] P. M. Farrell, W. R. MacGillivray, and M. C. Standage, “Quantum-electrodynamic calculation of hyperfine-state populations in atomic sodium,” *Physical Review A*, vol. 37, no. 11, pp. 4240–4251, Jun. 1988, doi: 10.1103/PhysRevA.37.4240.
- [75] J. R. Ackerhalt, P. L. Knight, and J. H. Eberly, “Radiation Reaction and Radiative Frequency Shifts,” *Physical Review Letters*, vol. 30, no. 10, pp. 456–460, Mar. 1973, doi: 10.1103/PhysRevLett.30.456.
- [76] J. R. Ackerhalt and J. H. Eberly, “Quantum electrodynamics and radiation reaction: Nonrelativistic atomic frequency shifts and lifetimes,” *Physical Review D*, vol. 10, no. 10, pp. 3350–3375, Nov. 1974, doi: 10.1103/PhysRevD.10.3350.
- [77] M. G. Boshier, “Spontaneous Decay Between Groups of Nearly Degenerate States,” Tech. Rep., 2009.
- [78] C. Cohen-Tannoudji, J. Dupont-Roc, and G. Grynberg, *Atom-Photon Interactions: Basic Processes and Applications*. Wiley, 1998.
- [79] K. Mølmer, “Friction and diffusion coefficients for cooling of atoms in laser fields with multidimensional periodicity,” *Physical Review A*, vol. 44, no. 9, pp. 5820–5832, Nov. 1991, doi: 10.1103/PhysRevA.44.5820.
- [80] D. J. Berkeland and M. G. Boshier, “Destabilization of dark states and optical spectroscopy in Zeeman-degenerate atomic systems,” *Physical Review A*, vol. 65, no. 3, p. 033413, Feb. 2002, doi: 10.1103/PhysRevA.65.033413.
- [81] T. Lindvall, M. Merimaa, I. Tittonen, and A. A. Madej, “Dark-state suppression and optimization of laser cooling and fluorescence in a trapped alkaline-

- earth-metal single ion,” *Physical Review A*, vol. 86, no. 3, p. 033403, Sep. 2012, doi: 10.1103/PhysRevA.86.033403.
- [82] J. F. Barry, “Laser cooling and slowing of a diatomic molecule,” Ph.D. dissertation, Yale University, 2013.
- [83] B. D. Agap’ev, M. B. Gorny, B. G. Matisov, and Y. V. Rozhdestvenski, “Coherent population trapping in quantum systems,” *Physics-Uspekhi*, vol. 36, no. 9, pp. 763–793, Sep. 1993, doi: 10.1070/PU1993v036n09ABEH002306.
- [84] J. J. Hudson, “Measuring the electric dipole moment of the electron with YbF molecules,” D. Phil. Thesis, University of Sussex, 2001. <http://www3.imperial.ac.uk/ccm/publications/extra>
- [85] P. W. Hess, “Improving the Limit on the Electron EDM: Data Acquisition and Systematics Studies in the ACME Experiment,” Ph.D. dissertation, Harvard University, 2014. http://www.doylegroup.harvard.edu/files/bufferpubs/theses/pwh_thesis.pdf
- [86] J. Binney and D. Skinner, *The Physics of Quantum Mechanics*. OUP Oxford, 2013.
- [87] J. M. Brown and A. Carrington, *Rotational Spectroscopy of Diatomic Molecules*. Cambridge University Press, 2003.
- [88] T. E. Wall *et al.*, “Lifetime of the $A(v' = 0)$ state and Franck-Condon factor of the $A-X(0-0)$ transition of CaF measured by the saturation of laser-induced fluorescence,” *Phys. Rev. A*, vol. 78, no. 6, p. 62509, Dec. 2008, doi: 10.1103/PhysRevA.78.062509.
- [89] J. M. Brown and B. J. Howard, “An approach to the anomalous commutation relations of rotational angular momenta in molecules,” *Molecular Physics*, vol. 31, no. 5, pp. 1517–1525, 1975.

-
- [90] T. Ma, C. Butler, J. Brown, C. Linton, and T. Steimle, “Optical Zeeman spectroscopy of ytterbium monofluoride, YbF.” *The Journal of Physical Chemistry. A*, vol. 113, no. 28, pp. 8038–44, Jul. 2009, doi: 10.1021/jp903596g.